

Numerical Modeling of Guided Waves in Anisotropic Composites with Application to Air-coupled Ultrasonic Inspection

Zur Erlangung des akademischen Grades eines

DOCTOR RERUM NATURALIUM

von der Mathematisch-Naturwissenschaftlich-Technischen Fakultät
der Universität Augsburg

vorgelegte

DISSERTATION

von

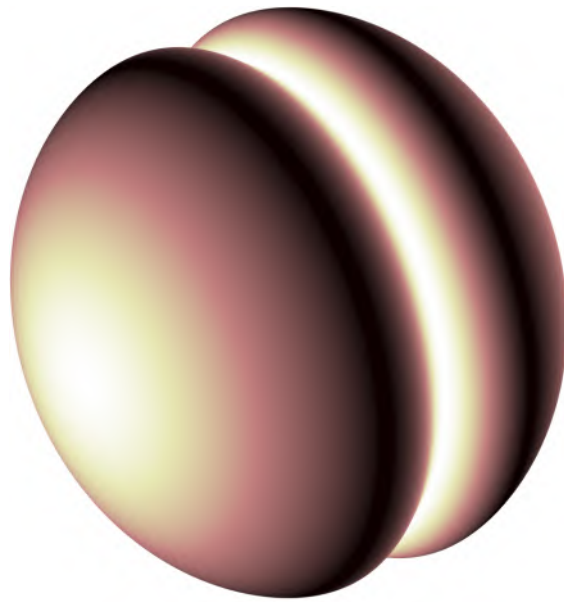
M. Sc. Armin Huber
geb. in Augsburg

Erstgutachter:
Zweitgutachter:
Drittgutachter:

Prof. Dr. rer. nat. habil. Markus Sause
Prof. Dr.-Ing. Michael Kupke
Prof. Michael Lowe

Tag der mündlichen Prüfung:

16. Dezember 2020



Phase velocity surface of fast quasishear waves emanating from a point source in a transversely isotropic fiber-epoxy system. The fibers are oriented parallel to the rotation axis of this 'yo-yo'.

Dedicated to

my wife Anja and to our children

Preface

This thesis has been motivated by my desire to get a comprehensive understanding of the physics of ultrasonic guided waves in solids. My field of application is the air-coupled ultrasonic inspection of aerospace vehicle components by means of Lamb waves. These components are manufactured from multilayered carbon fiber reinforced plastics. In order to excite a particular Lamb wave mode in a laminate, ultrasound must be transmitted under the correct angle of excitation with respect to the surface normal. The initial task for the work presented here was the calculation of Lamb wave dispersion diagrams from which those excitation angles can be obtained. This task was accomplished after some time of intense work in MATLAB[®], and thereby the aim of the project in terms of guided wave modeling was satisfied. However, my drive to get deeper into the physics and calculate fascinating phenomena like internal field distributions of Lamb waves or wave front surfaces of elastic waves in transversely isotropic fiber-epoxy systems made me go on. Although the programming was quite a struggle many times, I found the excitement experienced whenever a result matched the literature so satisfying that I would go so far to call this work a passion of mine. After about two years, a substantial amount of functionality had been created, and I felt that I should make it available to the scientific community. In fact, I considered it a waste of resources if just I could use the code every now and then, and in the meantime it would rest on the hard drive. Moreover, there was no free software for the dispersion curve calculation for multilayered composites available, and it is evident from researcher requests, which can be found in the internet, that the community only waited for a free software to appear. Therefore, I released the Dispersion Calculator as a free software in November 2018 to fill the gap, and from what I can oversee, like from user reports from different countries, the Dispersion Calculator has made a quite good impact in the community. With this in mind, I am highly motivated to continue with the work on the Dispersion Calculator after this thesis is completed. After all, users have asked me do so because there is still plenty work to do, and, beside my own curiosity, what could be more inspiring than a user telling you that he is looking forward to the next Dispersion Calculator release? Knowing that people need my work is exactly what makes me enjoy going to work every day.

Two developments are presented in this thesis. The first one is of course the Dispersion Calculator, featuring the unique capability of calculating laminates consisting of several hundreds of layers. The second is an Adaptive End-Effector, enabling

the automated single-sided air-coupled ultrasonic inspection of components with varying thicknesses and curvatures. For its operation, a so-called excitation angle map of the component to be inspected must be calculated. Therefore, after the introduction in Chapter 1, a comprehensive study of elastic wave modeling in solids is given in Chapter 2. The functionality, key features, and performance of the Dispersion Calculator are presented. The nondestructive inspection method of air-coupled ultrasonic testing is covered in Chapter 3. First, we discuss the conventional inspection modes, and then we present the new and superior inspection method based on the Adaptive End-Effector. Finally, we summarize the outcome of the present thesis in Chapter 4. It is my sincere hope that both the Dispersion Calculator and this thesis will be helpful to the reader in his own research in the field of ultrasonic guided waves.

I would like to thank Prof. Dr. Markus Sause for supervising my doctoral thesis and for answering my frequent emails so promptly. He has supported me by measuring the engineering constants of SAERTEX[®]7006919/RIMR135 and by compiling the Dispersion Calculator releases. Thanks to his aid, our paper made it into the Journal of the Acoustical Society of America. I would also like to thank Prof. Dr. Michael Kupke for the opportunity to conduct the research in the field of ultrasonics at the Center for Lightweight Production Technology of the German Aerospace Center in Augsburg. Another great supporter of my work is my group leader, Dr. Alfons Schuster. I am particularly grateful to Prof. Michael Lowe, Prof. Michel Castaings, and Prof. Stanislav Rokhlin for their sound advice and valuable time spent on discussions that helped me to write the Dispersion Calculator. I should emphasize that without Prof. Lowe's software DISPERSE, I could not have written the Dispersion Calculator and in turn this thesis as they exist today. Also, my brother, Sigurd, has inspired me in many discussions on physics, even if it was on the general theory of relativity. Whereas I am the only author of the Dispersion Calculator, the Adaptive End-Effector is a product of teamwork. Therefore, I would like to thank Manfred Schönheits who spent many nights and weekends on the integration of the Adaptive End-Effector into the robotic cell. He has also contributed greatly to the development of the software tool chain. I am also grateful to Philipp Gänswürger for developing the layout of the Adaptive End-Effector and for the construction of its mechanical components. My special thanks goes to my wife, Anja, for supporting me in my work. With her patience, she enabled me working on the Dispersion Calculator many nights and weekends, while she took care of the three children. Last but not least, I want to express my gratitude to my parents for enabling me to become a scientist.

Armin Huber

Augsburg, Germany
December 2019

Contents

1	Introduction	1
1.1	Modeling of Guided Waves	1
1.2	Air-coupled Ultrasonic Inspection	5
2	Modeling of Guided Waves	7
2.1	Field Equations	8
2.1.1	Stiffness Tensor	10
2.1.2	Matrix Form of Stiffness	10
2.1.3	Engineering Constants	12
2.1.4	Transformed Equations	14
2.1.5	Homogenized Stiffness Tensor	17
2.1.6	Expanded Field Equations	19
2.2	Bulk Waves	22
2.2.1	Elastic Waves in Bulk Material	24
2.2.2	Bulk Waves on Interfaces	39
2.3	Multilayered Transversely Isotropic Waveguides	46
2.3.1	Geometrical Setup and General Description	47
2.3.2	General Boundary Conditions	48
2.3.3	Transfer Matrix Method	49
2.3.4	Stiffness Matrix Method	61
2.3.5	Special Boundary Conditions	69
2.3.6	Group Velocity, Propagation Time, and Excitation Angle	72
2.4	Isotropic Waveguides	74
2.4.1	Christoffel's Equation for Isotropic Media	75
2.4.2	Lamb Waves	76
2.4.3	Shear Horizontal Waves	83
2.5	Dispersion Curve Tracing	87
2.6	Dispersion Calculator	94
2.6.1	Development History	94
2.6.2	Dispersion Calculator and DISPERSE	96
2.7	Numerical Examples	103
2.7.1	Validation	103
2.7.2	Guided Wave Characteristics	111
2.7.3	Large Numbers of Layers	123

3	Air-coupled Ultrasonic Inspection	128
3.1	Fundamental Concepts and Application	128
3.1.1	Normal Transmission Mode	132
3.1.2	Focused Slanted Reflection Mode	133
3.1.3	Comparison	141
3.2	Adaptive End-Effector	147
3.2.1	Aircraft Skin Element Demonstrator	147
3.2.2	Software Toolchain	149
3.2.3	End-Effector Design	153
3.2.4	Experimental Validation	156
4	Conclusions and Outlook	162
4.1	Dispersion Calculator	162
4.2	Adaptive End-Effector	165
A	Dispersion Calculator User's Manual	167
B	Material Parameters	203
C	Polynomial Forms of the Christoffel Matrix	205
D	Transfer Matrix	208
E	Stiffness Matrix	209
F	Flaw List	210
	Acronyms and Symbols	211
	Bibliography	217
	Curriculum Vitae	231

1 Introduction

In Sec. 1.1, we retrace the history of guided wave modeling from their origins in the 1880s up to the most recent developments. We point out briefly our reasons why we chose to apply the stiffness matrix method for our own implementation. In Sec. 1.2, we give a brief historical review of the nondestructive inspection by means of guided waves, and explain in short how we intend to improve the state-of-the-art.

1.1 Modeling of Guided Waves

The first work in the field was done by Lord Rayleigh, who in 1885 studied the propagation of waves along the free surface of a semi-infinite elastic solid [1]. Rayleigh calculated the phase velocity of those surface waves, termed *Rayleigh waves* since then. In 1911, Love described a shear horizontally polarized elastic wave propagating along the interface of two solids with different elastic properties in rigid contact [2]. Since then, this wave type is known as the *Love wave*. Lamb in 1917 studied the propagation of free waves in plates [3]. *Lamb waves* in its original sense have polarization only in the sagittal plane, spanned by the propagation direction along the plate and by the out-of-plane-direction. Lamb presented distinct solutions for modes with symmetric and antisymmetric displacement patterns. Nowadays, waves with only sagittal polarization are also termed as *pure* Lamb waves, whereas waves including also a not too prominent shear horizontal polarization component are called Lamb waves or Lamb-like waves in honor of their original investigator. These kind of Lamb waves occur in anisotropic media such as composites, which Lamb did not deal with, of course. In 1924, Stonely investigated the propagation of surface waves along the interface of two solids, since then referred to as *Stonely waves* [4]. In an attempt to consider a Stonely wave propagating along the interface between a solid and water, Scholte in 1947 discovered a new and abnormal type of wave, the *Scholte wave*, propagating with a speed lower than any of the bulk wave velocities in the solid and water [5].

The first investigation of guided wave propagation in a layered flat plate was conducted by Thomson in 1950 [6]. He introduced the *transfer matrix method* (TMM), where the transfer matrix relates the displacements and stresses at the top of a layer to those at its bottom. Through the multiplication of the individual layer transfer matrices, assuming the continuity of stresses and displacements across the layer boundaries, a global transfer matrix is obtained, relating the displacements and stresses at the top of the whole structure to those at its bottom.

Modal solutions are obtained through imposing the boundary condition of stress free top and bottom surfaces. A small error in Thomson's work was corrected by Haskell [7]. The advent of digital computers in the 1960s and early 1970s boosted the modeling of guided waves in multilayered structures. The TMM was implemented by many researchers, mostly to investigate seismological phenomena [8–17]. Nayfeh and Chimenti [18, 19] and Nayfeh [20, 21] extended the TMM to generally anisotropic multilayered media. This work is well-documented in the excellent book of Nayfeh [22]. However, Dunkin discovered in 1965 that the TMM becomes unstable when the product of the layer thickness and the frequency becomes large [23]. Numerically, the problem occurs when bulk waves contributing to a Lamb wave in one or more layers become evanescent. This leads to growing and decaying exponential functions, quickly overwhelming the precision of a computer, and leading to a singular transfer matrix. In practice, this means that a dispersion curve can only be calculated up to a certain frequency-thickness product. Many attempts have been undertaken to overcome the problem, mostly with limited success and at the expense of the simple form of the original formulation [24–32].

A different approach is the *global matrix method* (GMM), originally proposed for isotropic media by Knopoff in 1964 [33], and employed by many researchers since then [34–39]. A well-organized and instructive discussion of the TMM and the GMM is provided by Lowe in Ref. [40]. In the GMM, a large single matrix comprises the equations of all layers. Schmidt and Tango [41] and Schmidt and Jensen [42, 43] have shown that this method is numerically stable if implemented properly. Mal extended the GMM to anisotropic multilayered media [44, 45]. Kausel and Roesset [46] conducted a reformulation for isotropic cases and Wang and Rajapakse [47] for an orthotropic layer in the plane of symmetry. Wang and Rokhlin used this approach for the computation of the cell stiffness matrix of a cross-ply composite [48, 49]. Another stable formulation for isotropic media was introduced by Kennett [50] and Kennett and Kerry [51], subsequently extended to generally anisotropic media by Fryer and Frazer [52, 53], and also obtained later by Rokhlin and Huang [54]. However, the drawback of the GMM is that it becomes slow upon calculating many layers, owing to the corresponding large size of the global matrix. The software package DISPERSE (Imperial College London, London, UK), which was created by Lowe and Pavlakovic [55], is based on the GMM¹. In 2014, Pant *et al.* applied the GMM on a multilayered composite laminate [56].

The probably most powerful computation method for multilayered problems is the *stiffness matrix method* (SMM), developed by Rokhlin and Wang [57, 58] in 2001, and well-documented in the book of Rokhlin *et al.* [59]. Rokhlin and Wang have rearranged the transfer matrix formulation in such a way that the numerical instability for large frequency-thickness products is avoided, namely by removing

¹Prof. Lowe plans to implement the spectral collocation method (see below) in DISPERSE.

the growing and decaying exponential functions from the diagonal elements of the transfer matrix. Hence, this matrix, now called *stiffness matrix*, cannot become singular anymore. In contrast to the transfer matrix, the stiffness matrix relates the stresses at the top and bottom of a layer (or of the whole structure, respectively) to the displacements at the top and bottom of the layer/structure. At the same time, the SMM formulation retains the concise form and efficiency of the TMM. In practice, we can now calculate dispersion diagrams without limitation in the frequency-thickness product for a theoretically unlimited number of anisotropic layers. The SMM is used by researchers like Kamal and Giurgiutiu [60] and Barski *et al.* [61, 62] for the calculation of guided wave dispersion curves for multilayered composites. Huber and Sause in 2018 used the SMM to calculate dispersion diagrams for composite layups containing up to four hundred layers [63]. Such thick-walled laminates are used in modern rocket booster pressure vessels for the ARIANE 6 launcher. The dispersion diagrams presented by Huber and Sause were obtained with the free software *Dispersion Calculator* (DC), released by Huber in 2018 [64].

As an alternative to root-finding methods, the *semi-analytical finite element* (SAFE) method was introduced by Gavric [65] in 1995 for the calculation of guided wave dispersion curves for a free rail. The SAFE method discretizes the waveguide's cross section into finite elements, allowing the modeling of guided waves in complex geometries. At the same time, the wave propagation direction is solved analytically, which makes this approach more efficient than a full *finite element method* (FEM) modeling. The SAFE approach has been used for many different scenarios. Hayashi *et al.* calculated guided wave dispersion curves for bar, rod, and rail examples [66]. Leaky waves propagating along waveguides of arbitrary cross sections surrounded by an infinite medium were considered by Castaings and Lowe [67]. Torsional waves propagating along arbitrary cross sectional waveguides immersed in a fluid [68] and elastic waves propagating along weld joints between plates [69] were modeled by Fan *et al.* Bartoli *et al.* and Marzani *et al.* investigated guided waves in viscoelastic waveguides of rectangular, arbitrary [70], and axisymmetric [71] cross sections. Another study of dispersion curve calculation for complex waveguides was conducted by Sorohan *et al.* [72]. The *local interaction simulation approach* (LISA), a method studied by Delsanto *et al.* for a three-dimensional case in 1997 [73] discretizes the structure into a lattice. The advantage of the LISA is that discontinuities in the material's properties can be modeled by changing the properties of the lattice at the corresponding locations. The LISA is applied for the modeling of isotropic as well as anisotropic specimens [74, 75].

The possibly most powerful and versatile discretizing method is the *spectral collocation method* (SCM), introduced by Adamou and Craster for guided wave modeling in elastic media in 2004 [76]. The SCM is similar to the SAFE approach in that it is using a one-dimensional mesh over the system's cross section, but the

SCM possesses a higher accuracy and speed of computation. Instead of solving a differential equation directly, the SCM uses a spectral approximation, which satisfies the differential equation and boundary conditions. Karpfinger *et al.* have applied the SCM for the modeling of wave dispersion along multilayered isotropic cylindrical structures [77] and later for axisymmetric wave modes in a porous elastic cylinder [78] as well as for a geophysical application involving boreholes [79, 80]. Yu *et al.* have combined the SCM with root-finding methods for the modeling of longitudinal guided waves in a multilayered tube [81]. Zharnikov *et al.* [82] used the SCM to obtain dispersion curves for anisotropic waveguides. Quintanilla *et al.* in 2015 have provided comprehensive studies of guided wave modeling in generally anisotropic media by means of the SCM [83, 84], later adding three-dimensional dispersion curve solutions [85]. The authors claim that the SCM is easier to code than root-finding methods, it is faster, and most importantly, it can definitely not miss any modal solution. In 2017, the same authors have developed a classification of multilayered anisotropic waveguides according to their symmetry and coupling properties [86]. All crystal classes and independent axes configurations can be assigned to one of only five different categories. A critical benefit is that modal solutions can be separated into mode families for which dispersion curves do not cross. This helps avoid the well-known jumping mode problem, which is present in root-finding methods in some situations. Furthermore, one can save time by computing only a single mode family if one is not interested in the other ones.

Since in the work presented here, our focus is on multilayered composites with up to several hundreds of layers, we decide to employ the SMM. It is so far the only stable computation method proven to be capable of efficiently calculating many layers. This has not yet been shown for the SCM. However, since we also want to benefit from the separation of the various mode families, similarly as it was demonstrated with the SCM, we implement mode family-specific characteristic functions and boundary conditions into the SMM. The advantage of the discretizing methods that they can model waveguides of complex cross sections, whereas the root-finding methods are limited to flat and cylindrical structures, does not help us in our plate-like laminates. Quite contrary, we benefit from the simple boundary conditions applicable in the flat case, giving us a boost in efficiency. Moreover, the modal solutions obtained for flat structures are valid in good approximation for curved structures with a radius significantly larger than the guided wave's wavelength. This is always the case in the air-coupled ultrasonic inspection scenarios presented in this work where the wavelength of the guided waves is in the range of millimeters to centimeters. This is small compared to the radii of curvature possessed by aircraft fuselages or rocket booster pressure vessels. Alternatively, in most cases, there is also one dimension for which the component is flat.

1.2 Air-coupled Ultrasonic Inspection

Guided waves have been used for the *nondestructive inspection* (NDI) for many decades. An early description of the flaw detection in sheets and tubes immersed in water by means of Rayleigh and Lamb waves was given by Viktorov already back in 1967 [87]. Only a few years later, Luukkala *et al.* proposed a contactless test method for paper and metal plates based on Lamb waves [88, 89]. Many applications have been established since then, and the advent of composite materials in automotive and aerospace industries, which took place in the early 1990s, has added significant complexity to the nondestructive testing and evaluation processes. The ability of guided waves to propagate many meters in a waveguide is utilized for pipe inspection [90, 91]. They are also used for the inspection of bonding [92], which is one of the most challenging tasks, especially in the case of kissing bonds [93]. Other relevant studies concerning NDI and *structural health monitoring* (SHM) on composite structures are found in Refs. [94–101]. *Air-coupled ultrasonic testing* (ACUT) could play an important role in future production lines. Often, the presence of a liquid coupling medium is unwanted because it might inflict damage to unsealed composite structures, beside other drawbacks. Furthermore, the air-coupled version is more suitable for inline NDI, thereby improving the cost-efficiency of the manufacturing process. All of the following researchers have used the air-coupled variant. Castaings *et al.* have done significant work on the single-sided ultrasonic testing of composites by using Lamb waves [102–105], while Solodov *et al.* have used them for transmissive inspection [106–108]. Mechanically induced fatigue on composites has been monitored by means of Lamb waves by Rheinforth *et al.* [109–111]. Holland and Chimenti have shown that the S_1 Lamb wave mode at zero group velocity allows for improved imaging capabilities [112], and Raisutis *et al.* have investigated the inspection of composite rods used in aerospace [113]. The interaction of the A_0 Lamb wave mode with delaminations in composites has been studied both experimentally and by FEM by Zenghua *et al.* [114]. The Spanish company Tecnatom [115] as well as the British University of Strathclyde together with the TWI Technology Centre [116] have achieved a remarkable progress in the automation of ACUT and other NDI methods. An automated air-coupled robot ultrasonic imaging system performing through transmission inspection was reported by Hillger *et al.* [117]. Huber demonstrated the automated inspection of a rocket booster pressure vessel demonstrator by means of Lamb waves in 2016 [118], and Schönheits *et al.* in 2019 developed a system enabling the automated inspection of components with varying thicknesses and curvatures [119].

One drawback of ACUT might be the large mismatch of the acoustic impedances of air and the solid to be tested. Consequently, there is a low transmission of ultrasound through the interface between air and metal or carbon fiber reinforced

plastics (CFRP). To deal with the problem, significant technical improvements have been achieved for instance in the field of electronics (digital filters, amplification, etc.), $\lambda/4$ coatings to reduce destructive interferences [120], and new piezo-composite materials for transducers with a reduced acoustic impedance [121]. In the 1990s, new transducer technologies have emerged like *capacitive micromachined ultrasound transducers* (CMUTs) [122–124] and electrostatic transducers [125]. The CMUTs offer a broader bandwidth and a much lower fabrication cost. Gerardo *et al.* have recently developed a new manufacturing process for inexpensive *polymer-based CMUTs* (polyCMUTs) [126, 127]. These transducers were developed for medical use initially, where the polymer’s acoustic impedance matches quite closely the one of human tissue. The Center for Lightweight Production Technology (ZLP) of the German Aerospace Center (DLR) is currently in a close cooperation with Gerardo to adapt the polyCMUTs for the use in SHM. Thanks to their flexibility, these low-cost polyCMUTs could be attached to aircraft structures and detect impacts live during the flight. Another possible application could be in ACUT where we may benefit from the reduced impedance mismatch between the polymer and air. A different technology is the thermo-acoustic sound generation using metallic and carbon materials for transducers [128, 129].

The problem we will tackle in this work is that the incidence angle adjusted to excite a Lamb wave changes with thickness and curvature variations present on components like aircraft skin elements. There is so far no system available, which automatically adapts the excitation angle on-the-fly during an inspection. Currently, such adaptations have to be done manually, a situation we intend to remedy.

2 Modeling of Guided Waves

This chapter provides a comprehensive discussion of the physics of guided waves and their numerical modeling with the ultimate goal of obtaining modal solutions in the form of dispersion diagrams. To enable a complete understanding of guided waves, a strong focus is laid on the basics of elastodynamics. In fact, guided waves evolve through the superposition of bulk waves reflecting between the parallel boundaries of a plate. Therefore, we start with the field equations in Sec. 2.1, and introduce the stiffness tensor for the various material symmetries, determining their elastic properties. Since our focus is on guided wave propagation along an arbitrary azimuthal angle in layered anisotropic composites, we will transform each layer's stiffness tensor from the crystallographic coordinate system into a global one. In Sec. 2.2, we use *Christoffel's equation* to calculate explicitly the wave front surfaces and polarization of bulk waves in the transversely isotropic fiber-epoxy system SAERTEX[®]7006919/RIMR135 (SAERTEX GmbH & Co. KG, Saerbeck, Germany) as well as their scattering on interfaces. Sec. 2.3 covers the modeling of guided waves in multilayered transversely isotropic media. First, we set up the TMM and use it to obtain modal solutions of shear horizontal waves in the decoupled case without encountering the numerical instability, which the TMM is known to suffer from. Then, we overcome the instability with the SMM, which we apply for the modeling of Lamb waves in the coupled and decoupled cases. To improve the robustness of the dispersion curve tracing, we introduce mode family-specific special characteristic equations and boundary conditions. Since isotropic materials are still widely spread and will probably also be so in the future, we cover the modeling of guided waves in isotropic single layers in Sec. 2.4. Modal solutions for Lamb waves are obtained numerically using the *Rayleigh-Lamb equations*, whereas analytic solutions exist for shear horizontal waves. Although dispersion diagrams for isotropic layers can be obtained comparatively fast, the speed of calculation is a particularly critical issue in the case of multilayered specimens. Therefore, Sec. 2.5 introduces the dispersion curve tracing algorithms implemented into the DC. Since the DC is, beside the Adaptive End-Effector (AEE), the main achievement of this thesis, Sec. 2.6 is dedicated to it, presenting its functionality, key features, and performance. Finally, we use the DC in Sec. 2.7 to compute a number of numerical examples. On the one hand, these examples serve for the validation of the DC and to proof its capabilities, in particular its ability to calculate laminates consisting of many layers. On the other hand, an in-depth study of the structure and behavior of guided waves in isotropic layers and multilayered composites is provided.

2.1 Field Equations

To carry out the physical-mathematical discussion of wave propagation in linearly elastic solids, the foundations of acoustic field theory in solids must be laid first. Therefore, we start the section by introducing the field equations. In Sec. 2.1.1, we will have a closer look at the stiffness tensor, defining the elastic properties of the solid wherein the elastic wave propagation takes place. We investigate the various symmetry properties that lead to a reduction in the number of independent material constants in the stiffness tensor. The outcome is quite fortunate, considering how complicated the explicit field equations would become if the full set of eighty-one constants had to be taken into account independently. In Sec. 2.1.2, we introduce *Voigt's notation* [130] and examine how the number of independent material constants is reduced even more thanks to the various materials' symmetry properties. In practice, the stiffness tensor is calculated from the engineering constants, which in turn are obtained experimentally. This will be the topic of Sec. 2.1.3. Since transversely isotropic laminates consist of a stacking of layers with different fiber orientations, we must transform the stiffness tensor for each layer into one global coordinate system, wherein we define the (guided) wave propagation to take place. Section 2.1.4 presents the corresponding transformation procedure. Although we do not use the *homogenized stiffness tensor* (HST) for the modeling of guided waves, we treat it in Sec. 2.1.5 since it provides a highly instructive picture of how the orientation of layers in a layup affects the effective stiffness of the laminate as a whole. Finally, we write out the field equations explicitly in Sec. 2.1.6. In discussing the aforementioned topics, we rely much on the excellent and highly instructive book of Nayfeh [22], and supplementary on the book of Auld [131]. Lowe gives a summary of useful equations related to the topic in the DISPERSE user's manual [132].

There exist two basic field equations and one *elastic constitutive equation*, which are the counterparts to *Maxwell's equations* describing electromagnetic fields [133]. The deformation caused by acoustical vibration in a body is given by the strain field $\boldsymbol{\varepsilon}$, which is related to the particle displacement field \mathbf{u} by the *strain-displacement relation*,

$$\boldsymbol{\varepsilon} = \nabla_s \mathbf{u}, \tag{2.1}$$

and the *equation of motion* is given by

$$\nabla \cdot \boldsymbol{\sigma} = \rho \frac{\partial^2 \mathbf{u}}{\partial t^2}, \tag{2.2}$$

where $\boldsymbol{\sigma}$ is the stress field and ρ is the density of the solid. $\nabla_s \mathbf{u}$ represents $\frac{1}{2}(\nabla \mathbf{u} + \nabla \mathbf{u}^T)$ [131]. The elastic constitutive equation, also known as *Hooke's law* [134],

$$\boldsymbol{\sigma} = \mathbf{c}\boldsymbol{\varepsilon}, \quad (2.3)$$

relates the stress field with the strain field via the stiffness tensor \mathbf{c} . Conversely, strain and stress are connected by the compliance tensor \mathbf{s} through

$$\boldsymbol{\varepsilon} = \mathbf{s}\boldsymbol{\sigma}, \quad (2.4)$$

where \mathbf{c} and \mathbf{s} contain the elastic material constants. The quantities \mathbf{u} , $\boldsymbol{\sigma}$, $\boldsymbol{\varepsilon}$, \mathbf{c} , and \mathbf{s} are tensors of rank one, two, two, four, and four, respectively. So far, we have used the standard practice in physics and engineering to give vector quantities by bold face letters in order to write the equations as compact as possible. However, in the following, it will be more convenient to use subscript notation. We introduce the Cartesian crystallographic coordinate system $x'_i = (x'_1, x'_2, x'_3)$, and rewrite Eq. (2.1) as

$$\varepsilon'_{kl} = \frac{1}{2} \left(\frac{\partial u'_l}{\partial x'_k} + \frac{\partial u'_k}{\partial x'_l} \right), \quad (2.5)$$

Eq. (2.2) as

$$\frac{\partial \sigma'_{ij}}{\partial x'_j} = \rho \frac{\partial^2 u'_i}{\partial t^2}, \quad (2.6)$$

and Hooke's law (2.3) and (2.4) as

$$\sigma'_{ij} = c'_{ijkl} \varepsilon'_{kl}, \quad \varepsilon'_{ij} = s'_{ijkl} \sigma'_{kl}, \quad i, j, k, l = 1, 2, 3. \quad (2.7)$$

In tensor analysis, the rank of a tensor depends on the number of its unrepeated indices. Repeated indices like j on the left-hand side of Eq. (2.6) lead to a contraction, which reduces the rank of its tensor by one according to *Einstein's notation* [135]. The resulting tensor on the left-hand side has rank one (vector) with the only free index i . Similarly, the products $c'_{ijkl} \varepsilon'_{kl}$ and $s'_{ijkl} \sigma'_{kl}$ on the right-hand sides in Eqs. (2.7) are reduced to a tensor of order two in virtue of the contraction of their repeated indices k and l . Accordingly, carrying out the left-hand Eq. (2.7) returns the stress components

$$\begin{aligned} \sigma'_{ij} = & c'_{ij11} \varepsilon'_{11} + c'_{ij12} \varepsilon'_{12} + c'_{ij13} \varepsilon'_{13} \\ & + c'_{ij21} \varepsilon'_{21} + c'_{ij22} \varepsilon'_{22} + c'_{ij23} \varepsilon'_{23} \\ & + c'_{ij31} \varepsilon'_{31} + c'_{ij32} \varepsilon'_{32} + c'_{ij33} \varepsilon'_{33}. \end{aligned} \quad (2.8)$$

2.1.1 Stiffness Tensor

Since each of the indices takes the values 1, 2, and 3, a tensor of order n has 3^n elements. Hence, σ'_{ij} , c'_{ijkl} , and ε'_{kl} have nine, eighty-one, and nine elements, respectively. Since σ'_{ij} and ε'_{kl} are symmetric, *i.e.*, $\sigma'_{ij} = \sigma'_{ji}$ and $\varepsilon'_{kl} = \varepsilon'_{lk}$, each one has only six independent elements. Using these symmetry properties in Eq. (2.7) yields

$$c'_{ijkl} = c'_{jikl} = c'_{ijlk} = c'_{jilk}, \quad (2.9)$$

thereby reducing the number of independent elements in c'_{ijkl} to thirty-six. The stress-strain relation can also be derived from the strain energy density U ,

$$U = \frac{1}{2} \sigma'_{ij} \varepsilon'_{ij} = \frac{1}{2} c'_{ijkl} \varepsilon'_{kl} \varepsilon'_{ij}. \quad (2.10)$$

Hence, one can express the stiffness tensor by

$$c'_{ijkl} = \frac{\partial^2 U}{\partial \varepsilon'_{ij} \partial \varepsilon'_{kl}}. \quad (2.11)$$

The commutativity of the differentiation implies that $c'_{ijkl} = c'_{klij}$. This reduces the number of independent elements in c'_{ijkl} further to twenty-one. That is the maximum number of independent elastic constants, which an anisotropic materials requires. Materials belonging to this class are called triclinic.

2.1.2 Matrix Form of Stiffness

Often, it is more convenient to express the stiffness tensor in matrix form. By using all of the aforementioned symmetry properties, we can write the stiffness matrix as

$$C'_{ij} = \begin{bmatrix} c'_{1111} & c'_{1122} & c'_{1133} & c'_{1123} & c'_{1113} & c'_{1112} \\ & c'_{2222} & c'_{2233} & c'_{2223} & c'_{2213} & c'_{2212} \\ & & c'_{3333} & c'_{3323} & c'_{3313} & c'_{3312} \\ & & & c'_{2323} & c'_{2313} & c'_{2312} \\ & & \text{sym} & & c'_{1313} & c'_{1312} \\ & & & & & c'_{1212} \end{bmatrix}. \quad (2.12)$$

By applying Voigt's notation, where $1 \rightarrow 11$, $2 \rightarrow 22$, $3 \rightarrow 33$, $4 \rightarrow 23$, $5 \rightarrow 13$, and $6 \rightarrow 12$, to the stiffness matrix, the left-hand side of Eqs. (2.7) is represented by

$$\begin{bmatrix} \sigma'_{11} \\ \sigma'_{22} \\ \sigma'_{33} \\ \sigma'_{23} \\ \sigma'_{13} \\ \sigma'_{12} \end{bmatrix} = \begin{bmatrix} C'_{11} & C'_{12} & C'_{13} & C'_{14} & C'_{15} & C'_{16} \\ & C'_{22} & C'_{23} & C'_{24} & C'_{25} & C'_{26} \\ & & C'_{33} & C'_{34} & C'_{35} & C'_{36} \\ & & & C'_{44} & C'_{45} & C'_{46} \\ & & \text{sym} & & C'_{55} & C'_{56} \\ & & & & & C'_{66} \end{bmatrix} \begin{bmatrix} \varepsilon'_{11} \\ \varepsilon'_{22} \\ \varepsilon'_{33} \\ \gamma'_{23} \\ \gamma'_{13} \\ \gamma'_{12} \end{bmatrix}, \quad (2.13)$$

where we introduce the shear strain components

$$\gamma'_{12} = 2\varepsilon'_{12}, \quad \gamma'_{13} = 2\varepsilon'_{13}, \quad \gamma'_{23} = 2\varepsilon'_{23}. \quad (2.14)$$

By using upper case C 's, the contracted Voigt's notation form is distinguished from the lower case c 's of the expanded tensor form. Equation (2.13) refers to **triclinic** materials, which have no material symmetry. Material symmetries lead to a further reduction in the number of independent coefficients. The stiffness matrices for various material classes are as follows:

Monoclinic:

$$C'_{ij} = \begin{bmatrix} C'_{11} & C'_{12} & C'_{13} & 0 & 0 & C'_{16} \\ & C'_{22} & C'_{23} & 0 & 0 & C'_{26} \\ & & C'_{33} & 0 & 0 & C'_{36} \\ & & & C'_{44} & C'_{45} & 0 \\ & & \text{sym} & & C'_{55} & 0 \\ & & & & & C'_{66} \end{bmatrix} \quad (2.15)$$

Orthotropic:

$$C'_{ij} = \begin{bmatrix} C'_{11} & C'_{12} & C'_{13} & 0 & 0 & 0 \\ & C'_{22} & C'_{23} & 0 & 0 & 0 \\ & & C'_{33} & 0 & 0 & 0 \\ & & & C'_{44} & 0 & 0 \\ & & \text{sym} & & C'_{55} & 0 \\ & & & & & C'_{66} \end{bmatrix} \quad (2.16)$$

Transversely isotropic:

$$C'_{ij} = \begin{bmatrix} C'_{11} & C'_{12} & C'_{12} & 0 & 0 & 0 \\ & C'_{22} & C'_{23} & 0 & 0 & 0 \\ & & C'_{22} & 0 & 0 & 0 \\ & & & \frac{C'_{22}-C'_{23}}{2} & 0 & 0 \\ & & \text{sym} & & C'_{55} & 0 \\ & & & & & C'_{55} \end{bmatrix} \quad (2.17)$$

Cubic:

$$C'_{ij} = \begin{bmatrix} C'_{11} & C'_{12} & C'_{12} & 0 & 0 & 0 \\ & C'_{11} & C'_{12} & 0 & 0 & 0 \\ & & C'_{11} & 0 & 0 & 0 \\ & & & C'_{44} & 0 & 0 \\ & \text{sym} & & & C'_{44} & 0 \\ & & & & & C'_{44} \end{bmatrix} \quad (2.18)$$

Isotropic:

$$C'_{ij} = \begin{bmatrix} C'_{11} & C'_{12} & C'_{12} & 0 & 0 & 0 \\ & C'_{11} & C'_{12} & 0 & 0 & 0 \\ & & C'_{11} & 0 & 0 & 0 \\ & & & \frac{C'_{11}-C'_{12}}{2} & 0 & 0 \\ & \text{sym} & & & \frac{C'_{11}-C'_{12}}{2} & 0 \\ & & & & & \frac{C'_{11}-C'_{12}}{2} \end{bmatrix} \quad (2.19)$$

2.1.3 Engineering Constants

In practice, the stiffness coefficients for orthotropic and higher symmetry materials are deduced from up to nine engineering constants, namely *Young's moduli* [136] along the axes of orthotropy E'_1 , E'_2 , E'_3 , the *shear moduli* in the planes perpendicular to the axes of orthotropy G'_{12} , G'_{13} , G'_{23} , and *Poisson's ratios* ν'_{12} , ν'_{13} , and ν'_{23} [137]. Because of the symmetry of the compliance matrix, the remaining Poisson's ratios are

$$\nu'_{21} = \frac{E'_2}{E'_1} \nu'_{12}, \quad \nu'_{31} = \frac{E'_3}{E'_1} \nu'_{13}, \quad \nu'_{32} = \frac{E'_3}{E'_2} \nu'_{23}. \quad (2.20)$$

These constants can be measured by tensile and compressive tests on macroscopic samples. A certain stress is applied to the sample, and the resulting strain is monitored. The strain-stress relation (2.4) of **orthotropic** materials is given by

$$\begin{bmatrix} \varepsilon'_{11} \\ \varepsilon'_{22} \\ \varepsilon'_{33} \\ \gamma'_{23} \\ \gamma'_{13} \\ \gamma'_{12} \end{bmatrix} = \begin{bmatrix} \frac{1}{E'_1} & -\frac{\nu'_{12}}{E'_1} & -\frac{\nu'_{13}}{E'_1} & 0 & 0 & 0 \\ & \frac{1}{E'_2} & -\frac{\nu'_{23}}{E'_2} & 0 & 0 & 0 \\ & & \frac{1}{E'_3} & 0 & 0 & 0 \\ & & & \frac{1}{G'_{23}} & 0 & 0 \\ & \text{sym} & & & \frac{1}{G'_{13}} & 0 \\ & & & & & \frac{1}{G'_{12}} \end{bmatrix} \begin{bmatrix} \sigma'_{11} \\ \sigma'_{22} \\ \sigma'_{33} \\ \sigma'_{23} \\ \sigma'_{13} \\ \sigma'_{12} \end{bmatrix}. \quad (2.21)$$

By inverting Eq. (2.21), we obtain the stiffness matrix for orthotropic material

$$\begin{bmatrix} \sigma'_{11} \\ \sigma'_{22} \\ \sigma'_{33} \\ \sigma'_{23} \\ \sigma'_{13} \\ \sigma'_{12} \end{bmatrix} = \begin{bmatrix} \frac{1-\nu'_{23}\nu'_{32}}{D} E'_1 & \frac{\nu'_{13}\nu'_{32}+\nu'_{12}}{D} E'_2 & \frac{\nu'_{12}\nu'_{23}+\nu'_{13}}{D} E'_3 & 0 & 0 & 0 \\ & \frac{1-\nu'_{13}\nu'_{31}}{D} E'_2 & \frac{\nu'_{21}\nu'_{13}+\nu'_{23}}{D} E'_3 & 0 & 0 & 0 \\ & & \frac{1-\nu'_{12}\nu'_{21}}{D} E'_3 & 0 & 0 & 0 \\ & \text{sym} & & G'_{23} & 0 & 0 \\ & & & & G'_{13} & 0 \\ & & & & & G'_{12} \end{bmatrix} \begin{bmatrix} \varepsilon'_{11} \\ \varepsilon'_{22} \\ \varepsilon'_{33} \\ \gamma'_{23} \\ \gamma'_{13} \\ \gamma'_{12} \end{bmatrix}, \quad (2.22)$$

corresponding to Eq. (2.16) with

$$D = 1 - \nu'_{12}\nu'_{21} - \nu'_{13}\nu'_{31} - \nu'_{23}\nu'_{32} - 2\nu'_{12}\nu'_{23}\nu'_{31}. \quad (2.23)$$

In case of **transversely isotropic** materials, the number of independent engineering constants is reduced to five since

$$\begin{aligned} E'_3 &= E'_2, \\ G'_{13} &= G'_{12}, \\ \nu'_{13} &= \nu'_{12}, \\ G'_{23} &= \frac{E'_2}{2(1 + \nu'_{23})}, \end{aligned} \quad (2.24)$$

yielding the stiffness matrix

$$\begin{bmatrix} \sigma'_{11} \\ \sigma'_{22} \\ \sigma'_{33} \\ \sigma'_{23} \\ \sigma'_{13} \\ \sigma'_{12} \end{bmatrix} = \begin{bmatrix} \frac{1-\nu'^2_{23}}{D} E'_1 & \frac{\nu'_{12}\nu'_{23}+\nu'_{12}}{D} E'_2 & C'_{12} & 0 & 0 & 0 \\ & \frac{1-\nu'_{12}\nu'_{21}}{D} E'_2 & \frac{\nu'_{21}\nu'_{12}+\nu'_{23}}{D} E'_2 & 0 & 0 & 0 \\ & & C'_{22} & 0 & 0 & 0 \\ & \text{sym} & & \frac{C'_{22}-C'_{23}}{2} & 0 & 0 \\ & & & & C'_{66} & 0 \\ & & & & & G'_{12} \end{bmatrix} \begin{bmatrix} \varepsilon'_{11} \\ \varepsilon'_{22} \\ \varepsilon'_{33} \\ \gamma'_{23} \\ \gamma'_{13} \\ \gamma'_{12} \end{bmatrix}, \quad (2.25)$$

corresponding to Eq. (2.17) with

$$D = 1 - \nu'^2_{23} - 2\nu'_{21}\nu'_{12} - 2\nu'_{12}\nu'_{23}\nu'_{21}. \quad (2.26)$$

A very convenient way to describe **isotropic** materials is through *Lamé's first and second parameters* λ and μ

$$\begin{aligned} \lambda &= \frac{E\nu}{(1+\nu)(1-2\nu)} = C_{12}, \\ \mu &= G = \frac{E}{2(1+\nu)} = C_{44} = \frac{C_{11} - C_{12}}{2}, \end{aligned} \quad (2.27)$$

where only two engineering constants, E and ν , are required. Here, we can drop the primed notation of the crystallographic coordinate system, and use a global coordinate system $x_i = (x_1, x_2, x_3)$ instead. The stiffness matrix in terms of Lamé's parameters is given as

$$\begin{bmatrix} \sigma_{11} \\ \sigma_{22} \\ \sigma_{33} \\ \sigma_{23} \\ \sigma_{13} \\ \sigma_{12} \end{bmatrix} = \begin{bmatrix} \lambda + 2\mu & \lambda & \lambda & 0 & 0 & 0 \\ & \lambda + 2\mu & \lambda & 0 & 0 & 0 \\ & & \lambda + 2\mu & 0 & 0 & 0 \\ & & & \mu & 0 & 0 \\ & \text{sym} & & & \mu & 0 \\ & & & & & \mu \end{bmatrix} \begin{bmatrix} \varepsilon_{11} \\ \varepsilon_{22} \\ \varepsilon_{33} \\ \gamma_{23} \\ \gamma_{13} \\ \gamma_{12} \end{bmatrix}, \quad (2.28)$$

corresponding to Eq. (2.19). Furthermore, we can use those parameters to directly determine the longitudinal bulk wave velocity

$$v_L = \sqrt{\frac{\lambda + 2\mu}{\rho}} = \sqrt{\frac{C_{11}}{\rho}}, \quad (2.29)$$

the transverse bulk wave velocity

$$v_T = \sqrt{\frac{\mu}{\rho}} = \sqrt{\frac{C_{44}}{\rho}}, \quad (2.30)$$

the plate wave velocity

$$c_{\text{Plate}} = \sqrt{\frac{E}{\rho(1 - \nu^2)}}, \quad (2.31)$$

and the approximate Rayleigh wave velocity

$$c_R \approx v_T \frac{0.87 + 1.12\nu}{1 + \nu}. \quad (2.32)$$

2.1.4 Transformed Equations

In this work, we conduct wave propagation analysis in multilayered composites such as sketched in Fig. 2.1. These are basically stackings of m layers with layer thicknesses d_m , consisting of a fiber-epoxy combination. For each layer, we assign a local (crystallographic) coordinate system $x'_{i(m)} = (x'_1, x'_2, x'_3)_{(m)}$ residing on the top of the m th layer, and we define the layers to lie parallel to the x'_1 - x'_2 -plane. The fibers are oriented along $x'_{1(m)}$, while $x'_{3(m)}$ is normal to the layer. To describe this system with arbitrary layer orientations in a convenient way, we use the non-primed global coordinate system $x_i = (x_1, x_2, x_3)$. With respect to this one, the

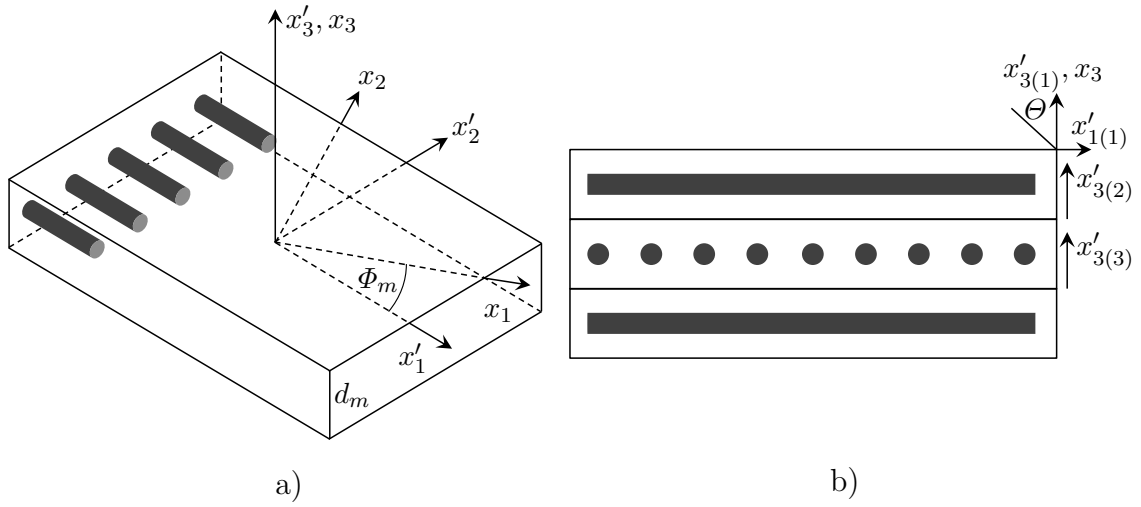


FIG. 2.1. (a) Single composite layer with local (crystallographic) coordinate system x'_i and global coordinate system x_i , $i = 1, 2, 3$. (b) Layered composite plate with $[0/90/0]$ orientation with respect to the x'_1 -axis.

local coordinate systems are yielded by a counterclockwise rotation of an angle Φ_m between x_1 and $x'_{1(m)}$ about the x_3 -axis. Hence, x_3 and $x'_{3(m)}$ coincide. Correspondingly, we must transform the stiffness tensor c'_{ijkl} from the local into the global coordinate system for each layer to get their respective transformed stiffness tensors $c_{ijkl(m)}$. For this task, we adopt the *orthogonal transformation method* proposed by Nayfeh [22]. Since the stiffness tensor c'_{ijkl} is a tensor of order four, its transformation from the local to the global coordinate system is achieved by

$$c_{mnop} = \beta_{mi}\beta_{nj}\beta_{ok}\beta_{pl}c'_{ijkl}, \quad (2.33)$$

where β_{ij} is a transformation tensor containing the cosines of the angles between the x_i and x'_i -axes, and which is written as

$$\beta_{ij} = \begin{bmatrix} \beta_{11} & \beta_{12} & \beta_{13} \\ \beta_{21} & \beta_{22} & \beta_{23} \\ \beta_{31} & \beta_{32} & \beta_{33} \end{bmatrix}. \quad (2.34)$$

For example, the calculation of the component c_{2233} is performed according to

$$c_{2233} = \beta_{2i}\beta_{2j}\beta_{3k}\beta_{3l}c'_{ijkl}. \quad (2.35)$$

If we specialize the transformation tensor to the above case of a rotation about the x_3 -axis, it is reduced to

$$\beta_{ij} = \begin{bmatrix} \cos \Phi & \sin \Phi & 0 \\ -\sin \Phi & \cos \Phi & 0 \\ 0 & 0 & 1 \end{bmatrix}. \quad (2.36)$$

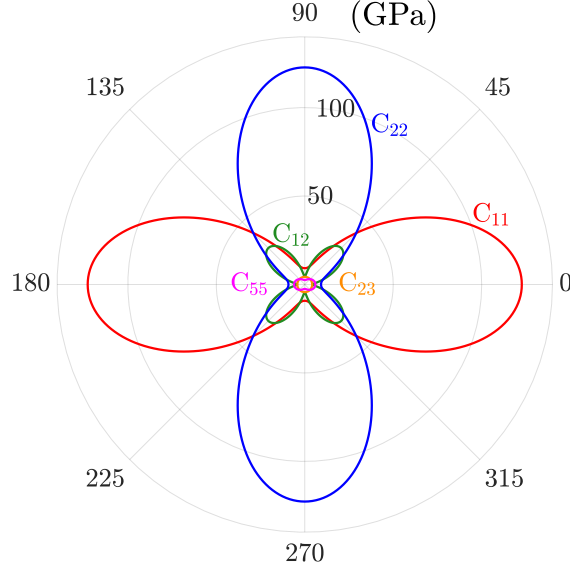


FIG. 2.2. Transformed stiffness matrix components versus azimuthal angle Φ of unidirectional SAERTEX[®]7006919/RIMR135.

Each layer by itself belongs to the transversely isotropic symmetry class. Therefore, by applying Eqs. (2.33) and (2.36) on Eq. (2.12) for orthotropic (Eq. (2.16)) or transversely isotropic (Eq. (2.17)) materials, and using Voigt's notation, we obtain

$$\begin{aligned}
C_{11} &= C'_{11} \cos^4 \Phi + C'_{22} \sin^4 \Phi + 2(C'_{12} + 2C'_{66}) \sin^2 \Phi \cos^2 \Phi, \\
C_{12} &= (C'_{11} + C'_{22} - 2C'_{12} - 4C'_{66}) \sin^2 \cos^2 + C'_{12}, \\
C_{13} &= C'_{13} \cos^2 \Phi + C'_{23} \sin^2 \Phi, \\
C_{16} &= (C'_{12} + 2C'_{66} - C'_{11}) \sin \Phi \cos^3 \Phi + (C'_{22} - C'_{12} - 2C'_{66}) \cos \Phi \sin^3 \Phi, \\
C_{22} &= C'_{11} \sin^4 \Phi + C'_{22} \cos^4 \Phi + 2(C'_{12} + 2C'_{66}) \sin^2 \Phi \cos^2 \Phi, \\
C_{23} &= C'_{23} \cos^2 \Phi + C'_{13} \sin^2 \Phi, \\
C_{26} &= (C'_{12} + 2C'_{66} - C'_{11}) \cos \Phi \sin^3 \Phi + (C'_{22} - C'_{12} - 2C'_{66}) \sin \Phi \cos^3 \Phi, \quad (2.37) \\
C_{33} &= C'_{33}, \\
C_{36} &= (C'_{23} - C'_{13}) \sin \Phi \cos \Phi, \\
C_{44} &= C'_{44} \cos^2 \Phi + C'_{55} \sin^2 \Phi, \\
C_{45} &= (C'_{44} - C'_{55}) \sin \Phi \cos \Phi, \\
C_{55} &= C'_{55} \cos^2 \Phi + C'_{44} \sin^2 \Phi, \\
C_{66} &= C'_{66} + (C'_{11} + C'_{22} - 2C'_{12} - 4C'_{66}) \sin^2 \Phi \cos^2 \Phi,
\end{aligned}$$

noticing that this transformed stiffness matrix has the form of monoclinic material symmetry. For $\Phi = 0^\circ$, the entries C_{16} , C_{26} , C_{36} , and C_{45} vanish so that

Eq. (2.37) takes the form of the nontransformed orthotropic and transversely isotropic stiffness matrices again. Figure 2.2 shows a calculation of the transformed stiffness matrix components C_{11} , C_{22} , C_{12} , C_{23} , and C_{55} versus Φ of the transversely isotropic fiber-epoxy system SAERTEX[®]7006919/RIMR135, clearly visualizing the in-plane anisotropy of the material. Its stiffness matrix components C'_{ij} are given in Appendix B. As an example, for $\Phi = 30^\circ$, we get the following transformed stiffness matrix:

$$C_{ij} = \begin{bmatrix} 75.7 & 22.9 & 4.3 & 0 & 0 & 35.3 \\ & 19.0 & 4.2 & 0 & 0 & 13.8 \\ & & 9.2 & 1.5 & 0 & 0.05 \\ & & & 3.4 & 0 & 0 \\ & \text{sym} & & & 5.1 & 0 \\ & & & & & 24.6 \end{bmatrix}. \quad (2.38)$$

To conduct our analysis in the global coordinate system, we further apply the transformations

$$\begin{aligned} x_i &= \beta_{ij}x'_j, \\ u_i &= \beta_{ij}u'_j, \\ \sigma_{mn} &= \beta_{mi}\beta_{nj}\sigma'_{ij}, \\ \varepsilon_{op} &= \beta_{ok}\beta_{pl}\varepsilon'_{kl}, \end{aligned} \quad (2.39)$$

using the same transformation matrix from Eq. (2.36). Accordingly, the strain-displacement field equation (2.5), the equation of motion (2.6), and Hooke's law (2.7) transform into

$$\varepsilon_{kl} = \frac{1}{2} \left(\frac{\partial u_l}{\partial x_k} + \frac{\partial u_k}{\partial x_l} \right), \quad (2.40)$$

$$\frac{\partial \sigma_{ij}}{\partial x_j} = \rho \frac{\partial^2 u_i}{\partial t^2}, \quad (2.41)$$

$$\sigma_{ij} = c_{ijkl}\varepsilon_{kl}. \quad (2.42)$$

2.1.5 Homogenized Stiffness Tensor

Once we have obtained the transformed stiffness matrices for each layer of a given layup, we can easily obtain its HST. This tensor is frequently used for the FEM modeling of structural mechanics of laminated structures since it is much more efficient to use an average stiffness tensor than modeling every layer. Unfortunately, the HST can be used for the modeling of guided waves only for a very low frequency range where the wavelengths of the bulk waves (of which the guided wave is composed of) are large compared to the layer thickness. Only then can the laminate

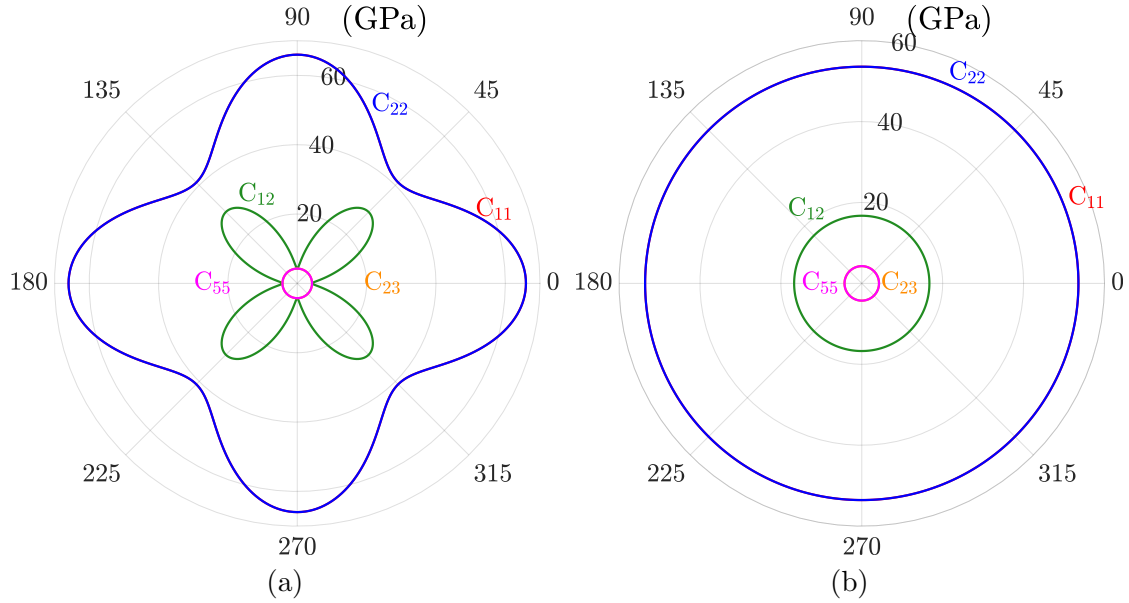


FIG. 2.3. HST components versus azimuthal angle Φ of SAERTEX[®]7006919/RIMR135. (a) [0/90] and (b) [0/90/45/-45] layup.

be considered an effective medium with averaged elastic properties. Otherwise, for short wavelengths, the individual layers take effect on the wave propagation. In this case, each set of bulk waves propagating in each layer, governed by its respective transformed stiffness matrix, must be modeled individually. More about this topic will be said in Sec. 2.7.3.

However, it is of great heuristic value to investigate the HST. The HST is calculated using the *classical laminate theory* (CLT). The transformed stiffness matrices are multiplied by their respective layer thickness-to-unit cell thickness ratio and summed up to obtain the HST of the unit cell. Since every unit cell (*e.g.* [0/90]¹) has the same HST, and because of the multiplication with the thickness ratios, the HST does not depend on the repetitions of the unit cell (*e.g.* [0/90]_{2s}), *i.e.*, it is equal to the HST of the unit cell.

Figure 2.3 shows the HST components C_{11} , C_{22} , C_{12} , C_{23} , and C_{55} versus Φ in two different unit cells made up of SAERTEX[®]7006919/RIMR135. By comparing Fig. 2.3(a) to Fig. 2.2, we notice that C_{11} and C_{22} coincide in a [0/90] unit cell. C_{23} and C_{55} appear to coincide as well, but this is just coincidence instead of an inherent property of transversely isotropic materials, unlike the case for C_{11} and C_{22} . Figure 2.3(b) shows the quasiisotropic behavior of a [0/90/45/-45] unit cell.

¹We abstain from repeatedly writing the degree symbol.

2.1.6 Expanded Field Equations

Having obtained the transformed field equations, we rewrite the equation of motion (2.41) in its expanded form

$$\frac{\partial \sigma_{11}}{\partial x_1} + \frac{\partial \sigma_{12}}{\partial x_2} + \frac{\partial \sigma_{13}}{\partial x_3} = \rho \frac{\partial^2 u_1}{\partial t^2}, \quad (2.43)$$

$$\frac{\partial \sigma_{12}}{\partial x_1} + \frac{\partial \sigma_{22}}{\partial x_2} + \frac{\partial \sigma_{23}}{\partial x_3} = \rho \frac{\partial^2 u_2}{\partial t^2}, \quad (2.44)$$

$$\frac{\partial \sigma_{13}}{\partial x_1} + \frac{\partial \sigma_{23}}{\partial x_2} + \frac{\partial \sigma_{33}}{\partial x_3} = \rho \frac{\partial^2 u_3}{\partial t^2}. \quad (2.45)$$

To utilize the field equations for the most general case (without material symmetry), we substitute the strain components on the right-hand side in Eq. (2.42) by Eq. (2.40), and substitute the result into the expanded equations of motion (2.43)-(2.45). Finally, we obtain three coupled partial differential equations for the displacement components u_i

$$\begin{aligned} & C_{11} \frac{\partial^2 u_1}{\partial x_1^2} + C_{66} \frac{\partial^2 u_1}{\partial x_2^2} + C_{55} \frac{\partial^2 u_1}{\partial x_3^2} + 2C_{16} \frac{\partial^2 u_1}{\partial x_1 \partial x_2} + 2C_{15} \frac{\partial^2 u_1}{\partial x_1 \partial x_3} \\ & + 2C_{56} \frac{\partial^2 u_1}{\partial x_2 \partial x_3} + C_{16} \frac{\partial^2 u_2}{\partial x_1^2} + C_{26} \frac{\partial^2 u_2}{\partial x_2^2} + C_{45} \frac{\partial^2 u_2}{\partial x_3^2} \\ & + (C_{12} + C_{66}) \frac{\partial^2 u_2}{\partial x_1 \partial x_2} + (C_{14} + C_{56}) \frac{\partial^2 u_2}{\partial x_1 \partial x_3} + (C_{46} + C_{25}) \frac{\partial^2 u_2}{\partial x_2 \partial x_3} \\ & + C_{15} \frac{\partial^2 u_3}{\partial x_1^2} + C_{46} \frac{\partial^2 u_3}{\partial x_2^2} + C_{35} \frac{\partial^2 u_3}{\partial x_3^2} + (C_{14} + C_{56}) \frac{\partial^2 u_3}{\partial x_1 \partial x_2} \\ & + (C_{13} + C_{55}) \frac{\partial^2 u_3}{\partial x_1 \partial x_3} + (C_{36} + C_{45}) \frac{\partial^2 u_3}{\partial x_2 \partial x_3} = \rho \frac{\partial^2 u_1}{\partial t^2}, \end{aligned} \quad (2.46)$$

$$\begin{aligned} & C_{16} \frac{\partial^2 u_1}{\partial x_1^2} + C_{26} \frac{\partial^2 u_1}{\partial x_2^2} + C_{45} \frac{\partial^2 u_1}{\partial x_3^2} + (C_{12} + C_{66}) \frac{\partial^2 u_1}{\partial x_1 \partial x_2} \\ & + (C_{14} + C_{56}) \frac{\partial^2 u_1}{\partial x_1 \partial x_3} + (C_{46} + C_{25}) \frac{\partial^2 u_1}{\partial x_2 \partial x_3} + C_{66} \frac{\partial^2 u_2}{\partial x_1^2} + C_{22} \frac{\partial^2 u_2}{\partial x_2^2} \\ & + C_{44} \frac{\partial^2 u_2}{\partial x_3^2} + 2C_{26} \frac{\partial^2 u_2}{\partial x_1 \partial x_2} + 2C_{46} \frac{\partial^2 u_2}{\partial x_1 \partial x_3} + 2C_{24} \frac{\partial^2 u_2}{\partial x_2 \partial x_3} \\ & + C_{56} \frac{\partial^2 u_3}{\partial x_1^2} + C_{24} \frac{\partial^2 u_3}{\partial x_2^2} + C_{34} \frac{\partial^2 u_3}{\partial x_3^2} + (C_{46} + C_{25}) \frac{\partial^2 u_3}{\partial x_1 \partial x_2} \\ & + (C_{36} + C_{45}) \frac{\partial^2 u_3}{\partial x_1 \partial x_3} + (C_{23} + C_{44}) \frac{\partial^2 u_3}{\partial x_2 \partial x_3} = \rho \frac{\partial^2 u_2}{\partial t^2}, \end{aligned} \quad (2.47)$$

$$\begin{aligned}
& C_{15} \frac{\partial^2 u_1}{\partial x_1^2} + C_{46} \frac{\partial^2 u_1}{\partial x_2^2} + C_{35} \frac{\partial^2 u_1}{\partial x_3^2} + (C_{14} + C_{56}) \frac{\partial^2 u_1}{\partial x_1 \partial x_2} \\
& + (C_{13} + C_{55}) \frac{\partial^2 u_1}{\partial x_1 \partial x_3} + (C_{36} + C_{45}) \frac{\partial^2 u_1}{\partial x_2 \partial x_3} + C_{56} \frac{\partial^2 u_2}{\partial x_1^2} + C_{24} \frac{\partial^2 u_2}{\partial x_2^2} \\
& + C_{34} \frac{\partial^2 u_2}{\partial x_3^2} + (C_{46} + C_{25}) \frac{\partial^2 u_2}{\partial x_1 \partial x_2} + (C_{36} + C_{45}) \frac{\partial^2 u_2}{\partial x_1 \partial x_3} \\
& + (C_{23} + C_{44}) \frac{\partial^2 u_2}{\partial x_2 \partial x_3} + C_{55} \frac{\partial^2 u_3}{\partial x_1^2} + C_{44} \frac{\partial^2 u_3}{\partial x_2^2} + C_{33} \frac{\partial^2 u_3}{\partial x_3^2} \\
& + 2C_{45} \frac{\partial^2 u_3}{\partial x_1 \partial x_2} + 2C_{35} \frac{\partial^2 u_3}{\partial x_1 \partial x_3} + 2C_{34} \frac{\partial^2 u_3}{\partial x_2 \partial x_3} = \rho \frac{\partial^2 u_3}{\partial t^2}.
\end{aligned} \tag{2.48}$$

The transformed stiffness matrices of orthotropic and transversely isotropic materials have the same form as the monoclinic stiffness matrix in the transformed as well as nontransformed case. Therefore, if we want to specialize Eqs. (2.46)-(2.48) to any of these symmetry classes, we take advantage of the vanishing of the components C_{14} , C_{15} , C_{24} , C_{25} , C_{34} , C_{35} , C_{46} , and C_{56} , and get

$$\begin{aligned}
& C_{11} \frac{\partial^2 u_1}{\partial x_1^2} + C_{66} \frac{\partial^2 u_1}{\partial x_2^2} + C_{55} \frac{\partial^2 u_1}{\partial x_3^2} + 2C_{16} \frac{\partial^2 u_1}{\partial x_1 \partial x_2} + C_{16} \frac{\partial^2 u_2}{\partial x_1^2} \\
& + C_{26} \frac{\partial^2 u_2}{\partial x_2^2} + C_{45} \frac{\partial^2 u_2}{\partial x_3^2} + (C_{12} + C_{66}) \frac{\partial^2 u_2}{\partial x_1 \partial x_2} \\
& + (C_{13} + C_{55}) \frac{\partial^2 u_3}{\partial x_1 \partial x_3} + (C_{36} + C_{45}) \frac{\partial^2 u_3}{\partial x_2 \partial x_3} = \rho \frac{\partial^2 u_1}{\partial t^2},
\end{aligned} \tag{2.49}$$

$$\begin{aligned}
& C_{16} \frac{\partial^2 u_1}{\partial x_1^2} + C_{26} \frac{\partial^2 u_1}{\partial x_2^2} + C_{45} \frac{\partial^2 u_1}{\partial x_3^2} + (C_{12} + C_{66}) \frac{\partial^2 u_1}{\partial x_1 \partial x_2} \\
& + C_{66} \frac{\partial^2 u_2}{\partial x_1^2} + C_{22} \frac{\partial^2 u_2}{\partial x_2^2} + C_{44} \frac{\partial^2 u_2}{\partial x_3^2} + 2C_{26} \frac{\partial^2 u_2}{\partial x_1 \partial x_2} \\
& + (C_{36} + C_{45}) \frac{\partial^2 u_3}{\partial x_1 \partial x_3} + (C_{23} + C_{44}) \frac{\partial^2 u_3}{\partial x_2 \partial x_3} = \rho \frac{\partial^2 u_2}{\partial t^2},
\end{aligned} \tag{2.50}$$

$$\begin{aligned}
& (C_{13} + C_{55}) \frac{\partial^2 u_1}{\partial x_1 \partial x_3} + (C_{36} + C_{45}) \frac{\partial^2 u_1}{\partial x_2 \partial x_3} + (C_{36} + C_{45}) \frac{\partial^2 u_2}{\partial x_1 \partial x_3} \\
& + (C_{23} + C_{44}) \frac{\partial^2 u_2}{\partial x_2 \partial x_3} + C_{55} \frac{\partial^2 u_3}{\partial x_1^2} + C_{44} \frac{\partial^2 u_3}{\partial x_2^2} + C_{33} \frac{\partial^2 u_3}{\partial x_3^2} \\
& + 2C_{45} \frac{\partial^2 u_3}{\partial x_1 \partial x_2} = \rho \frac{\partial^2 u_3}{\partial t^2}.
\end{aligned} \tag{2.51}$$

An interesting situation occurs if we consider wave propagation along axes of symmetry. Then, with $\Phi = 0^\circ$, C_{16} , C_{26} , C_{36} , and C_{45} vanish, and we can give the field equations in the nontransformed crystallographic coordinate system x'_i . We choose the wave propagation to take place in the x'_1 - x'_3 -plane so that all field variables will be independent of the x'_2 -coordinate. Hence, Eqs. (2.49)-(2.51) turn into

$$C'_{11} \frac{\partial^2 u'_1}{\partial x'^2_1} + C'_{55} \frac{\partial^2 u'_1}{\partial x'^2_3} + (C'_{13} + C'_{55}) \frac{\partial^2 u'_3}{\partial x'_1 \partial x'_3} = \rho \frac{\partial^2 u'_1}{\partial t^2}, \quad (2.52)$$

$$C'_{66} \frac{\partial^2 u'_2}{\partial x'^2_1} + C'_{44} \frac{\partial^2 u'_2}{\partial x'^2_3} = \rho \frac{\partial^2 u'_2}{\partial t^2}, \quad (2.53)$$

$$(C'_{13} + C'_{55}) \frac{\partial^2 u'_1}{\partial x'_1 \partial x'_3} + C'_{55} \frac{\partial^2 u'_3}{\partial x'^2_1} + C'_{33} \frac{\partial^2 u'_3}{\partial x'^2_3} = \rho \frac{\partial^2 u'_3}{\partial t^2}. \quad (2.54)$$

These equations show partial decoupling. Equation (2.53) has only one independent variable u'_2 describing shear horizontally polarized wave propagation, while Eq. (2.52) and Eq. (2.54) define a coupled wave propagation with the polarization (displacement) components u'_1 and u'_3 in the x'_1 - x'_3 -plane (sagittal). In Sec. 2.2, we will have a closer look at these bulk waves, and benefit greatly from their decoupling in Sec. 2.3 in case of wave propagation along axes of symmetry.

Finally, we write the field equations for isotropic media in the global coordinate system x_i as follows:

$$\begin{aligned} & (\lambda + \mu) \left(\frac{\partial^2 u_1}{\partial x_1^2} + \frac{\partial^2 u_2}{\partial x_1 \partial x_2} + \frac{\partial^2 u_3}{\partial x_1 \partial x_3} \right) + \mu \left(\frac{\partial^2 u_1}{\partial x_1^2} + \frac{\partial^2 u_1}{\partial x_2^2} + \frac{\partial^2 u_1}{\partial x_3^2} \right) \\ & = \rho \frac{\partial^2 u_1}{\partial t^2}, \end{aligned} \quad (2.55)$$

$$\begin{aligned} & (\lambda + \mu) \left(\frac{\partial^2 u_1}{\partial x_1 \partial x_2} + \frac{\partial^2 u_2}{\partial x_2^2} + \frac{\partial^2 u_3}{\partial x_2 \partial x_3} \right) + \mu \left(\frac{\partial^2 u_2}{\partial x_1^2} + \frac{\partial^2 u_2}{\partial x_2^2} + \frac{\partial^2 u_2}{\partial x_3^2} \right) \\ & = \rho \frac{\partial^2 u_2}{\partial t^2}, \end{aligned} \quad (2.56)$$

$$\begin{aligned} & (\lambda + \mu) \left(\frac{\partial^2 u_1}{\partial x_1 \partial x_3} + \frac{\partial^2 u_2}{\partial x_2 \partial x_3} + \frac{\partial^2 u_3}{\partial x_3^2} \right) + \mu \left(\frac{\partial^2 u_3}{\partial x_1^2} + \frac{\partial^2 u_3}{\partial x_2^2} + \frac{\partial^2 u_3}{\partial x_3^2} \right) \\ & = \rho \frac{\partial^2 u_3}{\partial t^2}. \end{aligned} \quad (2.57)$$

Again, we choose the wave propagation to take place in the x_1 - x_3 -plane so that all field variables will be independent of x_2 . Then, Eqs. (2.55)-(2.57) reduce to

$$(\lambda + 2\mu) \frac{\partial^2 u_1}{\partial x_1^2} + \mu \frac{\partial^2 u_1}{\partial x_3^2} + (\lambda + \mu) \frac{\partial^2 u_3}{\partial x_1 \partial x_3} = \rho \frac{\partial^2 u_1}{\partial t^2}, \quad (2.58)$$

$$\mu \left(\frac{\partial^2 u_2}{\partial x_1^2} + \frac{\partial^2 u_2}{\partial x_3^2} \right) = \rho \frac{\partial^2 u_2}{\partial t^2}, \quad (2.59)$$

$$(\lambda + \mu) \frac{\partial^2 u_1}{\partial x_1 \partial x_3} + \mu \frac{\partial^2 u_3}{\partial x_1^2} + (\lambda + 2\mu) \frac{\partial^2 u_3}{\partial x_3^2} = \rho \frac{\partial^2 u_3}{\partial t^2}, \quad (2.60)$$

which are the isotropic counterparts to Eqs. (2.52)-(2.54). Since Lamé's parameters are independent from the propagation direction, so are the partial decoupling properties discussed above, *i.e.*, shear horizontal and sagittal motion are decoupled for any propagation direction in isotropic materials. We will utilize Eqs. (2.58)-(2.60) in Sec. 2.4.

Basically, if the solid in which the wave propagation takes place is infinite, the field equations presented in this section are sufficient to describe the motion. This will be the case in the discussion of bulk waves in Sec. 2.2.1. If the solid is finite, however, appropriate boundary conditions must be invoked, as we will do it for the modeling of guided waves in plate-like waveguides in Secs. 2.3 and 2.4.

2.2 Bulk Waves

Guided waves develop from the propagation and superposition of bulk waves. Therefore, if we want to model the behavior of guided waves, we must actually model the propagation of bulk waves in waveguides. Bulk waves propagate in infinite homogeneous bodies without being reflected from interfaces and boundaries. In isotropic materials, the phase velocity of bulk waves is independent from the propagation direction \mathbf{n} , and the polarization vector \mathbf{p} is along \mathbf{n} for *longitudinal waves* (L) and perpendicular for *shear vertical* (SV) as well as *shear horizontal waves* (SH). Therefore, if we consider bulk waves emanating from a point source in an isotropic bulk material, the phase velocity surfaces of the three wave types are spherical with their radii being the longitudinal velocity according to Eq. (2.29) for L waves and the transverse velocity according to Eq. (2.30) for SH and SV waves. Hence, the longitudinal phase velocity surface is the fastest, while both transverse surfaces coincide at a lower phase velocity. The group velocity surfaces coincide with the phase velocity surfaces. Another representation is the slowness surface,

which is the inverse of the phase velocity surface. L waves are polarized along the radial direction of the phase velocity surface, and SH and SV waves normal to it so that all polarization vectors $\mathbf{p}_{(q)}$, $q = 1, 2, 3$, are mutually orthogonal, and no coupling between the various bulk wave types can occur. These kind of waves where \mathbf{p} is oriented either along ($\mathbf{p} \times \mathbf{n} = 0$) or normal ($\mathbf{p} \cdot \mathbf{n} = 0$) to \mathbf{n} are termed *pure* modes. Therefore, bulk waves in isotropic materials are always pure.

In anisotropic materials, however, the bulk waves' phase velocities depend on the propagation direction, and the phase velocity surfaces of the shear waves do not coincide in general so that we have a *fast shear wave* (S_{fast}) and a *slow shear wave* (S_{slow}). Furthermore, in general, the group velocity surfaces are not coincident with the phase velocity surfaces. According to Auld [131], page 236, pure modes can exist in anisotropic materials only for certain propagation directions, called *pure mode directions*. Nayfeh points into the same direction in his book [22], page thirty-two, stating that “none of the three polarization vectors a priori satisfies either $\mathbf{p} \times \mathbf{n} = 0$ or $\mathbf{p} \cdot \mathbf{n} = 0$.” Because of that, the bulk waves in anisotropic materials are termed *quasilongitudinal*, *fast quasishear*, and *slow quasishear waves*. However, we confirm below what Fedorov [138] and Musgrave [139] have demonstrated, namely that S_{slow} indeed satisfies $\mathbf{p} \cdot \mathbf{n} = 0$ a priori in transversely isotropic material, *i.e.*, S_{slow} is a pure shear mode for any propagation direction. Furthermore, we find that its polarization vector lies always in the x'_2 - x'_3 -plane, *i.e.*, normal to the fibers, which is the actual reason why S_{slow} is pure. By contrast, L and S_{fast} are pure only for wave propagation along certain directions, and their polarization vectors are not restricted to lie in a certain plane. Therefore, we call S_{slow} just *slow shear wave* without the prefix *quasi*. On the other hand, we agree with Nayfeh that if there is one pure longitudinal wave ($\mathbf{p} \times \mathbf{n} = 0$), then the other two modes are pure shear, and if there is one pure shear wave ($\mathbf{p} \cdot \mathbf{n} = 0$) there is no guarantee that the other modes are pure. Similarly as in isotropic materials, the polarization vectors of the bulk waves are mutually orthogonal. Auld has shown in his book [131], page 219, that due to the symmetry of the *Christoffel matrix* this must always be so.

In Sec. 2.2.1, we first derive Christoffel's equation [140, 141], and then use it to calculate and plot the phase and group velocities, the slownesses as well as the polarization and energy deviation angles of all three bulk wave types in transversely isotropic SAERTEX[®]7006919/RIMR135 as function of the propagation direction. Since waveguides involve interfaces, we treat the physics of the scattering of bulk waves on such interfaces in Sec. 2.2.2, leading us directly to *Snell–Descartes' law of refraction* [142]. At the end of this section, we present numerical examples of bulk waves scattering on an interface between a fluid and SAERTEX as well as isotropic media. Beside the books of Nayfeh and Auld, the one of Rokhlin *et al.* [59] was helpful in the coding and writing of the following discussions.

2.2.1 Elastic Waves in Bulk Material

Christoffel's Equation

We start with the derivation of Christoffel's equation, thereby laying the foundation not only for this section but also beyond. First, we combine the strain-displacement field equation (2.40), the equation of motion (2.41), and Hook's law (2.42) to get

$$\rho \frac{\partial^2 u_i}{\partial t^2} = \frac{1}{2} c_{ijkl} \frac{\partial}{\partial x_j} \left(\frac{\partial u_k}{\partial x_l} + \frac{\partial u_l}{\partial x_k} \right). \quad (2.61)$$

Using the various symmetry properties of c_{ijkl} reduces Eq. (2.61) to

$$\rho \frac{\partial^2 u_i}{\partial t^2} = c_{ijkl} \frac{\partial^2 u_l}{\partial x_j \partial x_k}, \quad (2.62)$$

which has the general form of solution for the displacement field components u_i in terms of the bulk wave amplitudes U_i , $i = 1, 2, 3$,

$$u_i = U_i e^{i\zeta(n_j x_j - v_p t)}, \quad (2.63)$$

where ζ is the bulk wavenumber, n_j are the propagation direction unit vector components n_1 , n_2 , and n_3 , and v_p is the phase velocity ($= \omega/\zeta$), with the angular frequency ω . Substituting Eq. (2.63) into Eq. (2.62) yields

$$\omega^2 U_i = \lambda_{ijkl} \zeta^2 n_j n_k U_l, \quad (2.64)$$

with

$$\lambda_{ijkl} = c_{ijkl} / \rho. \quad (2.65)$$

By using the Kronecker delta property $U_i = U_l \delta_{il}$, we can rewrite Eq. (2.64) in the characteristic equation form, known as Christoffel's equation

$$(\lambda_{ijkl} n_j n_k - v_p^2 \delta_{il}) U_l = 0. \quad (2.66)$$

We introduce the second order tensor Λ_{il} with the elements

$$\begin{aligned} \Lambda_{il} &= \lambda_{ijkl} n_j n_k = \\ &= \lambda_{i11} n_1^2 + \lambda_{i22} n_2^2 + \lambda_{i33} n_3^2 + (\lambda_{i12} + \lambda_{i21}) n_1 n_2 \\ &\quad + (\lambda_{i13} + \lambda_{i31}) n_1 n_3 + (\lambda_{i23} + \lambda_{i32}) n_2 n_3, \end{aligned} \quad (2.67)$$

for generally anisotropic (triclinic) materials. Now, we can write Christoffel's equation in the more compact form

$$(\Lambda_{il} - v_p^2 \delta_{il}) U_l = 0. \quad (2.68)$$

We refer to Eq. (2.68) as the *phase velocity form* of Christoffel's equation.

Phase Velocity, Group Velocity, Slowness, and Polarization

We have now obtained three homogeneous linear equations for the displacement amplitudes U_l of the bulk waves. Their phase velocities are given by the eigenvalues v_p^2 , and the eigenvectors U_l define the polarization directions. To continue our discussion, we write Christoffel's equation in matrix form, and since we are not treating a layered structure in this section, we do our analysis in the crystallographic coordinate system x'_i . Hence, we have

$$\begin{bmatrix} \Lambda'_{11} - v_p^2 & \Lambda'_{12} & \Lambda'_{13} \\ \text{sym} & \Lambda'_{22} - v_p^2 & \Lambda'_{23} \\ & & \Lambda'_{33} - v_p^2 \end{bmatrix} \begin{bmatrix} U'_1 \\ U'_2 \\ U'_3 \end{bmatrix} = 0, \quad (2.69)$$

with the components Λ'_{ij} , which result from Eq. (2.67) as

$$\begin{aligned} \rho\Lambda'_{11} &= C'_{11}n_1'^2 + C'_{66}n_2'^2 + C'_{55}n_3'^2 + 2C'_{16}n'_1n'_2 + 2C'_{15}n'_1n'_3 + 2C'_{56}n'_2n'_3, \\ \rho\Lambda'_{12} &= C'_{16}n_1'^2 + C'_{26}n_2'^2 + C'_{45}n_3'^2 + (C'_{12} + C'_{66})n'_1n'_2 + (C'_{14} + C'_{56})n'_1n'_3 \\ &\quad + (C'_{46} + C'_{25})n'_2n'_3, \\ \rho\Lambda'_{13} &= C'_{15}n_1'^2 + C'_{46}n_2'^2 + C'_{35}n_3'^2 + (C'_{14} + C'_{56})n'_1n'_2 + (C'_{13} + C'_{55})n'_1n'_3 \\ &\quad + (C'_{36} + C'_{45})n'_2n'_3, \\ \rho\Lambda'_{22} &= C'_{66}n_1'^2 + C'_{22}n_2'^2 + C'_{44}n_3'^2 + 2C'_{26}n'_1n'_2 + 2C'_{46}n'_1n'_3 + 2C'_{24}n'_2n'_3, \\ \rho\Lambda'_{23} &= C'_{56}n_1'^2 + C'_{24}n_2'^2 + C'_{34}n_3'^2 + (C'_{46} + C'_{25})n'_1n'_2 + (C'_{36} + C'_{45})n'_1n'_3 \\ &\quad + (C'_{23} + C'_{44})n'_2n'_3, \\ \rho\Lambda'_{33} &= C'_{55}n_1'^2 + C'_{44}n_2'^2 + C'_{33}n_3'^2 + 2C'_{45}n'_1n'_2 + 2C'_{35}n'_1n'_3 + 2C'_{34}n'_2n'_3, \end{aligned} \quad (2.70)$$

where we used Voigt's notation. The 3×3 matrix in Eq. (2.69) is referred to as the *Christoffel matrix*. Specializing Eq. (2.70) to orthotropic and transversely isotropic materials in the nontransformed form in accordance with Eqs. (2.16)-(2.17) delivers

$$\begin{aligned} \rho\Lambda'_{11} &= C'_{11}n_1'^2 + C'_{66}n_2'^2 + C'_{55}n_3'^2, \\ \rho\Lambda'_{12} &= (C'_{12} + C'_{66})n'_1n'_2, \\ \rho\Lambda'_{13} &= (C'_{13} + C'_{55})n'_1n'_3, \\ \rho\Lambda'_{22} &= C'_{66}n_1'^2 + C'_{22}n_2'^2 + C'_{44}n_3'^2, \\ \rho\Lambda'_{23} &= (C'_{23} + C'_{44})n'_2n'_3, \\ \rho\Lambda'_{33} &= C'_{55}n_1'^2 + C'_{44}n_2'^2 + C'_{33}n_3'^2. \end{aligned} \quad (2.71)$$

Nontrivial solutions for U'_1 , U'_2 , and U'_3 require the vanishing of the Christoffel matrix determinant in Eq. (2.69), yielding the sixth-degree polynomial

$$v_p^6 + A_1v_p^4 + A_2v_p^2 + A_3 = 0, \quad (2.72)$$

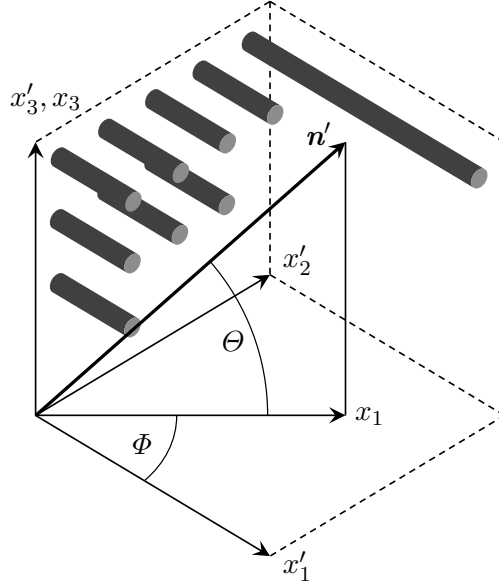


FIG. 2.4. Crystallographic and global coordinate systems x'_i, x_i and fiber orientation in transversely isotropic material. Bulk waves propagate along \mathbf{n}' .

with the coefficients A_1, A_2 , and A_3 given in Appendix C. Equation (2.72) admits six solutions for v_p (three for v_p^2). In Appendix C, Eq. (C.3), analytical expressions are presented for the six solutions², and Eq. (C.4) shows how to deduce the phase velocities $v_{p(L)}$, $v_{p(S_{fast})}$, and $v_{p(S_{slow})}$ from them. Once we have the three roots $v_{p(q)}$, we can use Christoffel's equation (2.69) to obtain the corresponding polarization vectors $\mathbf{p}'_{(q)}$. Their components with respect to the coordinate system x'_i are given by the displacement amplitude ratios

$$p'_{2(q)} = \frac{U'_{2(q)}}{U'_{1(q)}} = \frac{\Lambda'_{23}(\Lambda'_{11} - v_{p(q)}^2) - \Lambda'_{13}\Lambda'_{12}}{\Lambda'_{13}(\Lambda'_{22} - v_{p(q)}^2) - \Lambda'_{12}\Lambda'_{23}}, \quad (2.73)$$

$$p'_{3(q)} = \frac{U'_{3(q)}}{U'_{1(q)}} = \frac{(\Lambda'_{11} - v_{p(q)}^2)(\Lambda'_{22} - v_{p(q)}^2) - \Lambda_{12}^2}{\Lambda'_{12}\Lambda'_{23} - \Lambda'_{13}(\Lambda'_{22} - v_{p(q)}^2)}. \quad (2.74)$$

By setting $U'_{1(q)} = 1$, we obtain the three polarization vectors $(1, p'_{2(q)}, p'_{3(q)})$. To get the polarization angles $\beta_{(q)}$, *i.e.*, the angles between the propagation direction and the polarization vectors, we use the dot product

$$\beta_{(q)} = \cos^{-1}(\mathbf{p}'_{(q)} \cdot \mathbf{n}'). \quad (2.75)$$

²Compared to root finding functions such as MATLAB's[®] "roots", analytical expressions have the advantages that they are calculated faster and no root sorting algorithm is required afterward.

Here, we normalized $\mathbf{p}'_{(q)}$ to the unit vector, while \mathbf{n}' is already one. We define also the deviation angle from the pure mode polarization $\delta_{(q)}$. For L waves, we have $\delta_L = \beta_L$, but guided by the fact that the polarization of pure shear modes is normal to the propagation direction, we define $\delta_{S_{\text{fast}}, S_{\text{slow}}} = 90^\circ - \beta_{S_{\text{fast}}, S_{\text{slow}}}$. Since S_{slow} has pure character for any propagation direction, *i.e.*, $\beta_{S_{\text{slow}}} = 90^\circ$, we get a global polarization angle deviation of $\delta_{S_{\text{slow}}} = 0^\circ$. Finally, we define a set of propagation direction unit vectors $\mathbf{n}'(\Phi, \Theta)$ with the components

$$\begin{aligned} n'_1 &= \cos \Theta \cos \Phi, \\ n'_2 &= \cos \Theta \sin \Phi, \\ n'_3 &= \sin \Theta, \end{aligned} \tag{2.76}$$

with $\Phi, \Theta \in [0^\circ, 90^\circ]$, as displayed in Fig. 2.4. Here, x'_1 is along the fiber direction, and x'_2 and x'_3 are normal to it. Θ defines the wave propagation with respect to the x'_1 - x'_2 -plane (elevation), and Φ is the angle between the propagation direction projected into the x'_1 - x'_2 -plane and x'_1 (azimuth). We feed these propagation direction vectors \mathbf{n}' and the stiffness matrix components C'_{ij} of SAERTEX[®]7006919/RIMR135 (see Appendix B) into Christoffel's equation (2.69). We are using certain steps $\Delta\Phi$, $\Delta\Theta$, and copy and rotate the data obtained for $\Phi, \Theta \in [0^\circ, 90^\circ]$ such that we achieve closed surfaces. Of particular significance are the phase velocities for wave propagation along and perpendicular to the fibers, like for $\Theta = 0^\circ, \Phi = 0, 90^\circ$. For $\Phi = 0^\circ$, we have $n'_1 = 1, n'_2, n'_3 = 0$, and obtain the bulk waves' phase (and group) velocities parallel to the fibers

$$v_L^\parallel = \sqrt{\frac{C'_{11}}{\rho}}, \quad v_{S_{\text{fast}}}^\parallel = \sqrt{\frac{C'_{55}}{\rho}}, \quad v_{S_{\text{slow}}}^\parallel = \sqrt{\frac{C'_{66}}{\rho}}, \tag{2.77}$$

and for $\Phi = 90^\circ$, with $n'_2 = 1, n'_1, n'_3 = 0$, we get the velocities normal to the fibers

$$v_L^\perp = \sqrt{\frac{C'_{22}}{\rho}}, \quad v_{S_{\text{fast}}}^\perp = \sqrt{\frac{C'_{66}}{\rho}}, \quad v_{S_{\text{slow}}}^\perp = \sqrt{\frac{C'_{44}}{\rho}}. \tag{2.78}$$

In transversely isotropic material, we get the same velocities for propagation normal to the fibers by setting $\Theta = 90^\circ$, with $n'_3 = 1, n'_1, n'_2 = 0$, namely

$$v_L^\perp = \sqrt{\frac{C'_{33}}{\rho}}, \quad v_{S_{\text{fast}}}^\perp = \sqrt{\frac{C'_{55}}{\rho}}, \quad v_{S_{\text{slow}}}^\perp = \sqrt{\frac{C'_{44}}{\rho}}, \tag{2.79}$$

appreciating the same simple form which those expressions have corresponding to isotropic materials in Eqs. 2.29 and 2.30. The values for SAERTEX[®]7006919/RIMR135 are listed in Table B.6.

With the now known phase velocities and polarization vectors, we can calculate the group velocity vector

$$v'_{gi} = \frac{\lambda'_{ijkl} n'_k p'_l p'_j}{v_p}, \quad i, j, k, l = 1, 2, 3, \quad (2.80)$$

where n'_k and $p'_{l,j}$ are the propagation and polarization unit vector components, respectively. Here, for brevity, we drop the bulk wave index (q) on the phase velocities $v_{p(q)}$ and polarization vectors $\mathbf{p}'_{(q)}$. For the derivation of Eq. (2.80), the interested reader is referred to Refs. [59, 138]. Carrying out the summation operation yields the group velocity components for triclinic materials

$$\begin{aligned} v'_{gi} = & (\lambda'_{i111} n'_1 p_1'^2 + \lambda'_{i112} n'_1 p'_2 p'_1 + \lambda'_{i113} n'_1 p'_3 p'_1 \\ & + \lambda'_{i121} n'_2 p_1'^2 + \lambda'_{i122} n'_2 p'_2 p'_1 + \lambda'_{i123} n'_2 p'_3 p'_1 \\ & + \lambda'_{i131} n'_3 p_1'^2 + \lambda'_{i132} n'_3 p'_2 p'_1 + \lambda'_{i133} n'_3 p'_3 p'_1 \\ & + \lambda'_{i211} n'_1 p'_1 p'_2 + \lambda'_{i212} n'_1 p_2'^2 + \lambda'_{i213} n'_1 p'_3 p'_2 \\ & + \lambda'_{i221} n'_2 p'_1 p'_2 + \lambda'_{i222} n'_2 p_2'^2 + \lambda'_{i223} n'_2 p'_3 p'_2 \\ & + \lambda'_{i231} n'_3 p'_1 p'_2 + \lambda'_{i232} n'_3 p_2'^2 + \lambda'_{i233} n'_3 p'_3 p'_2 \\ & + \lambda'_{i311} n'_1 p'_1 p'_3 + \lambda'_{i312} n'_1 p'_2 p'_3 + \lambda'_{i313} n'_1 p_3'^2 \\ & + \lambda'_{i321} n'_2 p'_1 p'_3 + \lambda'_{i322} n'_2 p'_2 p'_3 + \lambda'_{i323} n'_2 p_3'^2 \\ & + \lambda'_{i331} n'_3 p'_1 p'_3 + \lambda'_{i332} n'_3 p'_2 p'_3 + \lambda'_{i333} n'_3 p_3'^2) / v_p, \end{aligned} \quad (2.81)$$

and specializing Eq. (2.81) to transversely isotropic symmetry gives

$$\begin{aligned} v'_{g1} = & (C'_{11} n'_1 p_1'^2 + C'_{12} n'_2 p'_2 p'_1 + C'_{13} n'_3 p'_3 p'_1 + C'_{66} (n'_1 p_2'^2 + n'_2 p'_1 p'_2) \\ & + C'_{55} (n'_1 p_3'^2 + n'_3 p'_1 p'_3)) / (\rho v_p), \\ v'_{g2} = & (C'_{12} n'_1 p'_1 p'_2 + C'_{22} n'_2 p_2'^2 + C'_{23} n'_3 p'_3 p'_2 + C'_{66} (n'_1 p'_2 p'_1 + n'_2 p_1'^2) \\ & + C'_{44} (n'_2 p_3'^2 + n'_3 p'_2 p'_3)) / (\rho v_p), \\ v'_{g3} = & (C'_{13} n'_1 p'_1 p'_3 + C'_{23} n'_2 p'_2 p'_3 + C'_{33} n'_3 p_3'^2 + C'_{55} (n'_1 p'_3 p'_1 + n'_3 p_1'^2) \\ & + C'_{44} (n'_2 p'_3 p'_2 + n'_3 p_2'^2)) / (\rho v_p). \end{aligned} \quad (2.82)$$

In general, the group velocity vector \mathbf{v}'_g deviates from the phase velocity vector \mathbf{v}'_p , where the latter is parallel to the wave vector $\boldsymbol{\zeta}'$ and the propagation direction unit vector \mathbf{n}' . In absence of attenuation, the group velocity is the same as the energy flow velocity, and its vector represents the actual direction of the acoustic beam. This situation leads also to differences in the magnitude of the phase and group velocities, as will be illustrated below. Similarly as in Eq. (2.75), we can compute the energy deviation angle $\gamma_{(q)}$ between the group/energy velocity of the q th bulk wave and the wave propagation direction by

$$\gamma_{(q)} = \cos^{-1} \left(\frac{\mathbf{v}'_{g(q)} \cdot \mathbf{n}'}{|\mathbf{v}'_{g(q)}|} \right). \quad (2.83)$$

Numerical Results

On the left-hand side in Fig. 2.5, the phase velocity surfaces of L (Fig. 2.5(a)), S_{fast} (Fig. 2.5(c)), and S_{slow} (Fig. 2.5(e)) waves are plotted. The bulk waves emanate from a point source located at $(0, 0, 0)$. The surfaces are not spherical, of course, and their degrees of deviation from spherical shapes depend on the specific anisotropy. We notice that the surfaces are rotationally symmetric about the x'_1 -axis, *i.e.*, about the fiber direction. Correspondingly, we have (transversely) isotropic behavior for wave propagation normal to the fibers ($\Phi = 90^\circ$). An interesting feature of the S_{fast} phase velocity surface is that it does not take its maximum on the x'_1 -axis ($\Phi, \Theta = 0^\circ$), like L and S_{slow} do, but at $\Theta = 71.92^\circ$. Figures 2.8(a), 2.8(d), and 2.8(g) show cross sections through the phase velocity surfaces of all three bulk waves at $\Phi = 0^\circ, 45^\circ$, and 90° , respectively. It is obvious that the greatest degree of anisotropy is present in the x'_1 - x'_3 -plane, shown in Fig. 2.8(a). L has the highest phase velocity (see Table 2.1), occurring along the fiber direction and the largest anisotropy of 3.65 between the $\Theta = 0^\circ$ and $\Theta = 90^\circ$ -directions. The corresponding anisotropies of S_{fast} and S_{slow} are 1 and 1.55, respectively. The highest and lowest velocities always belong to pure modes. As Φ increases, the degree of anisotropy decreases until isotropy is reached in the x'_2 - x'_3 -plane. A unique situation occurs at $\Phi, \Theta = 0^\circ$ where S_{fast} and S_{slow} are degenerate.

On the right-hand side in Fig. 2.5, the group velocity surfaces of L (Fig. 2.5(b)), S_{fast} (Fig. 2.5(d)), and S_{slow} (Fig. 2.5(f)) waves are presented. These surfaces are calculated from the absolute values of the group velocity vectors. The group velocity surfaces coincide with the phase velocity surfaces in the pure mode directions, *i.e.*, along and normal to fibers, where the velocities are given by Eqs. (2.77) and (2.78). This can be seen directly from the colorbars, covering the same ranges. An exception from this is, however, S_{fast} . While it has the maximum phase velocity of $v_{\text{pmax}} = 2.332 \text{ ms/m}$ at $\Theta = 71.92^\circ$, its maximum group velocity of $v_{\text{gmax}} = 2.930 \text{ ms/m}$ is significantly higher at $\Theta = 83.75^\circ$. More insight is provided by the cross sections through the group velocity surfaces at $\Phi = 0^\circ, 45^\circ$, and 90° , presented in Figs. 2.8(b), 2.8(e), and 2.8(h). At $\Phi = 90^\circ$, the phase and group velocities coincide, as expected. By contrast, at $\Phi = 0^\circ, 45^\circ$, the group velocity of L shows a quite different behavior from the phase velocity. While it remains almost constant within a range of $\pm 45^\circ$ centered around the fiber direction ($\Theta = 0^\circ$), the most variation takes place in a small range centered around $\Theta = 90^\circ$. S_{fast} features the strongest local anisotropy of all bulk waves around the maximum at $\Theta = 83.75^\circ$, where its group velocity slightly exceeds that of L.

The deviation angles γ between the phase and group velocity vectors as function of the propagation direction are shown in Fig. 2.6 for L (Fig. 2.6(b)), S_{fast} (Fig. 2.6(d)), and S_{slow} (Fig. 2.6(f)). L possesses the highest deviation of $\gamma_{\text{max}} = 61.72^\circ$ at $\Theta = 74.01^\circ$. For the pure mode directions parallel and normal to the

TABLE 2.1. Key data of the bulk waves' phase velocity surfaces in SAERTEX[®]7006919/RIMR135.

	$v_{p\max}$ (m/ms)	$\Theta_{v\max}$ ($^\circ$)	$v_{p\min}$ (m/ms)	$\Theta_{v\min}$ ($^\circ$)	δ_{\max} ($^\circ$)	$\Theta_{\delta_{\max}}$ ($^\circ$)	γ_{\max} ($^\circ$)	$\Theta_{\gamma_{\max}}$ ($^\circ$)
L	9.186	0	2.517	90	54.24	69.57	61.72	74.01
S _{fast}	2.332	71.92	2.035	0, 90	54.24	69.57	42.37	84.20
S _{slow}	2.035	0	1.313	90	0	–	24.35	57.17

fibers, γ vanishes. The deviation angle surface of S_{fast} is not only particularly narrow compared to that of L and S_{slow}, it features also local maxima close to the fiber direction. This feature is better analyzed in the cross sections drawn for $\Phi = 0^\circ$, 45° , and 89° in Figs. 2.9(a), 2.9(c), and 2.9(e). Considering the situation at $\Phi = 0^\circ$ in Fig. 2.9(a), S_{fast} has its global energy deviation angle maximum of $\gamma_{\max} = 42.37^\circ$ at $\Theta = 84.20^\circ$, and a local maximum of $\gamma = 9.02^\circ$ at $\Theta = 39.4^\circ$. At $\Phi = 89^\circ$ (Fig. 2.9(c)), the energy deviation has already diminished strongly. Owing to the nature of S_{fast}, it now possesses the dominating energy deviation angle of all bulk waves for the complete Θ -range.

Let us now discuss the polarization properties of the bulk waves. The polarization deviation surface in Fig. 2.7 depicts the deviation angle δ from pure mode polarization as function of the wave propagation direction. As mentioned above, it turns out that only L and S_{fast} waves show polarization angle deviations other than zero from their respective pure mode directions. With the definition of the polarization deviation angle δ invoked above, the corresponding surfaces of L and S_{fast} waves coincide. Conversely, the polarization angles β_L and $\beta_{S_{\text{fast}}}$ add up to 90° . This must be so because of the orthogonality of the polarization vectors. Like the other surfaces, the polarization deviation surface is rotationally symmetric about the x'_1 -axis, and it takes its maximum of $\delta_{\max} = 54.24^\circ$ at $\Theta = 69.57^\circ$. This means that L is actually more transverse than longitudinal, and S_{fast} is more longitudinal than transverse in this situation. It can readily be seen that the deviation angle becomes zero for wave propagation along the fiber direction (x'_1 -axis) and normal to it (x'_2 - x'_3 -plane). These are the propagation directions for which pure L and S_{fast} modes occur. Although we appreciate the esthetics of this surface, it is also worth looking at the cross sections taken at $\Phi = 0^\circ$, 45° , 89° , as shown on the right-hand side in Fig. 2.9. For wave propagation in the $\Phi = 0^\circ$ -plane (Fig. 2.9(b)), we have pure mode propagation along the x_1 -direction, which coincides with the x'_1 -axis, unlike the case for wave propagation in the $\Phi = 45^\circ$, 89° -planes (Figs. 2.9(d) and 2.9(f)). Notice the strong decrease in the deviation angle occurring at $\Phi = 89^\circ$. Pure mode propagation along x_3 is possible in all situations since this direction is normal to the fibers.

Finally, we choose some explicit propagation directions, and calculate the slowness vectors and polarization vectors of the three bulk waves. In this discussion, we appreciate that the slowness s , being the inverse phase velocity v_p , scales directly with the wavenumber ζ via the angular frequency $\omega = 2\pi f$ so that we have

$$\zeta = \omega v_p^{-1} = \omega s \quad \rightarrow \quad s = \zeta \omega^{-1}. \quad (2.84)$$

Therefore, by assigning a frequency f to the slowness, we get the wavenumber. Figure 2.10(a) shows pure modes propagating along the fibers. As stated above, this is the only situation where both shear waves, here labeled S_1 and S_2 , are degenerate so that they cannot be distinguished, basically. This is because both modes are polarized normal to the fibers. In Fig. 2.10(b), pure modes propagate normal to the fibers at $\Theta = 10^\circ$. S_{fast} and S_{slow} now have different slownesses, because S_{fast} is polarized parallel to the fibers while S_{slow} is polarized normal to them. Figures 2.11(a) and 2.11(b) display bulk waves propagating along $\Phi = 0^\circ$, $\Theta = 45^\circ$ and $\Phi = 30^\circ$, $\Theta = 5^\circ$, respectively. The polarization angles are $\beta_L = 39.84^\circ$, $\beta_{S_{\text{fast}}} = 50.16^\circ$, and $\beta_{S_{\text{slow}}} = 90^\circ$ in Fig. 2.11(a) and $\beta_L = 27.38^\circ$, $\beta_{S_{\text{fast}}} = 62.62^\circ$, and $\beta_{S_{\text{slow}}} = 90^\circ$ in Fig. 2.11(b). The polarization vectors are mutually orthogonal as usual. In both Figs. 2.10 and 2.11, the polarization vector of S_{slow} lies always in the x'_2 - x'_3 -plane, *i.e.*, normal to the fibers. This is an inherent feature of S_{slow} .

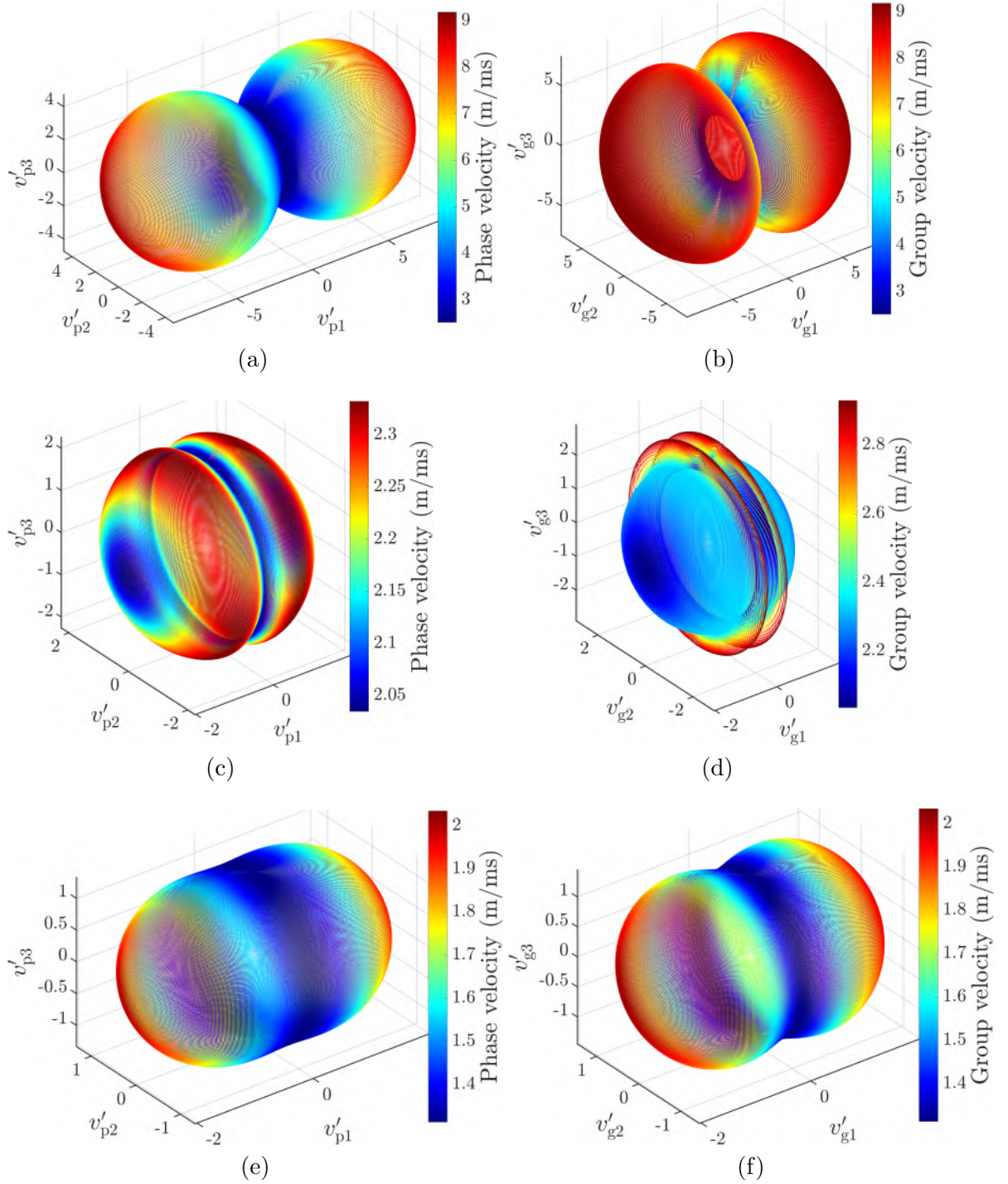


FIG. 2.5. Phase (left) and group velocity surfaces (right) of quasilongitudinal (top), fast quasishear (center), and slow shear (bottom) bulk waves propagating in transversely isotropic SAERTEX[®]7006919/RIMR135.

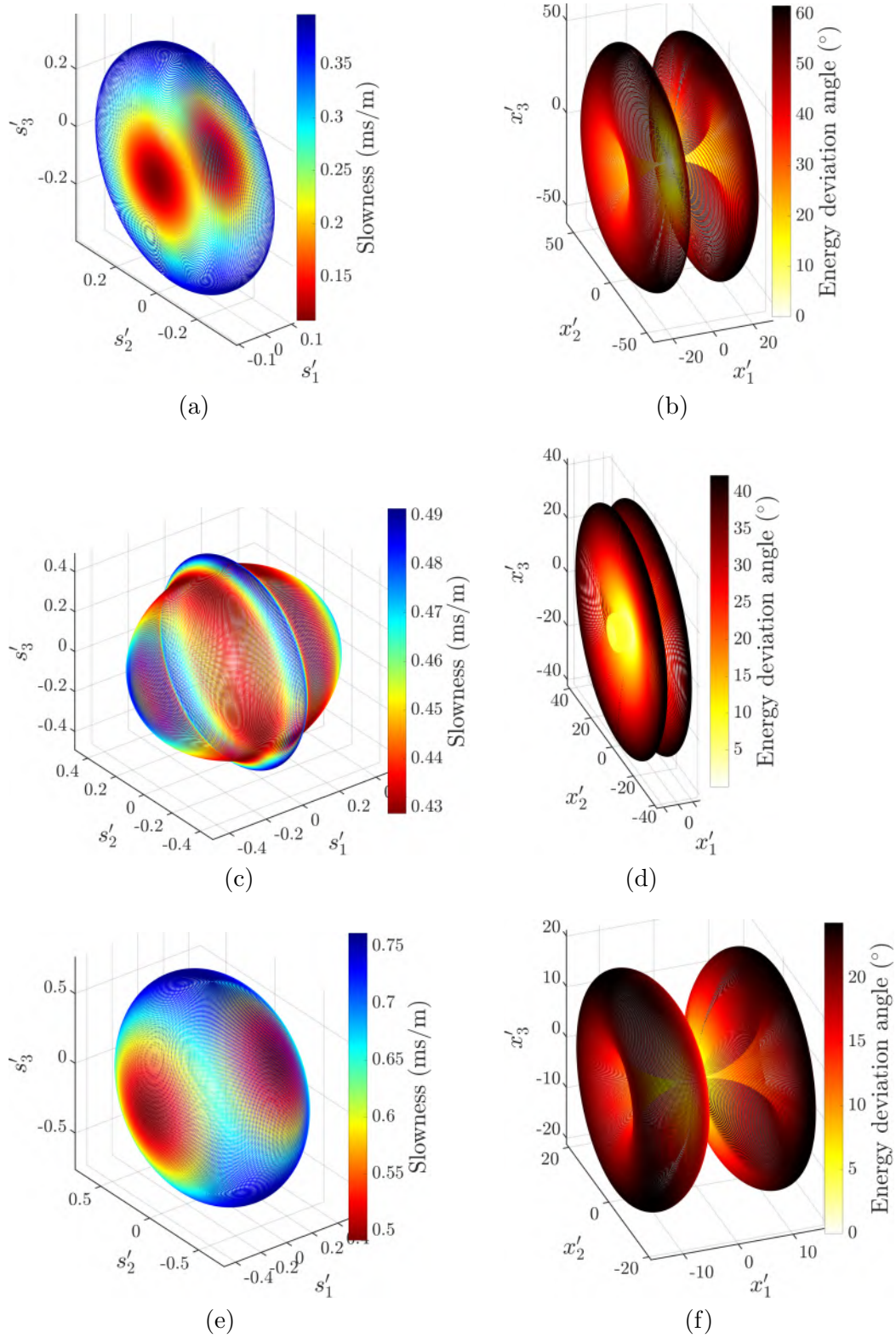


FIG. 2.6. Slowness (left) and energy deviation surfaces (right) of quasilongitudinal (top), fast quasishear (center), and slow shear (bottom) bulk waves propagating in transversely isotropic SAERTEX[®] 7006919/RIMR135. 33

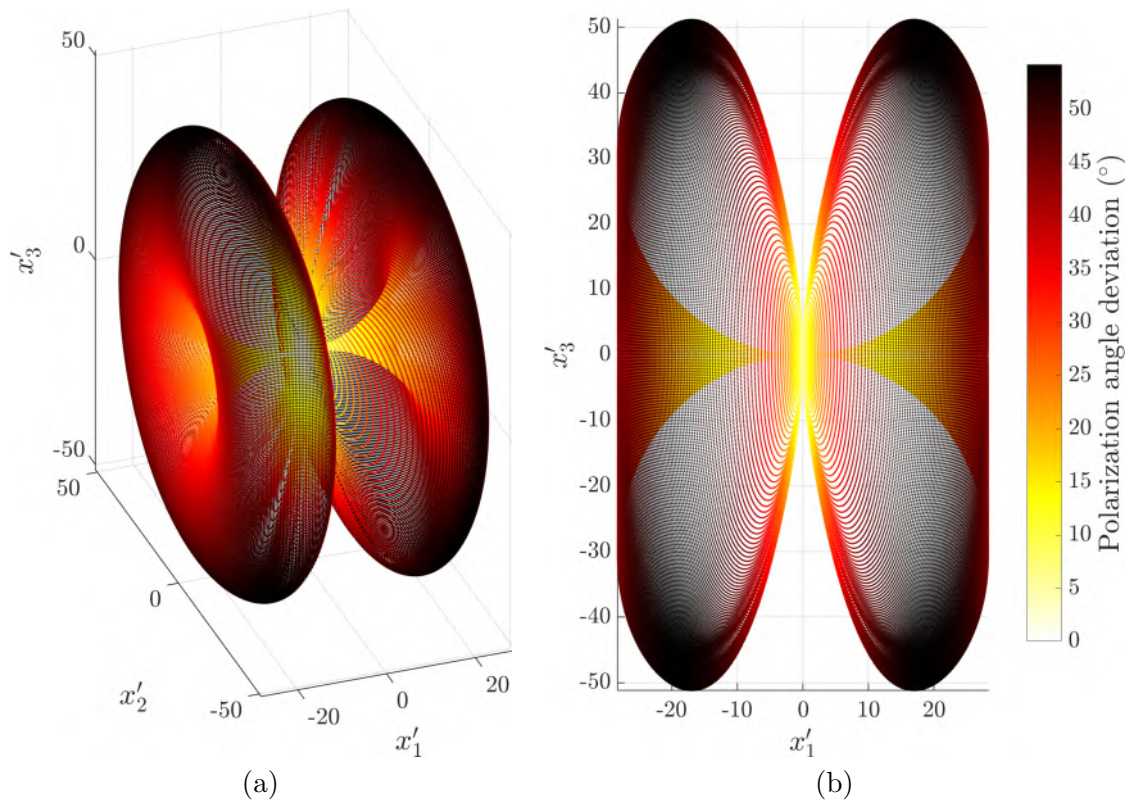


FIG. 2.7. (a) Perspective view and (b) view into the x'_1 - x'_3 -plane of the polarization angle deviation surface of quasilongitudinal and fast quasishear bulk waves in SAERTEX® 7006919/RIMR135. The polarization angle deviation of slow shear waves is zero.

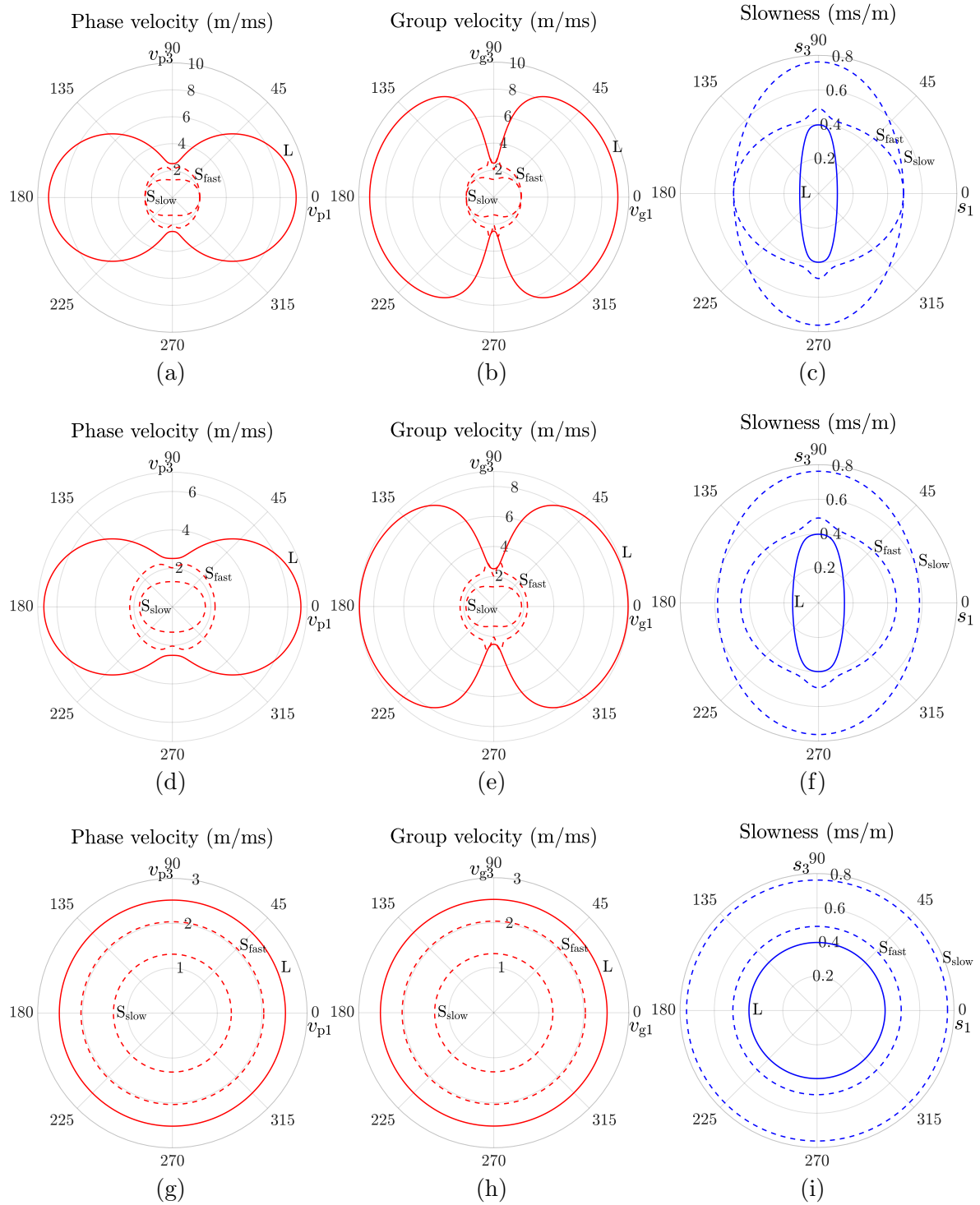


FIG. 2.8. Phase velocity (left), group velocity (center), and slowness (right) of bulk waves propagating in the $\Phi = 0^\circ$ (top), 45° (center), and 90° (bottom) plane in SAERTEX[®]7006919/RIMR135.

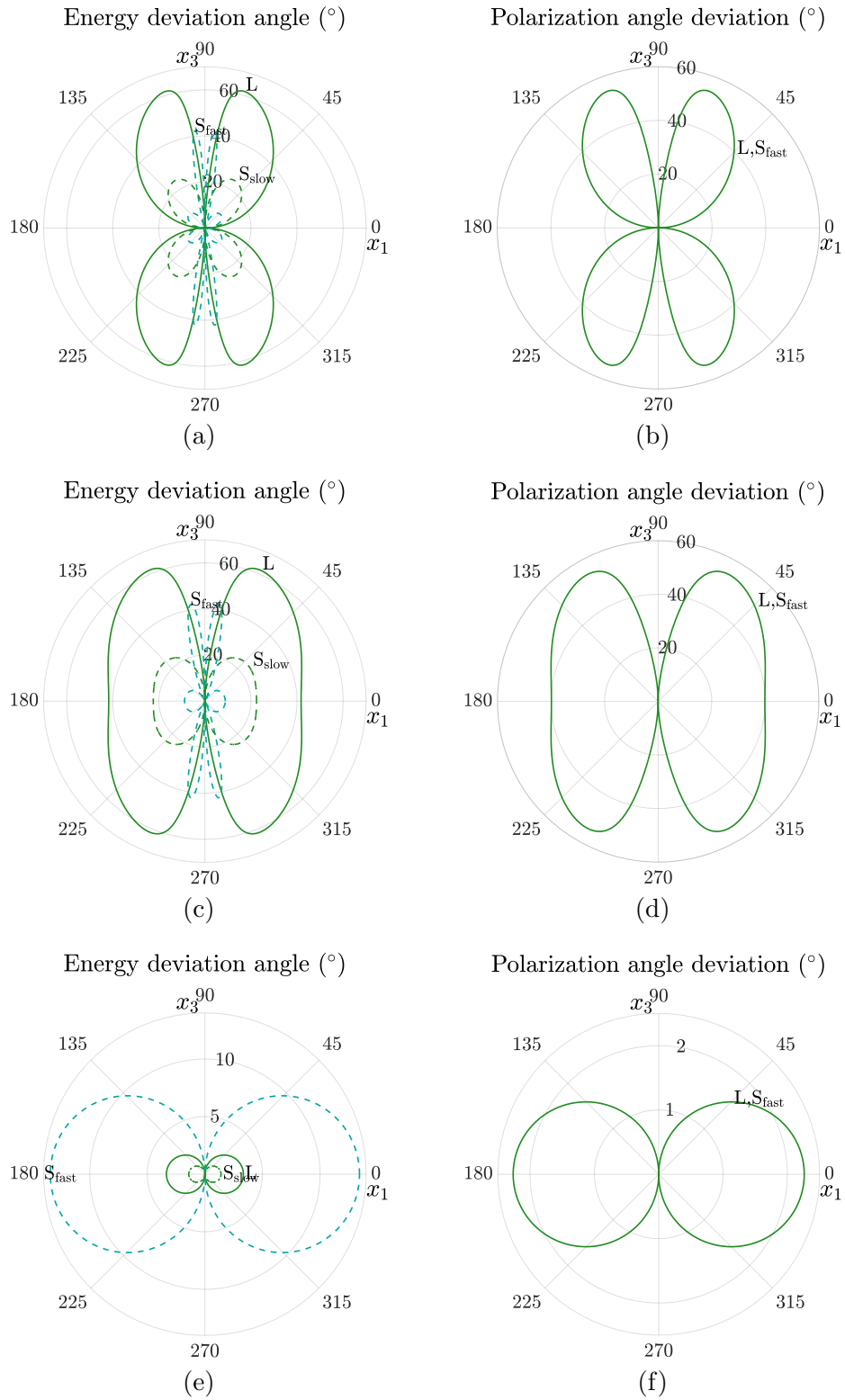
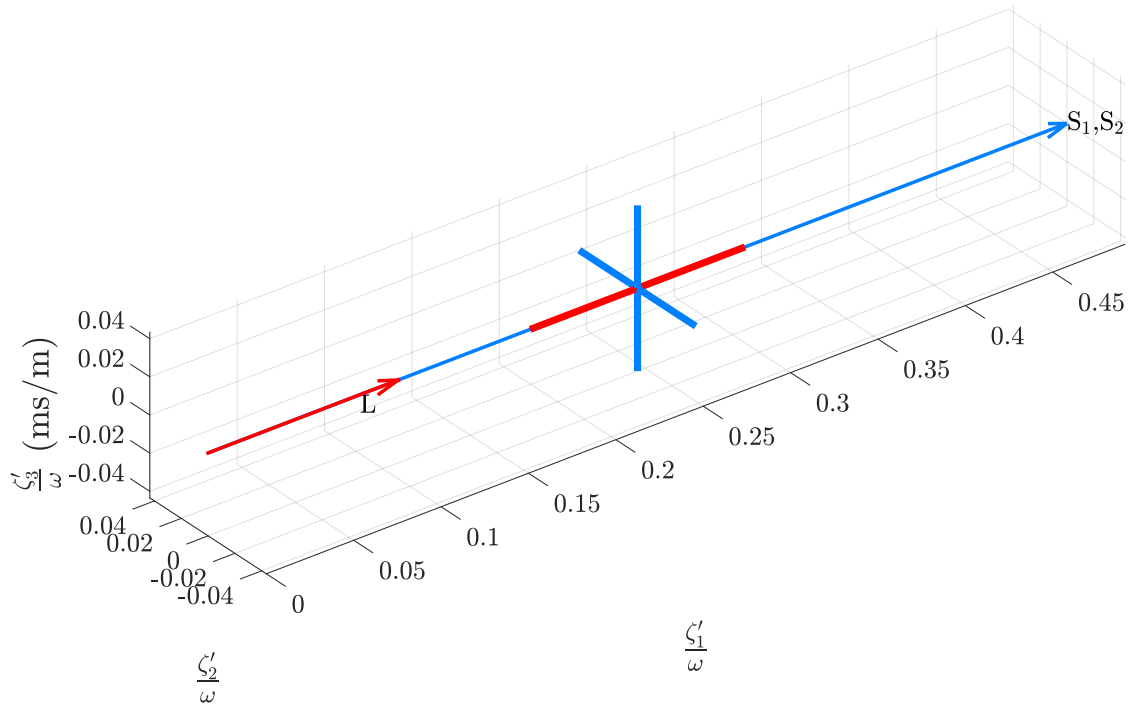
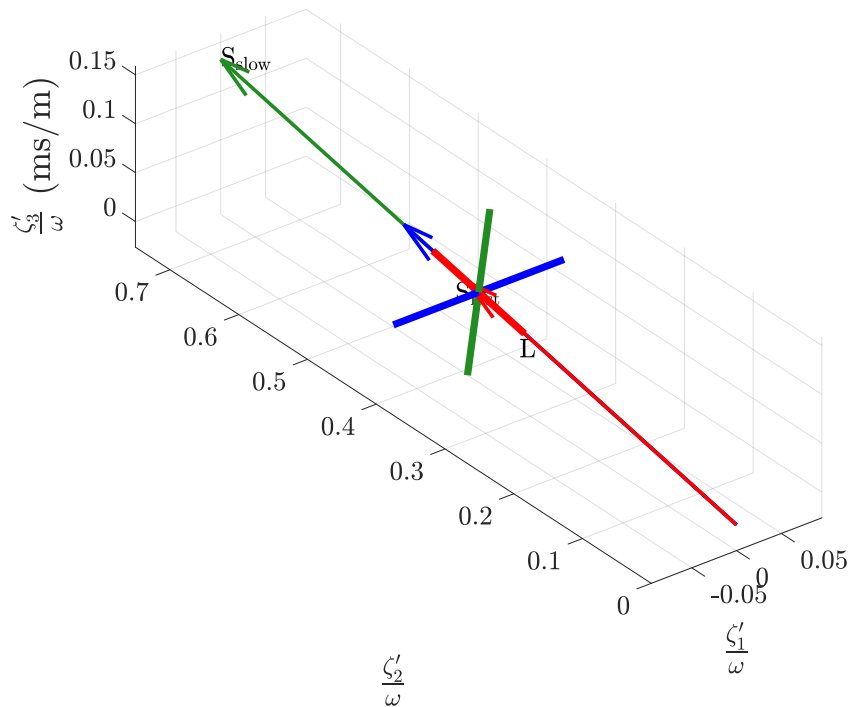


FIG. 2.9. Energy deviation angle (left) and polarization angle deviation (right) of bulk waves propagating in the $\Phi = 0^\circ$ (top), 45° (center), and 89° (bottom) plane in SAERTEX[®] 7006919/RIMR135.



(a)



(b)

FIG. 2.10. Slowness vectors and polarization of bulk waves propagating (a) along the fibers ($\Phi, \Theta = 0^\circ$) and (b) perpendicular to the fibers ($\Phi = 90^\circ, \Theta = 10^\circ$) in SAERTEX[®]7006919/RIMR135. In picture (a), the two shear waves are degenerate. Both pictures show pure modes since the polarization vectors are either along or normal to the propagation direction. This situation occurs only for wave propagation along or normal to the fibers. 37

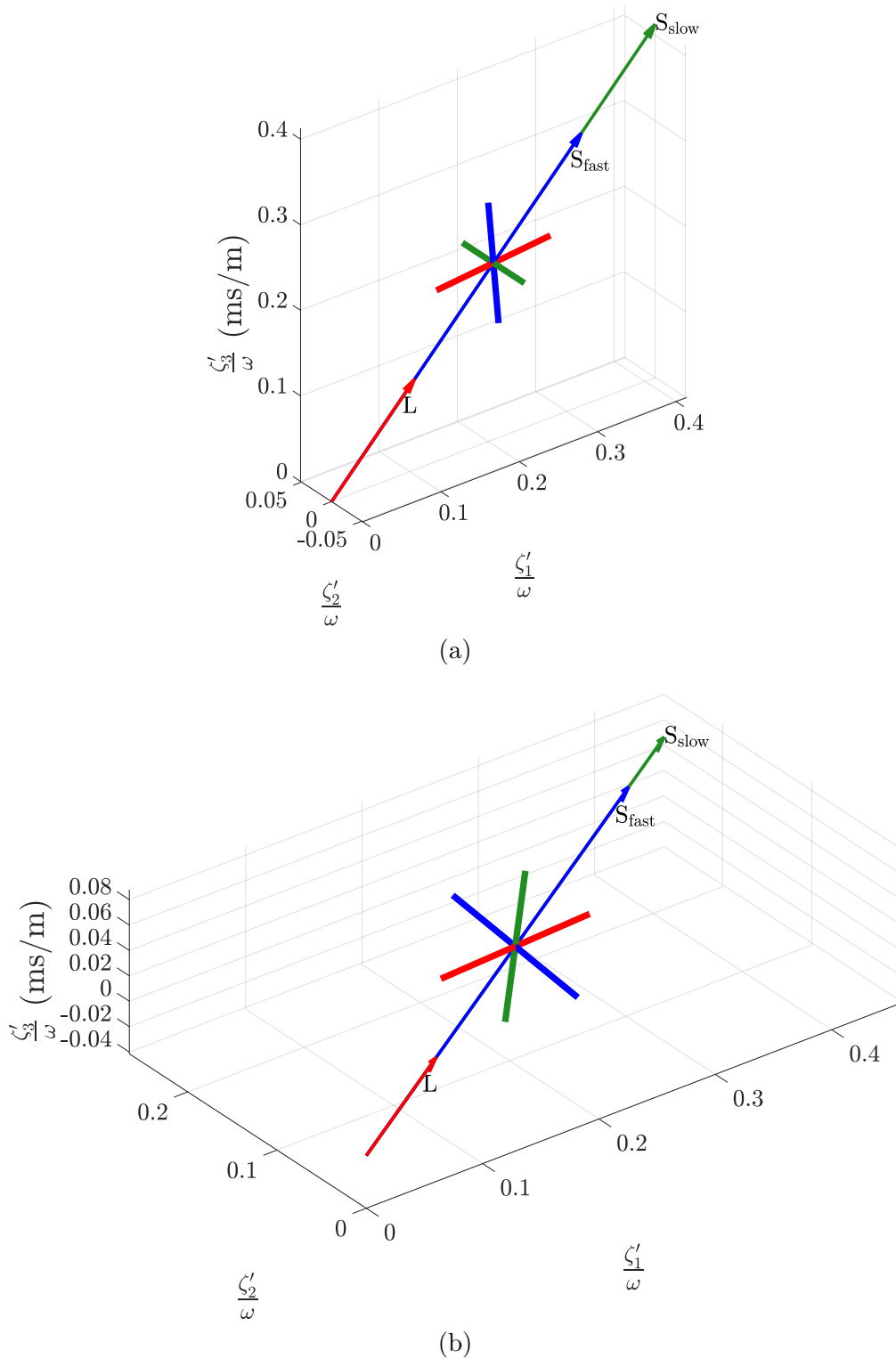


FIG. 2.11. Slowness vectors and polarization of bulk waves propagating along (a) $\Phi = 0^\circ$, $\Theta = 45^\circ$ and (b) $\Phi = 30^\circ$, $\Theta = 5^\circ$ in SAERTEX[®]7006919/RIMR135. S_{slow} is always pure with its polarization oriented normal to the fibers. The polarization vectors are always mutually orthogonal.

2.2.2 Bulk Waves on Interfaces

If a plane wave incidents on a boundary or interface, a certain number of scattered waves are generated. Depending on the properties of the media sharing the boundary, up to six wave components can be generated, namely three reflected waves in the originating medium and three transmitted waves in the continuing medium. We consider the situation depicted in Fig. 2.12. Here, the upper half space is filled by a nonviscous fluid such as air or water and the lower one by a transversely isotropic composite. Similarly as before, the fibers are oriented along the x'_1 -direction. The boundary lies in the x'_1 - x'_2 -plane with x'_3 normal to it. A plane wave is incident at an angle Θ_{in} ³ with respect to x'_3 . Its wavenumber ζ_{in} is given by

$$\zeta_{\text{in}} = \omega s_{\text{in}}, \quad (2.85)$$

where s_{in} is the slowness in the fluid. Since the fluid does not support shear waves (because the shear modulus is zero), only a pressure wave with longitudinal polarization can exist. At the boundary, a certain proportion of the incoming energy is reflected, resulting in a pressure wave propagating back into the fluid at an angle $-\Theta_{\text{in}}$ with $\zeta_{\text{r}} = \zeta_{\text{in}}$, $s_{\text{r}} = s_{\text{in}}$. The remaining energy is transmitted into the composite where up to three bulk waves with the wavenumbers ζ_{L} , $\zeta_{\text{S}_{\text{fast}}}$, $\zeta_{\text{S}_{\text{slow}}}$ and slownesses s_{L} , $s_{\text{S}_{\text{fast}}}$, $s_{\text{S}_{\text{slow}}}$, in accordance with Eq. (2.85), are generated. Notice that all five wave components propagate in a plane x_1 - x_3 rotated about x'_3 by an angle Φ . The scattered waves are refracted according to Snell's law such that they all (reflected and transmitted waves) share with the incident wave the same projected wavenumber along the boundary $\zeta_{\text{in}1}$, *i.e.*,

$$\zeta_{\text{in}} \sin \Theta_{\text{in}} = \zeta_{(q)} \sin \Theta_{(q)} = \zeta_{\text{in}1}, \quad q = 1, 2, 3, 4, \quad (2.86)$$

where $\zeta_{(q)}$ stands for the wavenumber of any scattered wave, and $\Theta_{(q)}$ is the corresponding reflection or refraction angle, respectively. With the use of Eq. (2.85), we can write Eq. (2.86) in terms of the slownesses of the scattered waves $s_{(q)}$ as

$$s_{\text{in}} \sin \Theta_{\text{in}} = s_{(q)} \sin \Theta_{(q)} = s_{\text{in}1}. \quad (2.87)$$

This important constraint is indicated by the two vertical guide lines, drawn parallel to the x'_3 -axis in Fig. 2.12. To illustrate our discussion, we calculate and plot the scattered waves that are generated in transversely isotropic SAERTEX[®]7006919/

³The incidence angle Θ_{in} (as well as the refraction angle) has the opposite definition compared to the propagation angle Θ defined in Sec. 2.2 (compare Figs. 2.12 and 2.4). In composites, the fiber orientation is usually referred to as the Φ , $\Theta = 0^\circ$ -direction, whereas the incidence angle Θ_{in} is given with respect to the surface normal so that $\Theta_{\text{in}} = 0^\circ$ is normal to the fibers.

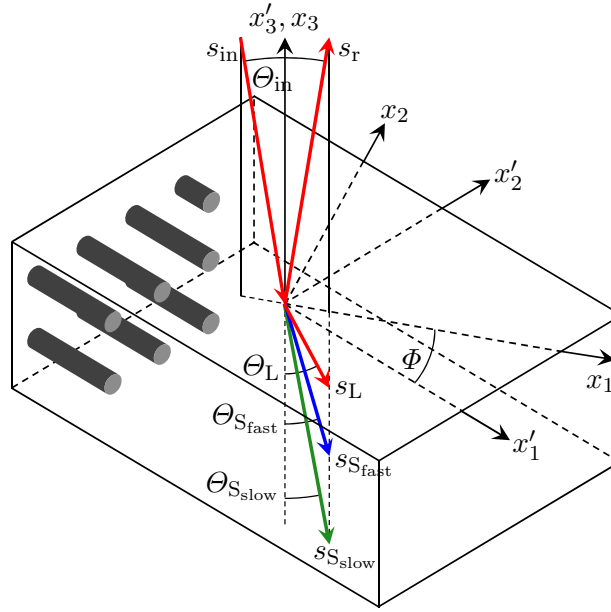


FIG. 2.12. Crystallographic and global coordinate systems x'_i, x_i and fiber orientation in transversely isotropic material. A plane wave incoming from a fluid generates three bulk waves in a composite and one reflected wave in the fluid.

RIMR135 as well as isotropic aluminum alloy 1100 and lead by plane wave incidence from air and water. The material parameters of aluminum alloy 1100 and lead are listed in Appendix B. Figure 2.13(a) shows plane wave incidence from air on SAERTEX at $\Phi = 60^\circ$, $\Theta_{\text{in}} = 3.5^\circ$. The radius of the blue semicircle in the upper half space is the slowness of air of 2.915 ms/m (assuming a phase velocity of 0.343 m/ms). The three profiles in the lower half space represent the slownesses of the three bulk waves. First, we draw a guide line parallel to x_3 through the point where the incident wave intersects the slowness profile of air. Then, we draw a second guide line mirrored about x_3 . Now, the slowness vectors $\zeta'_{(q)}/\omega$ of all scattered waves can be constructed simply by drawing lines from the origin to the points where the right guide line intersects the slowness profiles. By assigning a frequency, the actual wavenumber can be obtained. Numerically, we follow a similar procedure to the one presented in Sec. 2.2.1. We generate the propagation unit vectors for the elevation angles $\Theta \in [0^\circ, 90^\circ]$ with a certain step $\Delta\Theta$ in the propagation plane Φ according to Eq. (2.76), and solve Christoffel's equation to get the slowness profiles of the three bulk waves. The projected slowness along the boundary $s_{\text{in}1}$ of the incident wave is obtained by using Eq. (2.87). Then, we calculate the $s_{1(q)}$ components of the bulk wave profiles, and seek the one from each profile that matches $s_{\text{in}1}$ best. The propagation angles $\Theta_{(q)}$ belonging to the three matching sample points are the refraction angles $\Theta_L, \Theta_{S_{\text{fast}}}$, and $\Theta_{S_{\text{slow}}}$. Obviously, the accuracy of these solutions depends upon the step size $\Delta\Theta$. By contrast, the

refraction angles of the bulk waves generated in isotropic materials can be obtained analytically from Eq. (2.87). Going back to our example in Fig. 2.13(a), we find the bulk waves refracted at $\Theta_L = 40.27^\circ$, $\Theta_{S_{\text{fast}}} = 24.23^\circ$, and $\Theta_{S_{\text{slow}}} = 13.64^\circ$. Upon increasing Θ_{in} , we encounter a situation where the right guide line takes a tangential position to the slowness profile of L ($q = 1$). The incidence angle corresponding to this situation is termed the first critical angle $\Theta_{\text{crit}(1)}$, and is given by

$$\Theta_{\text{crit}(q)} = \sin^{-1} \frac{s_{(q)}^{\Theta=0^\circ}}{s_{\text{in}}}, \quad q = 1, 2, 3, \quad (2.88)$$

where $s_{(q)}^{\Theta=0^\circ}$ is the slowness of the q th bulk wave for propagation along the boundary (and along the fibers). No propagating L wave can be constructed beyond the angle $\Theta_{\text{crit}(1)}$. Physically, L becomes evanescent, *i.e.*, its amplitude decays exponentially with depth. Similar situations occur for S_{fast} ($q = 2$) and S_{slow} ($q = 3$) in this order upon further increasing Θ_{in} . In the present example, we obtain critical angles for L, S_{fast} , and S_{slow} of, respectively, $\Theta_{\text{crit}(1,2,3)} = 3.96^\circ$, 8.58° , and 13.00° . Beyond all critical angles, the incident wave suffers total internal reflection in the fluid. In isotropic materials and in transversely isotropic materials in case of wave propagation in the plane of isotropy (see Fig. 2.8(i)), we get the critical angles by replacing $s_{(q)}^{\Theta=0^\circ}$ in Eq. (2.88) with $s_{(q)}$, representing the bulk wave slownesses s_L , $s_{SV}/s_{S_{\text{fast}}}$, and $s_{SH}/s_{S_{\text{slow}}}$, respectively. Here, we recall that in isotropic materials, we have $s_{SV} = s_{SH}$. To determine the polarization vectors of the bulk waves shown in Fig. 2.13(a), we use Eq. (2.75) with the propagation unit vectors $\mathbf{n}'_{(q)}$, obtaining $\beta_L = 54.08^\circ$, $\beta_{S_{\text{fast}}} = 44.81^\circ$, and $\beta_{S_{\text{slow}}} = 90^\circ$. Figure 2.13(b) shows the bulk waves propagating in the three-dimensional crystallographic coordinate system. The bold lines emanating from the middle of the slowness vectors of each bulk wave indicate their polarization. The properties of the bulk waves calculated in this example are summarized in Table 2.2, and those for the following examples in Tables 2.3-2.5. In Fig. 2.14, we have replaced air by water as a fluid, and let the plane wave impinge from the same direction as in the prior example. Since the slowness of water of 0.667 ms/m is now much closer to the bulk waves' slownesses than before, we get much smaller refraction angles but larger critical angles. As can be seen in Fig. 2.15, the situation in isotropic materials is less sophisticated. We stay with water as a fluid, but change the incidence angle to $\Theta_{\text{in}} = 10^\circ$, and choose aluminum alloy 1100 as a continuing medium. The resulting bulk waves are independent from the azimuthal angle Φ , of course. These are the pure L and SV modes with polarization within the plane of display. SH is actually not generated because the incident wave carries no shear horizontal polarization component. In our final example, we replace aluminum by lead, and choose $\Theta_{\text{in}} = 60^\circ$, leading to the interesting situation depicted in Fig. 2.16. L is evanescent because $\Theta_{\text{in}} > \Theta_{\text{crit}(1)}$, whereas no critical angle exists for the shear waves.

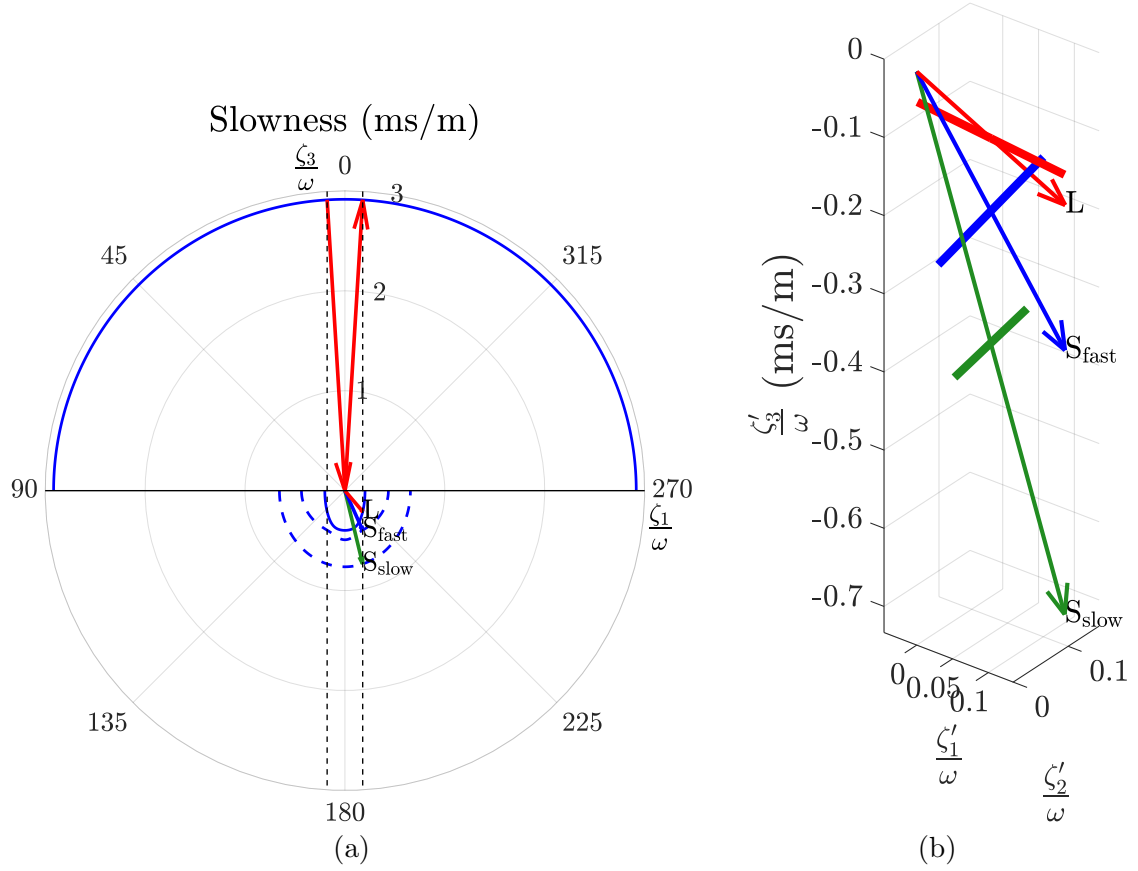


FIG. 2.13. Bulk waves generated in SAERTEX[®]7006919/RIMR135 through plane wave incidence from air at $\Phi = 60^\circ$, $\Theta_{\text{in}} = 3.5^\circ$. The upper half space is covered by air, the lower one by SAERTEX. (a) Construction of the bulk waves' propagation directions based on Snell's law. (b) Propagation directions and polarization of the generated bulk waves in 3-D space.

TABLE 2.2. Critical angles and bulk waves generated in SAERTEX[®]7006919/RIMR135 upon plane wave incidence from air.

Incidence angles: $\Phi = 60^\circ$, $\Theta_{\text{in}} = 3.5^\circ$				
	$\Theta_{\text{crit}} (^\circ)$	$\Theta_{\text{refr}} (^\circ)$	s (ms/m)	$\beta (^\circ)$
L	3.96	40.27	0.275	54.07
S _{fast}	8.58	24.23	0.434	44.81
S _{slow}	13.00	13.64	0.755	90

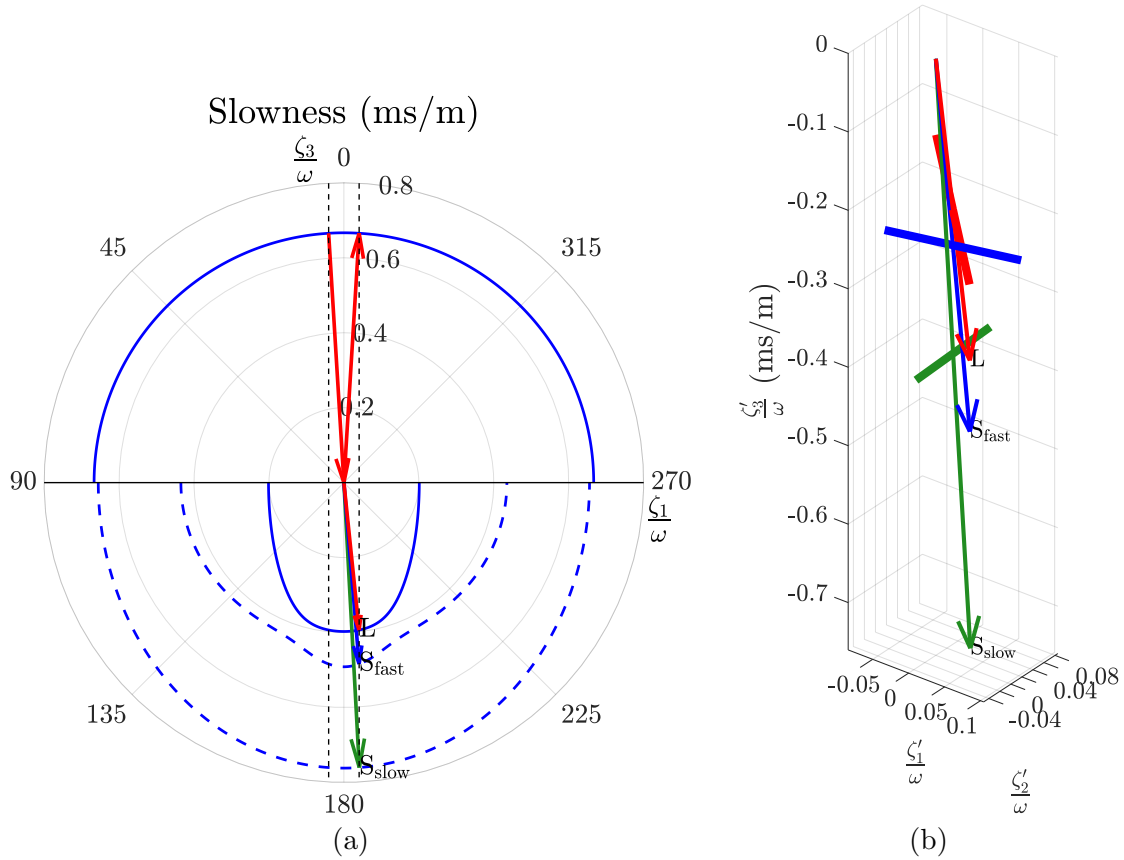


FIG. 2.14. Bulk waves generated in SAERTEX[®]7006919/RIMR135 through plane wave incidence from water at $\Phi = 60^\circ$, $\Theta_{in} = 3.5^\circ$. The upper half space is covered by air, the lower one by SAERTEX. (a) Construction of the bulk waves' propagation directions based on Snell's law. (b) Propagation directions and polarization of the generated bulk waves in 3-D space.

TABLE 2.3. Critical angles and bulk waves generated in SAERTEX[®]7006919/RIMR135 upon plane wave incidence from water.

Incidence angles: $\Phi = 60^\circ$, $\Theta_{in} = 3.5^\circ$				
	Θ_{crit} ($^\circ$)	Θ_{refr} ($^\circ$)	s (ms/m)	β ($^\circ$)
L	17.57	5.91	0.395	7.20
S_{fast}	40.73	4.81	0.486	84.30
S_{slow}	79.50	3.06	0.761	90

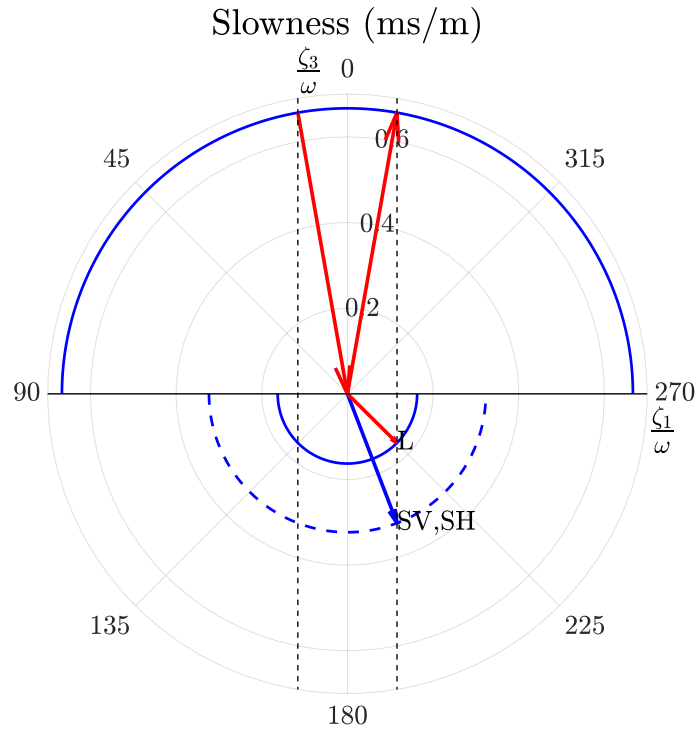


FIG. 2.15. Bulk waves generated in aluminum alloy 1100 through plane wave incidence from water at $\Theta_{\text{in}} = 10^\circ$. The upper half space is covered by water, the lower one by aluminum. SH is actually not generated because the incident wave carries no shear horizontal polarization component.

TABLE 2.4. Critical angles and bulk waves generated in aluminum alloy 1100 upon plane wave incidence from water.

Incidence angle: $\Theta_{\text{in}} = 10^\circ$				
	$\Theta_{\text{crit}} (^\circ)$	$\Theta_{\text{refr}} (^\circ)$	s (ms/m)	$\beta (^\circ)$
L	14.14	45.32	0.163	0
SV, SH	29.00	20.99	0.323	90

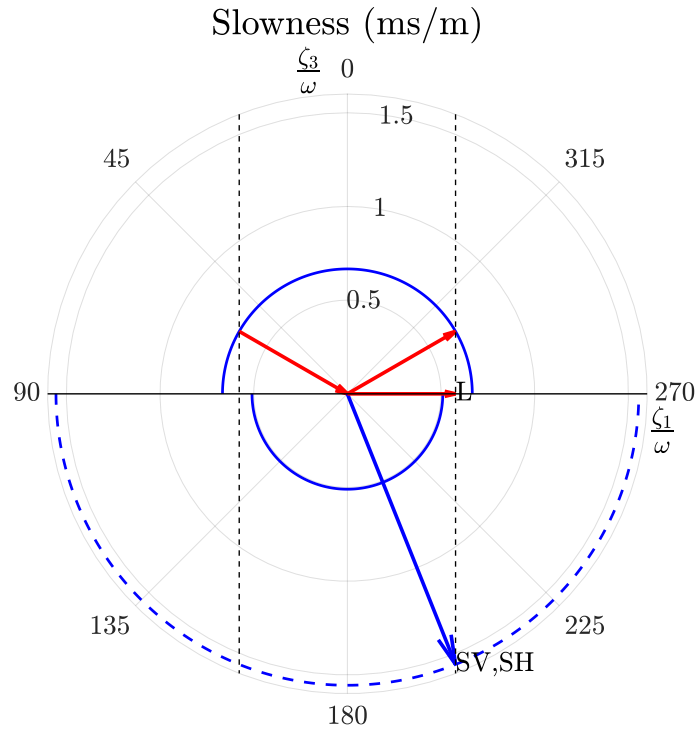


FIG. 2.16. Bulk waves generated in lead through plane wave incidence from water at $\Theta_{\text{in}} = 60^\circ$. The upper half space is covered by water, the lower one by lead.

TABLE 2.5. Critical angles and bulk waves generated in lead upon plane wave incidence from water.

Incidence angle: $\Theta_{\text{in}} = 60^\circ$				
	$\Theta_{\text{crit}} (^\circ)$	$\Theta_{\text{refr}} (^\circ)$	s (ms/m)	$\beta (^\circ)$
L	49.79	90	0.577	–
SV, SH	–	21.79	1.555	90

2.3 Multilayered Transversely Isotropic Waveguides

In Sec. 2.2.1, we used Christoffel's equation to determine the phase velocity of bulk waves propagating in infinite bodies as function of the propagation direction, and in Sec. 2.2.2, we investigated how bulk waves are scattered on interfaces by using Snell's law. In the present section, we set up a multilayered transversely isotropic system and combine Christoffel's equation and Snell's law to model the behavior of bulk waves - and thereby of guided waves - in such a system. Although the solutions are derived for flat structures, they can also be applied to curved systems in good approximation as long as the radius of curvature is much larger than the wavelength of the guided waves. It is important to understand that guided waves evolve through the propagation and superposition of bulk waves. Therefore, in the context of guided wave modeling, bulk waves are often referred to as partial waves. All bulk waves in every layer must act in concert in accordance with Snell's law to allow for a propagating guided wave, and the waveguide constitutes the geometry, for which we seek the case of resonance. In case of resonance, we have a propagating wave along the waveguide's axis, representing also a resonant standing wave in the transverse direction. This phenomenon is often referred to as *transverse resonance* in the literature. The bulk waves must be reflected forth and back with the correct wave vectors and propagation angles so that they undergo a phase shift of an integral multiple of 2π between each roundtrip and consequently interfere constructively. Therefore, it is of fundamental importance to find the propagation directions of the bulk waves. Since boundaries and interfaces are involved in a waveguide, guided waves show dispersion, *i.e.*, the phase velocity (and group velocity) is frequency-dependent. Thus, in order to obtain the dispersion diagrams we are looking for, we will solve the problem for extended frequency ranges.

The section is organized as follows. In Sec. 2.3.1, we describe the geometrical setup and definitions, followed by the general boundary conditions in Sec. 2.3.2. In Sec. 2.3.3, we introduce the TMM and apply it for the modeling of shear horizontal waves without encountering the numerical instability. This discussion is based on the book of Nayfeh [22]. We perform adaptations on the characteristic equations and develop a new routine for the calculation of the through thickness stress and displacement components. Section 2.3.4 contains a comprehensive discussion of the SMM, covering both the general case where Lamb and shear horizontal waves are coupled, as well as the decoupled case. In this section, we rely strongly on the papers published by Rokhlin and Wang [57, 58] and subsequently by Kamal [60]. Another highly recommended source is the book of Rokhlin *et al.* [59]. Again, we introduce adaptations, namely on the algorithm for the global stiffness matrix for symmetric layups as well as on the calculation of the transmitted and reflected bulk wave amplitudes in a multilayered system. For the calculation of the stress and displacement components in a single layer, we use a much simpler relation

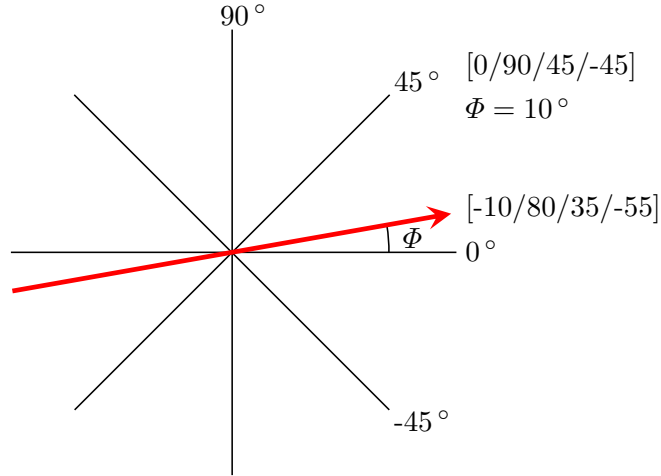


FIG. 2.17. Wave propagation along a propagation angle of $\Phi = 10^\circ$ in a $[0/90/45/-45]$ layup. A positive angle Φ results in a counterclockwise rotation of the propagation direction with respect to the fiber orientations, yielding the effective layup $[0/90/45/-45]-10 = [-10/80/35/-55]$.

than the *backpropagation recursive algorithm* proposed by Rokhlin and Wang. In Sec. 2.3.5, we discuss in detail which mode families occur depending on the symmetry and coupling properties of layups, and we summarize the special characteristic equations and boundary conditions, which allow us to solve for each mode family separately. Finally, in Sec. 2.3.6, we show the calculation of the group velocity, propagation time, as well as excitation angle and present exemplary dispersion diagrams.

2.3.1 Geometrical Setup and General Description

In Sec. 2.1.4, we introduced the notation for a multilayered anisotropic system like a composite plate, consisting of an arbitrary number of transversely isotropic layers m with the thicknesses d_m . As sketched in Fig. 2.1(b), we have assigned local (crystallographic) coordinate systems $x'_{i(m)} = (x'_1, x'_2, x'_3)_{(m)}$, residing on top of each layer such that the fibers are oriented along $x'_{1(m)}$, while $x'_{3(m)}$ is normal to the m th layer. Furthermore, we have invoked the global coordinate system $x_i = (x_1, x_2, x_3)$. The local coordinate systems are rotated counterclockwise by arbitrary angles Φ_m between x_1 and $x'_{1(m)}$ about the x_3 -axis. We choose the global coordinate system such that the x_1 - x_3 -plane coincides with the incidence plane of the incoming plane wave, as depicted in Fig. 2.12. Guided wave propagation is inherently along the x_1 -direction. We calculate each layer's transformed stiffness matrix components $C'_{ij(m)}$ in the global coordinate system according to Eq. (2.37). For example, if we consider a layup like $[0/90/45/-45]$, as sketched in Fig. 2.17, and

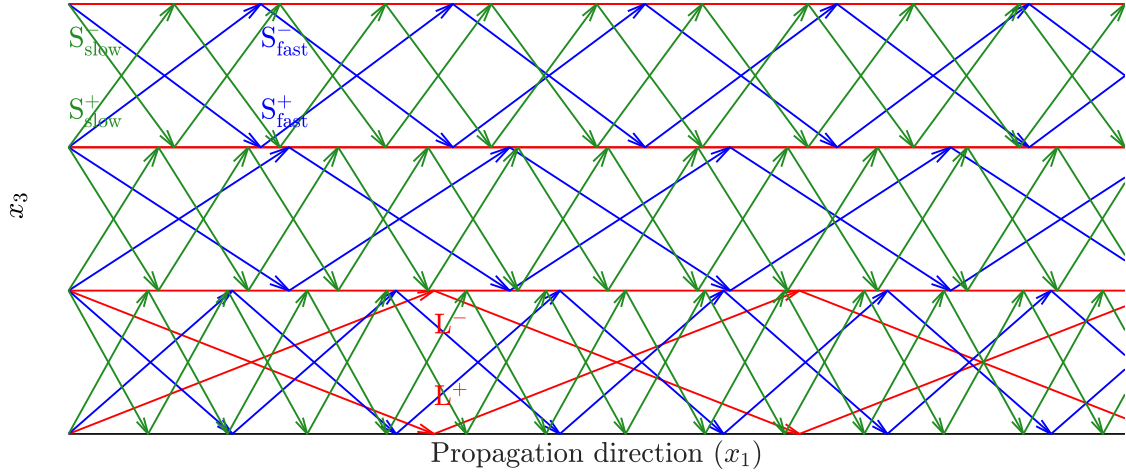


FIG. 2.18. Bulk wave pattern of the B_3^4 Lamb wave at 1.6 MHz·mm for wave propagation along 0° in SAERTEX[®]7006919/RIMR135 [0/45/90]. L^- and L^+ are evanescent in the upper two layers.

we want to perform our analysis for wave propagation along the $\Phi = 10^\circ$ -direction in this layup, we need to transform the m th stiffness matrix for its respective rotation angles $\Phi_m = -10^\circ, 80^\circ, 35^\circ, -55^\circ$.

When an incident wave hits the top interface of the first (uppermost in our definition) layer, up to three scattered waves will be generated in this layer, namely L , SV , and SH in isotropic materials and L , S_{fast} , and S_{slow} in transversely isotropic materials. These waves propagate downward ($-x_3$) at their respective refraction angles until they reach the bottom interface of the first layer. Here, a certain proportion of energy is transmitted into the second layer while the rest gets reflected, propagating upward ($+x_3$) at the same refraction angles. Hence, a maximum of six bulk waves are propagating in the first and in all following layers, namely L^- , L^+ , SV^- , SV^+ , and SH^- , SH^+ in isotropic materials and L^- , L^+ , S_{fast}^- , S_{fast}^+ , and S_{slow}^- , S_{slow}^+ in transversely isotropic materials. Figure 2.18 shows such a bulk wave pattern in a layup consisting of three layers. In this particular case, L^- and L^+ are evanescent in the upper two layers.

2.3.2 General Boundary Conditions

While the bulk waves in an infinite medium are unconditionally described by the field equations (2.1), (2.2), and (2.3), the presence of interfaces leads to restrictions on the guided waves' motion that have to be accounted for by the introduction of boundary conditions. Firstly, we assume rigid bonding between the layers, implying

⁴The modal nomenclature used in this work is explained in Sec. 2.3.5.

the continuity of stresses and displacements over the layers' boundaries, namely

$$u_i = \bar{u}_i, \quad \sigma_{i3} = \bar{\sigma}_{i3}, \quad i = 1, 2, 3, \quad (2.89)$$

where u_i, σ_{i3} correspond to the originating layer and $\bar{u}_i, \bar{\sigma}_{i3}$ to the continuing layer. Secondly, we assume the plate to be surrounded by a vacuum. This means that no energy can leak into the surrounding medium. Therefore, we require the vanishing of the stress components at the top ($x_3 = 0$) and bottom ($x_3 = -d$) of the plate, that is,

$$\sigma_{i3}^0, \sigma_{i3}^{-d} = 0, \quad i = 1, 2, 3. \quad (2.90)$$

Using the acoustical impedances $Z = \rho v_p$ of aluminum alloy 1100 ($\rho = 2710 \text{ kg/m}^3$, $v_p = 6142 \text{ m/s}$), air ($\rho = 1.2 \text{ kg/m}^3$, $v_p = 343 \text{ m/s}$), and water ($\rho = 1000 \text{ kg/m}^3$, $v_p = 1500 \text{ m/s}$), and calculating the transmission $T = 2Z_1/(Z_1 + Z_2)$ through the respective interface delivers values of $T_{\text{air/alu}} = 4.9 \times 10^{-5}$ and $T_{\text{water/alu}} = 0.17$. This demonstrates that assuming a vacuum ($T_{\text{vacuum/alu}} = 0$) is a very good approximation for air as a surrounding medium, but not for water.

2.3.3 Transfer Matrix Method

In this section, the global transfer matrix is formulated for the general case, *i.e.*, the composite contains layers with arbitrary fiber orientations Φ_m , and the guided wave's propagation direction Φ is also arbitrary in the x'_1 - x'_2 -plane. Then, the modal solutions for pure shear horizontally polarized waves in the special case of wave propagation along axes of symmetry are presented. Since shear horizontal waves are never evanescent, we can use the TMM to solve them without encountering the numerical instability. Calculating dispersion curves for shear horizontal waves with the TMM is also faster than by using the SMM. However, for the calculation of pure and coupled Lamb waves, we need the SMM since the TMM suffers from the numerical instability in these cases.

General Layered Composite

Whereas in Sec. 2.2.1, we solved Christoffel's equation (2.68) for the phase velocity v_p in terms of the propagation direction \mathbf{n}' , we now solve it for the propagation directions of the bulk waves for which all of them have the same wavenumber component ξ ($= \omega/c_p$) along x_1 , as required by Snell's law. Therefore, we recast Eq. (2.63) into

$$(u_1, u_2, u_3) = (U_1, U_2, U_3)e^{i\xi(x_1 + \alpha x_3 - c_p t)}, \quad (2.91)$$

where c_p is the phase velocity component along x_1 and α is the ratio of the bulk waves' wavenumber components along the x_3 and x_1 -directions $\alpha = \zeta_3/\zeta_1 = \zeta_3/\xi$.

Thus, referring back to Figs. 2.13-2.16⁵, we have the horizontal component of the slowness $s_1 = 1/c_p$ and the vertical component $s_3 = \alpha/c_p$ so that we can give the slowness as

$$s^2 = \frac{\alpha^2}{c_p^2} + \frac{1}{c_p^2}, \quad (2.92)$$

or equivalently

$$\alpha^2 = s^2 c_p^2 - 1. \quad (2.93)$$

By substituting Eq. (2.91) into the displacement field equations (2.49)-(2.51), three coupled equations are obtained,

$$\begin{bmatrix} C_{11} - \rho c_p^2 + C_{55} \alpha^2 & C_{16} + C_{45} \alpha^2 & (C_{13} + C_{55}) \alpha \\ & C_{66} - \rho c_p^2 + C_{44} \alpha^2 & (C_{36} + C_{45}) \alpha \\ \text{sym} & & C_{55} - \rho c_p^2 + C_{33} \alpha^2 \end{bmatrix} \begin{bmatrix} U_1 \\ U_2 \\ U_3 \end{bmatrix} = 0, \quad (2.94)$$

which we refer to as the *wavenumber ratio form* of Christoffel's equation, while the 3×3 matrix is the corresponding Christoffel matrix M_{ij} , $i, j = 1, 2, 3$. Similarly as in Sec. 2.2.1, we have now obtained three homogeneous linear equations for the displacement amplitudes U_i of the bulk waves. Nontrivial solutions for U_1 , U_2 , and U_3 require the vanishing of the determinant of the Christoffel matrix in Eq. (2.94), yielding the sixth-degree polynomial equation

$$\alpha^6 + A_1 \alpha^4 + A_2 \alpha^2 + A_3 = 0, \quad (2.95)$$

with the coefficients A_1 , A_2 , and A_3 given in Appendix C. Equation (2.95) has six solutions α_q , $q = 1, 2, \dots, 6$, and again we use the analytical expressions given in Appendix C to find them. As assigned in Eq. (C.5), we obtain three pairs of solutions, corresponding to the downward and upward propagating bulk waves,

$$\alpha_{L^-} = -\alpha_{L^+}, \quad \alpha_{S_{\text{fast}}^-} = -\alpha_{S_{\text{fast}}^+}, \quad \alpha_{S_{\text{slow}}^-} = -\alpha_{S_{\text{slow}}^+}. \quad (2.96)$$

Bulk wave patterns like the one shown in Fig. 2.18 are constructed from α_q . Substituting α_q into Christoffel's equation (2.94) delivers the bulk waves' displacement amplitude ratios $V_q = U_{2q}/U_{1q}$ and $W_q = U_{3q}/U_{1q}$, namely

$$V_q = \frac{m_{11}(\alpha_q)m_{23}(\alpha_q) - m_{13}(\alpha_q)m_{12}(\alpha_q)}{m_{13}(\alpha_q)m_{22}(\alpha_q) - m_{12}(\alpha_q)m_{23}(\alpha_q)}, \quad (2.97)$$

$$W_q = \frac{m_{11}(\alpha_q)m_{22}(\alpha_q) - m_{12}(\alpha_q)^2}{m_{12}(\alpha_q)m_{23}(\alpha_q) - m_{22}(\alpha_q)m_{13}(\alpha_q)}, \quad (2.98)$$

⁵See a graphic illustration of α in Sec. 2.4, Figs. 2.30 and 2.34.

where the elements $m_{ij}(\alpha_q)$ are the components of the Christoffel matrix. Now, for convenience, the new variable $\sigma_{ij}^* = \sigma_{ij}/i\xi$ is introduced. Thus, the displacement and stress field components can be written as

$$\begin{aligned} (u_1, u_2, u_3) &= \sum_{q=1}^6 (1, V_q, W_q) U_{1q} e^{i\xi(x_1 + \alpha_q x_3 - c_p t)}, \\ (\sigma_{33}^*, \sigma_{13}^*, \sigma_{23}^*) &= \sum_{q=1}^6 (D_{1q}, D_{2q}, D_{3q}) U_{1q} e^{i\xi(x_1 + \alpha_q x_3 - c_p t)}, \end{aligned} \quad (2.99)$$

where the stress amplitudes are obtained from Eq. (2.8) as

$$\begin{aligned} D_{1q} &= C_{13} + C_{36}V_q + C_{33}\alpha_q W_q, \\ D_{2q} &= C_{55}(\alpha_q + W_q) + C_{45}\alpha_q V_q, \\ D_{3q} &= C_{45}(\alpha_q + W_q) + C_{44}\alpha_q V_q. \end{aligned} \quad (2.100)$$

Thanks to the symmetry properties of α_q given in Eq. (2.96), the amplitude ratios Eqs. (2.97) and (2.98) have the properties

$$\begin{aligned} V_2 &= V_1, & V_4 &= V_3, & V_6 &= V_5, \\ W_2 &= -W_1, & W_4 &= -W_3, & W_6 &= -W_5, \end{aligned} \quad (2.101)$$

and likewise the stress amplitudes from Eq. (2.100)

$$\begin{aligned} D_{12} &= D_{11}, & D_{14} &= D_{13}, & D_{16} &= D_{15}, \\ D_{22} &= -D_{21}, & D_{24} &= -D_{23}, & D_{26} &= -D_{25}, \\ D_{32} &= -D_{31}, & D_{34} &= -D_{33}, & D_{36} &= -D_{35}. \end{aligned} \quad (2.102)$$

Let us consider a multilayered plate, consisting of m layers. We rewrite Eqs. (2.99) in matrix form, relating the displacement and stress components at the top \mathbf{u}_m , $\boldsymbol{\sigma}_m^*$ ($x_{3(m)} = 0$) and bottom \mathbf{u}_{m+1} , $\boldsymbol{\sigma}_{m+1}^*$ ($x_{3(m)} = -d_m$) of the m th layer to the wave amplitude vectors \mathbf{U}_m^\pm

$$\begin{aligned} \begin{bmatrix} \mathbf{u}_m \\ \boldsymbol{\sigma}_m^* \end{bmatrix} &= \begin{bmatrix} \mathbf{P}^- & \mathbf{P}^+ \mathbf{H} \\ \mathbf{D}^- & \mathbf{D}^+ \mathbf{H} \end{bmatrix}_m \begin{bmatrix} \mathbf{U}_m^- \\ \mathbf{U}_m^+ \end{bmatrix}, \\ \begin{bmatrix} \mathbf{u}_{m+1} \\ \boldsymbol{\sigma}_{m+1}^* \end{bmatrix} &= \begin{bmatrix} \mathbf{P}^- \mathbf{H} & \mathbf{P}^+ \\ \mathbf{D}^- \mathbf{H} & \mathbf{D}^+ \end{bmatrix}_m \begin{bmatrix} \mathbf{U}_m^- \\ \mathbf{U}_m^+ \end{bmatrix}, \end{aligned} \quad (2.103)$$

where d_m is the thickness of the m th layer and

$$\begin{aligned} \mathbf{P}^- &= \begin{bmatrix} 1 & 1 & 1 \\ V_1 & V_3 & V_5 \\ W_1 & W_3 & W_5 \end{bmatrix}, & \mathbf{P}^+ &= \begin{bmatrix} 1 & 1 & 1 \\ V_1 & V_3 & V_5 \\ -W_1 & -W_3 & -W_5 \end{bmatrix}, \\ \mathbf{D}^- &= \begin{bmatrix} D_{11} & D_{13} & D_{15} \\ D_{21} & D_{23} & D_{25} \\ D_{31} & D_{33} & D_{35} \end{bmatrix}, & \mathbf{D}^+ &= \begin{bmatrix} D_{11} & D_{13} & D_{15} \\ -D_{21} & -D_{23} & -D_{25} \\ -D_{31} & -D_{33} & -D_{35} \end{bmatrix}, \\ \mathbf{H} &= \begin{bmatrix} e^{i\xi\alpha_1 x_3} & 0 & 0 \\ 0 & e^{i\xi\alpha_3 x_3} & 0 \\ 0 & 0 & e^{i\xi\alpha_5 x_3} \end{bmatrix}, & \mathbf{U}^\pm &= \begin{bmatrix} U_{11} \\ U_{12} \\ U_{13} \end{bmatrix}, \end{aligned} \quad (2.104)$$

where we suppress the common factor $e^{i\xi(x_1 - c_p t)}$ for brevity. By eliminating the displacement amplitude vectors \mathbf{U}_m^\pm from Eqs. (2.103), we relate the displacement and stress field components at the top of the m th layer to those at its bottom

$$\begin{bmatrix} \mathbf{u}_{m+1} \\ \boldsymbol{\sigma}_{m+1}^* \end{bmatrix} = \begin{bmatrix} \mathbf{P}^- \mathbf{H} & \mathbf{P}^+ \\ \mathbf{D}^- \mathbf{H} & \mathbf{D}^+ \end{bmatrix}_m \begin{bmatrix} \mathbf{P}^- & \mathbf{P}^+ \mathbf{H} \\ \mathbf{D}^- & \mathbf{D}^+ \mathbf{H} \end{bmatrix}_m^{-1} \begin{bmatrix} \mathbf{u}_m \\ \boldsymbol{\sigma}_m^* \end{bmatrix} = \mathbf{A}_m \begin{bmatrix} \mathbf{u}_m \\ \boldsymbol{\sigma}_m^* \end{bmatrix}, \quad (2.105)$$

where \mathbf{A}_m is the local transfer matrix of the m th layer. Equation (2.105) is written out explicitly in Appendix D. By presenting the transfer matrix as given in Eq. (2.105), we have adopted the form introduced by Rokhlin *et al.* in Refs. [57,59] because it is more suitable to compare it with the stiffness matrix presented in Sec. 2.3.4, Eq. (2.141). Of course, Eq. (2.105) is equivalent to the transfer matrix representation given by Nayfeh in Ref. [22]. The global transfer matrix \mathbf{A} is obtained by the multiplication of the individual local transfer matrices

$$\mathbf{A} = \mathbf{A}_m \mathbf{A}_{m-1} \dots \mathbf{A}_1. \quad (2.106)$$

The global transfer matrix relates the displacements and stresses at the top of the whole plate ($x_3 = 0$) to those at its bottom ($x_3 = -d$)

$$\begin{bmatrix} \mathbf{u}_{-d} \\ \boldsymbol{\sigma}_{-d}^* \end{bmatrix} = \mathbf{A} \begin{bmatrix} \mathbf{u}_0 \\ \boldsymbol{\sigma}_0^* \end{bmatrix}, \quad (2.107)$$

where d is the thickness of the plate. To find modal solutions to Eq. (2.107), we use the stress free upper and lower surfaces condition specified in Eq. (2.90), and write Eq. (2.107) in the form

$$\begin{bmatrix} u_1 \\ u_2 \\ u_3 \\ 0 \\ 0 \\ 0 \end{bmatrix}_{-d} = \mathbf{A} \begin{bmatrix} u_1 \\ u_2 \\ u_3 \\ 0 \\ 0 \\ 0 \end{bmatrix}_0 \rightarrow \begin{bmatrix} 0 \\ 0 \\ 0 \end{bmatrix} = \begin{bmatrix} a_{41} & a_{42} & a_{43} \\ a_{51} & a_{52} & a_{53} \\ a_{61} & a_{62} & a_{63} \end{bmatrix} \begin{bmatrix} u_1 \\ u_2 \\ u_3 \end{bmatrix}_0, \quad (2.108)$$

which requires the 3×3 submatrix to be singular. Therefore, the characteristic function for the system is

$$\det \begin{bmatrix} a_{41} & a_{42} & a_{43} \\ a_{51} & a_{52} & a_{53} \\ a_{61} & a_{62} & a_{63} \end{bmatrix} = 0. \quad (2.109)$$

Equation (2.109) can be solved numerically in order to determine the guided wave's phase velocity dispersion versus the frequency or wavenumber.

However, the TMM suffers from a well-known numerical instability. The problem occurs with increasing frequency or layer thickness when the critical angle in one or more layers is reached so that bulk waves become evanescent, as the case for L^- and L^+ in the upper two layers in Fig. 2.18. Then, instead of having sinusoidal wave functions $e^{i\xi x_3}$, the wavenumber ξ turns complex, leading to decaying functions $e^{\pm\xi x_3}$. These functions can become very small and very large. In principle, these terms possess no problem since they cancel out upon carrying out the transfer matrix operation. However, they quickly fall below the precision of a computer, providing only a finite number of significant digits, thereby causing the numerical instability. In practice, on a computer with increasing frequency or layer thickness, the \mathbf{H} matrix will eventually contain only zeros. From Eq. (2.105), we see that in the two matrices from which the transfer matrix \mathbf{A}_m is calculated, entire columns will turn zero, rendering the matrices singular. The numerical instability comes from the fact that the inverse of the right-hand matrix is undefined. The problem cannot be solved by simply increasing the computer's precision, due to the extreme behavior of the exponential functions with real arguments. Instead, a complete reformulation of the problem is needed to avoid the singular matrices. This will be the topic in Sec. 2.3.4.

Propagation Along Axes of Symmetry

The physical reason why we do not encounter the numerical instability in the following algorithms is because shear horizontal waves are never evanescent. Practically, this means that we do not face the decaying exponential functions and therefore no singular matrices with undefined inverses can occur. In fact, we can perform the matrix inversion analytically if we solve for the shear horizontally polarized modes in the case of wave propagation along axes of symmetry. Then, the solutions decouple into pure Lamb modes, governed by the field equations (2.52) and (2.54), and pure shear horizontal modes, described by Eq. (2.53), but this occurs only in layups containing solely layers with $\Phi_m = 0^\circ, 90^\circ$ fiber orientations, while the wave propagation must be along either of those directions as well. Hence, x_3 coincides with x'_3 , and x_1 can coincide with either x'_1 or x'_2 for 0° or 90° orientation, respectively (see Fig. 2.1(a)). As shown in Fig. 2.19(a), for guided wave propagation

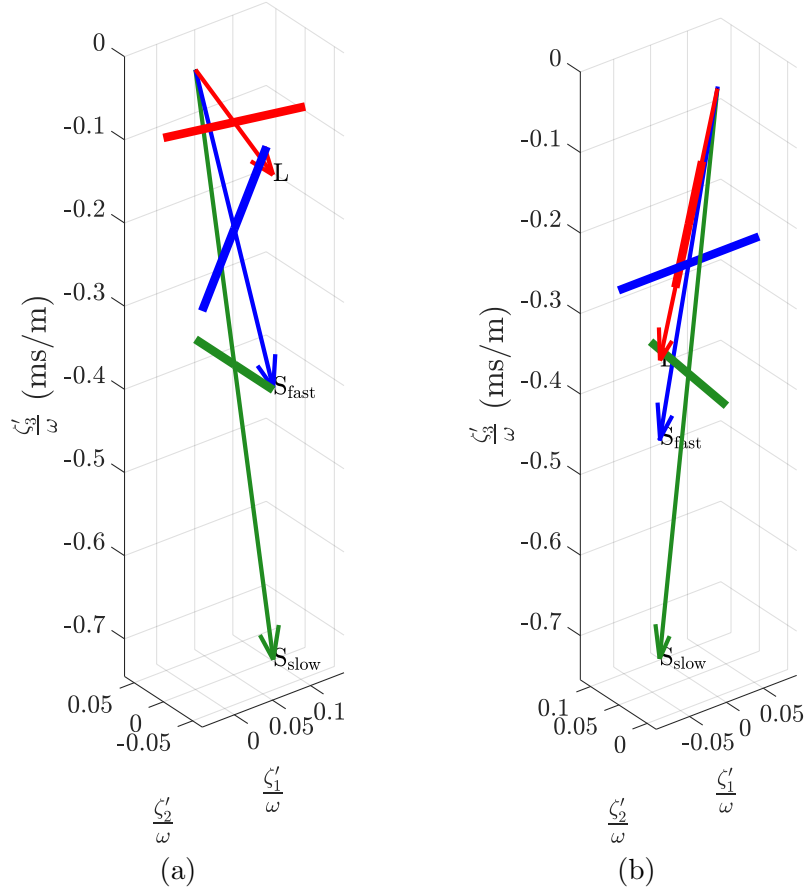


FIG. 2.19. Bulk waves generated in SAERTEX[®]7006919/RIMR135 through plane wave incidence from air at (a) $\Theta_{\text{in}} = 2^\circ$, $\Phi_m = 0^\circ$ and (b) $\Phi_m = 90^\circ$. Both pictures show partial decoupling so that pure Lamb and shear horizontal waves can evolve.

along 0° , L and S_{fast} are coupled with polarization in the x'_1 - x'_3 -plane, while S_{slow} with its polarization in the x'_2 - x'_3 -plane is decoupled from L and S_{fast} . Therefore, L and S_{fast} contribute to a pure Lamb wave and S_{slow} to a pure shear horizontal mode. However, for wave propagation along 90° , Fig. 2.19(b) shows that S_{fast} and S_{slow} have exchanged their roles. Now, the pure Lamb wave evolves through the coupling of L and S_{slow} , while S_{fast} contributes to the pure shear horizontal mode. We notice also that the polarization vector of S_{slow} lies in the x'_2 - x'_3 -plane in both cases. We showed in Sec. 2.2.1 that this is the case for any propagation direction, unlike the case for L and S_{fast} . In this section, we focus on the pure shear horizontal mode only. Pure Lamb modes are treated in Sec. 2.3.4. Therefore, the governing equation of motion, written in the global coordinate system x_i , is

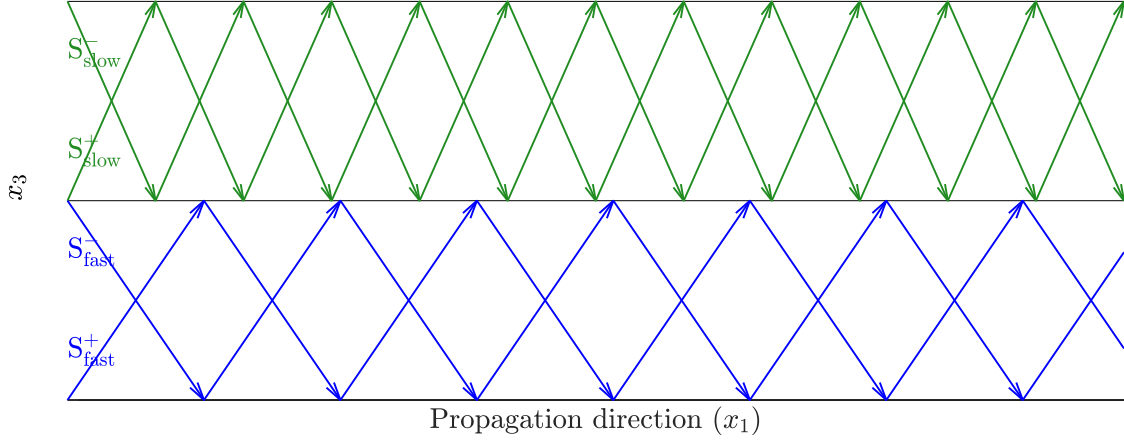


FIG. 2.20. Bulk wave pattern of the pure B'_2 shear horizontal wave at 2 MHz·mm for wave propagation along 0° in SAERTEX[®]7006919/RIMR135 [0/90].

$$C_{66} \frac{\partial^2 u_2}{\partial x_1^2} + C_{44} \frac{\partial^2 u_2}{\partial x_3^2} = \rho \frac{\partial^2 u_2}{\partial t^2}, \quad (2.110)$$

and the corresponding stress-strain relation

$$\sigma_{23} = C_{44} \frac{\partial u_2}{\partial x_3}, \quad (2.111)$$

with the formal solution

$$u_2 = U_2 e^{i\xi(x_1 + \alpha x_3 - c_p t)}, \quad (2.112)$$

yielding

$$\alpha_{1,2} = \pm \sqrt{\frac{\rho c_p^2 - C_{66}}{C_{44}}}, \quad (2.113)$$

so that the displacement and stress field components are given by

$$u_2 = \sum_{q=1}^2 U_{2q} e^{i\xi(x_1 + \alpha_q x_3 - c_p t)}, \quad (2.114)$$

$$\sigma_{23}^* = \sum_{q=1}^2 D_{3q} U_{2q} e^{i\xi(x_1 + \alpha_q x_3 - c_p t)},$$

respectively, where the stress amplitude is obtained from Eq. (2.111), namely

$$D_{3q} = C_{44} \alpha_q. \quad (2.115)$$

The two values for α correspond to the downward and upward propagating bulk waves S_{slow}^- and S_{slow}^+ in case of guided wave propagation along 0° (fiber direction), and S_{fast}^- and S_{fast}^+ for propagation along 90° , as shown in Fig. 2.20. In the following derivation of the transfer matrix, we adopt the formalism introduced by Nayfeh in Ref. [22]. Accordingly, by using superposition and suppressing the common factor $e^{i\xi(x_1 - c_p t)}$, the displacement and stress field components are given by

$$\begin{bmatrix} u_2 \\ \sigma_{23}^* \end{bmatrix}_m = \begin{bmatrix} 1 & 1 \\ C_{44}\alpha_1 & -C_{44}\alpha_1 \end{bmatrix}_m \begin{bmatrix} U_{21}e^{i\xi\alpha_1 x_3} \\ U_{22}e^{-i\xi\alpha_1 x_3} \end{bmatrix}_m. \quad (2.116)$$

Denoting the 2×2 matrix in Eq. (2.116) as \mathbf{X}_m , and defining

$$\mathbf{E}_m = \begin{bmatrix} e^{i\xi\alpha_1 x_3} & 0 \\ 0 & e^{-i\xi\alpha_1 x_3} \end{bmatrix}, \quad (2.117)$$

we use Nayfeh's formalism for the local transfer matrix of the m th layer \mathbf{A}_m

$$\mathbf{A}_m = \mathbf{X}_m \mathbf{E}_m \mathbf{X}_m^{-1}. \quad (2.118)$$

We can perform the inversion of \mathbf{X}_m analytically

$$\mathbf{X}_m^{-1} = \begin{bmatrix} 1/2 & 1/(2C_{44}\alpha_1) \\ 1/2 & -1/(2C_{44}\alpha_1) \end{bmatrix}, \quad (2.119)$$

and then carry out Eq. (2.118) to obtain

$$\begin{bmatrix} u_2 \\ \sigma_{23}^* \end{bmatrix}_{m+1} = \begin{bmatrix} \cos \eta_m & i/D_m \sin \eta_m \\ iD_m \sin \eta_m & \cos \eta_m \end{bmatrix} \begin{bmatrix} u_2 \\ \sigma_{23}^* \end{bmatrix}_m = \mathbf{A}_m \begin{bmatrix} u_2 \\ \sigma_{23}^* \end{bmatrix}_m, \quad (2.120)$$

where $\eta_m = \alpha_m \xi d_m$ and $D_m = \alpha_m C_{44}$. With the 2×2 matrix in Eq. (2.120), we have obtained an analytical expression for the individual local transfer matrix, which contains the matrix inversion a priori so that we do not have to perform it during the numerical computation procedure. Similarly to what we have shown for the general case, Eq. (2.120) relates the displacement and stress field components at the top of the m th layer ($x_{3(m)} = 0$) to those at its bottom ($x_{3(m)} = -d_m$). Finally, the global transfer matrix \mathbf{A} is again obtained by the multiplication of the individual local transfer matrices according to Eq. (2.106), leading us to

$$\begin{bmatrix} u_2 \\ \sigma_{23}^* \end{bmatrix}_{-d} = \begin{bmatrix} a_{11} & a_{12} \\ a_{21} & a_{22} \end{bmatrix} \begin{bmatrix} u_2 \\ \sigma_{23}^* \end{bmatrix}_0, \quad (2.121)$$

relating the displacement and stress at the bottom surface of the plate ($x_3 = -d$) to that at the top surface of the plate ($x_3 = 0$). Modal solutions are determined by

imposing stress free plate surfaces, which leads to the simple characteristic function

$$a_{21} = 0. \quad (2.122)$$

If the plate consists of an n -times repetition of a unit cell, the condition

$$\begin{bmatrix} u_2 \\ \sigma_{23}^* \end{bmatrix}_{-d} = \begin{bmatrix} u_2 \\ \sigma_{23}^* \end{bmatrix}_0 e^{i\xi d}, \quad (2.123)$$

must be satisfied. Then, the characteristic function for modal solutions is

$$\det \begin{bmatrix} a_{11} - 1 & a_{12} \\ a_{21} & a_{22} - 1 \end{bmatrix} = 0. \quad (2.124)$$

Notice that the fundamental shear horizontal mode is nondispersive in the decoupled case with $c_p = \sqrt{C_{66}/\rho}$.

Based on the above formalism for shear horizontal modes, we introduce adaptations on Eqs. (2.120), (2.122), and (2.124) since we could not obtain the modal solutions with them for every layup type and mode shape symmetry. Furthermore, we develop a calculation routine for the internal stress and displacement field components σ_{23}^* and u_2 in shear horizontal modes. The displacement field is required to identify, if it exists, the symmetric or antisymmetric character of the modes.

The following discussion is conducted for symmetric and nonsymmetric layups separately. The reason for this is that guided waves, be it Lamb or shear horizontal modes, have a definite symmetric or antisymmetric character in terms of the displacement field component u_1 for Lamb modes and u_2 for shear horizontal modes only in symmetric layups. This can be a single layer or a layup that is mirrored in terms of its fiber orientation as well as the layer thickness with respect to the middle plane of the laminate. Then, $u_{1,2}$ have the same absolute value and sign at the top and bottom surfaces of the plate in such cases of symmetric modes, and the same absolute value but opposite signs at the outer surfaces in cases of antisymmetric modes.

In the following, the local transfer matrix contained in Eq. (2.120) is denoted as \mathbf{A}_m^c , where the ‘‘c’’ indicates that the matrix contains complex values. A second matrix \mathbf{A}_m^r is introduced that is actually \mathbf{A}_m^c , but without the two imaginary numbers ‘‘i’’ in it. This matrix contains only real values

$$\mathbf{A}_m^r = \begin{bmatrix} \cos \eta_m & \sin \eta_m / D_m \\ D_m \sin \eta_m & \cos \eta_m \end{bmatrix}. \quad (2.125)$$

Symmetric Layups For a single layer, the characteristic function for symmetric and antisymmetric shear horizontal modes is

$$a_{21(m)}^r = 0, \quad m = 1. \quad (2.126)$$

For antisymmetric modes in layups containing more than one layer, a TMM style solution could not be found yet. The solution of these is presented in Sec. 2.3.4. Here, we present only the solutions for symmetric modes. A simple symmetric multilayered layup is $[0/90]_s$, having four layers. To obtain the global transfer matrix, we multiply the local transfer matrices

$$\mathbf{A}^r = \mathbf{A}_2^r \mathbf{A}_1^r, \quad (2.127)$$

and then solve the characteristic function

$$a_{21}^r = 0. \quad (2.128)$$

In fact, it is sufficient to multiply only the local transfer matrices of one half of the symmetric layup in Eqs. (2.127), (2.129), and (2.130). Multiplying all local transfer matrices yields the same dispersion curves.

In case of multiple repetitions, like $[0/90]_{ns}$, $n = 2, 3, \dots$, the solution depends on the order p of the respective mode. The fundamental shear horizontal mode (which is nondispersive) has the order $p = 0$. The higher order modes are counted in their sequence of increasing cut-off frequencies by $p = 1, 2, \dots$, *i.e.*, from left to right in the dispersion diagram. If the mode order is an integer multiple of the number of repetitions n , *i.e.*, $p = n, 2n, \dots$, we use

$$\mathbf{A}^r = \mathbf{A}_m^r \mathbf{A}_{m-1}^r \dots \mathbf{A}_1^r \quad (2.129)$$

and solve Eq. (2.128). Otherwise, we need

$$\mathbf{A}^c = \mathbf{A}_m^c \mathbf{A}_{m-1}^c \dots \mathbf{A}_1^c, \quad (2.130)$$

and then solve

$$\det \begin{bmatrix} a_{11}^c - 1 & a_{12}^c \\ a_{21}^c & a_{22}^c + 1 \end{bmatrix} = 0. \quad (2.131)$$

Notice the different sign in Eq. (2.131) as compared to Eq. (2.124).

Nonsymmetric Layups As stated above, no separation into symmetric and antisymmetric modes is possible in nonsymmetric layups. The simplest layup $[0/90]$ has to be processed by Eqs. (2.127) and (2.128), and multiple repetitions $[0/90]_n$, $n = 2, 3, \dots$, in the same way as shown for symmetric layups. All characteristic functions are summarized in Table 2.7.

Displacement and Stress Field Calculation In the following, we return the imaginary identity to the local transfer matrices \mathbf{A}_m^r with only real numbers in it. This is achieved by the elementwise multiplication

$$\mathbf{A}_m^c = \mathbf{A}_m^r \circ \begin{bmatrix} 1 & i \\ i & 1 \end{bmatrix}. \quad (2.132)$$

An m -layered plate has $m + 1$ interfaces, where $m = 1$ corresponds to the top surface and $m + 1$ corresponds to the bottom surface. First, we calculate the displacement and stress field components $u_{2(m)}$ and $\sigma_{23(m)}^*$ at all interfaces, assuming their continuity at the interfaces, as stated by Eq. (2.89). We start with the uppermost layer $m = 1$. At the top of this layer, we set the displacement to $u_{2(1)} = 1$ and the stress to $\sigma_{23(1)}^* = 0$. Then, we obtain $u_{2(2)}$ and $\sigma_{23(2)}^*$ at the bottom of this layer via its local transfer matrix

$$\begin{bmatrix} u_2 \\ \sigma_{23}^* \end{bmatrix}_2 = \begin{bmatrix} a_{11(1)}^c & a_{12(1)}^c \\ a_{21(1)}^c & a_{22(1)}^c \end{bmatrix} \begin{bmatrix} u_2 \\ \sigma_{23}^* \end{bmatrix}_1, \quad (2.133)$$

which results in

$$u_{2(2)} = a_{11(1)}^c, \quad \sigma_{23(2)}^* = a_{21(1)}^c. \quad (2.134)$$

To get $u_{2(3)}$ and $\sigma_{23(3)}^*$ at the bottom of the second layer ($m = 2$), we multiply the local transfer matrices of the first and second layers

$$\mathbf{A}^{*c} = \mathbf{A}_{(1)}^c \mathbf{A}_{(2)}^c. \quad (2.135)$$

Here, \mathbf{A}^{*c} is the transfer matrix relating the displacement and stress field components at the top of the uppermost layer (*i.e.*, at the top of the plate), to those at the bottom of the second layer. Substituting \mathbf{A}^{*c} into Eq. (2.133) and considering the stress free upper plate surface yields

$$u_{2(3)} = a_{11}^{*c}, \quad \sigma_{23(3)}^* = a_{21}^{*c}. \quad (2.136)$$

We repeat this procedure until we have obtained the displacement $u_{2(m+1)}$ and stress $\sigma_{23(m+1)}^*$ at the bottom of the plate. Once we have the displacements and stresses at all interfaces, we can calculate both components inside each layer. The now known displacements $u_{2(m)}^0$ and stresses $\sigma_{23(m)}^{*0}$ at the top ($x'_{3(m)} = 0$) and bottom $u_{2(m)}^{-d}$, $\sigma_{23(m)}^{*-d}$, ($x'_{3(m)} = -d_m$) interface of the m th layer can be written in terms of their respective local transfer matrix and amplitudes $U_{2q(m)}^u$, $U_{2q(m)}^\sigma$ ⁶

$$\begin{aligned} u_{2(m)}^0 &= a_{11(m)}^c U_{21(m)}^u + a_{12(m)}^c U_{22(m)}^u e^{i\xi\alpha_m d_m}, \\ u_{2(m)}^{-d} &= a_{11(m)}^c U_{21(m)}^u e^{i\xi\alpha_m d_m} + a_{12(m)}^c U_{22(m)}^u, \\ \sigma_{23(m)}^{*0} &= a_{21(m)}^c U_{21(m)}^\sigma + a_{22(m)}^c U_{22(m)}^\sigma e^{i\xi\alpha_m d_m}, \\ \sigma_{23(m)}^{*-d} &= a_{21(m)}^c U_{21(m)}^\sigma e^{i\xi\alpha_m d_m} + a_{22(m)}^c U_{22(m)}^\sigma. \end{aligned} \quad (2.137)$$

⁶These are not the physical bulk wave amplitudes given in Eq. (2.116).

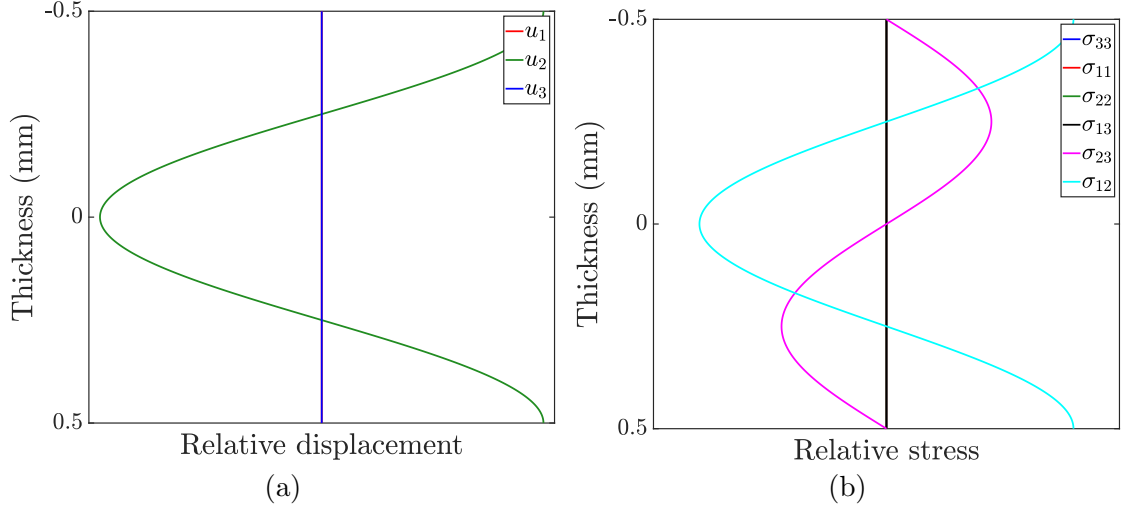


FIG. 2.21. (a) Through thickness displacement and (b) stress profiles of the S'_1 shear horizontal wave for propagation parallel and normal to the fibers in unidirectional SAERTEX[®]7006919/RIMR135. This mode is determined as symmetric since the displacement component u_2 has the same sign at the top and bottom of the plate. Unlike the stress component σ_{12} , σ_{23} is zero at the surfaces since we assume the plate to be surrounded by a vacuum. All other stress components vanish completely. Unlike what we observe in Lamb waves, the displacement profiles of pure shear horizontal waves are not frequency-dependent.

Here, we suppress the common factor $e^{i\xi(x_1 - c_p t)}$ since we are interested only in the x_3 -dependency of the displacement and stress. From Eqs. (2.137), we deduce the amplitudes as

$$\begin{aligned}
 U_{21(m)}^u &= \frac{u_{2(m)}^0 - \frac{u_{2(m)}^0 e^{i\xi\alpha_m d_m} - u_{2(m)}^{-d}}{e^{2i\xi\alpha_m d_m} - 1} e^{i\xi\alpha_m d_m}}{a_{11(m)}^c}, \\
 U_{22(m)}^u &= \frac{u_{2(m)}^0 e^{i\xi\alpha_m d_m} - u_{2(m)}^{-d}}{a_{12(m)}^c (e^{2i\xi\alpha_m d_m} - 1)}, \\
 U_{21(m)}^\sigma &= \frac{\sigma_{23(m)}^{*0} - \frac{\sigma_{23(m)}^{*0} e^{i\xi\alpha_m d_m} - \sigma_{23(m)}^{*-d}}{e^{2i\xi\alpha_m d_m} - 1} e^{i\xi\alpha_m d_m}}{a_{21(m)}^c}, \\
 U_{22(m)}^\sigma &= \frac{\sigma_{23(m)}^{*0} e^{i\xi\alpha_m d_m} - \sigma_{23(m)}^{*-d}}{a_{22(m)}^c (e^{2i\xi\alpha_m d_m} - 1)}.
 \end{aligned} \tag{2.138}$$

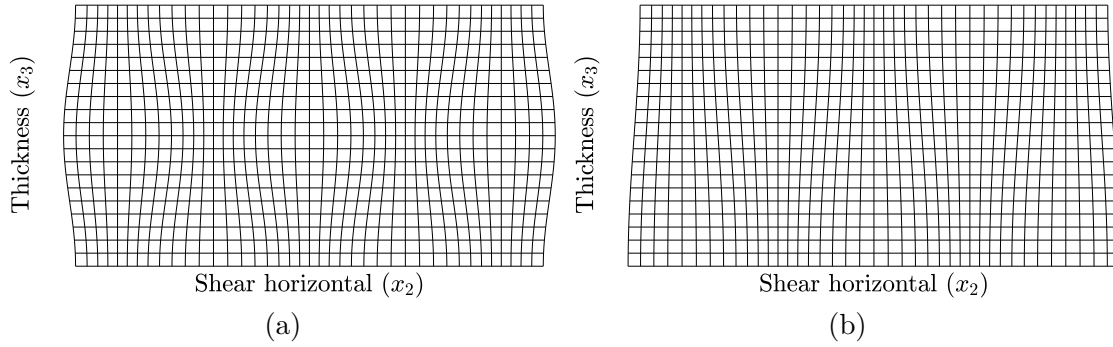


FIG. 2.22. Displacement patterns of (a) S'_1 and (b) A'_1 shear horizontal waves for propagation parallel or normal to the fibers in unidirectional SAERTEX[®]7006919/RIMR135. The propagation direction is normal to the image plane, and displacement takes place only in the x_2 -direction. The displacement is scaled up for clarity.

Now, we can calculate the displacement and stress at any point x_3 inside the m th layer by using

$$\begin{aligned} u_{2(m)} &= a_{11(m)}^c U_{21(m)}^u e^{i\xi\alpha_m x_{3(m)}} + a_{12(m)}^c U_{22(m)}^u e^{i\xi\alpha_m (d_m - x_{3(m)})}, \\ \sigma_{23(m)}^* &= a_{21(m)}^c U_{21(m)}^\sigma e^{i\xi\alpha_m x_{3(m)}} + a_{22(m)}^c U_{22(m)}^\sigma e^{i\xi\alpha_m (d_m - x_{3(m)})}. \end{aligned} \quad (2.139)$$

This procedure can be done for every layer in order to obtain the complete displacement and stress profiles of a layup, as shown in Fig. 2.21. For the calculation of the only other nonzero stress component σ_{12} , however, we must use a routine based on the stiffness matrix (2.166) and the backpropagation recursive algorithm discussed in Sec. 2.3.4. Through the reintroduction of the factor $e^{i\xi(x_1 - c_p t)}$, we can animate displacement patterns, giving us beautiful impressions of the mode shapes of guided waves. The reader is encouraged to download the DC [64] and try this out by himself. Figure 2.22 shows single frames from such animations.

If symmetric and antisymmetric shear horizontal modes exist, we can determine their character very fast. We just set the displacement at the top of the plate to $u_2^0 = 1$. Then, the displacement at the bottom of the plate is given by $u_2^{-d} = a_{11}^c$, where \mathbf{A}^c is the global transfer matrix. If $u_2^{-d} = 1$, the shear horizontal mode is symmetric, and if $u_2^{-d} = -1$, the shear horizontal mode is antisymmetric.

2.3.4 Stiffness Matrix Method

Similarly as in Sec. 2.3.3, the stiffness matrix is first introduced for the general case, and then it is specialized to the case when the decoupling of Lamb and shear horizontal modes occurs. The calculation of the displacement and stress field components is presented for both cases.

General Layered Composite

In Sec. 2.3.3, we have discussed that the numerical instability of the TMM results from the presence of singular matrices for which the inverse is undefined. The singular matrices in turn come from the exponential terms covering entire columns in those matrices. In case some bulk waves are evanescent, these columns will be filled by zeros. Rokhlin and Wang [57] have rearranged the transfer matrix formulation in such a way that the exponential terms are absent from the diagonal elements, thereby avoiding the singular matrices and the numerical instability altogether. Accordingly, we reorganize Eqs. (2.103) into

$$\begin{aligned} \begin{bmatrix} \mathbf{u}_m \\ \mathbf{u}_{m+1} \end{bmatrix} &= \begin{bmatrix} \mathbf{P}^- & \mathbf{P}^+ \mathbf{H} \\ \mathbf{P}^- \mathbf{H} & \mathbf{P}^+ \end{bmatrix}_m \begin{bmatrix} \mathbf{U}_m^- \\ \mathbf{U}_m^+ \end{bmatrix}, \\ \begin{bmatrix} \boldsymbol{\sigma}_m^* \\ \boldsymbol{\sigma}_{m+1}^* \end{bmatrix} &= \begin{bmatrix} \mathbf{D}^- & \mathbf{D}^+ \mathbf{H} \\ \mathbf{D}^- \mathbf{H} & \mathbf{D}^+ \end{bmatrix}_m \begin{bmatrix} \mathbf{U}_m^- \\ \mathbf{U}_m^+ \end{bmatrix}, \end{aligned} \quad (2.140)$$

relating the displacement and stress components at the top $\mathbf{u}_m, \boldsymbol{\sigma}_m^*$ ($x_{3(m)} = 0$) and bottom $\mathbf{u}_{m+1}, \boldsymbol{\sigma}_{m+1}^*$ ($x_{3(m)} = -d_m$) of the m th layer to the wave amplitude vectors \mathbf{U}_m^\pm . Similarly as performed to obtain the transfer matrix in Sec. 2.3.3, we eliminate the displacement amplitude vectors from Eqs. (2.140) to relate the stresses at the top $\boldsymbol{\sigma}_m^*$ and bottom $\boldsymbol{\sigma}_{m+1}^*$ of the m th layer to the displacements at the top \mathbf{u}_m and bottom \mathbf{u}_{m+1} via the stiffness matrix \mathbf{K}_m

$$\begin{bmatrix} \boldsymbol{\sigma}_m^* \\ \boldsymbol{\sigma}_{m+1}^* \end{bmatrix} = \begin{bmatrix} \mathbf{D}^- & \mathbf{D}^+ \mathbf{H} \\ \mathbf{D}^- \mathbf{H} & \mathbf{D}^+ \end{bmatrix}_m \begin{bmatrix} \mathbf{P}^- & \mathbf{P}^+ \mathbf{H} \\ \mathbf{P}^- \mathbf{H} & \mathbf{P}^+ \end{bmatrix}_m^{-1} \begin{bmatrix} \mathbf{u}_m \\ \mathbf{u}_{m+1} \end{bmatrix} = \mathbf{K}_m \begin{bmatrix} \mathbf{u}_m \\ \mathbf{u}_{m+1} \end{bmatrix}. \quad (2.141)$$

Kamal and Giurgiutiu [60] have written out Eq. (2.141) in a form that is well suited for its implementation into code, and which is reproduced in Appendix E. In order to obtain the global stiffness matrix of a multilayered plate, the local layer stiffness matrices \mathbf{K}_m must be calculated first. Consider the local stiffness matrices of two neighboring layers

$$\begin{bmatrix} \boldsymbol{\sigma}_1^* \\ \boldsymbol{\sigma}_2^* \end{bmatrix} = \begin{bmatrix} \mathbf{K}_{11}^A & \mathbf{K}_{12}^A \\ \mathbf{K}_{21}^A & \mathbf{K}_{22}^A \end{bmatrix} \begin{bmatrix} \mathbf{u}_1 \\ \mathbf{u}_2 \end{bmatrix}, \quad \begin{bmatrix} \boldsymbol{\sigma}_2^* \\ \boldsymbol{\sigma}_3^* \end{bmatrix} = \begin{bmatrix} \mathbf{K}_{11}^B & \mathbf{K}_{12}^B \\ \mathbf{K}_{21}^B & \mathbf{K}_{22}^B \end{bmatrix} \begin{bmatrix} \mathbf{u}_2 \\ \mathbf{u}_3 \end{bmatrix}. \quad (2.142)$$

Rokhlin and Wang's recursive algorithm is used to combine them

$$\begin{bmatrix} \boldsymbol{\sigma}_1^* \\ \boldsymbol{\sigma}_3^* \end{bmatrix} = \begin{bmatrix} \mathbf{K}_{11}^A + \mathbf{K}_{12}^A (\mathbf{K}_{11}^B - \mathbf{K}_{22}^A)^{-1} \mathbf{K}_{21}^A & -\mathbf{K}_{12}^A (\mathbf{K}_{11}^B - \mathbf{K}_{22}^A)^{-1} \mathbf{K}_{12}^B \\ \mathbf{K}_{21}^B (\mathbf{K}_{11}^B - \mathbf{K}_{22}^A)^{-1} \mathbf{K}_{21}^A & \mathbf{K}_{22}^B - \mathbf{K}_{21}^B (\mathbf{K}_{11}^B - \mathbf{K}_{22}^A)^{-1} \mathbf{K}_{12}^B \end{bmatrix} \begin{bmatrix} \mathbf{u}_1 \\ \mathbf{u}_3 \end{bmatrix}. \quad (2.143)$$

Calling the obtained matrix \mathbf{K}^A and the stiffness matrix of the third layer \mathbf{K}^B , we can recursively use Eq. (2.143) to obtain the global stiffness matrix, relating the

stresses and displacements at the top and bottom of the whole plate. If the plate consists of a periodic repetition of a unit cell, we denote the stiffness matrix of the unit cell \mathbf{K}^A , and use Eq. (2.143) with $\mathbf{K}^B = \mathbf{K}^A$ as many times as repetitions are contained in the plate. By that way, we obtain the global stiffness matrix very efficiently without recursively multiplying every single local stiffness matrix in every repetition. If the layout is symmetric, we have to calculate the stiffness matrix of one half of the layout \mathbf{K}^A . Our alternative formalism to the one presented by Rokhlin and Wang for the global stiffness matrix \mathbf{K} is given by

$$\begin{bmatrix} \sigma_1^* \\ \sigma_3^* \end{bmatrix} = \begin{bmatrix} \mathbf{K}_{11}^A + \mathbf{K}_{12}^A(\mathbf{K}_{22}^A \circ \mathbf{I} - \mathbf{K}_{22}^A)^{-1} \mathbf{K}_{21}^A & -\mathbf{K}_{12}^A(\mathbf{K}_{22}^A \circ \mathbf{I} - \mathbf{K}_{22}^A)^{-1}(\mathbf{K}_{21}^A \circ \mathbf{I}) \\ (\mathbf{K}_{12}^A \circ \mathbf{I})(\mathbf{K}_{22}^A \circ \mathbf{I} - \mathbf{K}_{22}^A)^{-1} \mathbf{K}_{21}^A & \mathbf{K}_{11}^A \circ \mathbf{I} - (\mathbf{K}_{12}^A \circ \mathbf{I})(\mathbf{K}_{22}^A \circ \mathbf{I} - \mathbf{K}_{22}^A)^{-1}(\mathbf{K}_{21}^A \circ \mathbf{I}) \end{bmatrix} \cdot \begin{bmatrix} \mathbf{u}_1 \\ \mathbf{u}_3 \end{bmatrix}, \quad (2.144)$$

with the symmetry identity matrix

$$\mathbf{I} = \begin{bmatrix} 1 & 1 & -1 \\ -1 & -1 & 1 \\ -1 & -1 & 1 \end{bmatrix}. \quad (2.145)$$

The characteristic function for modal solutions is

$$\det \mathbf{K} = 0. \quad (2.146)$$

For the calculation of the displacement and stress field components in a single layer, we abstain from using Rokhlin and Wang's backpropagation recursive algorithm, which is introduced below, but suggest to use Eq. (2.140) in the form

$$\begin{bmatrix} \sigma_0^* \\ \sigma_{-d}^* \end{bmatrix} = \begin{bmatrix} \mathbf{D}^- & \mathbf{D}^+ \mathbf{H} \\ \mathbf{D}^- \mathbf{H} & \mathbf{D}^+ \end{bmatrix} \begin{bmatrix} \mathbf{U}^- \\ \mathbf{U}^+ \end{bmatrix} = \mathbf{D} \begin{bmatrix} \mathbf{U}^- \\ \mathbf{U}^+ \end{bmatrix} = 0, \quad (2.147)$$

where \mathbf{U}^- comprises the displacement amplitudes of the three downward propagating bulk waves U_q , $q = 1, 3, 5$, and \mathbf{U}^+ contains the amplitudes of the three upward propagating ones U_q , $q = 2, 4, 6$. The usual procedure is to set one bulk wave amplitude to unity. Then, we can determine the amplitudes of the other bulk waves in terms of the first one. With setting $U_1 = 1$, our approach yields

$$\begin{bmatrix} U_2 \\ U_3 \\ U_4 \\ U_5 \\ U_6 \end{bmatrix} = - \begin{bmatrix} d_{22} & d_{23} & d_{24} & d_{25} & d_{26} \\ d_{32} & d_{33} & d_{34} & d_{35} & d_{36} \\ d_{42} & d_{43} & d_{44} & d_{45} & d_{46} \\ d_{52} & d_{53} & d_{54} & d_{55} & d_{56} \\ d_{62} & d_{63} & d_{64} & d_{65} & d_{66} \end{bmatrix}^{-1} \begin{bmatrix} d_{21} \\ d_{31} \\ d_{41} \\ d_{51} \\ d_{61} \end{bmatrix}. \quad (2.148)$$

Now, we can calculate the displacement and stress field components at any coordinate x_3 using

$$\begin{aligned}
u_1 &= U_1 e^{i\xi\alpha_1 x_3} + U_2 e^{i\xi\alpha_3 x_3} + U_3 e^{i\xi\alpha_5 x_3} \\
&\quad + U_4 e^{i\xi\alpha_1(d-x_3)} + U_5 e^{i\xi\alpha_3(d-x_3)} + U_6 e^{i\xi\alpha_5(d-x_3)}, \\
u_2 &= V_1 U_1 e^{i\xi\alpha_1 x_3} + V_3 U_2 e^{i\xi\alpha_3 x_3} + V_5 U_3 e^{i\xi\alpha_5 x_3} \\
&\quad + V_1 U_4 e^{i\xi\alpha_1(d-x_3)} + V_3 U_5 e^{i\xi\alpha_3(d-x_3)} + V_5 U_6 e^{i\xi\alpha_5(d-x_3)}, \\
u_3 &= W_1 U_1 e^{i\xi\alpha_1 x_3} + W_3 U_2 e^{i\xi\alpha_3 x_3} + W_5 U_3 e^{i\xi\alpha_5 x_3} \\
&\quad - W_1 U_4 e^{i\xi\alpha_1(d-x_3)} - W_3 U_5 e^{i\xi\alpha_3(d-x_3)} - W_5 U_6 e^{i\xi\alpha_5(d-x_3)}, \\
\sigma_{33}^* &= D_{11} U_1 e^{i\xi\alpha_1 x_3} + D_{13} U_2 e^{i\xi\alpha_3 x_3} + D_{15} U_3 e^{i\xi\alpha_5 x_3} \\
&\quad + D_{11} U_4 e^{i\xi\alpha_1(d-x_3)} + D_{13} U_5 e^{i\xi\alpha_3(d-x_3)} + D_{15} U_6 e^{i\xi\alpha_5(d-x_3)}, \\
\sigma_{13}^* &= D_{21} U_1 e^{i\xi\alpha_1 x_3} + D_{23} U_2 e^{i\xi\alpha_3 x_3} + D_{25} U_3 e^{i\xi\alpha_5 x_3} \\
&\quad - D_{21} U_4 e^{i\xi\alpha_1(d-x_3)} - D_{23} U_5 e^{i\xi\alpha_3(d-x_3)} - D_{25} U_6 e^{i\xi\alpha_5(d-x_3)}, \\
\sigma_{23}^* &= D_{31} U_1 e^{i\xi\alpha_1 x_3} + D_{33} U_2 e^{i\xi\alpha_3 x_3} + D_{35} U_3 e^{i\xi\alpha_5 x_3} \\
&\quad - D_{31} U_4 e^{i\xi\alpha_1(d-x_3)} - D_{33} U_5 e^{i\xi\alpha_3(d-x_3)} - D_{35} U_6 e^{i\xi\alpha_5(d-x_3)}.
\end{aligned} \tag{2.149}$$

For the remaining stress components σ_{11}^* , σ_{12}^* , and σ_{22}^* , we obtain the stress amplitudes from Eq. (2.8) and substitute them into the corresponding Eqs. 2.149. To distinguish symmetric from antisymmetric modes, we calculate u_1 for $x_3 = 0, d$. If both values have the same sign, the mode is symmetric, and if they have the opposite sign, the mode is antisymmetric.

The calculation of the displacements and stresses in a multilayered system is more sophisticated. According to Ref. [57], the displacement at the top and bottom of the system is given by

$$\mathbf{u}_0 = \mathbf{P}_0^- \mathbf{U}_{\text{in}} + \mathbf{P}_0^+ \mathbf{U}_{\text{r}}, \quad \mathbf{u}_{-d} = \mathbf{P}_{-d}^- \mathbf{U}_{\text{t}}, \tag{2.150}$$

where \mathbf{U}_{in} , \mathbf{U}_{r} , and \mathbf{U}_{t} are the incident, reflected, and transmitted three bulk wave amplitudes, respectively. However, instead of using the explicit relations for the stresses, as shown in Ref. [57], we suggest to use $\boldsymbol{\sigma}_0^*, \boldsymbol{\sigma}_{-d}^* = 0$. Therefore, by substituting Eq. (2.150) into

$$\begin{bmatrix} \boldsymbol{\sigma}_0^* \\ \boldsymbol{\sigma}_{-d}^* \end{bmatrix} = \begin{bmatrix} \mathbf{K}_{11} & \mathbf{K}_{12} \\ \mathbf{K}_{21} & \mathbf{K}_{22} \end{bmatrix} \begin{bmatrix} \mathbf{u}_0 \\ \mathbf{u}_{-d} \end{bmatrix} = 0, \tag{2.151}$$

we obtain the simpler relation for stress-free surfaces

$$\begin{bmatrix} \mathbf{U}_{\text{r}} \\ \mathbf{U}_{\text{t}} \end{bmatrix} = \begin{bmatrix} -\mathbf{K}_{11} \mathbf{P}_0^+ & -\mathbf{K}_{12} \mathbf{P}_{-d}^- \\ \mathbf{K}_{21} \mathbf{P}_0^+ & \mathbf{K}_{22} \mathbf{P}_{-d}^- \end{bmatrix}^{-1} \begin{bmatrix} \mathbf{K}_{11} \mathbf{P}_0^- \\ -\mathbf{K}_{21} \mathbf{P}_0^- \end{bmatrix} \mathbf{U}_{\text{in}}, \tag{2.152}$$

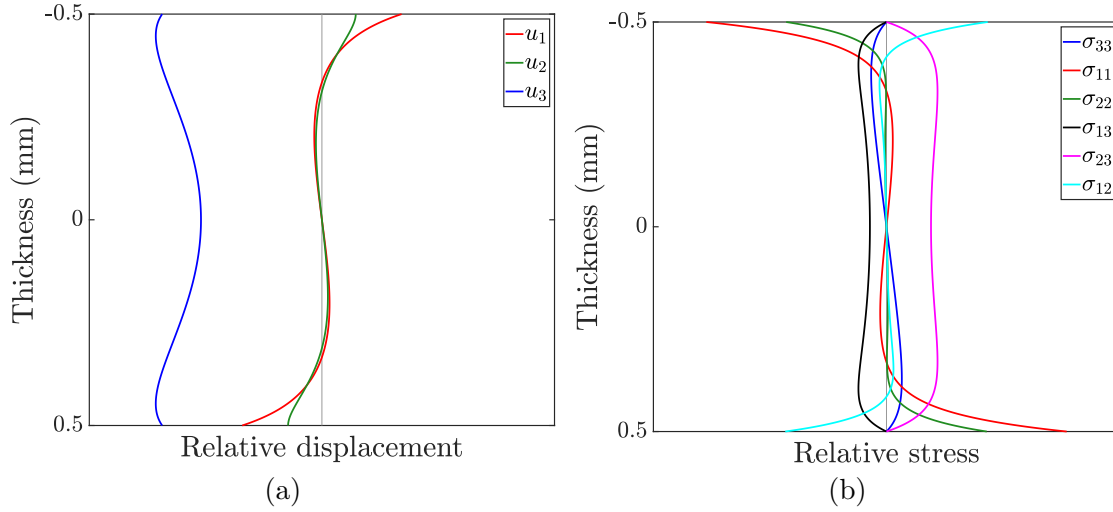


FIG. 2.23. Through thickness (a) displacement and (b) stress profiles of the A_0 Lamb wave at $2\text{ MHz}\cdot\text{mm}$ for propagation along 45° in unidirectional SAERTEX[®]7006919/RIMR135. The antisymmetric character of this mode is determined by the displacement component u_1 having opposite signs at the top and bottom of the plate.

with

$$\mathbf{U}_{\text{in}} = \begin{bmatrix} 1 \\ 0 \\ 0 \end{bmatrix}. \quad (2.153)$$

Notice that \mathbf{K}_{ij} are submatrices of the global stiffness matrix. With the now known reflection and transmission coefficients \mathbf{U}_r and \mathbf{U}_t , we can solve Eq. (2.150). In order to get the displacements and stresses at the inner interfaces, we use the backpropagation recursive algorithm proposed by Rokhlin and Wang. In contrast to our procedure presented in Sec. 2.3.3, now we have to start with the lowermost layer m . We have already obtained the displacements at the bottom of this layer \mathbf{u}_{-d} . Then, \mathbf{u}_m at the top of this layer is given by

$$\mathbf{u}_m = (\mathbf{K}_{11}^m - \mathbf{K}_{22}^*)^{-1} \mathbf{K}_{21}^* \mathbf{u}_0 - (\mathbf{K}_{11}^m - \mathbf{K}_{22}^*)^{-1} \mathbf{K}_{12}^m \mathbf{u}_{m+1}, \quad (2.154)$$

where \mathbf{K}^m is the local stiffness matrix of the m th layer and \mathbf{K}^* is the total stiffness matrix of the top $m - 1$ layers. We repeat this procedure until we have the displacements at the bottom of the top layer. Now, we calculate the six bulk wave amplitudes for each layer by

$$\begin{bmatrix} \mathbf{U}_m^- \\ \mathbf{U}_m^+ \end{bmatrix} = \begin{bmatrix} \mathbf{P}^- & \mathbf{P}^+ \mathbf{H} \\ \mathbf{P}^- \mathbf{H} & \mathbf{P}^+ \end{bmatrix}_m^{-1} \begin{bmatrix} \mathbf{u}_m \\ \mathbf{u}_{m+1} \end{bmatrix}. \quad (2.155)$$

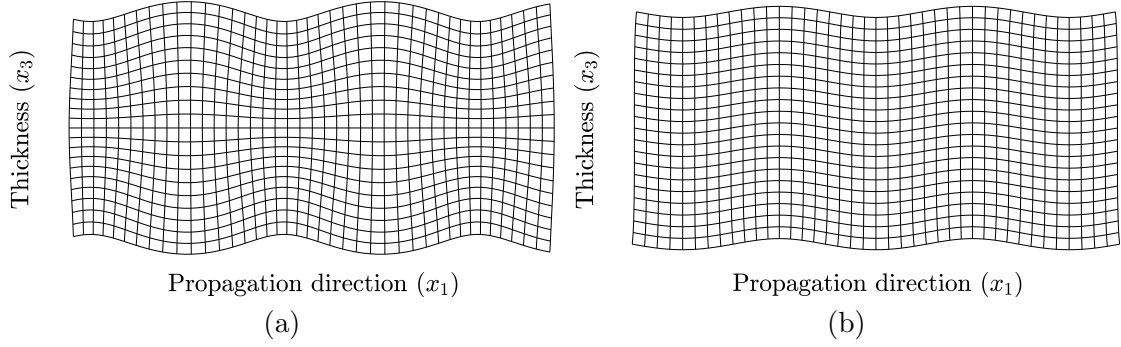


FIG. 2.24. Displacement patterns of (a) S_0 and (b) A_0 Lamb waves at 1.4 MHz·mm for propagation along 45° in unidirectional SAERTEX[®]7006919/RIMR135. The displacement is scaled up for clarity.

Finally, we use Eqs. (2.149) for each layer to get their respective displacement and stress field components inside the layers at the locations $x_{3(m)}$. To distinguish between symmetric and antisymmetric modes in multilayered systems, we reduce Eq. (2.150) to

$$u_1^0 = 1 + [1 \quad 1 \quad 1] \mathbf{U}_r, \quad u_1^{-d} = [1 \quad 1 \quad 1] \mathbf{U}_t. \quad (2.156)$$

Propagation Along Axes of Symmetry

Lamb Waves We have already discussed the decoupling into pure Lamb and shear horizontal waves in Sec. 2.3.3. Accordingly, pure Lamb waves are formed through the superposition of only four bulk waves per layer (two downward and two upward propagating ones), possessing displacement only in the x_1 - x_3 -plane (see exemplary bulk wave pattern in Fig. 2.25). Therefore, Eq. (2.91) reduces to

$$(u_1, u_3) = (U_1, U_3)e^{i\xi\alpha x_3}, \quad (2.157)$$

wherein the common factor $e^{i\xi(x_1 - c_p t)}$ is suppressed. Substituting Eq. (2.157) into the expanded displacement field equations (2.52) and (2.54) delivers

$$\begin{bmatrix} C_{11} - \rho c_p^2 + C_{55}\alpha^2 & (C_{13} + C_{55})\alpha \\ \text{sym} & C_{55} - \rho c_p^2 + C_{33}\alpha^2 \end{bmatrix} \begin{bmatrix} U_1 \\ U_3 \end{bmatrix} = 0. \quad (2.158)$$

Nontrivial solutions for U_1, U_3 require the vanishing of the Christoffel matrix determinant in Eq. (2.158), yielding the fourth-degree polynomial equation

$$A_1\alpha^4 + A_2\alpha^2 + A_3 = 0, \quad (2.159)$$

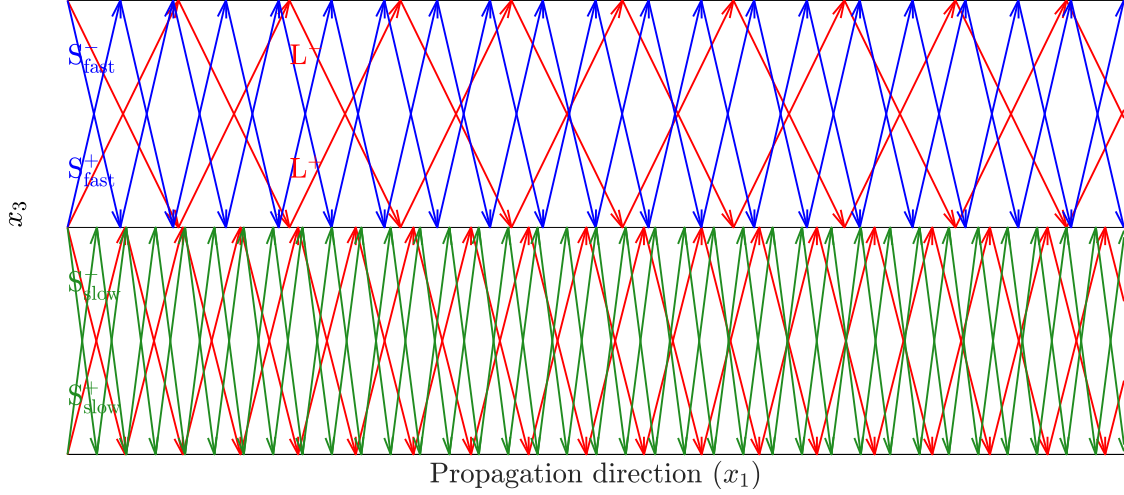


FIG. 2.25. Bulk wave pattern of the pure B_4 Lamb wave at 2 MHz·mm for wave propagation along 0° in SAERTEX[®]7006919/RIMR135 [0/90].

with the coefficients

$$\begin{aligned} A_1 &= C_{33}C_{55}, \\ A_2 &= C_{55}(C_{55} - \rho c_p^2) + C_{33}(C_{11} - \rho c_p^2) - (C_{13} + C_{55})^2, \\ A_3 &= (C_{55} - \rho c_p^2)(C_{11} - \rho c_p^2). \end{aligned} \quad (2.160)$$

Equation (2.159) admits four solutions α_q , $q = 1, 2, 3, 4$, given by

$$\alpha_q = \pm \sqrt{\frac{-A_2 \pm \sqrt{A_2^2 - 4A_1A_3}}{2A_1}}. \quad (2.161)$$

The four values for α correspond to the upward and downward propagation bulk waves L^+ and L^- and either S_{fast}^- and S_{fast}^+ in case of guided wave propagation along 0° (fiber direction), or S_{slow}^- and S_{slow}^+ for propagation along 90° , as shown in Fig. 2.25. Substituting α_q into Christoffel's equation (2.158) delivers the bulk wave amplitude ratio $W_q = U_{3q}/U_{1q}$, namely

$$W_q = \frac{-m_{11}(\alpha_q)}{m_{12}(\alpha_q)} = \frac{\rho c_p^2 - C_{11} - C_{55}\alpha_q^2}{(C_{13} + C_{55})\alpha_q}. \quad (2.162)$$

Now, the displacement and stress field components are represented as

$$\begin{aligned} (u_1, u_3) &= \sum_{q=1}^4 (1, W_q) U_{1q} e^{i\xi\alpha_q x_3}, \\ (\sigma_{33}^*, \sigma_{13}^*) &= \sum_{q=1}^4 (D_{1q}, D_{2q}) U_{1q} e^{i\xi\alpha_q x_3}, \end{aligned} \quad (2.163)$$

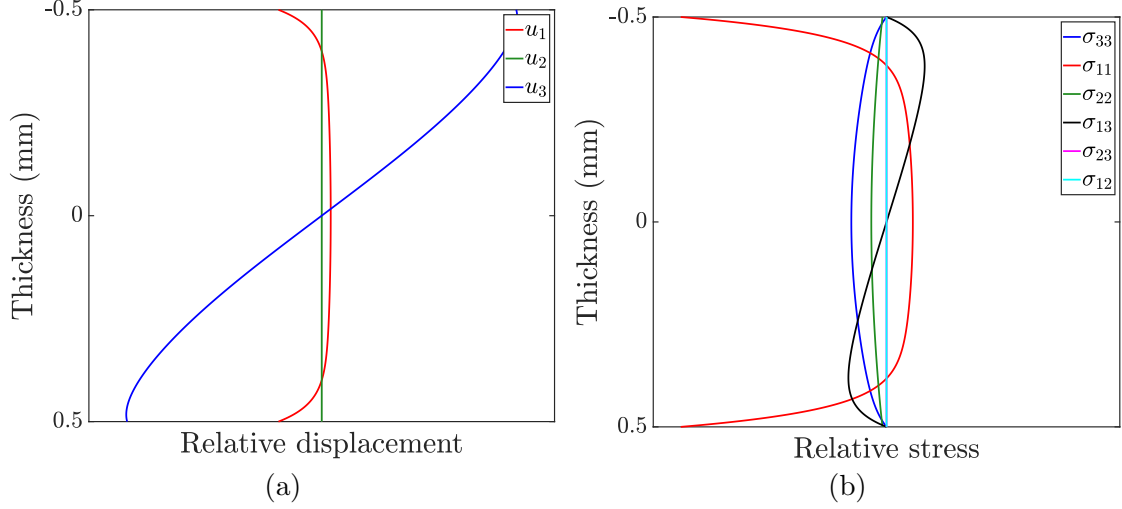


FIG. 2.26. Through thickness (a) displacement and (b) stress profiles of the pure S_0 Lamb wave at 2 MHz-mm for propagation along 0° in unidirectional SAERTEX[®]7006919/RIMR135. The symmetric character of this mode is determined by the displacement component u_1 having equal signs at the top and bottom of the plate.

with the stress amplitudes obtained from Eq. (2.8)

$$\begin{aligned} D_{1q} &= C_{13} + C_{33}\alpha_q W_q, \\ D_{2q} &= C_{55}(\alpha_q + W_q). \end{aligned} \quad (2.164)$$

Finally, the stiffness matrix in Eq. (E.1) turns into Eq. (E.2). All further operations, which have been explained for the general layered case, can be conducted also in their reduced form in the decoupled case, and do not need to be repeated here. We note only that the symmetry identity matrix is now given as

$$\mathbf{I} = \begin{bmatrix} 1 & -1 \\ -1 & 1 \end{bmatrix}. \quad (2.165)$$

Shear Horizontal Waves As stated in Sec. 2.3.3, we have no TMM style solution for antisymmetric shear horizontal modes in symmetric multilayered systems. Instead, we use a relation offered by Wang and Rokhlin [58], where the local stiffness matrix of the m th layer is given as

$$\mathbf{K}_m = \frac{iC_{44}\alpha\xi}{e^2 - 1} \begin{bmatrix} -1 - e^2 & 2e \\ -2e & 1 + e^2 \end{bmatrix}, \quad (2.166)$$

where $e = e^{i\xi\alpha d_m}$ and $\alpha = \sqrt{(\rho c_p^2 - C_{66})/C_{44}}$. Now, we can apply Eqs. (2.142)-(2.144) to obtain the global stiffness matrix (with the symmetry identity $\mathbf{I} =$

TABLE 2.6. Possible configurations in transversely isotropic specimens.

symmetric	decoupled	modes
✓	✓	S, A, S', A'
✓	×	S, A ^a
×	✓	B, B'
×	×	B

^aS and A exist also in nonsymmetric layups in certain cases, see below.

–1). However, in order to get the displacement and stress, we have to compute the individual local transfer matrices \mathbf{A}_m^c according to Eq. (2.120). This can be done by entering the corresponding phase velocities, which we obtained during the dispersion curve tracing procedure with the use of Eq. (2.166). Then, we can apply Eqs. (2.133)-(2.139).

2.3.5 Special Boundary Conditions

So far, we have obtained the characteristic equations for guided waves in multilayered transversely isotropic waveguides, and we have seen that different mode families can occur depending on the symmetry and coupling properties of the layup. In principle, we could solve for the modal solutions in both the coupled and decoupled cases with one and the same characteristic function (2.146). However, it is not only faster to use special characteristic functions and boundary conditions for the various mode families. Besides obtaining the additional information of what families the traced modes belong to, the main benefit is a reduction or even complete avoidance of the well-known jumping mode problem occurring during the dispersion curve tracing. Here, the tracing algorithm jumps to a crossing mode such that the wrong mode is traced from the crossing point onward. Therefore, we invoke the individual characteristic functions and boundary conditions for each mode family, summarized in Table 2.7. To enable this, we must first determine which kind of mode families we have to expect in a given layup. Basically, there exist the following six different mode families:

1. Symmetric Lamb waves (S)
2. Symmetric shear horizontal waves (S')
3. Antisymmetric Lamb waves (A)

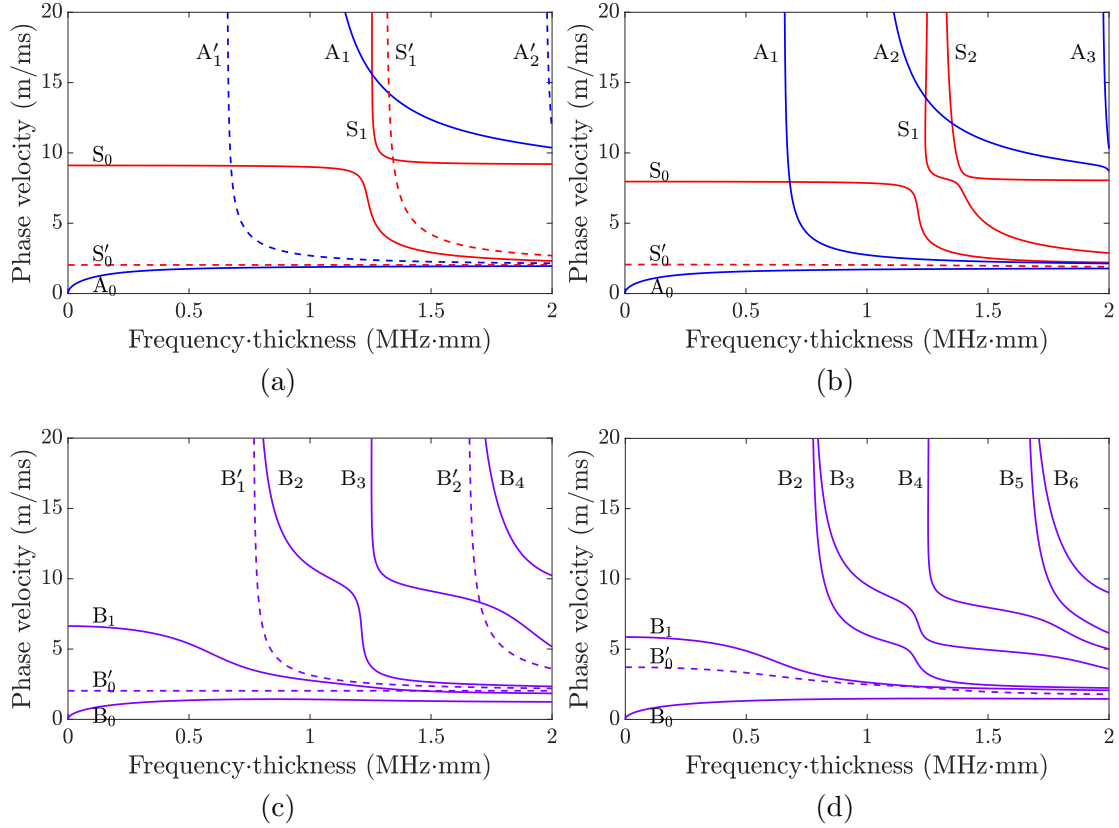


FIG. 2.27. Dispersion diagrams for wave propagation along (a) 0° in unidirectional, (b) 30° in unidirectional, (c) 0° in $[0/90]$, and (d) 30° in $[0/90]$ SAERTEX[®]7006919/RIMR135.

4. Antisymmetric shear horizontal waves (A')
5. Nonsymmetric Lamb waves (B)
6. Nonsymmetric shear horizontal waves (B')

Guided waves in the coupled case are called Lamb waves anyway in reminiscence to Sir Horace Lamb who described Lamb waves mathematically for the first time in 1917 [3]⁷. Lamb dealt only with isotropic media wherein the coupling does not occur. In this work, we denote guided waves in nonsymmetric layups unconventionally with the letter “B”. The decoupling into Lamb and shear horizontal waves

⁷Some researchers use the terms “Lamb-like” or “shear horizontal-like” for coupled modes with predominantly sagittal or shear horizontal displacement, respectively, but we avoid them since “predominant” is a rather loose definition.

TABLE 2.7. Special characteristic functions and boundary conditions for the tracing of the six mode families.

Family	Situation	Characteristic functions & boundary conditions
S		$\det \mathbf{K} = 0, \det \mathbf{K} = \min, u_1^{++a}$
A		$\det \mathbf{K} = 0, \det \mathbf{K} = \min, u_1^{+-b}$
B		$\det \mathbf{K} = 0, \det \mathbf{K} = \min$
S', B'	Single layer/Single unit cell	$a_{21(1)}^r = 0 / a_{21}^r = 0$
	Periodic, $p = n, 2n, \dots$	$a_{21}^r = 0$
	Periodic, $p \neq n, 2n, \dots$	$\det \begin{bmatrix} a_{11}^c - 1 & a_{12}^c \\ a_{21}^c & a_{22}^c + 1 \end{bmatrix} = 0$
A'	Single layer	$a_{21(m)}^r = 0$
	Else	$\det \mathbf{K} = 0$
S'_0, B'_0	Decoupled case	Nondispersive, $c_p = \sqrt{C_{66}/\rho}$

^a u_1 at the plate's top and bottom have the same sign.

^b u_1 at the plate's top and bottom have the opposite sign.

and the separation into symmetric and antisymmetric modes obeys the following rules:

1. Lamb and shear horizontal waves decouple if the laminate consists solely of 0° and 90° layers, and the wave propagation is along either direction.
2. Symmetric and antisymmetric modes can be distinguished if the laminate is symmetric (including a single layer), or if the laminate is nonsymmetric and the propagation direction is centered, like 40° in $[0/80]$ or 45° in $[0/45/90]$.

Of the six mode families named above, a maximum of four different ones can occur in symmetric layups and a maximum of two can appear in nonsymmetric layups. By contrast, in isotropic materials, we can always distinguish S, A, S', and A'. The four possible configurations in transversely isotropic materials are listed in Table 2.6. Accordingly, in the decoupled case in symmetric layups, we have symmetric and antisymmetric Lamb and shear horizontal waves. For each of those families, the dispersion curves do not cross. Therefore, by using the special characteristic functions and boundary conditions corresponding to those four families, the jumping mode problem cannot occur at all. This situation is illustrated in Fig. 2.27(a). There are four crossing points between modes belonging to different mode families. Without the mode family-specific characteristic functions and boundary conditions, there would be a high risk of mode jumping at those points. If we consider a symmetric layup with arbitrary fiber orientations and

wave propagation directions (coupled case), we can only distinguish between symmetric and antisymmetric modes. Now, the crossing of Lamb waves belonging to the same family can occur (although it does not in Fig. 2.27(b)), and appropriate algorithms are required to control the jumping mode behavior in this case. As can be seen in Fig. 2.27(c), in the decoupled case in nonsymmetric layups, we can only separate Lamb and shear horizontal waves, whereas in the coupled case shown in Fig. 2.27(d), there is no separation into different mode families possible at all. In summary, the crossing of Lamb wave dispersion curves can occur in the cases treated in Figs. 2.27(b), 2.27(c), and 2.27(d). Pure shear horizontal modes are special in that they never cross each other even if they belong to different families, as the case in Fig. 2.27(a). Because of that, we don't need to check the signs of the displacement u_2 at the plate's top and bottom during the tracing. This is done only to classify the modes in the course of the initial *frequency sweep*, as explained in Sec. 2.5. Moreover, the curve tracings of both families are already distinguished through the use of different characteristic functions, except if the plate is single-layered (see Table 2.7). The fundamental pure shear horizontal waves S'_0 and B'_0 don't need to be traced since they are nondispersive.

2.3.6 Group Velocity, Propagation Time, and Excitation Angle

Once we have obtained a phase velocity dispersion curve, we can calculate the group velocity c_g using the relation

$$c_g = \frac{d\omega}{d\xi}. \quad (2.167)$$

By substituting $\xi = \omega/c_p$, we have

$$\begin{aligned} c_g &= d\omega \left(d \left(\frac{\omega}{c_p} \right) \right)^{-1} \\ &= d\omega \left(\frac{d\omega}{c_p} - \omega \frac{dc_p}{c_p^2} \right)^{-1} \\ &= c_p^2 \left(c_p - \omega \frac{dc_p}{d\omega} \right)^{-1}, \end{aligned} \quad (2.168)$$

or with $\omega = 2\pi f$

$$c_g = c_p^2 \left(c_p - fd \frac{dc_p}{d(fd)} \right)^{-1}, \quad (2.169)$$

where fd specifies the frequency-thickness product. We should be aware though that Eq. (2.169) is actually valid only for isotropic media, but in the DC and in

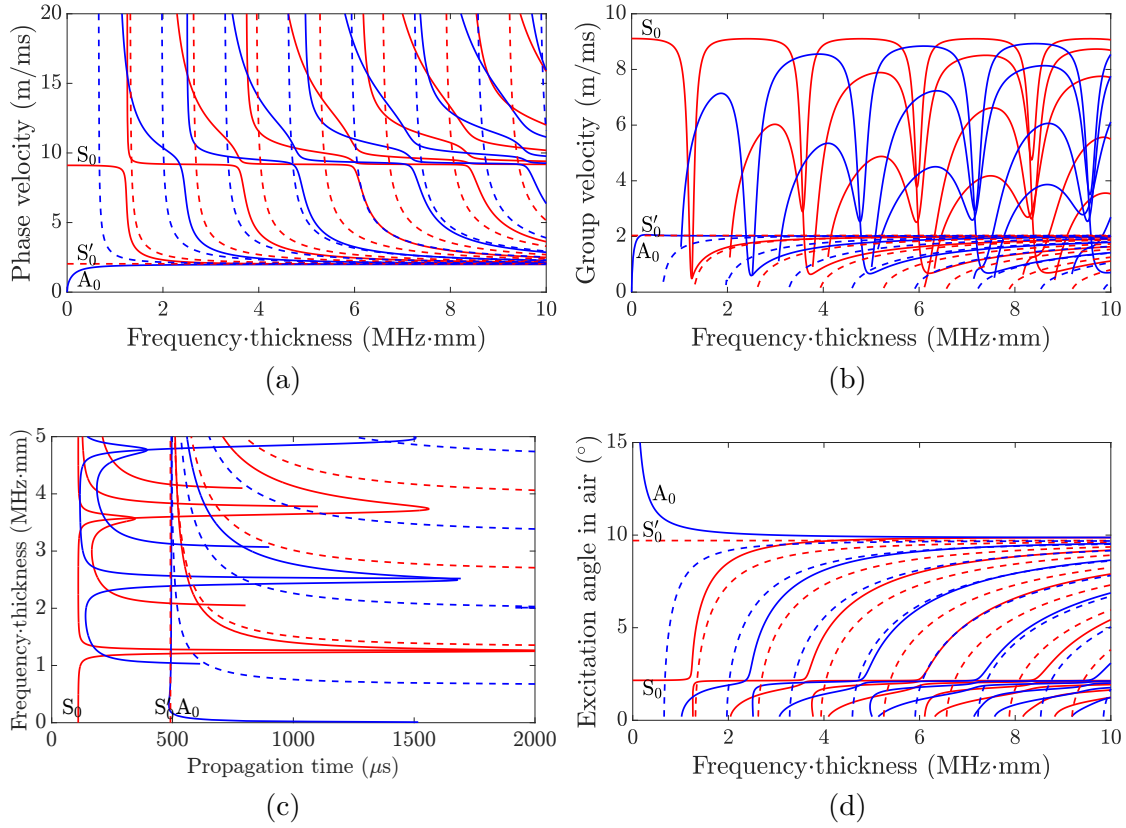


FIG. 2.28. Dispersion diagrams for wave propagation along 0° in unidirectional SAERTEX[®]7006919/RIMR135. (a) Phase velocity, (b) group velocity, (c) propagation time at 1 m distance, and (d) excitation angle in air.

this thesis it is used as an approximative solution also for anisotropic media. This issue will be reworked in a future release of the DC. To carry out Eq. (2.169) programmatically, the phase velocity dispersion curve is fitted so that its derivative can be taken from the fitted function. Figures 2.28(a) and 2.28(b) show the phase velocity and group velocity dispersion, respectively, of Lamb and shear horizontal waves in unidirectional SAERTEX[®]7006919/RIMR13 for wave propagation along the fiber direction. By comparing both diagrams, we notice that wherever the derivative of c_p with respect to fd becomes zero, we have $c_g = c_p$. On the other hand, if the derivative of c_p with respect to fd becomes infinity, *i.e.*, at the cut-off frequency, c_g approaches zero. For a more detailed discussion on the group velocity in anisotropic composites, the reader is referred to Refs. [143–145].

A special dispersion diagram representation used for the interpretation of acoustical emission signals is the frequency versus propagation time at a certain propagation

distance, shown in Fig. 2.28(c). By choosing a propagation distance, the frequency-propagation time diagram can be calculated directly from the group velocity. In acoustical emission experiments, the inspector receives the signal of voltage as a function of propagation time. Sause [146] and Sause and Hamstad [147] use this kind of diagram to ascribe guided wave modes to the received signals. The diagram displayed in Fig. 2.28(c) is calculated for a propagation distance of 1 m.

The excitation angle Θ_{in} can be calculated easily by applying Snell's law. Therefore, writing Eq. (2.86) as

$$\zeta_{\text{in}} \sin \Theta_{\text{in}} = \xi, \quad (2.170)$$

we find

$$\Theta_{\text{in}} = \sin^{-1} \frac{c_{\text{in}}}{c_{\text{p}}}, \quad (2.171)$$

where c_{in} is the phase velocity in the fluid surrounding the plate and ξ is the wavenumber of the excited guided wave. The excitation angle dispersion with air as a surrounding medium is shown in Fig. 2.28(d). Since in this work, we want to calculate the ultrasonic transducer orientation with respect to a composite laminate such that we can excite the desired Lamb wave mode for the purpose of nondestructive inspection, this is ultimately the dispersion diagram we are looking for. In this diagram, of course, we can ignore the shear horizontal modes since they cannot be excited in the plate via air as a coupling medium.

2.4 Isotropic Waveguides

Although the main focus in this work is on composites, we also discuss the numerical modeling of guided waves in isotropic single layers since they are still important and widely spread in aerospace and automotive industries. In this discussion, we benefit from the great simplification in the analysis thanks to the reduction to only two direction-independent material parameters, namely Poisson's ratio ν and Young's modulus E . In Sec. 2.4.1, we derive the bulk waves' phase velocities for isotropic media from Christoffel's equation, relying on the book of Nayfeh [22]. Then, in Sec. 2.4.2, we first set up the numerical model for Lamb waves as usual, namely based on the superposition of the contributing bulk waves. Then, we put a different approach aside, namely the Rayleigh-Lamb equations, which allow a faster calculation, and which provide distinct solutions for symmetric and antisymmetric Lamb waves inherently. While the Rayleigh-Lamb equations still need to be solved numerically, we will derive analytic equations for symmetric and antisymmetric shear horizontal waves in Sec. 2.4.3. In the derivation of the Rayleigh-Lamb equations and partially also for the analytic equations for the shear horizontal modes, we

follow the book of Rose [148]. An excellent discussion of guided waves in isotropic layers is also provided in the book of Auld [149]. Dispersion diagrams are presented at the very end of this section.

2.4.1 Christoffel's Equation for Isotropic Media

As a starting point, we rewrite Eq. (2.64) as

$$v_p^2 U_i = \lambda_{ijkl} n_j n_k U_l, \quad (2.172)$$

with

$$\lambda_{ijkl} = c_{ijkl}/\rho, \quad i, j, k, l = 1, 2, 3. \quad (2.173)$$

Again, $v_p (= \omega/\zeta)$ is the phase velocity of the three bulk waves L, SV, and SH, U_i are their displacement amplitudes, n_j are the propagation direction unit vector components, ω is the angular frequency, ζ is the bulk wavenumber, and ρ is the material's density. By imposing isotropic symmetry conditions, we can write the stiffness tensor as

$$c_{ijkl} = \lambda \delta_{ij} \delta_{kl} + \mu (\delta_{ik} \delta_{jl} + \delta_{il} \delta_{jk}), \quad (2.174)$$

using Lamé's parameters λ and μ , in accordance with Eq. (2.28). Now, we normalize the polarization vector to unity so that $U_i U_i = 1$, and by multiplying Eq. (2.172) with U_i , we obtain

$$v_p^2 = \lambda_{ijkl} n_j n_k U_l U_i. \quad (2.175)$$

Then, using Eq. (2.174), we arrive at

$$\rho v_p^2 = (\lambda + \mu) n_j n_k U_k U_j + \mu. \quad (2.176)$$

We already pointed out that there exist only pure modes in isotropic media. For a pure longitudinal mode where \mathbf{U} is directed along \mathbf{n} , we have $n_j U_j = 1$ so that Eq. (2.176) reduces to

$$v_L = \sqrt{\frac{\lambda + 2\mu}{\rho}}. \quad (2.177)$$

In case of a pure shear wave where \mathbf{U} is directed normal to \mathbf{n} , we have $n_j U_j = 0$ resulting in

$$v_T = \sqrt{\frac{\mu}{\rho}}. \quad (2.178)$$

2.4.2 Lamb Waves

Since Lamb waves in isotropic media consist of two downward (L^- , SV^-) and two upward propagating bulk waves (L^+ , SV^+) (see Fig. 2.29), similarly like in anisotropic media in the decoupled case and wave propagation along the fibers, we follow the same procedure as presented in Sec. 2.3.4, with specializing to isotropic material parameters. Hence, by substituting the formal solution

$$(u_1, u_3) = (U_1, U_3)e^{i\xi\alpha x_3}, \quad (2.179)$$

where we suppress the common factor $e^{i\xi(x_1 - c_p t)}$, into the field equations (2.58) and (2.60), we get

$$\begin{bmatrix} \lambda + 2\mu - \rho c_p^2 + \mu\alpha^2 & (\lambda + \mu)\alpha \\ \text{sym} & \mu - \rho c_p^2 + (\lambda + 2\mu)\alpha^2 \end{bmatrix} \begin{bmatrix} U_1 \\ U_3 \end{bmatrix} = 0, \quad (2.180)$$

or equivalently

$$\rho \begin{bmatrix} v_L^2 - c_p^2 + v_T^2\alpha^2 & (v_L^2 - v_T^2)\alpha \\ \text{sym} & v_T^2 - c_p^2 + v_L^2\alpha^2 \end{bmatrix} \begin{bmatrix} U_1 \\ U_3 \end{bmatrix} = 0. \quad (2.181)$$

Nontrivial solutions for U_1, U_3 require the vanishing of the determinant of the Christoffel matrix in Eq. (2.181), yielding the fourth-degree polynomial equation

$$A_1\alpha^4 + A_2\alpha^2 + A_3 = 0, \quad (2.182)$$

with the coefficients

$$\begin{aligned} A_1 &= v_L^2 v_T^2, \\ A_2 &= -c_p^2 v_L^2 - c_p^2 v_T^2 + 2v_L^2 v_T^2, \\ A_3 &= c_p^4 - c_p^2 v_L^2 - c_p^2 v_T^2 + v_L^2 v_T^2. \end{aligned} \quad (2.183)$$

Equation (2.182) admits four solutions α_q , $q = 1, 2, 3, 4$, according to

$$\alpha_q = \pm \sqrt{\frac{-A_2 \pm \sqrt{A_2^2 - 4A_1A_3}}{2A_1}}, \quad (2.184)$$

namely

$$\alpha_{1,2} = \pm \sqrt{\frac{c_p^2}{v_L^2} - 1}, \quad \alpha_{3,4} = \pm \sqrt{\frac{c_p^2}{v_T^2} - 1}. \quad (2.185)$$

These geometric relations are illustrated in Fig. 2.30. As compared with Eqs. (2.93) and (2.113), we now have very direct expressions for α , since the slownesses s_L

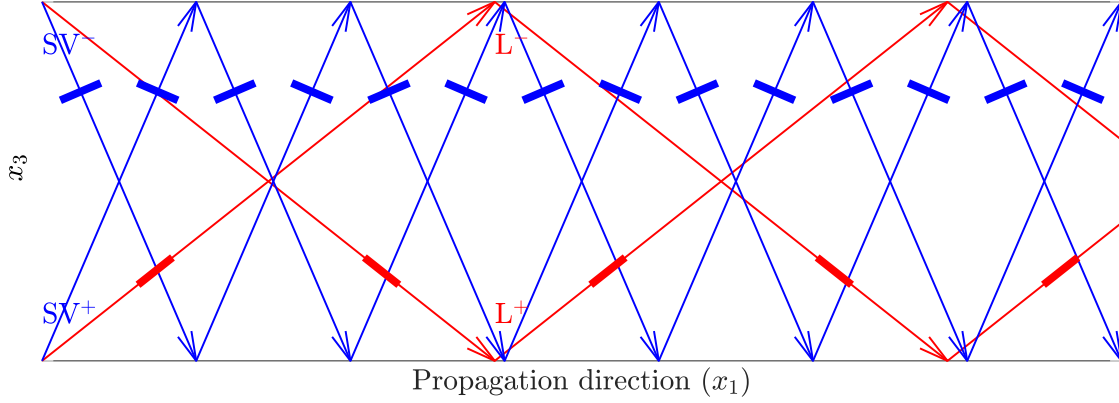


FIG. 2.29. Bulk wave pattern of the A_4 Lamb wave at 10 MHz·mm in aluminum alloy 1100. The bold lines indicate the polarization directions.

and s_{SV} are unambiguously given by the inverse longitudinal and transverse phase velocities v_L^{-1} and v_T^{-1} , respectively. The four values for α correspond to the upward and downward propagation bulk waves L^+ , L^- , SV^+ , and SV^- . Substituting α_q into Eq. (2.181) delivers the bulk wave amplitude ratio $W_q = U_{3q}/U_{1q}$, namely

$$W_q = \frac{-m_{11}(\alpha_q)}{m_{12}(\alpha_q)} = \frac{c_p^2 - v_L^2 - v_T^2 \alpha_q^2}{(v_L^2 - v_T^2) \alpha_q}. \quad (2.186)$$

By using superposition, we obtain for the displacement and stress field components

$$\begin{aligned} (u_1, u_3) &= \sum_{q=1}^4 (1, W_q) U_{1q} e^{i\xi \alpha_q x_3}, \\ (\sigma_{33}^*, \sigma_{13}^*) &= \sum_{q=1}^4 (D_{1q}, D_{2q}) U_{1q} e^{i\xi \alpha_q x_3}, \end{aligned} \quad (2.187)$$

with the stress amplitudes obtained from Eq. (2.8) as

$$\begin{aligned} D_{1q} &= \lambda + (\lambda + 2\mu) \alpha_q W_q, \\ D_{2q} &= \mu(\alpha_q + W_q). \end{aligned} \quad (2.188)$$

Then, again, we arrive at the stiffness matrix given in Appendix E, and since we have only one layer, the next and final step would be to apply the stress free upper and lower plate surface boundary condition and solve

$$\det \mathbf{K} = 0, \quad (2.189)$$

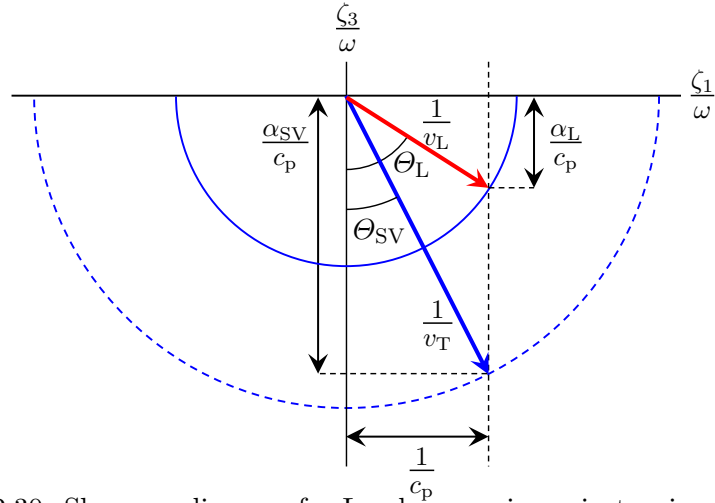


FIG. 2.30. Slowness diagram for Lamb waves in an isotropic plate.

for modal solutions. However, we will use the stiffness matrix later only for the calculation of the through thickness displacement and stress components. To obtain modal solutions, we use the Rayleigh-Lamb equations, named after their investigators [1, 3]. These equations work more efficiently in the case of isotropic materials than the application of the SMM. The method of *displacement potentials*, originally used by Lamb and adopted by other authors like Viktorov [87], Achenbach [150], and Rose [148], is used to derive the Rayleigh-Lamb equations. Basically, this method can be applied only to isotropic materials in a convenient way because in this case the equations of motion are sufficiently simple. In anisotropic materials, however, we have to use the method of the superposition of bulk waves, as we did so far. The latter approach has the advantage of providing more insight into the bulk waves' propagation, which the guided wave modes result from.

By applying *Helmholtz decomposition* to the displacement field components, and substituting the result into the equations of motion (2.58) and (2.60), we obtain two uncoupled equations namely

$$\frac{\partial^2 \mathcal{Y}}{\partial x_1^2} + \frac{\partial^2 \mathcal{Y}}{\partial x_3^2} = \frac{1}{v_L^2} \frac{\partial^2 \mathcal{Y}}{\partial t^2}, \quad (2.190)$$

governing longitudinal waves and

$$\frac{\partial^2 \Psi}{\partial x_1^2} + \frac{\partial^2 \Psi}{\partial x_3^2} = \frac{1}{v_T^2} \frac{\partial^2 \Psi}{\partial t^2}, \quad (2.191)$$

governing shear waves. Assuming plane strain, the displacements and stresses can

be given as

$$\begin{aligned}
u_1 &= \frac{\partial \Upsilon}{\partial x_1} + \frac{\partial \Psi}{\partial x_3}, \\
u_3 &= \frac{\partial \Upsilon}{\partial x_3} - \frac{\partial \Psi}{\partial x_1}, \\
\sigma_{33} &= \lambda \left(\frac{\partial u_1}{\partial x_1} + \frac{\partial u_3}{\partial x_3} \right) + 2\mu \frac{\partial u_3}{\partial x_3}, \\
&= \lambda \left(\frac{\partial^2 \Upsilon}{\partial x_1^2} + \frac{\partial^2 \Upsilon}{\partial x_3^2} \right) + 2\mu \left(\frac{\partial^2 \Upsilon}{\partial x_3^2} - \frac{\partial^2 \Psi}{\partial x_1 \partial x_3} \right), \\
\sigma_{13} &= \mu \left(\frac{\partial u_3}{\partial x_1} + \frac{\partial u_1}{\partial x_3} \right) = \mu \left(\frac{\partial^2 \Upsilon}{\partial x_1 \partial x_3} - \frac{\partial^2 \Psi}{\partial x_1^2} + \frac{\partial^2 \Psi}{\partial x_3^2} \right).
\end{aligned} \tag{2.192}$$

The general form of solution is assumed as

$$\begin{aligned}
\Upsilon &= \Upsilon(x_3) e^{i\xi(x_1 - c_p t)}, \\
\Psi &= \Psi(x_3) e^{i\xi(x_1 - c_p t)},
\end{aligned} \tag{2.193}$$

with

$$\begin{aligned}
\Upsilon &= A_1 \sin(px_3) + A_2 \cos(px_3), \\
\Psi &= B_1 \sin(qx_3) + B_2 \cos(qx_3),
\end{aligned} \tag{2.194}$$

and

$$p = \xi \sqrt{\frac{c_p^2}{v_L^2} - 1} = \xi \alpha_L, \quad q = \xi \sqrt{\frac{c_p^2}{v_T^2} - 1} = \xi \alpha_{SV}. \tag{2.195}$$

These equations describe standing waves in the x_3 -direction (transverse resonance) and propagating waves in the x_1 -direction. By substituting Eqs. (2.193) into Eqs. (2.192), and suppressing the common factor $e^{i\xi(x_1 - c_p t)}$, we obtain the displacements and stresses

$$\begin{aligned}
u_1 &= i\xi \Upsilon + \frac{d\Psi}{dx_3}, \\
u_3 &= \frac{d\Upsilon}{dx_3} - i\xi \Psi, \\
\sigma_{33} &= \lambda \left(-\xi^2 \Upsilon + \frac{d^2 \Upsilon}{dx_3^2} \right) + 2\mu \left(\frac{d^2 \Upsilon}{dx_3^2} - i\xi \frac{d\Psi}{dx_3} \right), \\
\sigma_{13} &= \mu \left(2i\xi \frac{d\Upsilon}{dx_3} + \xi^2 \Psi + \frac{d^2 \Psi}{dx_3^2} \right).
\end{aligned} \tag{2.196}$$

Since the field components contain sines and cosines, we can separate the solutions into symmetric and antisymmetric modes. If the displacement component u_1 contains cosines, the mode is symmetric about the midplane of the plate, and if u_1 contains sines, it is antisymmetric. The reverse holds for the displacement component u_3 . Hence, we have

$$\begin{aligned}
\Upsilon &= A_2 \cos(px_3), \\
\Psi &= B_1 \sin(qx_3), \\
u_1 &= i\xi A_2 \cos(px_3) + qB_1 \cos(qx_3), \\
u_3 &= -pA_2 \sin(px_3) - i\xi B_1 \sin(qx_3), \\
\sigma_{33} &= -\lambda(\xi^2 + p^2)A_2 \cos(px_3) - 2\mu(p^2 A_2 \cos(px_3) + i\xi q B_1 \cos(qx_3)), \\
\sigma_{13} &= \mu(-2i\xi p A_2 \sin(px_3) + (\xi^2 - q^2)B_1 \sin(qx_3)),
\end{aligned} \tag{2.197}$$

for symmetric modes and

$$\begin{aligned}
\Upsilon &= A_1 \sin(px_3), \\
\Psi &= B_2 \cos(qx_3), \\
u_1 &= i\xi A_1 \sin(px_3) - qB_2 \sin(qx_3), \\
u_3 &= pA_1 \cos(px_3) - i\xi B_2 \cos(qx_3), \\
\sigma_{33} &= -\lambda(\xi^2 + p^2)A_1 \sin(px_3) - 2\mu(p^2 A_1 \sin(px_3) + i\xi q B_2 \sin(qx_3)), \\
\sigma_{13} &= \mu(2i\xi p A_1 \cos(px_3) + (\xi^2 - q^2)B_2 \cos(qx_3)),
\end{aligned} \tag{2.198}$$

for antisymmetric modes. Now, as usual, the constants A_1 , A_2 , B_1 , and B_2 , as well as the phase velocity dispersion are found by applying the stress free upper and lower plate surfaces boundary condition

$$\sigma_{i3}^0, \sigma_{i3}^{-d} = 0, \quad i = 1, 3. \tag{2.199}$$

To ensure nontrivial solutions, the determinant of the coefficient matrix of the resultant homogeneous equation system must vanish, yielding the relation

$$\frac{(\xi^2 - q^2) \sin(qh)}{2i\xi p \sin(ph)} = \frac{-2\mu i \xi q \cos(qh)}{(\lambda \xi^2 + \lambda p^2 + 2\mu p^2) \cos(ph)}, \tag{2.200}$$

where $h = d/2$ is the half thickness of the plate. Equation (2.200) can be manipulated into

$$\frac{\tan(qh)}{\tan(ph)} = \frac{4\xi^2 p q \mu}{(\lambda \xi^2 + \lambda p^2 + 2\mu p^2)(\xi^2 - q^2)}. \tag{2.201}$$

We simplify the denominator on the right-hand side of Eq. (2.201) by using the definitions of p , q , c_p , v_L , and v_T . With $\lambda = \rho v_L^2 - 2\mu$, we obtain

$$\begin{aligned}
\lambda \xi^2 + \lambda p^2 + 2\mu p^2 &= \lambda(\xi^2 + p^2) + 2\mu p^2 \\
&= (\rho v_L^2 - 2\mu)(\xi^2 + p^2) + 2\mu p^2 \\
&= \rho v_L^2(\xi^2 + p^2) - 2\mu \xi^2,
\end{aligned} \tag{2.202}$$

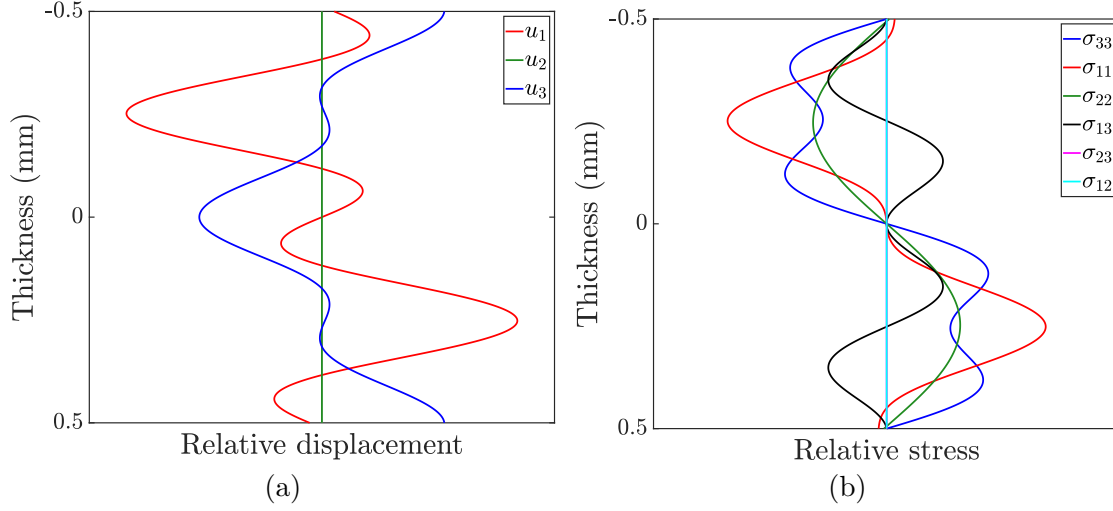


FIG. 2.31. Through thickness (a) displacement and (b) stress profiles of the A_4 Lamb wave at 10 MHz·mm in aluminum alloy 1100.

and with Eqs. (2.195) and $v_T^2 = \mu/\rho$

$$\lambda\xi^2 + \lambda p^2 + 2\mu p^2 = \rho\omega^2 - 2\rho v_T^2 \xi^2, \quad (2.203)$$

so that we have

$$\rho v_T^2 \left(\left(\frac{\omega}{v_T} \right)^2 - 2\xi^2 \right) = \rho v_T^2 (q^2 - \xi^2) = \mu (q^2 - \xi^2). \quad (2.204)$$

Finally, substituting Eq. (2.204) into Eq. (2.201) delivers the phase velocity dispersion for symmetric modes

$$\frac{\tan(qh)}{\tan(ph)} + \frac{4\xi^2 pq}{(q^2 - \xi^2)^2} = 0, \quad (2.205)$$

and in a similar manner, we obtain the characteristic equation for antisymmetric modes

$$\frac{\tan(qh)}{\tan(ph)} + \frac{(q^2 - \xi^2)^2}{4\xi^2 pq} = 0. \quad (2.206)$$

These equations are known as the Rayleigh-Lamb equations, and although they look rather simple, they can be solved only numerically.

For the calculation of the displacement and stress components, we apply our procedure for single layers, as presented in Sec. 2.3.4. Therefore, we have to generate

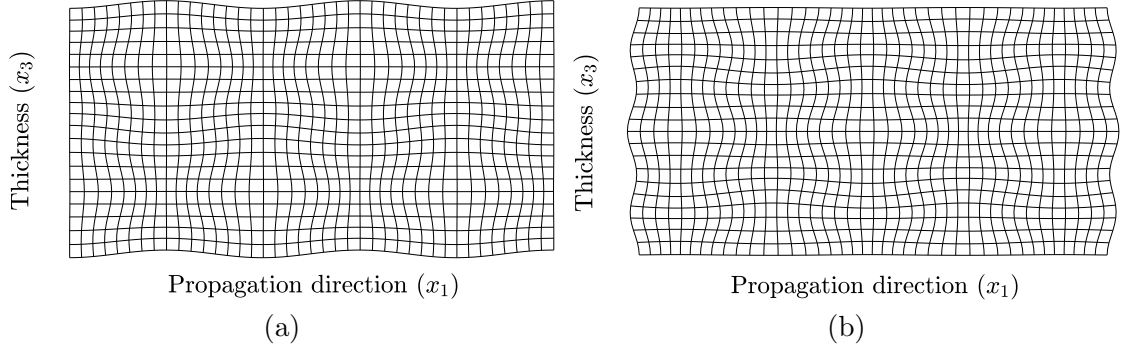


FIG. 2.32. Displacement patterns of (a) A_4 and (b) S_4 Lamb waves at 10 MHz·mm in aluminum alloy 1100. The displacement is scaled up for clarity.

the matrix \mathbf{D} , as required for the solution of Eq. (2.147). Since we have obtained c_p at a given frequency with the Rayleigh-Lamb equations, we can easily calculate the required quantities ξ , α_q , W_q , D_{1q} , and D_{2q} , $q = 1, 2, 3, 4$, using Eqs. (2.185), (2.186), and (2.188). Then, we set the bulk wave amplitude U_1 as unity and determine the amplitudes of the other three bulk waves in terms of the first one. Hence Eq. (2.148) takes the form

$$\begin{bmatrix} U_2 \\ U_3 \\ U_4 \end{bmatrix} = - \begin{bmatrix} d_{22} & d_{23} & d_{24} \\ d_{32} & d_{33} & d_{34} \\ d_{42} & d_{43} & d_{44} \end{bmatrix}^{-1} \begin{bmatrix} d_{21} \\ d_{31} \\ d_{41} \end{bmatrix}. \quad (2.207)$$

Now, we can calculate the displacement and stress field components at any coordinate x_3 by using

$$\begin{aligned} u_1 &= U_1 e^{i\xi\alpha_1 x_3} + U_2 e^{i\xi\alpha_3 x_3} + U_3 e^{i\xi\alpha_1(d-x_3)} + U_4 e^{i\xi\alpha_3(d-x_3)}, \\ u_3 &= W_1 U_1 e^{i\xi\alpha_1 x_3} + W_3 U_2 e^{i\xi\alpha_3 x_3} \\ &\quad - W_1 U_3 e^{i\xi\alpha_1(d-x_3)} - W_3 U_4 e^{i\xi\alpha_3(d-x_3)}, \\ \sigma_{33}^* &= D_{11} U_1 e^{i\xi\alpha_1 x_3} + D_{13} U_2 e^{i\xi\alpha_3 x_3} \\ &\quad + D_{11} U_3 e^{i\xi\alpha_1(d-x_3)} + D_{13} U_4 e^{i\xi\alpha_3(d-x_3)}, \\ \sigma_{13}^* &= D_{21} U_1 e^{i\xi\alpha_1 x_3} + D_{23} U_2 e^{i\xi\alpha_3 x_3} \\ &\quad - D_{21} U_3 e^{i\xi\alpha_1(d-x_3)} - D_{23} U_4 e^{i\xi\alpha_3(d-x_3)}. \end{aligned} \quad (2.208)$$

Since we have distinct Rayleigh-Lamb equations for symmetric and antisymmetric modes, we do not need to implement a mode family determination algorithm based on the displacement component u_1 , as required for Lamb waves in anisotropic waveguides.

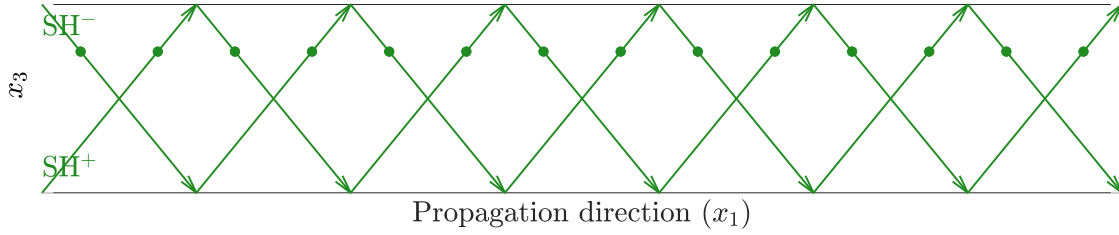


FIG. 2.33. Bulk wave pattern of the A'_3 shear horizontal wave at 10 MHz·mm in aluminum alloy 1100. The polarization is directed normal to the image plane.

2.4.3 Shear Horizontal Waves

Similarly as discussed in Sec. 2.3.3 for anisotropic media in the decoupled case, shear horizontal waves in isotropic media are formed through the superposition of only two upward and downward propagating shear waves with horizontal displacement u_2 directed parallel to x_2 , *i.e.*, normal to the image plane in Fig. 2.33. Since only one bulk wave type contributes to any guided SH mode, and since we treat here only a single layer, we can derive analytic expressions for the phase velocity and group velocity dispersion. The governing equation of motion is

$$\frac{\partial^2 u_2}{\partial x_1^2} + \frac{\partial^2 u_2}{\partial x_3^2} = \frac{1}{v_T^2} \frac{\partial^2 u_2}{\partial t^2}, \quad (2.209)$$

and the corresponding stress-strain relation

$$\sigma_{23} = \mu \frac{\partial u_2}{\partial x_3}. \quad (2.210)$$

with the formal solution

$$u_2 = U_2 e^{i\xi(x_1 + \alpha x_3 - c_p t)}, \quad (2.211)$$

yielding

$$\alpha_{1,2} = \pm \sqrt{\frac{c_P^2}{v_T^2} - 1}. \quad (2.212)$$

This geometric relation is illustrated in Fig. 2.34. The two values for α correspond to the upward and downward propagating waves SH^+ and SH^- so that we can write the displacement and stress field components as

$$\begin{aligned} u_2 &= \sum_{q=1}^2 U_{2q} e^{i\xi(x_1 + \alpha_q x_3 - c_p t)}, \\ \sigma_{23}^* &= \sum_{q=1}^2 D_{3q} U_{2q} e^{i\xi(x_1 + \alpha_q x_3 - c_p t)}, \end{aligned} \quad (2.213)$$

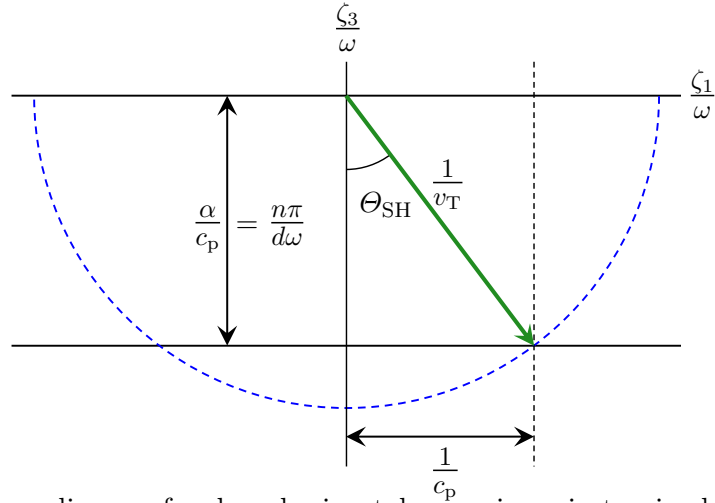


FIG. 2.34. Slowness diagram for shear horizontal waves in an isotropic plate of thickness d .

respectively, where the stress amplitude is obtained from Eq. (2.210), namely

$$D_{3q} = \mu\alpha_q. \quad (2.214)$$

By using superposition and suppressing the common factor $e^{i\xi(x_1 - c_p t)}$, we write the displacement and stress field components as

$$\begin{bmatrix} u_2 \\ \sigma_{23}^* \end{bmatrix} = \begin{bmatrix} 1 & 1 \\ \mu\alpha_1 & -\mu\alpha_1 \end{bmatrix} \begin{bmatrix} U_{21}e^{i\xi\alpha_1 x_3} \\ U_{22}e^{-i\xi\alpha_1 x_3} \end{bmatrix}, \quad (2.215)$$

and similarly to Eq. (2.120), we arrive at

$$\begin{bmatrix} u_2 \\ \sigma_{23}^* \end{bmatrix}_{x_3=-d} = \begin{bmatrix} \cos \eta & i/D \sin \eta \\ iD \sin \eta & \cos \eta \end{bmatrix} \begin{bmatrix} u_2 \\ \sigma_{23}^* \end{bmatrix}_{x_3=0}, \quad (2.216)$$

where $\eta = \alpha_1 \xi d$ and $D = \mu\alpha_1$. Eq. (2.216) relates the displacement and stress field components at the top of the plate ($x_3 = 0$) to those at its bottom ($x_3 = -d$). Imposing stress free plate surfaces leads to the characteristic function

$$iD \sin \eta = 0. \quad (2.217)$$

Since $\sin \eta = 0$ for $\eta = n\pi$ with $n \in \{0, 1, 2, \dots\}$, we get the relation

$$\alpha_1 \xi d = n\pi, \quad (2.218)$$

and with $\xi = \omega/c_p$ and $\omega = 2\pi f$, we reach at

$$\frac{\alpha_1}{c_p} = \frac{n\pi}{d\omega} = \frac{n}{2df}. \quad (2.219)$$

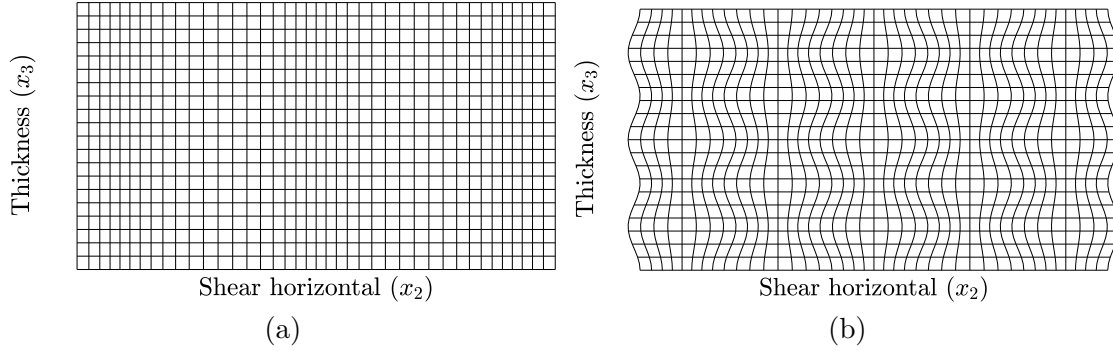


FIG. 2.35. Displacement patterns of (a) S'_0 and (b) S'_3 shear horizontal waves in aluminum alloy 1100. Notice that the propagation direction is normal to the image plane. The displacement is scaled up for clarity.

By substituting Eq. (2.212) into Eq. (2.219), we find the explicit phase velocity dispersion given by

$$c_p = \frac{2fdv_T}{\sqrt{4(fd)^2 - (nv_T)^2}}. \quad (2.220)$$

Symmetric modes are obtained for $n \in \{0, 2, 4, \dots\}$ and antisymmetric ones for $n \in \{1, 3, 5, \dots\}$. Setting $n = 0$ in Eq. (2.220) tells us that the fundamental SH mode (S'_0) is nondispersive with $c_p = v_T$, and substituting this into Eq. (2.212) yields $\alpha = 0$, *i.e.*, the bulk waves contributing to S'_0 are evanescent. For the group velocity, we write Eq. (2.219) as

$$\frac{\omega^2}{v_T^2} - \xi^2 = \left(\frac{n\pi}{d}\right)^2, \quad (2.221)$$

and take the differentials, resulting in

$$\frac{2\omega d\omega}{v_T^2} - 2\xi d\xi = 0. \quad (2.222)$$

Solving this equation for the group velocity $c_g = d\omega/d\xi$, we get

$$\frac{d\omega}{d\xi} = \frac{\xi v_T^2}{\omega^2}. \quad (2.223)$$

Finally, by substituting Eq. (2.221) into Eq. (2.223), we obtain the explicit group velocity dispersion as

$$c_g = v_T \sqrt{1 - \left(\frac{nv_T}{2fd}\right)^2}. \quad (2.224)$$

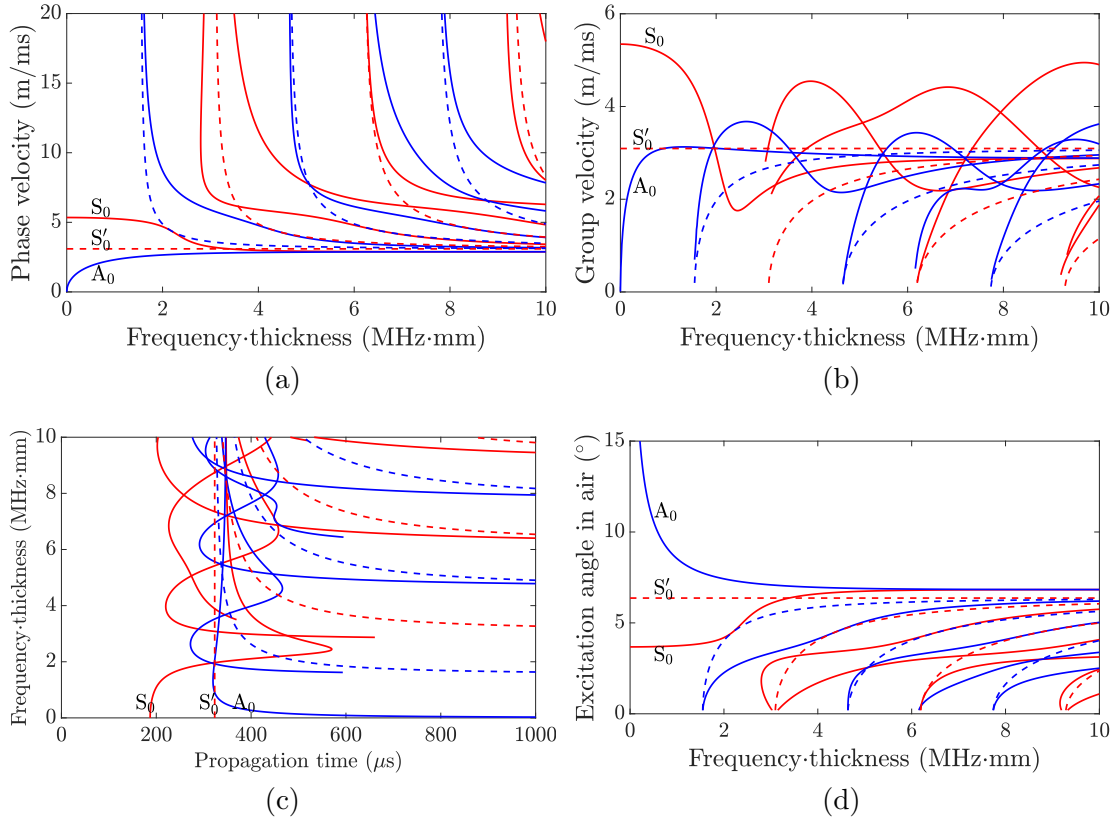


FIG. 2.36. Dispersion diagrams for aluminum alloy 1100. (a) Phase velocity, (b) group velocity, (c) propagation time at 1 m distance, and (d) excitation angle in air.

Eqs. (2.220) and (2.224) have been shown earlier by Rose in Ref. [148]. They allow us to obtain the dispersion curves analytically in an instant rather than numerically. Also, since tracing algorithms are unnecessary, the coding effort reduces tremendously.

By setting $U_{2q} = 1$ in Eqs. (2.213), we find the displacement and stress field components, respectively, as

$$\begin{aligned} u_2 &= e^{i\xi\alpha_1 x_3} + e^{i\xi\alpha_1(d-x_3)}, \\ \sigma_{23}^* &= \mu\alpha_1 e^{i\xi\alpha_1} - \mu\alpha_1 e^{i\xi\alpha_1(d-x_3)}, \end{aligned} \quad (2.225)$$

for symmetric modes and

$$\begin{aligned} u_2 &= e^{i\xi\alpha_1 x_3} - e^{i\xi\alpha_1(d-x_3)}, \\ \sigma_{23}^* &= \mu\alpha_1 e^{i\xi\alpha_1 x_3} + \mu\alpha_1 e^{i\xi\alpha_1(d-x_3)}, \end{aligned} \quad (2.226)$$

for antisymmetric modes.

2.5 Dispersion Curve Tracing

In Secs. 2.3 and 2.4, we have described the mathematical procedure for obtaining the modal solutions for guided waves in plate-like structures. In programming a software for the dispersion diagram calculation, it is of course the first step to code this math into correctly and efficiently working algorithms. Thorough testing, validation, and optimization are essential at this stage. The second important step is to increase the calculation speed as much as possible. This will be the topic of the current section.

The first Lamb wave dispersion diagrams obtained in the frame of this work were calculated for isotropic plates using the Rayleigh-Lamb equations. Thanks to their concise nature, and since the considered plates represented just one layer, the calculations took only limited processing time. The frequency and phase velocity range as well as appropriate frequency and phase velocity steps for which the dispersion curves should be obtained, were defined. The general procedure was then to choose the first frequency step, and evaluate the characteristic function (the Rayleigh-Lamb equations in this case) at every phase velocity step. We call this procedure a *phase velocity sweep*. Modal solutions were found wherever the Rayleigh-Lamb equations changed the sign between two phase velocity steps. Figure 2.37(a) shows the evaluation of the Rayleigh-Lamb equation for symmetric modes (2.205) at 1 MHz in 10 mm thick aluminum alloy 1100. The six dots in this graph mark the transitions through zero. The respective phase velocities lie on the corresponding symmetric dispersion curves at 1 MHz in the dispersion diagram shown in Fig. 2.38(a). We notice that every transition through zero is followed by a jump between positive and negative infinity. Therefore, we must also check whether the absolute value of the characteristic function drawn in Fig. 2.37(b) is a minimum. By repeating this procedure at every frequency step, the dispersion curves were obtained. A bisection algorithm was implemented to converge upon the modal solutions (phase velocity) until the desired resolution was reached. This procedure was sufficient for isotropic plates. Unfortunately, the MATLAB[®]-script does not exist anymore to compare its performance with the DC, but, depending on the parameters, the DC is today faster by one to two orders of magnitude and more accurate and reliable.

However, the procedure described above proved insufficient for multilayered transversely isotropic specimens for several reasons. First of all, it turned out to perform extremely slow, especially if there were many layers involved. The application of the SMM on the complicated equations, although highly efficient, is much more computationally expensive than solving the Rayleigh-Lamb equations, and the processing cost scales linearly with the number of layers. Secondly, the dispersion diagrams can be much more complicated than in isotropic cases. A good example is shown for wave propagation along 45° in 2 mm thick unidirectional

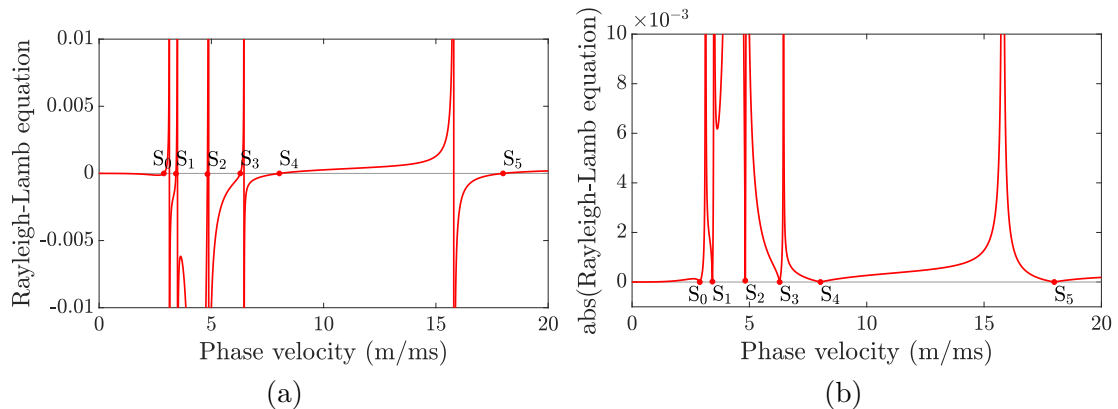


FIG. 2.37. (a) Solution of the Rayleigh-Lamb equation for symmetric modes at 1 MHz in 10 mm thick aluminum alloy 1100. (b) The minima in the absolute value mark the modal solutions.

SAERTEX[®]7006919/RIMR135 in Fig. 2.38(b). In contrast to Fig. 2.38(a), there occur mode crossings, even multiple times within a short frequency range for some curves. There are also much higher curvature gradients and modes approaching each other involved. If two modes get very close, either because they cross or just approach each other, the two sign changes of the characteristic function cannot be resolved anymore (two sign changes are as if there was none). The same happens when the zero transition that is associated with a modal solution and the accompanying jump between positive and negative infinity are too close. Typically, phase velocity steps between 10 m/s and 100 m/s were used, and decreasing that number would result in an even slower calculation. Furthermore, as the crossing of modes occurred, it proved very difficult to assign a found modal solution to the correct dispersion curve.

Therefore, a different approach was necessary, namely the *dispersion curve tracing*. Instead of sweeping the whole phase velocity range at each frequency step, we follow each dispersion curve, one by one, thereby saving processing time since we spare most of the space between the dispersion curves. The basic idea is to make an as accurate as possible guess where the next sample point of a dispersion curve should lie, based on the already determined sample points. However, as we will discuss below, such a routine must be highly elaborate to trace a dispersion diagram like the one shown in Fig. 2.38(b) reliably. Lowe has described the dispersion curve tracing routine used by DISPERSE in Refs. [39,40,132]. Basically, he applies an extrapolation method to make a guess for the next sample point. This works in the wavenumber space since the curves are more straight there than in the frequency space where the DC operates. A different method was implemented in the

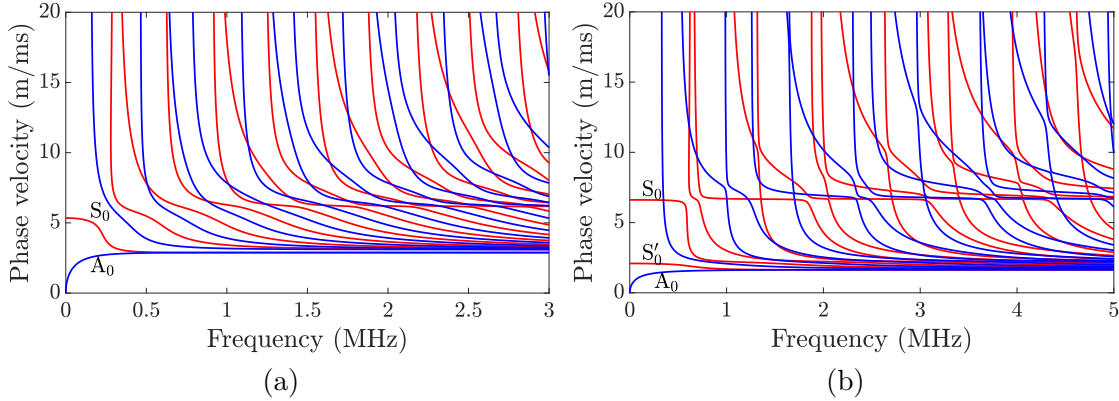


FIG. 2.38. Lamb wave dispersion diagrams for (a) 10 mm thick aluminum alloy 1100 and (b) wave propagation along 45° in 2 mm thick unidirectional SAERTEX[®]7006919/RIMR135

DC, described in the following. For this method, the first requisite is robustness, followed by efficiency.

The DC starts with a frequency sweep at the top phase velocity (20 m/ms in Fig. 2.38) to detect the cut-off frequencies of all modes in the frequency range of interest. In this frequency sweep, the characteristic function is evaluated at every frequency step. The detected modes are classified into the six possible mode families listed in Sec. 2.3.5. Then, the starting points of the fundamental modes S_0 and A_0 are sought by phase velocity sweeps at 1 Hz. Usually, phase velocity steps of 1 m/s or 10 m/s are used for these sweeps. For S_0 in isotropic plates, the plate wave velocity given by Eq. (2.31) defines the starting point. The evaluation of the characteristic function $\det \mathbf{K}$, as required by the SMM, yields qualitatively a similar result like the Rayleigh-Lamb equations shown in Fig. 2.37. Once the phase velocity sweep has discovered a sign change that is also a minimum between two phase velocity steps, the bisection algorithm starts, as sketched in Fig. 2.39. At each iteration m , the characteristic function value must be known at three phase velocities a_m , b_m , c_m . The red dot marks the exact location of the zero. Suppose we have detected the zero between the phase velocities a_0 and c_0 by the phase velocity sweep. In the following bisection iterations, we only need to calculate the characteristic function at b_m and retrieve those values at a_m and c_m from the preceding iterations instead of calculating a_m , b_m , and c_m in every iteration. This increases the computational speed remarkably.

Let us now discuss the tracing of the S_0 Lamb wave in 10 mm thick aluminum alloy 1100 as an example. Consider situation **A** in Fig. 2.40. Suppose the sample at 210 kHz has already been obtained, and we are now searching for the 220 kHz sample ($i = 23$). It is expected at a lower phase velocity. It is therefore taken the

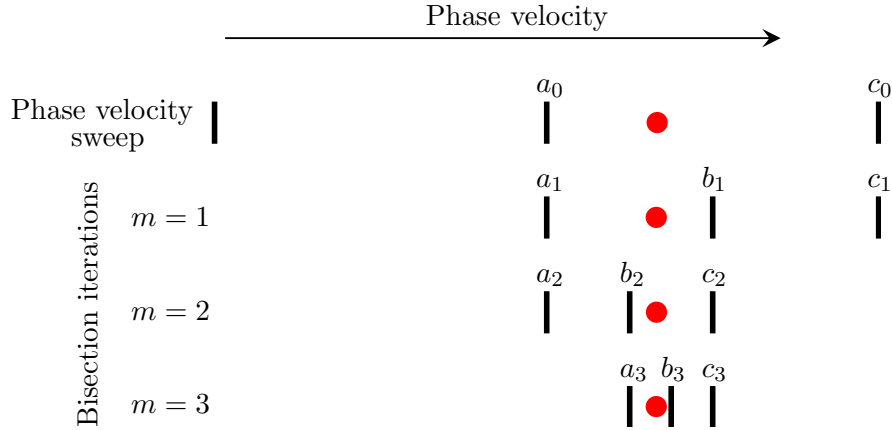


FIG. 2.39. Schematic of the bisection routine. The modal solution, indicated by the red spot, is detected between the phase velocities a_0 and c_0 . Then, bisection is applied to converge upon the solution. The efficiency is greatly improved by calculating the characteristic function only at the phase velocities b_m and retrieving the values at a_m and c_m from the preceding iterations.

difference between the phase velocities at the 200 kHz and at the 210 kHz sample Δ_{i-1} . The curvature is determined to be negative here. The 220 kHz sample is expected to lie within the search interval Γ_i , which spans from the 210 kHz sample's phase velocity down by the multiple $\Gamma_i = j^- \Delta_{i-1}$. The 220 kHz sample is indeed found therein. As the tracing progresses, we pass the turning point **B**, reach situation **C**, and search for the 270 kHz sample ($i = 28$). Since the curvature is positive here, we now use a smaller multiple $j^+ < j^-$, and find the 270 kHz sample lying within the search interval $\Gamma_i = j^+ \Delta_{i-1}$, where Δ_i is the phase velocity difference between the 250 kHz and 260 kHz samples. The factors j^- and j^+ have to be chosen carefully. If they are too small, a sample point cannot be reached, and if taken too large, the computation will take longer than necessary. The factor j^- , as used for negative curvature, must be large enough to cover strong negative curvature gradients in dispersion curves like those of S_0 and other modes in Fig. 2.38(b). As obvious in Fig. 2.38(a), these curvature gradients are not so pronounced in case of isotropic plates. To give the reader an idea of how large j^- should be, the default values in the DC are set to two for isotropic media and ten for transversely isotropic ones. Basically, j^+ , as used for positive curvature, could be chosen as $j^+ < 1$ if the curvature was positive everywhere in a dispersion curve. But this is the case only for shear horizontal modes. Otherwise, on Lamb waves, the tracing could not go through turning points into negative curvature. Therefore, j^+ is set to two for isotropic media and five for transversely isotropic ones by default.

Basically, with the described method, we perform some kind of simple extrapo-

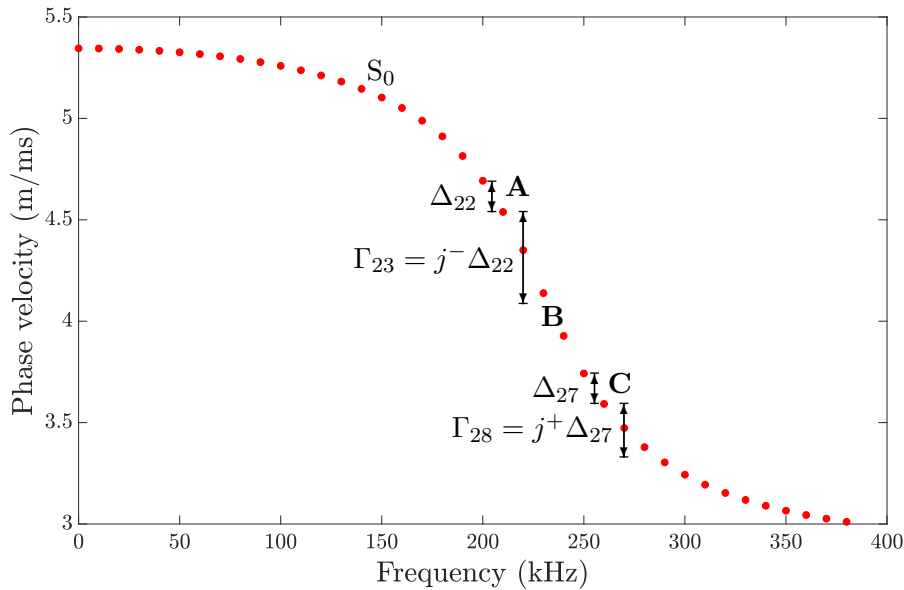


FIG. 2.40. The modal solution at each frequency step is sought by phase velocity sweeps performed within the search interval Γ_i . The width of Γ_i is a multiple j^\pm of the phase velocity difference Δ_{i-1} between the two preceding samples.

lation. An extrapolation method in its actual sense, like Lowe did it, was tested as well. The already obtained samples were fitted, and the fitted function evaluated at the next frequency step of interest. However, due to the highly unpredictable course of the dispersion curves in the frequency space, the fit went off frequently, and the method failed. By contrast, the “simple extrapolation” method used by the DC nowadays performs very well. This method utilizes the fact that all modes tend to lower phase velocities with increasing frequency, except A_0 and B_0 . To trace A_0 and B_0 , the search intervals must reach a certain multiple $j^\pm \Delta_i$ above the last known sample. In principle, we determine well-chosen search intervals that cover much less phase velocity range than those used by the preceding method described at the beginning of this section, where the search intervals covered the complete phase velocity range of the dispersion diagram. This enables us also to resolve modal solutions located extremely close to each other.

In the following, we discuss the algorithm used to find the modal solution within the search interval with high precision and speed. The determination of the modal solution in the search intervals works in two steps, similarly like the initial phase velocity sweeps at 1 Hz. However, during the tracing, we benefit from the fact that the search interval is already so small that the sign change can likely be resolved without the need to divide the search interval into equally spaced sections, *i.e.*, without any phase velocity sweep. If this is the case, we can immediately start with the bisection of the search interval. Otherwise, if no sign change is found

between the outer limits of the search interval, a k -loop, $k = 1, 2, \dots$, is initiated, wherein the search interval is divided into 5^k sections until a change in sign is detected. After that, the bisection of the critical section starts if it is still larger than the desired resolution. This makes clear how important it is to have small search intervals by choosing as small as possible, but as large as necessary values for j^- and j^+ . It allows us to find modal solutions with a lower number of sections 5^k and therefore save processing time, or, respectively, to find solutions at all with a chosen number k . Since the width of the search intervals increases as a dispersion curve becomes steeper, the tracing efficiency decreases with increasing steepness. In the DC, k is set to six for isotropic plates and five for transversely isotropic ones by default, thus determining the ability to find modal solutions. If the maximum number of sections has been reached, and the solution still not been found, this does not necessarily cause problems in the curve tracing because there is a routine involved that replaces missing solutions (*i.e.*, samples). This routine fits the already known samples and extrapolates them to the current frequency step. However, if too many samples are missing, the fit goes off, and the tracing fails. There are scenarios where very high numbers of k would be necessary to find a solution, causing a very long computation since the algorithm must loop through every iteration k and calculate five times more sections in each iteration. Therefore, it is better to choose k not too large, but rather let the extrapolation routine replace the missing sample. As default resolutions, the DC uses 10^{-6} m/s and 10^{-2} m/s for isotropic and transversely isotropic specimens, respectively. The modes are traced one after the other and for each mode family separately, starting with the fundamental modes and continuing with increasing mode order. In order to avoid that the tracing algorithm jumps to the next lower mode that has been traced before, search intervals which reach the next lower mode are cut just above this mode. However, if a dispersion curve crosses one (or several) lower modes that have already been traced, we need an additional algorithm to enable the tracing through those crossings. This algorithm is implemented in coupled cases in transversely isotropic specimens, where the crossing of modes belonging to the same mode family can appear. This situation is depicted in Fig. 2.41, showing the symmetric modes in a small area, taken from the dispersion diagram in Fig. 2.38(b). Suppose we have already traced S_2 , and now we continue with the tracing of S_3 . Exemplary search intervals are drawn at each frequency step. Clearly, we could afford to make them smaller by choosing smaller numbers for j^- and j^+ , but we want to be prepared for bigger curvature gradients that are likely to occur. At 1330 kHz, S_3 turns down toward S_2 , and the search intervals are cut above S_2 to prevent the algorithm from jumping to this mode. Then, between 1350 kHz and 1360 kHz, S_3 crosses S_2 . The algorithm loops through all iterations k to be sure that S_3 is definitely not located above S_2 anymore. Hence, it should continue below. Therefore, a second search interval is determined below S_2 , and the search

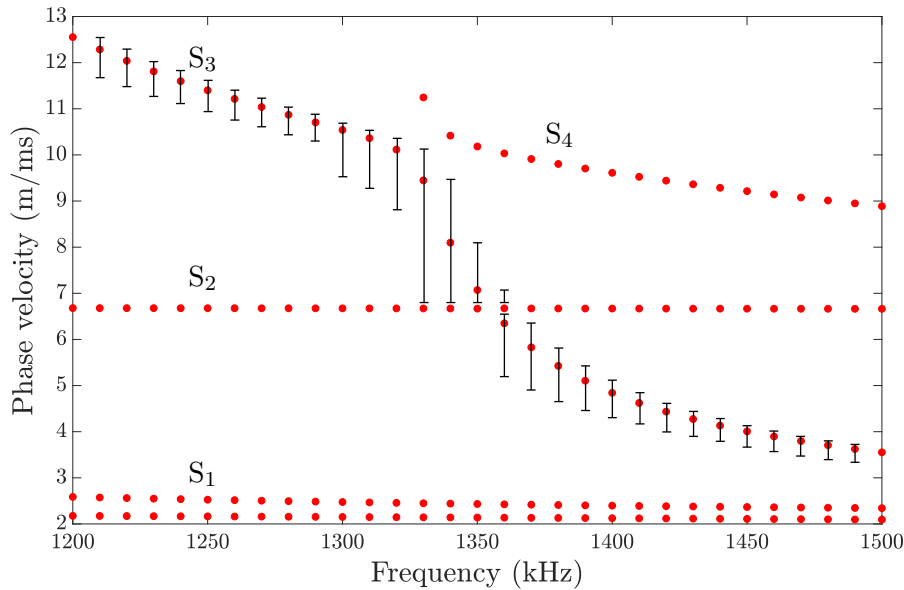


FIG. 2.41. A robust algorithm allows the tracing of S_3 as it crosses below S_2 . The search intervals do not touch S_2 to prevent the tracing algorithm from jumping from S_3 to S_2 .

restarted therein with $k = 1$. Eventually, the modal solution is found so that the tracing can continue in the usual way below S_2 . If the second search would have been unsuccessful either, the extrapolation routine would have interfered as a third “search” and have replaced the sample. This routine is slow but very robust, which is considered most important. Since the algorithm loops through every iteration k before continuing the search below the mode to be crossed, this is another reason to choose k not too large. Of course though, before a mode has the chance to cross an already traced lower mode, this very lower mode must have crossed the higher mode before the higher mode was traced. Ultimately, the jumping to yet unknown modes cannot be avoided a priori.

Since the higher order modes are almost parallel to the phase velocity axis around their cut-off frequency, the phase velocity sweeps do not work there very well, leaving the dispersion curves often incomplete. Therefore, frequency sweeps are performed at certain phase velocity steps to complete the curves up to the phase velocity limit. Figure 2.42 illustrates the completion of the tracing of S_1 in 10 mm thick aluminum alloy 1100. Its cut-off frequency at 20 m/ms is 286.129 kHz. Since we have chosen frequency steps of 10 kHz, the phase velocity sweeps start at 290 kHz, leaving the curve incomplete below 290 kHz. The frequency sweeps continue the curve at point **D**, which is above the 290 kHz sample by a certain phase velocity step. A fixed search interval width can be defined in the DC, which involves a certain offset to higher frequencies in order to allow for the tracing routine to overcome the point **E** where the dispersion curve turns to higher frequencies again.

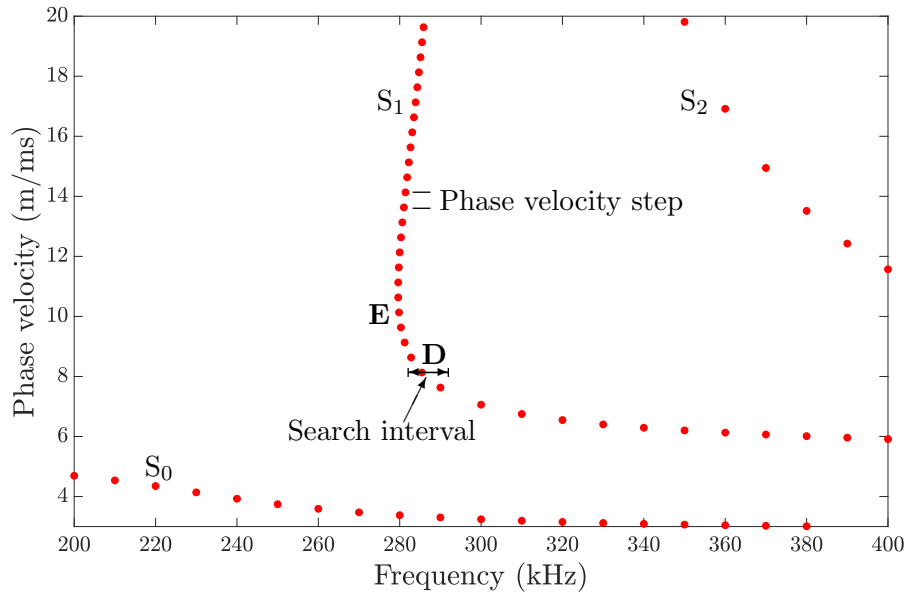


FIG. 2.42. Since the phase velocity sweeps at the frequency steps often leave the dispersion curves incomplete around their cut-off frequency, frequency sweeps at certain phase velocity steps are performed to complete the curves.

2.6 Dispersion Calculator

The MATLAB[®]-based DC is an interactive and fully validated stand-alone software for the computation of dispersion curves and mode shapes of guided waves in isotropic and transversely isotropic composite plates, for which the user can enter the corresponding material parameters and layups. Almost all calculations and quantitative plots presented in this work have been obtained with the DC (and therefore can be reproduced by the interested reader). The DC can be downloaded free of charge on the DLR-homepage [64]. A copy of the DC user's manual is given in Appendix A. Since the DC is, beside the Adaptive End-Effector, the main achievement of this thesis, one section should be dedicated to it. Section 2.6.1 outlines the motivation for its development as well as the development history. In Sec. 2.6.2, we briefly introduce the functionality and key features of the DC, and then we compare it to DISPERSE to give the reader an idea of its performance.

2.6.1 Development History

The task that triggered the development of the DC was the calculation of Lamb wave excitation angles for the air-coupled ultrasonic inspection of rocket booster pressure vessels of the future launcher Ariane 6. This task was to be accomplished in the frame of a joint project, called *Procomp*, with the DLR and MT Aerospace,

Augsburg, Germany, as participants. The Ariane 6 boosters are intended to be made of CFRP in order to make them lighter, and therefore enable the launcher to carry more payload. In some areas, such pressure vessels can consist of up to four hundred layers, which is a challenging task to calculate them. To facilitate the calculation, it is a common practice to group layers, but this is not possible in this case because the layups are very complicated and irregular in terms of the winding angle (fiber orientation) and the layer thicknesses. Therefore, every single layer has to be calculated, and DISPERSE was purchased to perform those calculations. DISPERSE has been developed by Lowe and Pavlakovic since the early 1990s, and it is today the leading software in its field. However, it turned out that DISPERSE in the version 2.0.20a was unable to calculate laminates containing several hundreds of layers. This is because the GMM, used by DISPERSE v2.0.20a, is unsuitable for the calculation of so many layers. Therefore, a new software had to be developed. The key requirement was that the software should be able to calculate at least four hundred layers, as required by the use case. The SMM is known to have this capability, and although it is seventeen years old, it is still unparalleled by any other stable computation method in this respect. The second requirement was the ability to distinguish the different mode families. In 2017, however, Barski *et al.* [62] stated that “Unfortunately, the applied method [the SMM] does not allow the full identification of what kind of wave mods [sic] are.”. In the same year, Quintanilla *et al.* [86] demonstrated the mode family determination with the SCM. Since the ability to calculate many layers was considered essential, the author implemented the SMM and introduced special boundary conditions to allow for the separate tracing of the different mode types, as discussed in Sec. 2.3. Parts of this work were published in the Journal of the Acoustical Society of America in 2018 [63].

The development of the DC started in 2016 with a MATLAB[®]-script for the dispersion curve calculation for isotropic plates. Since then, a tremendous amount of time and effort has been committed to the development of more scripts and functions, into validation and optimization⁸. DISPERSE always served as a guide and benchmark for the development of the DC, as well as for its validation. Clearly, without DISPERSE, the DC (and this thesis) would not exist in the way it does today. The decision to create a software from the scripts and to publish it was made only in mid 2018, triggering the work on the graphical user interface (GUI) and the initial release in November 2018. It was never planned, neither by the author nor by the Procomp project, which this thesis is funded from, to extend the functionality so much and even create a software from it. This came with time, similarly as the desire to write this doctoral thesis on the topic. In that sense, the DC is a product of passion and commitment. However, everything could

⁸The current version DC v1.5, available at the time this thesis is completed, has grown to thirty thousand lines of code.

not have been done without spending a lot of time on it. This was possible only thanks to the great freedom that was granted to the author by the DLR. Nowadays, the DC has already attracted interest in the scientific community. For instance, it serves for the analysis of acoustic emission signals done by Markus Sause, Professor for mechanical engineering at the University of Augsburg, Germany, and also by Marvin Hamstad, Professor Emeritus for mechanical engineering at the University of Denver, Colorado, USA. Michel Castaings, Professor for physical acoustics at the Institut National Polytechnique, Bordeaux, France, uses the DC in his lab and for the education of students as well. The DC is used in the group of Victor Giurgiutiu, Professor for mechanical engineering at the University of South Carolina, South Carolina, USA.

Regarding future work, there is plenty to do. At the time this thesis is written, only plates can be calculated, and although their modal solutions are valid for structures with a small curvature in good approximation, the modeling of wave propagation along the circumference of a cylinder, as the case in pipe inspection applications, is worth to be implemented. The same for guided waves in rods. More complicated geometries can only be solved by the FEM or by the SAFE and SCM methods. Another interesting topic are hybrids from isotropic and transversely isotropic materials such as fiber metal laminates (FML), *e.g.*, glass laminate aluminum reinforced epoxy (GLARE). Of particular importance is the influence of the surrounding medium on the dispersion characteristics, also referred to as *fluid loading*. In the present work, we assume the plates to be surrounded by a vacuum, which is a good approximation for air due to the large mismatch of the acoustical impedances between a solid and a gas. However, as the surrounding medium becomes denser and acoustically faster, the amount of energy leaking into the surrounding medium increases, and the dispersion curves change accordingly. Also, currently, the materials are assumed to be fully elastic. Therefore, a future model should also take attenuation caused by viscoelasticity into account. Apart from these topics, there are users asking for updates occasionally.

2.6.2 Dispersion Calculator and DISPERSE

Since DISPERSE is the benchmark for the DC, as well as for any software calculating dispersion curves, it suggests itself to conduct a comparison of both software. The author is aware that this attempt might be somewhat critical, considering that DISPERSE is a commercial software sold by Prof. Lowe. It is tried to keep the comparison well-balanced and fair and on a strictly technical level. The author wants to avoid any harm to the business of Prof. Lowe. For this reason, prior to the publication of the DC, the author asked Prof. Lowe for his acceptance, which he gave. In the following, a comparison between DISPERSE and the DC in terms of layout, functionality, and performance is presented.

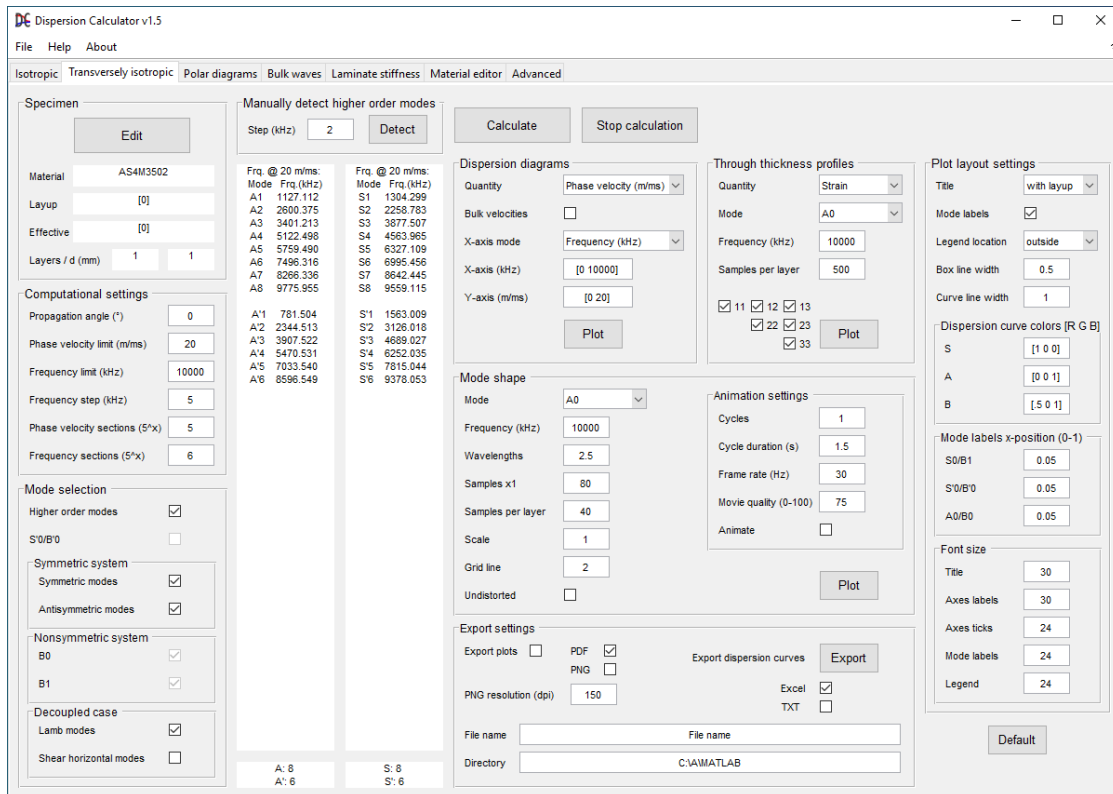


FIG. 2.43. The “Transversely isotropic” tab of the DC v1.5.

Layout

The GUI of the DC (see the “Transversely isotropic” tab in Fig. 2.43) is basically different from DISPERSE’s GUI (compare Fig. 2.44) in that it only provides the parameter setting interfaces like editable fields and buttons as well as some output windows displaying data and other information as numbers or text. All plots like dispersion diagrams or mode shapes are displayed in extra windows that open upon pressing the corresponding plot button. This basic arrangement is of course a matter of personal preference, but without the need to spare space for a plot window inside the GUI, there is no need to arrange options in sub menus, where they are out of sight of the user initially. Instead, the DC provides all options that are related to one superordinate topic in just one tab⁹. For instance, in the “Isotropic” tab, the user can set up the specimen, define the computational parameters, and calculate the dispersion curves, through thickness profiles, mode shapes, adjust the plot layout, and manage the export of data and plots. Having all options in sight improves the handling of the software and allows the unexperienced

⁹The only exception from this are the menus where transversely isotropic specimens are defined.

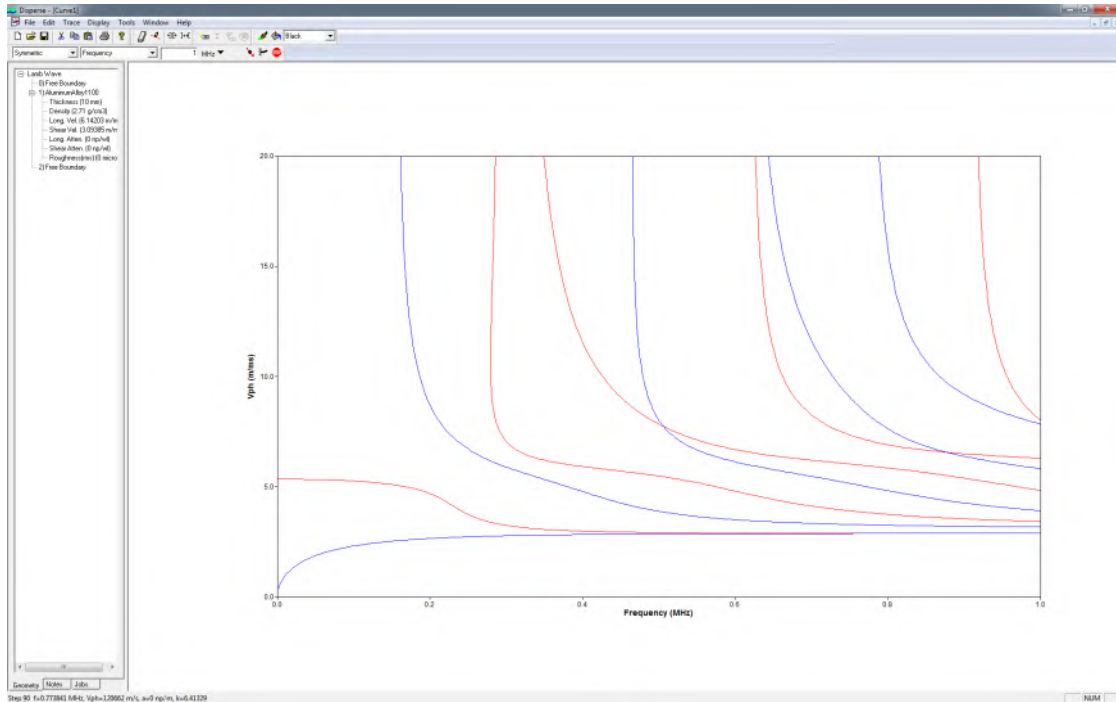


FIG. 2.44. The main window of DISPERSE v2.0.20a.

user to achieve the desired results fast. On the other hand, DISPERSE is much more versatile and consequently offers more options, which simply cannot fit into one tab or menu. It calculates more different material classes, geometries, and involves physics like viscoelasticity and fluid loading, requiring more options than the modeling which the DC does.

The visualization of the results is considered very important in the DC. Basically, the visualization of data acts as the interface between the obtained binary numbers stored on the computer and the perception of the user. Therefore, the plots should have the best possible quality, and this is best achieved in extra windows to make optimal use of the screen size. The functionality is completed by comfortable export functions for plots and raw data.

Accordingly, the layout of the DC is rather simple, currently consisting of seven tabs, of which five cover the superordinate topics, one allows the user to enter material parameters, and the last one contains advanced dispersion curve tracing options. The following tabs are available:

1. **Isotropic.** For the calculation of dispersion diagrams and mode shapes for isotropic plates (Sec. 2.4).
2. **Transversely isotropic.** For the calculation of dispersion diagrams and mode shapes for multilayered transversely isotropic plates (Sec. 2.3).

3. **Polar diagrams.** For the calculation of polar dispersion diagrams for multilayered transversely isotropic plates (Sec. 2.7.2).
4. **Bulk waves.** For the calculation of the bulk waves' phase and group velocities, slownesses, and polarization propagating in transversely isotropic media as well as their scattering on solid-fluid interfaces (Sec. 2.2).
5. **Laminate stiffness.** For the calculation of the HST of laminates (Sec. 2.1.5).
6. **Material editor.** To enter engineering constants or stiffness matrix components of isotropic and transversely isotropic materials (Secs. 2.1.2 and 2.1.3).
7. **Advanced.** Contains the advanced options for the dispersion curve tracing algorithms (Sec. 2.5).

The functionality and handling of these tabs are explained in the DC's manual, which is accessible via the "Help" button in the DC, and which is also reproduced in Appendix A. Clearly, such kind of GUI layout can only be maintained as long as there are not too many options so that they still fit on one screen in a convenient way. Therefore, as new functionality will be implemented in the future, it is likely that menus will have to be introduced into the DC's GUI. However, the high quality plotting in extra windows will be maintained.

Versatility

Concerning functionality, DISPERSE is much more versatile than the DC. The extensive DISPERSE user's manual [132] gives proof of that fact. All the future work topics discussed in Sec. 2.6.1 and more features are covered by DISPERSE. Basically, DISPERSE can handle more material symmetry classes beside isotropic and transversely isotropic ones, namely also orthotropic and cubic as well as combinations of them. A very interesting feature provided by DISPERSE is the simulation of an ultrasonic A-scan (amplitude versus time) corresponding to a single selected mode and frequency, or the simulation of an A-scan containing all modes (components and sum) at a selected frequency. On the other hand, the DC allows more modeling of elastic wave propagation in bulk material, and it calculates polar dispersion diagrams.

Many Layers

In Sec. 2.6.1, the key requirement for the DC was established that it should be able to calculate four hundred layers. In Sec. 2.7.3, dispersion diagrams for laminates consisting of four hundred and one thousand layers are presented to proof that the DC meets this key requirement. The number of layers appears to be theoretically

unlimited. It will just take an unlimited amount of time. The largest layup that could be calculated with DISPERSE was $[0/90]_{15s}$, containing sixty layers.

Mode Family Determination

Both software distinguish the six mode families listed in Sec. 2.3.5, which occur depending on the symmetry and coupling properties of a laminate. In addition, the DC distinguishes symmetric and antisymmetric modes in the special case when the laminate is nonsymmetric and the propagation direction is centered, like 40° in $[0/80]$ or 45° in $[0/45/90]$.

Speed and Robustness

To compare both software in terms of dispersion curve tracing speed and robustness, we assume a 2 mm thick unidirectional layer SAERTEX[®]7006919/RIMR135, and calculate dispersion diagrams for wave propagation along 0° and 45° with respect to the fiber direction with both software, using only the default parameters. These calculations are performed on an i7-2700K central processing unit (CPU) at 4×3.5 GHz (Intel, Santa Clara, CA, USA). For wave propagation along the fibers, both the DC and DISPERSE (see Figs. 2.45(a) and 2.45(b), respectively) calculate the dispersion diagram correctly¹⁰. With DISPERSE, two modes in the upper right corner in Fig. 2.45(b) were obtained by manual retracing. With manual tracing, the user can perform sweeps to find modal solutions by dragging rectangles over the region of interest in the dispersion diagram, and start tracings to complete dispersion curves from locations where modal solutions are found. Regarding computation time, it turns out that DISPERSE is extremely fast, taking well below one second plus some seconds for the manual retracing, while the DC needs 26 sec. The diagrams for 45° wave propagation are displayed in Figs. 2.45(c) and 2.45(d). Again, while the DC requires comparatively long 425 sec, DISPERSE completes the calculation after only 4 sec and some extra seconds for the manual retracing of some parts of the dispersion curves. Although the DC calculates these dispersion diagrams without any problem, it should be noted clearly that the DC also fails in the tracing of dispersion curves occasionally, without having the possibility of manual retracing. In practice, the user can always find examples where one software has problems and the other does not. One thing that occurs in DISPERSE is that it can find spurious solutions when the phase velocity of the guided wave is equal to any of the bulk velocities in the layers of the laminate. In such cases, DISPERSE stops tracing a given dispersion curve at the phase velocity in question, and draws a horizontal line instead. This can be taken care of by manual tracing. Overall, both software have a comparable robustness in the dispersion curve tracing.

¹⁰The conformity of the dispersion curves obtained with both software is studied in Sec. 2.7.1.

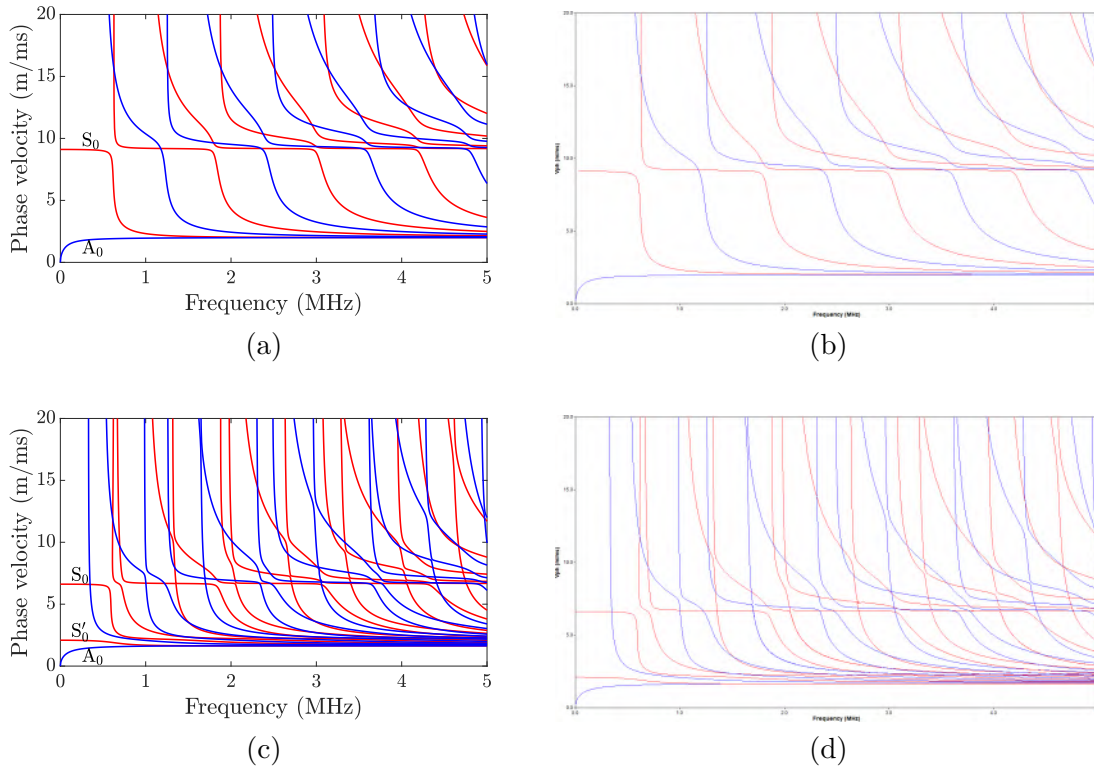


FIG. 2.45. Lamb wave dispersion diagrams for wave propagation along (a), (b) 0° and (c), (d) 45° in 2 mm thick unidirectional SAERTEX[®]7006919/RIMR135. The left-hand side diagrams are calculated by the DC, the right-hand side ones by DISPERSE.

Although the DC calculates very slowly compared to DISPERSE, there are statements from DC users proving that it is actually not slow, but rather that DISPERSE is exceptionally fast. Below, four quotes from experienced researchers are given to put the performance of the DC into perspective. All quotes were received in the course of electronic mail correspondence.

The first assessment was done by Dr. Marvin Hamstad, Professor Emeritus for mechanical engineering at the University of Denver, Colorado, USA, on 24 November 2018:

“I did one run so far for a 84 mm thick steel plate. The calculation was much faster than the NASA program I have used for this same calculation.”

The second rating was given by Michel Castaings, Professor for physical acoustics at the Institut National Polytechnique (INP), Bordeaux, France, on 26 November

2018:

“The computation is very fast and seems to find all solutions quite properly. Moreover, the code offers numerous options and a convenient graphical user interface.”

Another electronic mail report given by Tobias Roelfes, scientist at ROSEN Technology and Research Center, Lingen, Germany, is reproduced here, giving a blueprint of how the DC helps other researchers in their fields. The following text was received in German on 15 October 2019:

“Within the scope of a publicly funded project we investigate fibre composites with guided ultrasonic wave modes for typical defects like delamination or similar. In order to get a better understanding of the wave propagation in this highly anisotropic material, we performed simulation calculations with a commercial FEM tool (ANSYS). Alternatively, the DC was also used. The calculated dispersion curves of both tools match perfectly.”

And most recently, Hanfei Mei, Ph.D. student in the group of Dr. Victor Giurgiutiu, Professor for mechanical engineering at the University of South Carolina, Columbia, South Carolina, USA, concluded on 21 January 2020:

“I have used the semi-analytical finite element (SAFE) approach to calculate dispersion curves in composite plates. I have been using Dispersion Calculator for a few days. It is really easy to use and very efficient. It is a powerful software for the computation of dispersion curves in isotropic and composite materials.”

In summary, the DC can calculate more layers, whereas DISPERSSE is faster and more versatile. In Table 2.8, it was tried to compare the performance by assigning numbers and Booleans to each category. Whereas we can give exact numbers for “Many layers” and “Speed”, on the other hand, “Versatility” and in particular “Robustness” can only be estimated roughly. Since certainly some readers may disagree with this assessment, it should be noted that the ratings for “Versatility” and “Robustness” should only be considered as the author’s opinion rather than a definite quantitative fact.

TABLE 2.8. Comparison of the DC v1.4 and DISPERSE v2.0.20a.

	DC	DISPERSE
Many layers	> 1000	60
Mode families	✓	✓
Speed	1	100 ^a
Robustness	80	80
Versatility	30	100

^a reduced if manual tracing required

2.7 Numerical Examples

Although we have already shown many computational results in this chapter, be it dispersion diagrams, mode shapes, or bulk wave patterns, they all served to visualize the mathematical discussions in the first place. An exception from this is Sec. 2.2, where we evaluated the propagation of bulk waves in infinite transversely isotropic materials and their scattering on interfaces quantitatively and comprehensively. The current section is dedicated to a quantitative discussion of the propagation of guided waves in isotropic and transversely isotropic single layers and multilayered laminates. The suitability of specific modes for NDI purposes will also be an issue. In Sec. 2.7.1, we compare dispersion diagrams calculated with the DC and with DISPERSE to proof that the DC is working correctly. This is accompanied by an in-depth analysis of mode shapes and bulk wave patterns in guided waves. Section 2.7.2 discusses how mode shapes depend on the frequency as well as mode order and introduces polar dispersion diagrams for transversely isotropic specimens. Finally, Sec. 2.7.3 demonstrates the most important capability of the DC, namely the calculation of layups containing four hundred and one thousand layers. We report also the interesting phenomenon of quasipure coupled modes and discuss possible approximative modeling techniques to save computation time.

2.7.1 Validation

In this section, we superpose dispersion curves calculated with the DC with those obtained with DISPERSE to proof that the DC is calculating correctly, and then we explain mode shapes under consideration of the corresponding bulk wave patterns. We perform this test on two exemplary layups, namely $[0/90]_{2s}$ and $[0/90]_4$ SAERTEX[®] 7006919/RIMR135 for wave propagation along 0° in both cases. The dispersion diagram corresponding to the $[0/90]_{2s}$ layup is shown in Fig. 2.46(a). The bold curves are calculated by DISPERSE for reference and the thin ones by the

TABLE 2.9. Deviation of the DC v1.4 from DISPERSE v2.0.20a in Fig. 2.46(a).

	S_0	S_2
Average deviation (m/ms)	1.89×10^{-5}	1.25×10^{-4}
Average deviation (%)	4.10×10^{-4}	8.83×10^{-4}
Maximum deviation (m/ms)	1.20×10^{-3}	3.46×10^{-2}
Maximum deviation (%)	1.93×10^{-2}	1.73×10^{-1}

DC. Since the layup is symmetric, we can determine symmetric (red/orange) and antisymmetric (blue) modes, and because we have only 0° and 90° layers and the wave propagation is along 0° , Lamb waves (solid lines) and shear horizontal waves (dashed lines) can be separated. Obviously, both software's dispersion curves are matching in terms of the shape and mode type. In order to give a quantitative measure of the conformity of both software, Table 2.9 lists the average and maximum deviation of the sample points of S_0 and S_2 . The dispersion curves consist of five thousand and 4171 sample points, respectively. Accordingly, the DC is in a remarkable 99.9994% agreement with DISPERSE. The dispersion diagram for the $[0/90]_4$ layup is shown in Fig. 2.46(b). Since the layup is nonsymmetric, the solutions can be separated only into shear horizontal and Lamb waves. Again, the results obtained with the DC match those from DISPERSE.

Let us take a closer look at the mode shapes. Notice that in those pictures the displacement is scaled up for clarity and that only the *shapes* can be compared from one mode shape to another but not the absolute displacements. Figure 2.47(a) displays the mode shape of S_5 at 10 MHz·mm from Fig. 2.46(a). Each layer's thickness is represented by five grid cells. Clearly, the mode shape is symmetric about a thought line located at the half thickness. To distinguish this mode from the antisymmetric ones, we used the special boundary condition that the in-plane displacement u_1 must have the same sign at the outer surfaces of the laminate. Such a relation is not intrinsic in a nonsymmetric layup. Considering for example the mode shape of B_{10} at 10 MHz·mm from Fig. 2.46(b), as displayed in Figure 2.47(b), we find that u_1 has the same sign on the top and bottom surfaces by chance, but this situation changes with the frequency-thickness product so that no characteristic special boundary condition based on u_1 can be established.

The bulk wave patterns shown in Figs. 2.47(c) and 2.47(d) help us in an attempt to interpret these mode shapes more physically. We notice that the in-plane displacement component u_1 is much smaller in the 0° layers than in the 90° layers. Consider Fig. 2.48(a). B_{10} at 10 MHz·mm in the $[0/90]_4$ layup is excited at an incidence angle in air of $\Theta_{\text{in}} = 7.33^\circ$, indicated by the red slowness vec-

TABLE 2.10. Relative bulk wave amplitudes in B_{10} at 10 MHz·mm for wave propagation along 0° in $0/90_4$ SAERTEX[®]7006919/RIMR135.

Layer	Layup	L	S_{fast}	S_{slow}
1	0	0.112/0.235	0.017	–
2	90	0.323	–	0.476
3	0	0.118/0.432	0.036	–
4	90	0.505	–	1
5	0	0.425/0.163	0.038	–
6	90	0.347	–	0.556
7	0	0.273/0.117	0.017	–
8	90	0.240	–	0.220

tor in the second quadrant. The third and fourth quadrant represent the top 0° layer. Guided by Snell's law and the slowness profiles, two propagating bulk waves S_{fast} and S_{slow} are generated at refraction angles of, respectively, $\Theta_{S_{\text{fast}}} = 53.63^\circ$ and $\Theta_{S_{\text{slow}}} = 36.74^\circ$, while L is evanescent. Only L and S_{fast} possess displacement in the x_1 - x_3 -plane and therefore contribute to the pure Lamb-type mode B_{10} , whereas S_{slow} has displacement only in the x_2 -direction, contributing to shear horizontal modes. Accordingly, only L and S_{fast} appear in the 0° layers of the bulk wave pattern in Figs. 2.47(c) and 2.47(d). Even without taking the bulk waves' amplitudes into consideration, we can now give a qualitative explanation why the displacement component u_1 is small in the 0° layers. Since L waves are evanescent, their (purely) longitudinal displacements, contributing to the u_1 -component of the total displacement field, decay exponentially with the depth. A close look at the top layer in Fig. 2.47(b) supports this finding. Figure 2.48(c) shows that S_{fast} is polarized almost normal to the x_1 -direction ($x'_1 = x_1$). In fact, with a refraction angle of $\Theta_{S_{\text{fast}}} = 53.63^\circ$ and the polarization angle of $\beta_{S_{\text{fast}}} = 57.40^\circ$, the polarization vector deviates by 86.23° from the x_1 -direction, therefore contributing only marginally to u_1 . By contrast, we have a substantial displacement component u_1 in the 90° layers. At the bottom of our $[0/90]_4$ layup, we have the (top-down) situation depicted in Fig. 2.48(b). Again, B_{10} is excited at an incidence angle in air of $\Theta_{\text{in}} = 7.33^\circ$. Now, the third and fourth quadrant represent the 90° layer. Three propagating bulk waves are generated with refraction angles of $\Theta_L = 69.39^\circ$, $\Theta_{S_{\text{fast}}} = 49.17^\circ$, and $\Theta_{S_{\text{slow}}} = 29.22^\circ$. Figure 2.48(d) shows the polarization vectors of the three bulk waves. All of them are pure modes. Only L and S_{slow} have displacement in the x_1 - x_3 -plane ($x'_2 = x_1$), contributing to B_{10} , while S_{fast} with

TABLE 2.11. Relative bulk wave amplitudes in S_5 at 10 MHz·mm for wave propagation along 0° in $0/90_{2s}$ SAERTEX[®]7006919/RIMR135.

Layer	Layup	L	S_{fast}	S_{slow}
1	0	0.092/0.240	0.015	–
2	90	0.281	–	0.478
3	0	0.146/0.144	0.035	–
4	90	1	–	0.386
5	90	1	–	0.386
6	0	0.145/0.145	0.035	–
7	90	0.280	–	0.476
8	0	0.239/0.092	0.015	–

its polarization along x_2 ($= x'_1$) contributes to shear horizontal modes. From this picture, we see that the contributing bulk waves S_{slow} and in particular L have substantial displacement components u_1 along x_1 ($= x'_2$). On the other hand, it is easy to imagine that the out-of-plane displacement u_3 is not sensitive to the layer orientation because the fibers are always oriented normal to x_3 .

To complete our investigation, we now take also the bulk waves' relative amplitudes listed in Table 2.10 into account. The evanescent bulk waves L propagating at the top and bottom of the 0° layers have different amplitudes, while the other nonevanescent waves propagating up and downward in a layer have the same amplitude. We find that the amplitudes of the shear waves propagating in the 0° layers are by one order of magnitude smaller than the amplitudes of the shear waves propagating in the 90° layers. The corresponding relation between the longitudinal waves is less pronounced. Similar observations can be made for the bulk wave amplitudes in S_5 in $[0/90]_{2s}$, as listed in Table 2.11. Here, we notice also that the amplitudes are symmetric about the center line of the layup with only minor deviations. Hence, our discussion of the small displacement components u_1 in the 0° layers is confirmed by the evaluation of the bulk waves' amplitudes.

Seen from the NDI point of view, S_5 and B_{10} at 10 MHz·mm would be an unsuitable choice even if it would be possible to excite just these very modes with so many other higher order modes located nearby in the dispersion diagram. Through the size of a transducer, it has a phase velocity spectrum in addition to the well-known frequency spectrum spanned by the bandwidth around the center frequency. This results in a two-dimensional zone of excitation in a dispersion diagram rather than in a point of excitation [102, 151]. Throughout the whole laminate, S_5 and B_{10}

show a comparatively weak out-of-plane displacement u_3 , whereas a substantial displacement u_3 is essential for the detection of in-plane-flaws like delaminations. In Sec. 2.7.2, however, we will show that mode shapes can change drastically with the frequency-thickness product. Usually, the fundamental modes A_0/B_0 and S_0/B_1 at rather low frequency-thickness products are used for NDI purposes. For instance, Fig. 2.49(a) depicts the mode shape of A_0 at 0.4 MHz·mm for wave propagation along 0° in $[0/90]_{2s}$ SAERTEX[®]7006919/RIMR135. The prominent and homogeneous out-of-plane displacement is well-suited for most inspection tasks. For comparison, Fig. 2.49(b) shows how drastically the shape of A_0 has changed at 10 MHz·mm. While the two 90° layers in the center of the laminate experience a considerable displacement, the layers above and below remain almost undeformed, with remarkably sharp boundaries between both areas.

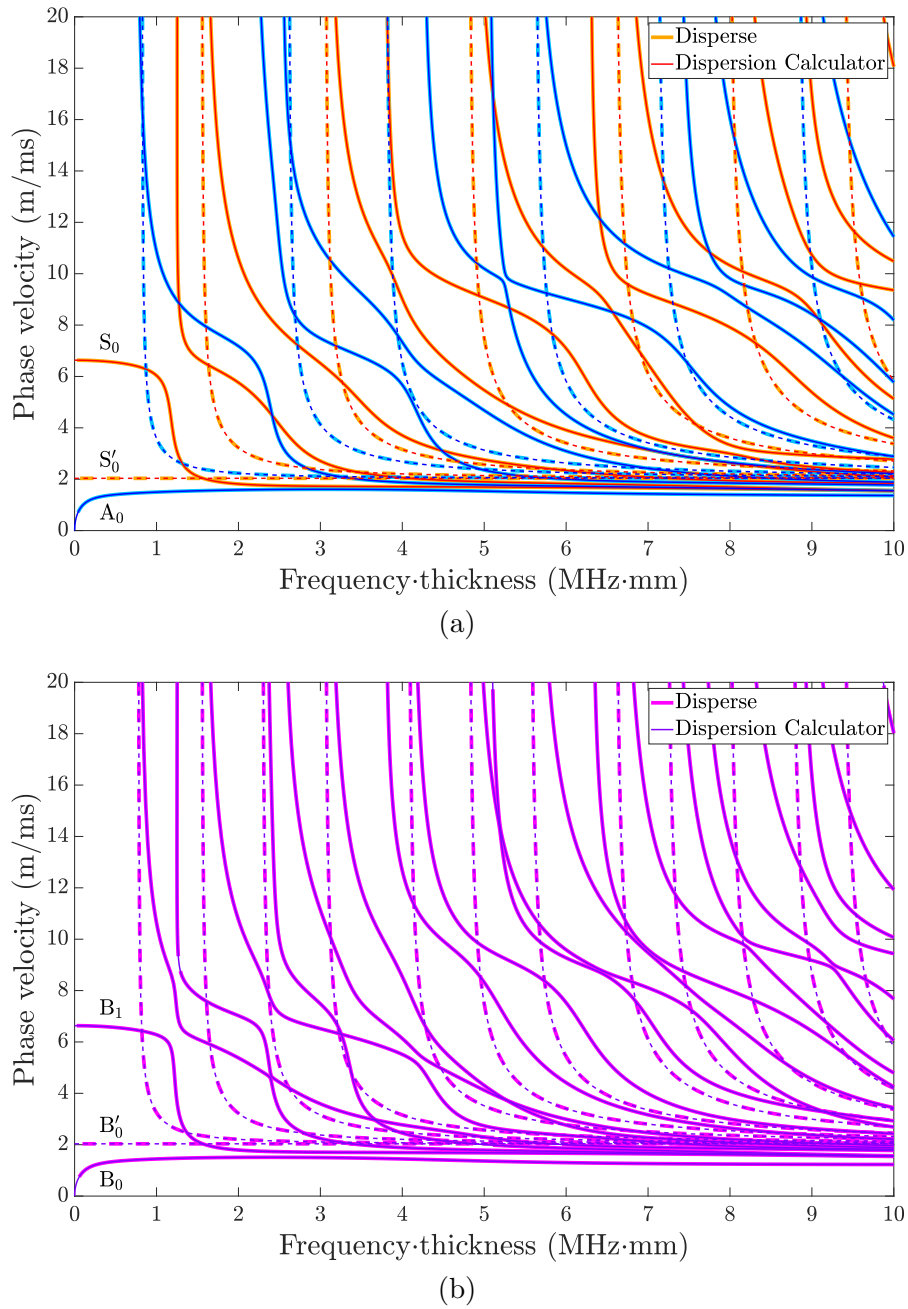


FIG. 2.46. Dispersion diagrams for wave propagation along 0° in two different layups of SAERTEX[®]7006919/RIMR135. (a) $[0/90]_{2s}$ layup. Lamb waves (solid lines) and shear horizontal waves (dashed lines) are decoupled, and can therefore be distinguished. Since the layup is symmetric, we can also classify symmetric (red/orange) and antisymmetric (blue) modes. (b) $[0/90]_4$ layup. Lamb and shear horizontal waves can be distinguished, but since the layup is nonsymmetric, so are the modes.

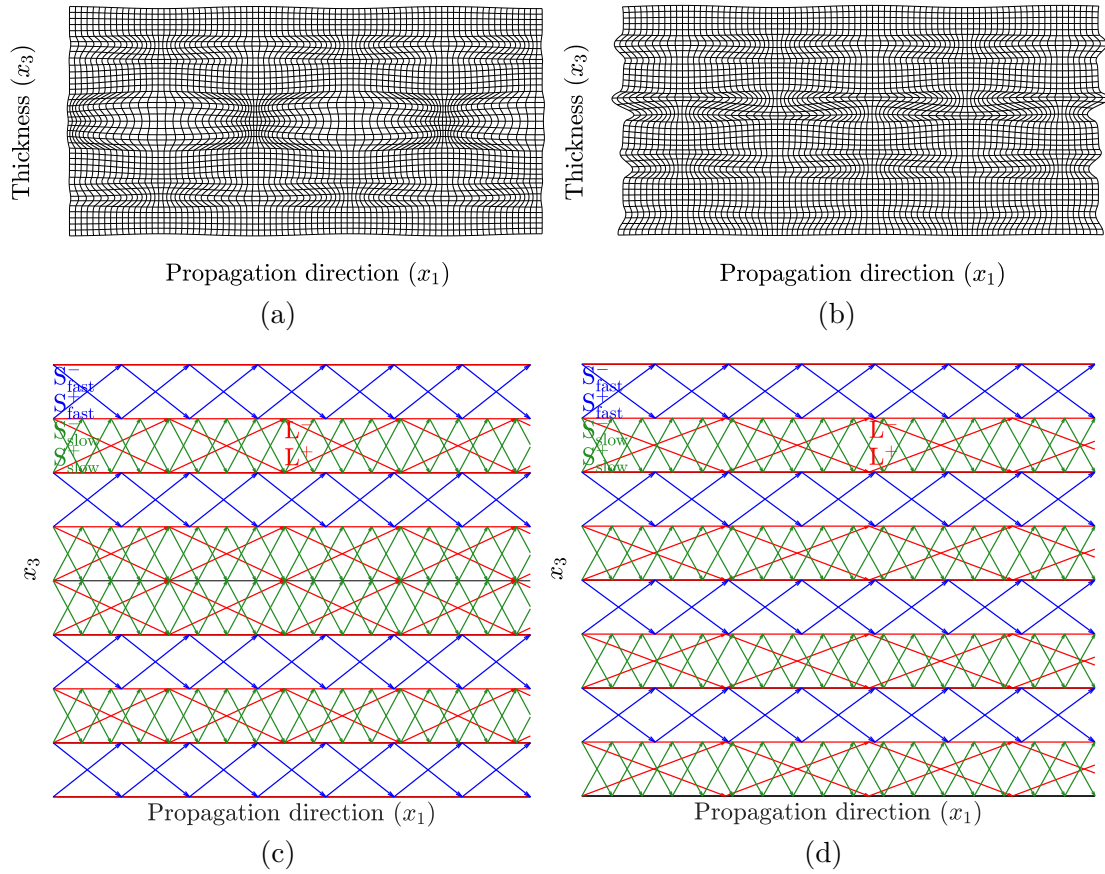


FIG. 2.47. Mode shapes and bulk wave patterns at 10 MHz-mm for wave propagation along 0° in SAERTEX[®]7006919/RIMR135. (a), (c) S_5 in $[0/90]_{2s}$. (b), (d) B_{10} in $[0/90]_4$.

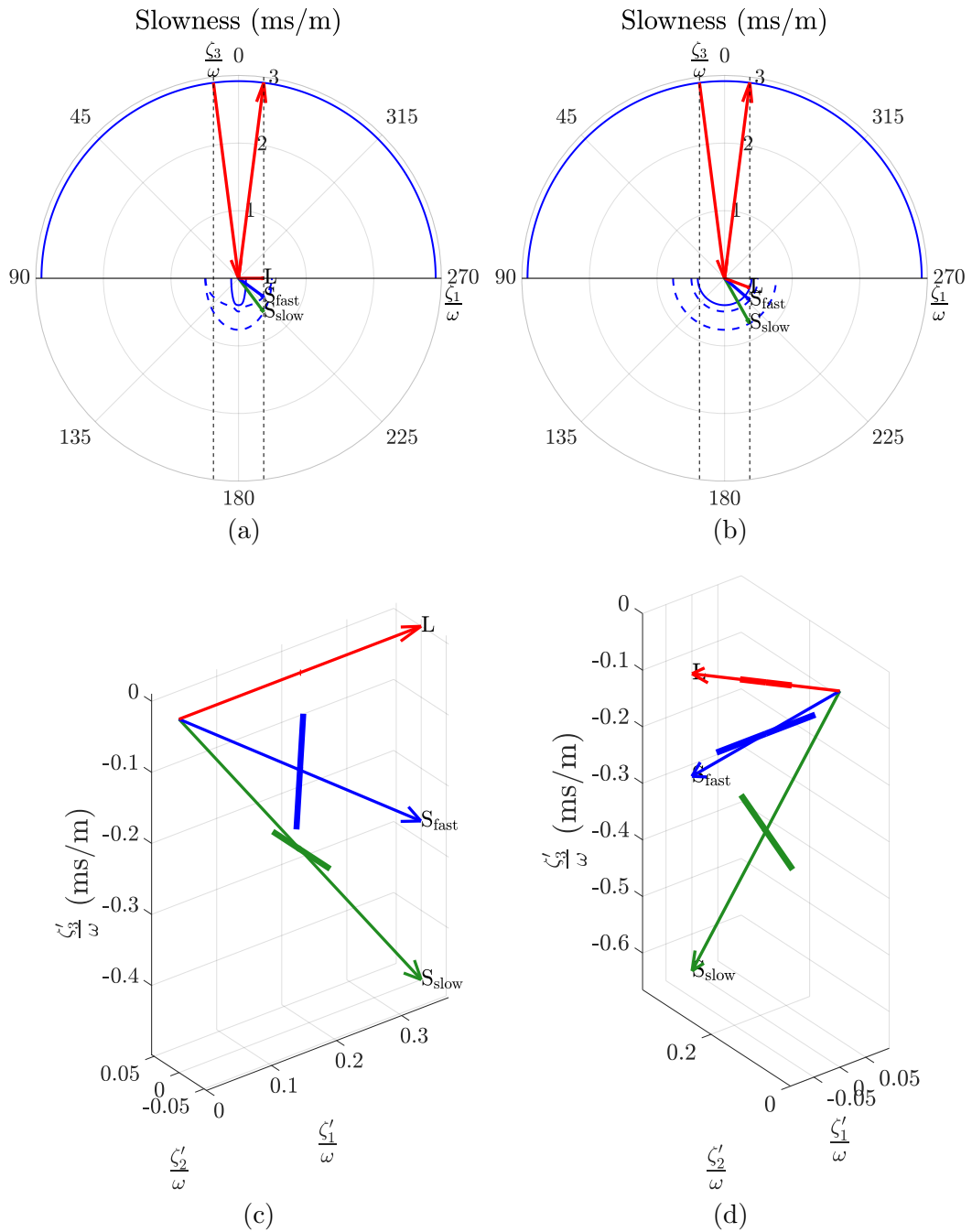


FIG. 2.48. Bulk waves generated in SAERTEX[®]7006919/RIMR135 upon plane wave incidence from air at $\Theta_{in} = 7.33^\circ$. (a), (c) $\Phi = 0^\circ$ and (b), (d) $\Phi = 90^\circ$. The upper half space is covered by air, the lower one by SAERTEX. (a), (b) Construction of the bulk wave propagation directions based on Snell's law. (b), (c) Propagation directions and polarization of the generated bulk waves in 3-D space.

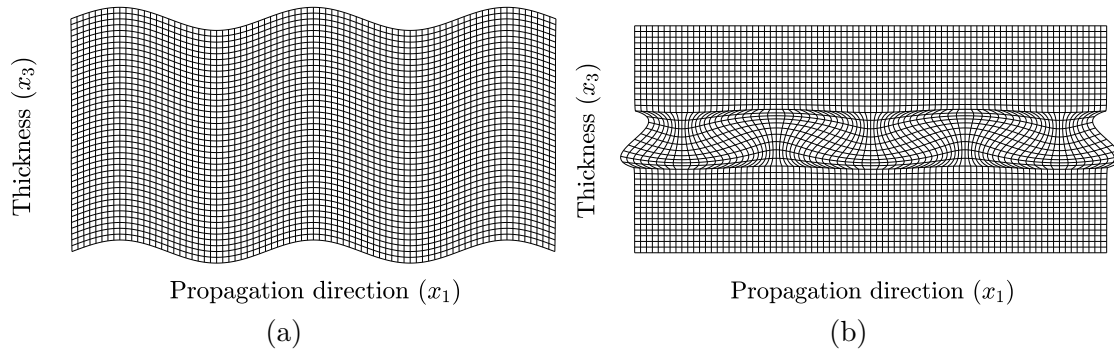


FIG. 2.49. Mode shapes of A_0 at (a) 0.4 MHz·mm and (b) 10 MHz·mm for wave propagation along 0° in $[0/90]_{2s}$ SAERTEX[®]7006919/RIMR135. The displacements are scaled up for clarity.

2.7.2 Guided Wave Characteristics

This section is of particular interest for any individual who performs NDI by means of guided waves. The section provides valuable knowledge which allows us to choose the appropriate mode for a certain inspection task. Firstly, we study dispersion diagrams in more detail. In fact, they allow more insight into the guided waves' characteristics and even into the behavior of the contributing bulk waves than one might think. Of particular interest are also the mode shapes. Guided waves turn out to have manifold shapes depending on the mode order and frequency. Hence, they are certainly worth dedicating a discussion to them not only because it is interesting, but also since the mode shapes determine whether a mode at a certain frequency can be used to detect flaws of specific shapes, positions, and orientations within a plate or layup. We will perform the corresponding study on an isotropic layer, knowing that the behavior in a transversely isotropic layer is qualitatively similar. For transversely isotropic samples on the other hand, we present the particularly interesting polar dispersion diagrams. This kind of diagram displays the anisotropy of guided wave propagation at a given frequency immediately, without the need for calculating multiple dispersion diagrams at different propagation angles.

Isotropic Layer

Figures 2.50(a) and 2.50(b) show the phase velocity of Lamb and shear horizontal waves as well as the longitudinal and transverse bulk velocities in aluminum alloy 1100. Let us start with a general examination of the dispersion diagrams. The fundamental antisymmetric Lamb wave A_0 starts at zero phase velocity while S_0 starts at the plate wave velocity of that material. Both fundamental modes tend

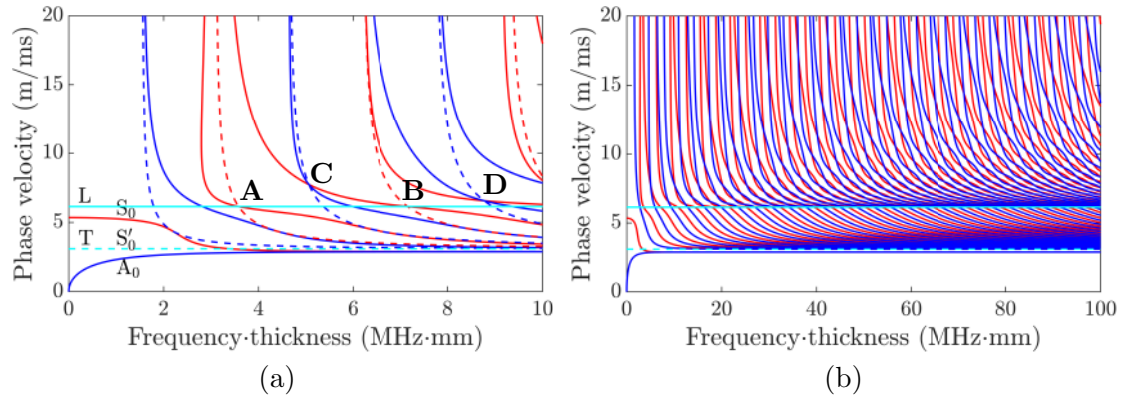


FIG. 2.50. Dispersion diagrams for aluminum alloy 1100. L and T indicate the longitudinal and transverse bulk velocities, respectively.

toward the Rayleigh wave velocity for high frequency-thickness products. The fundamental shear horizontal wave S'_0 is nondispersive at the transverse bulk velocity. The higher order modes start at their respective cut-off frequencies, and approach the transverse bulk velocity asymptotically. Lamb wave dispersion curves tend to “stay” longer at the longitudinal bulk wave velocity with increasing frequency-thickness products, thereby forming plateau-like shapes just above L. This effect is somewhat more pronounced for symmetric modes due to their more longitudinally dominated displacement patterns. Below the longitudinal and transverse bulk velocities, the corresponding bulk waves contributing to the guided waves become evanescent. Accordingly, A_0 always consists of evanescent waves only, while S_0 has propagating shear vertical wave contributors at low frequencies and thicknesses that become evanescent when S_0 falls below T. S'_0 consists of evanescent shear horizontal bulk waves propagating exactly at the transverse bulk velocity. Higher order modes never fall below T. Therefore, guided shear horizontal waves are never evanescent, which is exactly the reason why we do not encounter the numerical instability when we calculate them using the TMM, as discussed in Sec. 2.3.3. By contrast, higher order Lamb waves consist of propagating longitudinal and shear vertical bulk waves above L, and evanescent longitudinal and propagating shear vertical bulk waves below L.

Based on the dispersion diagram shown in Fig. 2.50(a), we would choose an ultrasonic transducer with a center frequency below 1 MHz·mm for the excitation of the fundamental modes. With increasing frequency-thickness, both modes A_0 and S_0 get closer to each other, increasing the unwanted risk that we excite both of them simultaneously. S_0 is more suitable for long range testing since it is less dispersive at low frequency-thicknesses than A_0 . A high dispersion means that the wave packets spread because the different frequency components propagate

at different speeds, resulting in a decrease of the amplitude with the propagation distance. On the other hand, A_0 allows a higher resolution due to its smaller wavelength, and, according to Castaings and Cawley [102], it is easier to excite thanks to the predominant out-of-plane displacement.

It is interesting as well as instructive for an NDI inspector to examine the mode shapes of guided waves in more detail since their displacement patterns allow direct conclusions whether or not a mode is appropriate for the flaw detection in a specimen. In Fig. 2.51, the modes shapes of the fundamental modes A_0 (left) and S_0 (right) are studied for increasing frequency-thickness products. While in A_0 , the top and bottom surfaces are displaced into the same direction x_3 , the opposite is the case for S_0 . Therefore, antisymmetric and symmetric modes are also called, respectively, *flexural* and *compressional* modes. At 1 MHz·mm (see Figs. 2.51(a) and 2.51(b)), we observe in A_0 a strong and quite evenly distributed out-of-plane displacement u_3 , while in S_0 , u_3 diminishes as we approach the center of the plate, rendering S_0 rather insensitive for in-plane flaws in the center. On the other hand, the in-plane displacement u_1 in A_0 vanishes at the half thickness, making A_0 insensitive there for out-of plane flaws like cracks. By contrast, S_0 would be a good choice to detect such flaws as it displays a substantial and evenly distributed displacement u_1 over the plate's thickness. Upon increasing the frequency or thickness of the plate, both displacement components get concentrated closer to the top and bottom surfaces, gradually turning the Lamb wave into two Rayleigh surface waves, as shown in Figs. 2.51(c) to 2.51(h). These waves are predestinated for the detection of surface or near-surface defects but they do not, however, interact with flaws located deeper in the specimen.

In Fig. 2.52, we perform a similar study on the higher order modes A_1 , S_1 , A_2 , and S_2 . On the left-hand side, A_1 (Figs. 2.52(a) and 2.52(c)) and A_2 (Figs. 2.52(e) and 2.52(g)) are displayed, and on the right-hand side are the symmetric counterparts. As the case in any resonance scenario, we expect a higher number of nodes occurring between the two boundaries confining the oscillation. Going back to A_0 and S_0 displayed in Fig. 2.51, we see that the left and right edges of the displacement patterns of A_0 describe one round trip 2π and those of S_0 one-and-a-half round trips 3π . Interestingly enough, A_1 and S_1 show the same characteristics. Only beginning with A_2 and S_2 , the number of round trips increases with the mode order, namely 4π and 5π , respectively. More nodes in both displacements u_1 and u_3 means that there are more areas throughout the thickness where the modes become insensitive to flaws. Figures 2.52(c) and 2.52(d) show A_1 and S_1 , and Figs. 2.52(g), 2.52(h) A_2 and S_2 at 20 MHz·mm. Accordingly, unlike the case for the fundamental modes, the higher order modes do not display a comparable behavior of turning into Rayleigh waves for high frequencies and thicknesses.

Finally, let us investigate specific points in the dispersion diagram in Fig. 2.50(a). Consider situations **A** and **B**. The Lamb waves S_1 and S_2 cross the longitudinal

TABLE 2.12. Bulk wave key data of A_2 and S_2 at 5.06 MHz·mm in 1 mm thick aluminum alloy 1100.

	A_2		S_2	
	L	SV	L	SV
Θ ($^\circ$)	52.48	23.55	52.59	23.59
v_p (m/ms)	6.142	3.094	6.142	3.094
λ (mm)	1.214	0.611	1.214	0.611
Relative amplitude	1	2.133	1	0.825
Phase L^-/SV^- ($^\circ$)	0	0	0	180
Phase L^+/SV^+ ($^\circ$)	180	180	0	180

bulk velocity L at 3.58 MHz·mm and, at twice that frequency-thickness product, at 7.16 MHz·mm, respectively. The corresponding mode shapes and bulk wave patterns are displayed in Figs. 2.53(a) to 2.53(d). Accordingly, the normal displacements u_3 at the upper and lower surface of the plate are zero, while only the longitudinal displacement u_1 is nonzero. As discussed above and shown in Figs. 2.53(c) and 2.53(d), the longitudinal bulk waves contributing to the guided waves turn evanescent below the longitudinal bulk velocity. Since shear wave motion is not supported in an assumed fluid surrounding the plate, the surfaces are traction free so that no energy gets lost to the surrounding medium but is retained by the guided wave. Such waves are highly suitable for long range applications like pipe inspection. This example demonstrates again how important it is for the inspector to have the corresponding dispersion diagram at hand. It allows him to choose the appropriate ultrasonic transducer and excite the desired mode at the optimal frequency. Similar traction free patterns can be achieved with A_2 at 5.06 MHz·mm (situation **C**) and with A_3 at 8.77 MHz·mm (situation **D**). These are the points where A_2 and A_3 cross S_2 and S_3 , respectively. Their mode shapes and bulk wave patterns are displayed in Figs. 2.53(e) to 2.53(h). In contrast to A_2 and A_3 , at these crossing points, S_2 and S_3 have zero longitudinal displacements u_1 at the plate's surfaces. By analyzing the bulk wave patterns, we can explain more physically how this behavior comes about.

The key data of the bulk waves in A_2 and S_2 at 5.06 MHz·mm are given in Table 2.12. Both modes have the same bulk wave patterns but different amplitudes and phases. The longitudinal wavelength is nearly twice the transverse one¹¹. In antisymmetric modes, the downward and upward propagating bulk waves have the

¹¹It is not exactly twice because 5.06 MHz·mm is not exactly where A_2 and S_2 cross each other, but our closest sample point. Notice also that the plate has a thickness of 1 mm.

opposite phase, while in symmetric modes they have the same phase. The special situation encountered in A_2 at $5.06 \text{ MHz}\cdot\text{mm}$ is that the longitudinal waves have the same phase as the shear vertical ones, apparently leading to a vanishing of u_3 at the plate's surfaces. In S_2 on the other hand, the longitudinal and shear vertical waves having the opposite phase lead to a vanishing of the longitudinal displacement u_1 at the surfaces. A similar constellation occurs in A_3 and S_3 at $8.77 \text{ MHz}\cdot\text{mm}$.

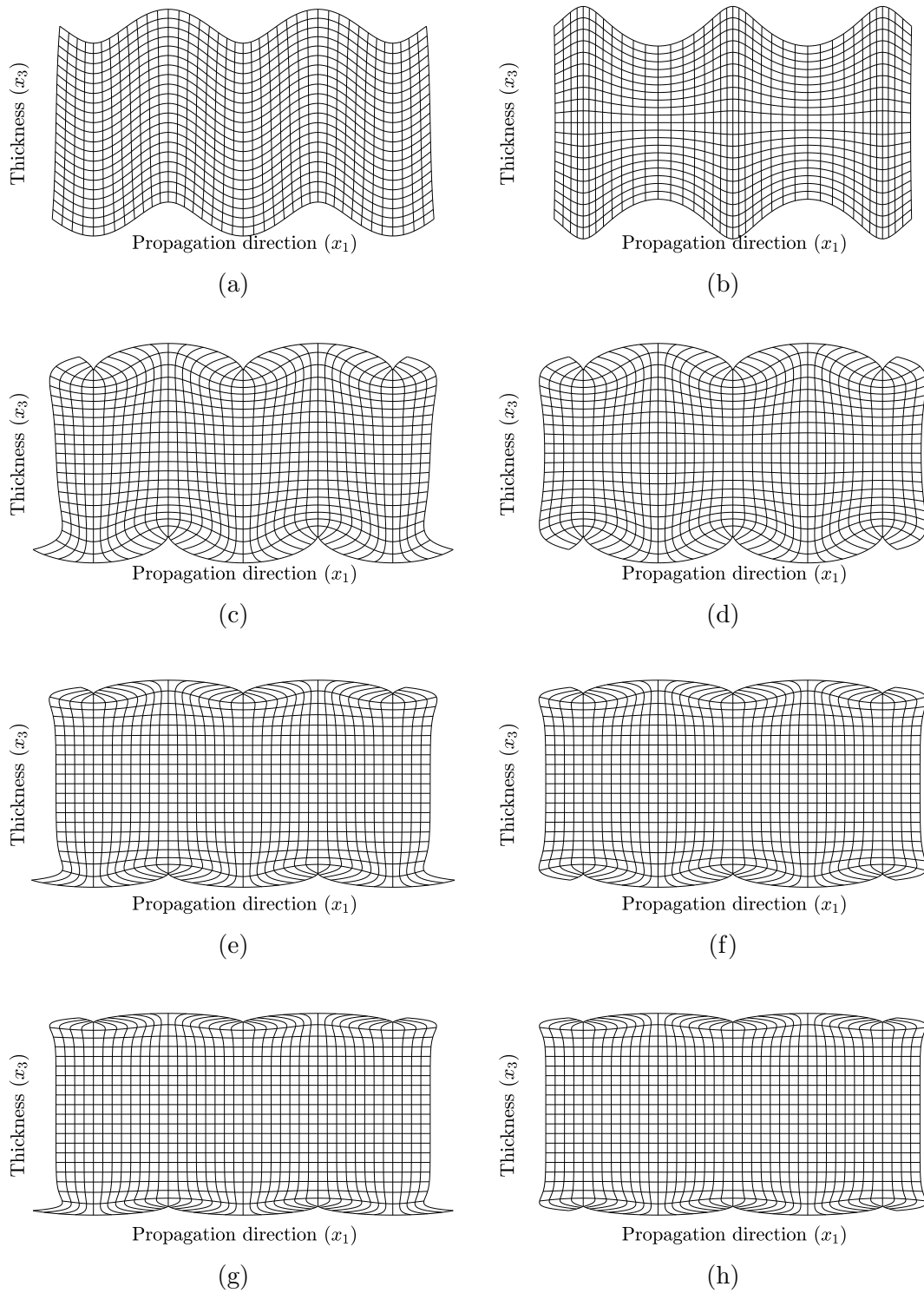


FIG. 2.51. Mode shapes of A_0 (left) and S_0 (right) at (a), (b) 1 MHz·mm, (c), (d) 10 MHz·mm, (e), (f) 20 MHz·mm, and (g), (h) 30 MHz·mm in aluminum alloy 1100. The displacements are highly exaggerated for clarity.

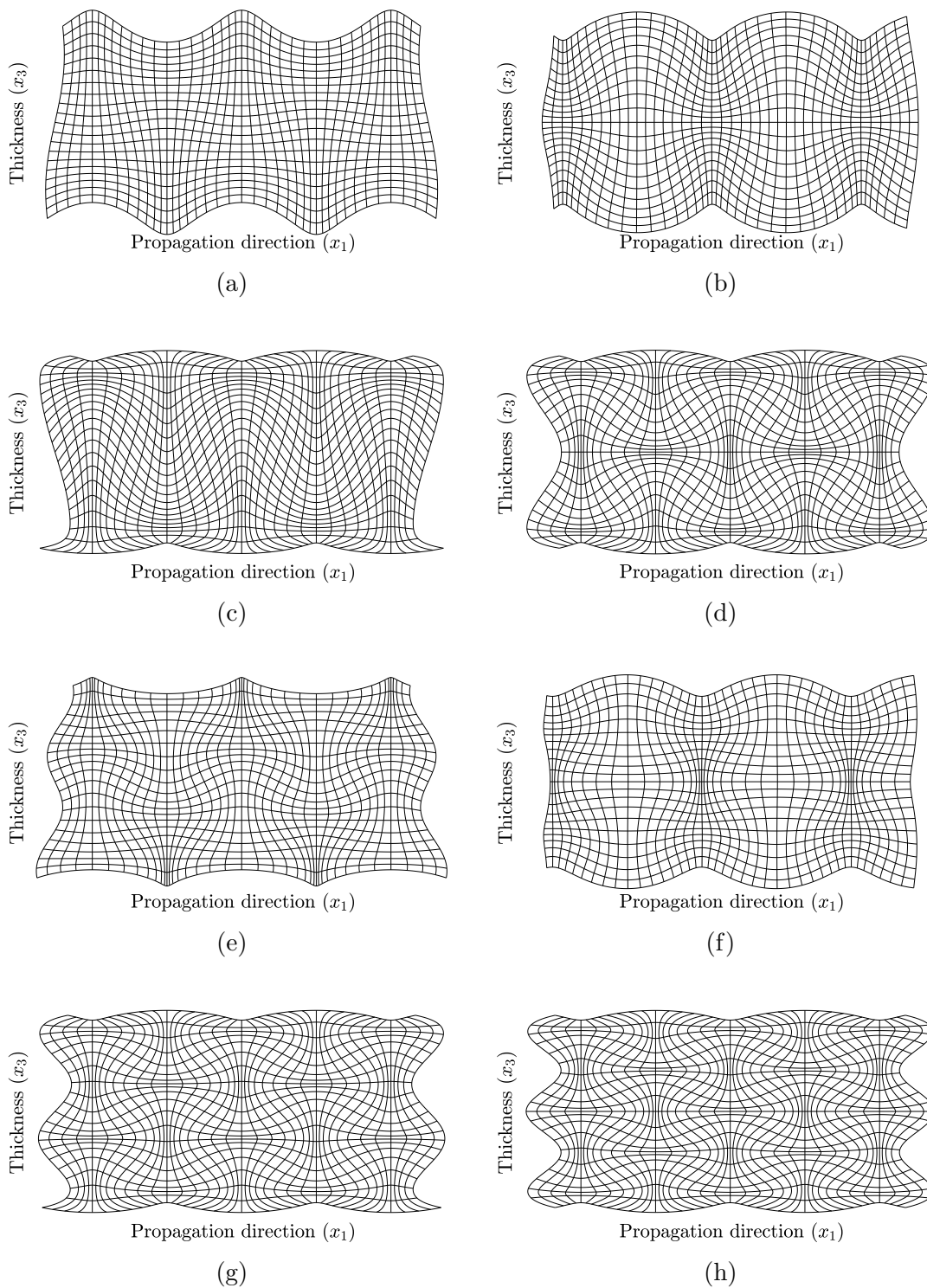


FIG. 2.52. Mode shapes of (a) A_1 and (b) S_1 at $3 \text{ MHz}\cdot\text{mm}$, (c) A_1 and (d) S_1 at $20 \text{ MHz}\cdot\text{mm}$, (e) A_2 and (f) S_2 at $6 \text{ MHz}\cdot\text{mm}$, and (g) A_2 and (h) S_2 at $20 \text{ MHz}\cdot\text{mm}$ in aluminum alloy 1100.

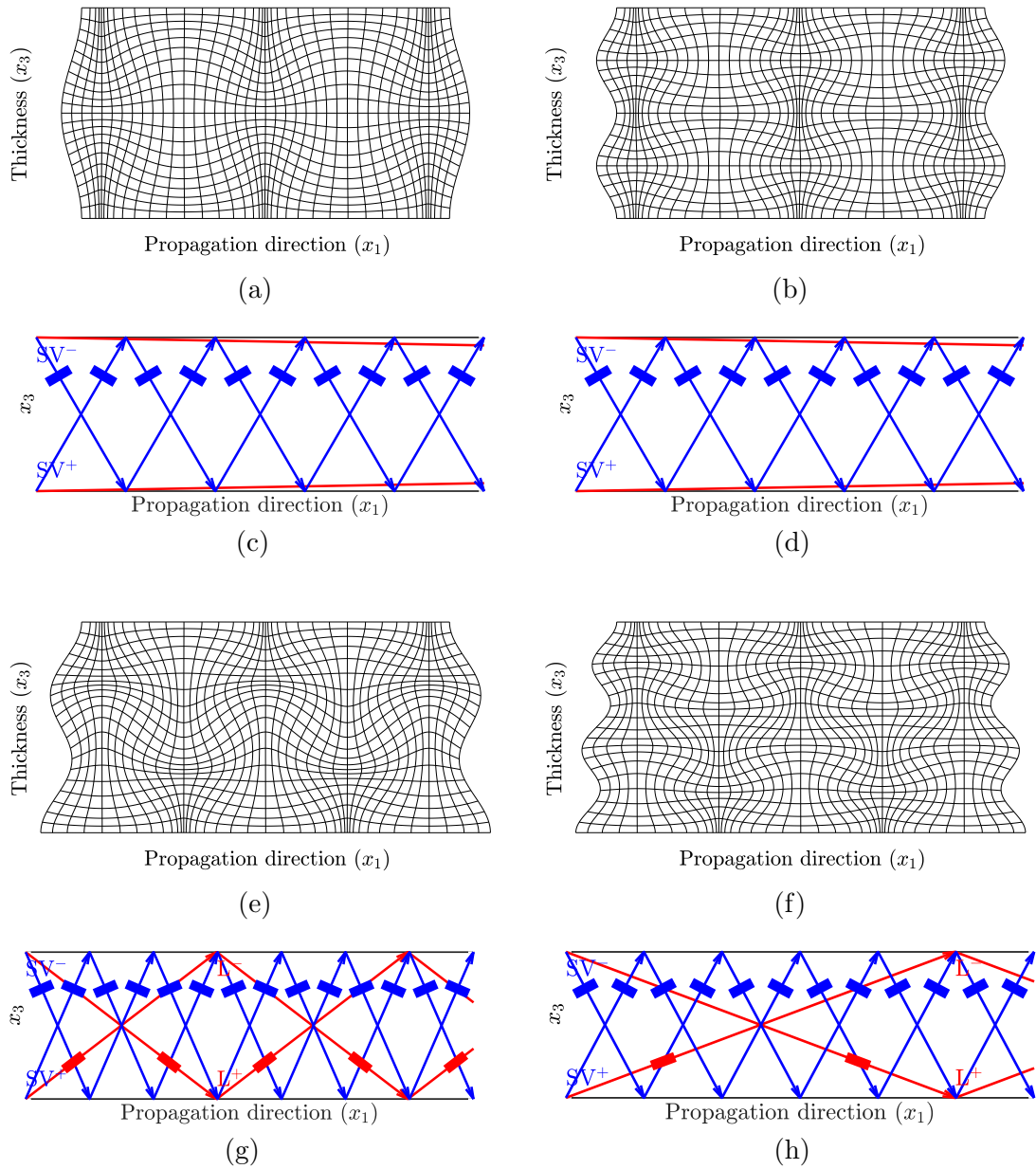


FIG. 2.53. Mode shapes and bulk wave patterns of (a), (c) S_1 at 3.58 MHz·mm, (b), (d) S_2 at 7.16 MHz·mm, (e), (g) A_2 at 5.06 MHz·mm, and (f), (h) A_3 at 8.77 MHz·mm in aluminum alloy 1100. The bold lines indicate the polarization directions of the longitudinal (red) and shear vertical bulk waves (blue).

Transversely Isotropic Layer and Layups

Figures 2.54(a) to 2.54(d) show the phase velocity of Lamb and shear horizontal waves as well as the bulk velocities for wave propagation along, respectively, 0° , 30° , 60° , and 90° in unidirectional SAERTEX[®]7006919/RIMR135. Beside the obvious anisotropy, the most striking difference to the dispersion diagram of aluminum alloy 1100 in Fig. 2.50(a) is the particular proximity of (most of) the symmetric modes to the longitudinal bulk velocity over broad frequency-thickness ranges. This behavior indicates that in these ranges the symmetric modes are dominated by longitudinal displacement u_1 in case of wave propagation along 0° and u_1 and u_2 in case of 30° and 60° wave propagation. For wave propagation along 90° , we do not observe such a plateau-like behavior, supposedly because the fast and slow shear bulk velocities are rather close to the longitudinal velocity. Antisymmetric modes with their more dominant normal displacement u_3 show much less plateau-like behavior around the longitudinal velocities in all dispersion diagrams. Similarly as in aluminum, the plateaus are more likely to appear with increasing frequency-thicknesses. As pointed out in Sec. 2.7.2, Lamb waves excited in such low-dispersive frequency-thickness ranges are particularly suitable for long range inspection tasks. We can also identify specific points in the dispersion diagrams where the corresponding modes have no normal displacement, making them suitable for long range testing, too. For instance, S_1 in Fig. 2.54(a) crosses the longitudinal bulk velocity at 2.4 MHz·mm, having no normal displacement and, in addition, being practically nondispersive. Accordingly, S_1 would be a very good candidate for long range inspection. However, although S_0 has some normal displacement (see Fig. 2.55(a)) at 0.4 MHz·mm, it would be an even better choice because there are no other modes nearby in the dispersion diagram.

It is particularly interesting to analyze the propagation direction dependent dispersion in a single layer or layup. For a polar dispersion diagram, the dispersion curves are traced in the frequency space as usual. This is done for every propagation angle from zero to ninety degrees (or to 360° if necessary) with a certain step. Usually, only the fundamental modes are considered for this kind of diagram. In principle, one could just calculate the phase velocity at the frequency of interest if one was interested only in the phase velocity and excitation angle. However, to get the group velocity and propagation time, we need complete curves for the fitting and derivation, as explained in Sec. 2.3.6. Furthermore, if the phase velocity is calculated at just one frequency, it is difficult to assign the found solutions to the correct mode, since the modes can cross each other. This risk increases with the frequency-thickness product.

Figure 2.56(a) shows the propagation direction-dependent phase velocities of the three fundamental modes S_0 , S'_0 , and A_0 in unidirectional SAERTEX[®] 7006919/RIMR135 at 0.4 MHz·mm together with the bulk waves' phase velocities. It is

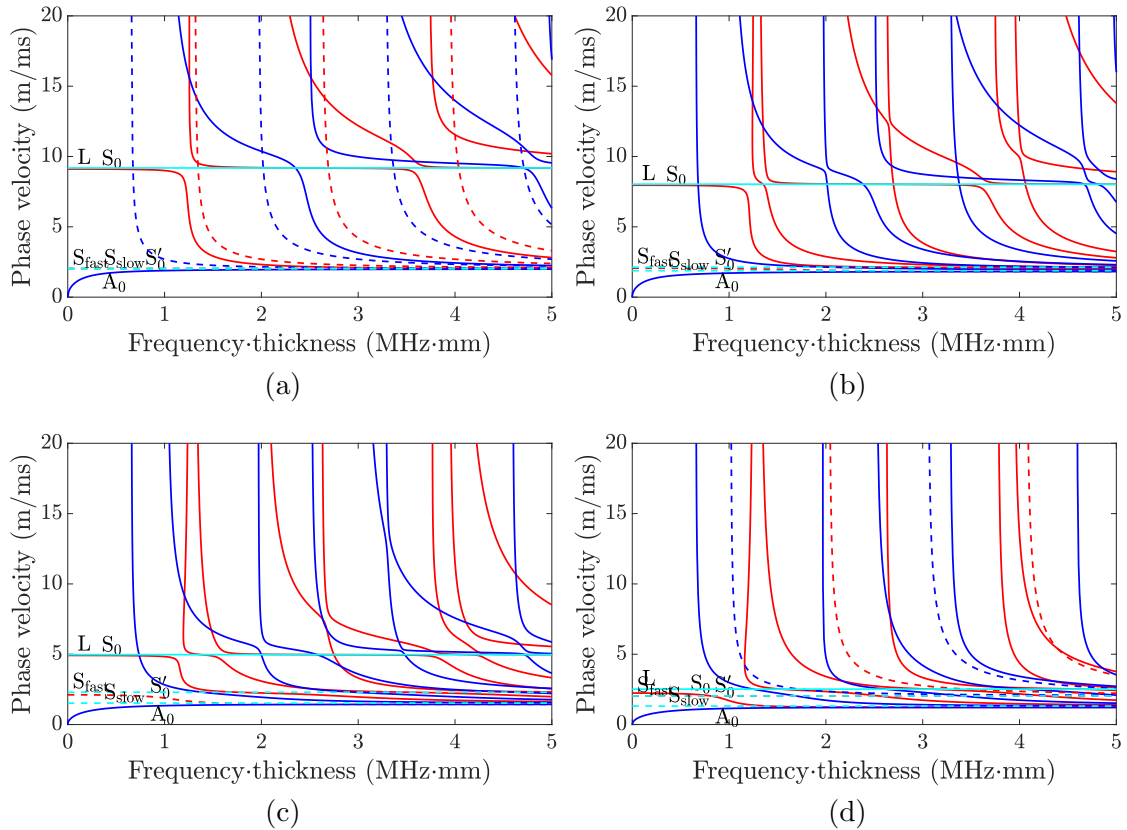


FIG. 2.54. Dispersion diagrams for wave propagation along (a) 0° , (b) 30° , (c) 60° , and (d) 90° in unidirectional SAERTEX[®]7006919/RIMR135. The light blue lines indicate the bulk waves' phase velocities.

striking how directly the anisotropic behavior of the guided waves is linked to the bulk velocities, especially in the case of S_0 . Calculating the through thickness displacement components of S_0 at $0.4 \text{ MHz}\cdot\text{mm}$ for 0° wave propagation, as shown in Fig. 2.55(a), reveals that S_0 is dominated by longitudinal displacement. Hence, the phase velocity of S_0 is close to that of the pure longitudinal bulk wave. In contrast, at $2 \text{ MHz}\cdot\text{mm}$, Fig. 2.55(b) shows that S_0 is dominated by normal displacement. Consequently, its phase velocity is close to that of the pure fast (and slow) shear bulk wave, as confirmed by Fig. 2.56. It is also noteworthy that the phase velocity variation with the propagation direction of A_0 is very weak compared to that of S_0 . The reason for this is because A_0 is dominated by normal displacement, which points normal to the fibers (out-of-plane) for any (in-plane) propagation direction. This is of course different for the longitudinal displacement, encountering the strong in-plane anisotropy. Figure 2.56(b) displays the group velocity. Since S_0 and S'_0 are only weakly dispersive at $0.4 \text{ MHz}\cdot\text{mm}$, their group and phase velocities

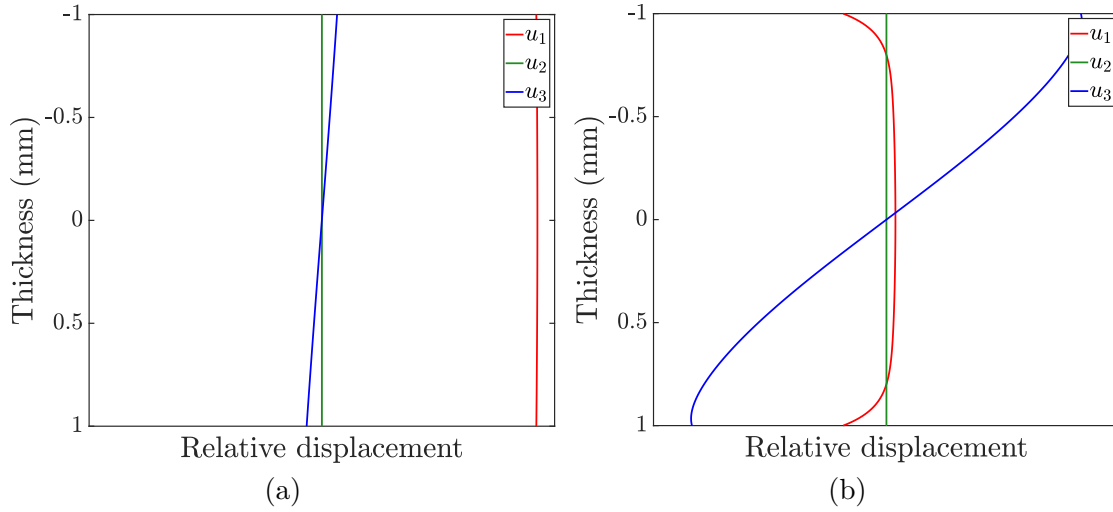


FIG. 2.55. Through thickness displacement components of the fundamental Lamb wave mode S_0 at (a) $0.4 \text{ MHz}\cdot\text{mm}$ and (b) $2 \text{ MHz}\cdot\text{mm}$ for wave propagation along 0° in unidirectional SAERTEX[®] 7006919/RIMR135.

are almost coincident, unlike the case for A_0 . A_0 is almost perfectly matching the slow shear bulk wave velocity. This will be the case with its phase velocity only at higher frequencies. The inverse character of both the propagation time and the excitation angle with respect to the phase velocity becomes obvious in Figs. 2.56(c) and 2.56(d).

It is also very instructive to compare the phase velocity diagram in Fig. 2.56(a) with the polar plot of the transformed stiffness matrix components given in Fig. 2.2. Although up to thirteen nonzero transformed stiffness matrix components (we remember that the transformed stiffness matrix of a transversely isotropic layer has monoclinic symmetry) contribute to the behavior of the phase velocity, it is obvious that S_0 is predominantly governed by C_{11} and C_{22} . Figure 2.57(a) depicts the polar phase velocity diagram of a $[0/90]_{4s}$ layup at $0.4 \text{ MHz}\cdot\text{mm}$. Comparing this diagram with the HST components displayed in Fig. 2.3(a), reveals an even better qualitative coincidence. Again, S_0 is dominated by C_{11} and C_{22} , as expected, while of the drawn HST components, C_{12} appears to have the most influence on the behavior of S'_0 , while A_0 behaves similarly as the coinciding C_{55} and C_{23} . Finally, Fig. 2.57(b) displays the phase velocity diagram corresponding to a quasiisotropic layup $[0/90/45/-45]_{2s}$ at $0.4 \text{ MHz}\cdot\text{mm}$. The same correlations between the HST components and the phase velocity are evident by comparing Fig. 2.57(b) with Fig. 2.3(b).

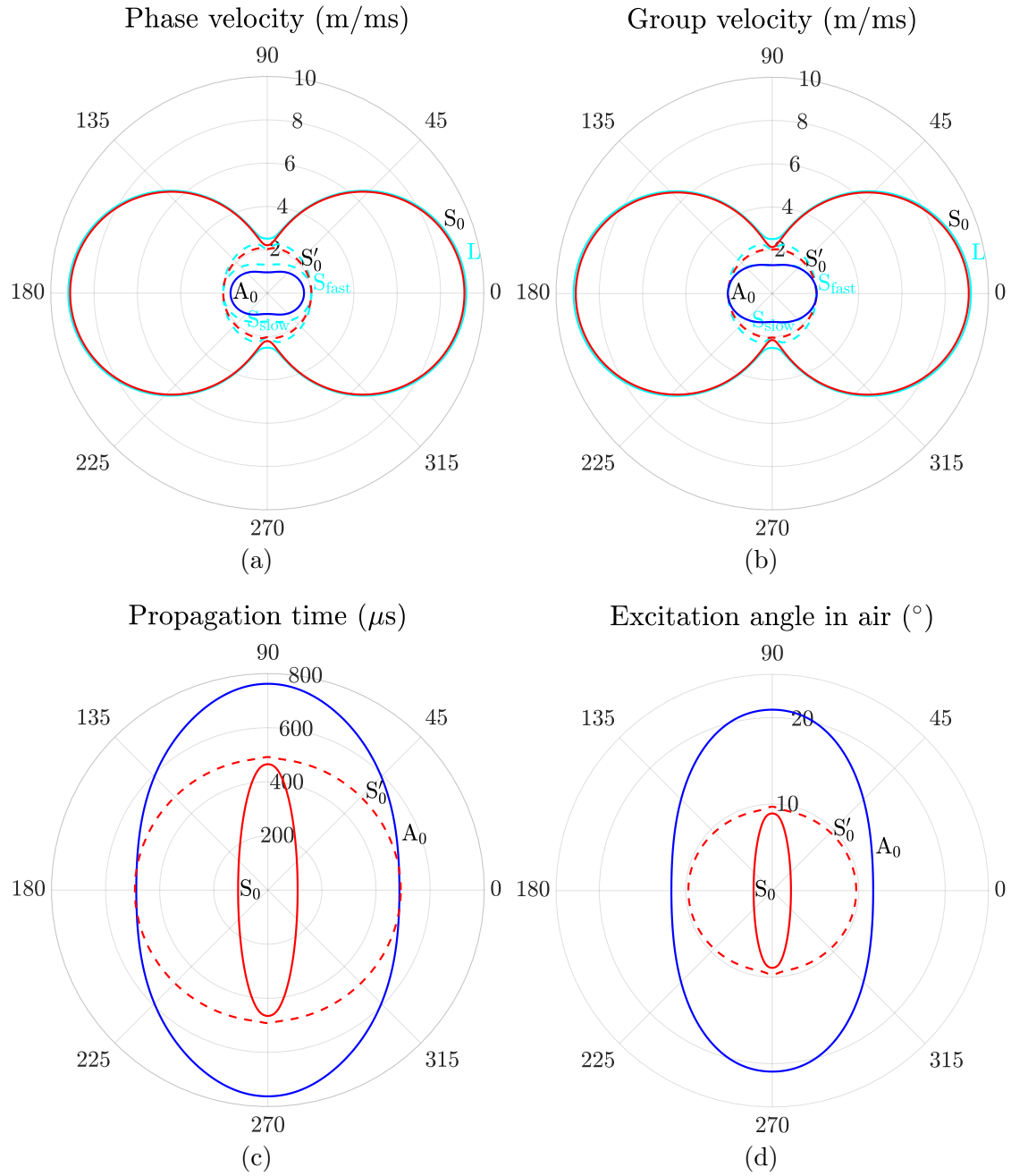


FIG. 2.56. Polar dispersion diagrams of the fundamental modes in unidirectional SAERTEX[®]7006919/RIMR135 at 0.4 MHz-mm. (a) Phase velocity, (b) group velocity, (c) propagation time at 1 m distance, and (d) Excitation angle in air. In images (a) and (b), the three bulk waves' phase velocities are drawn in light blue color.

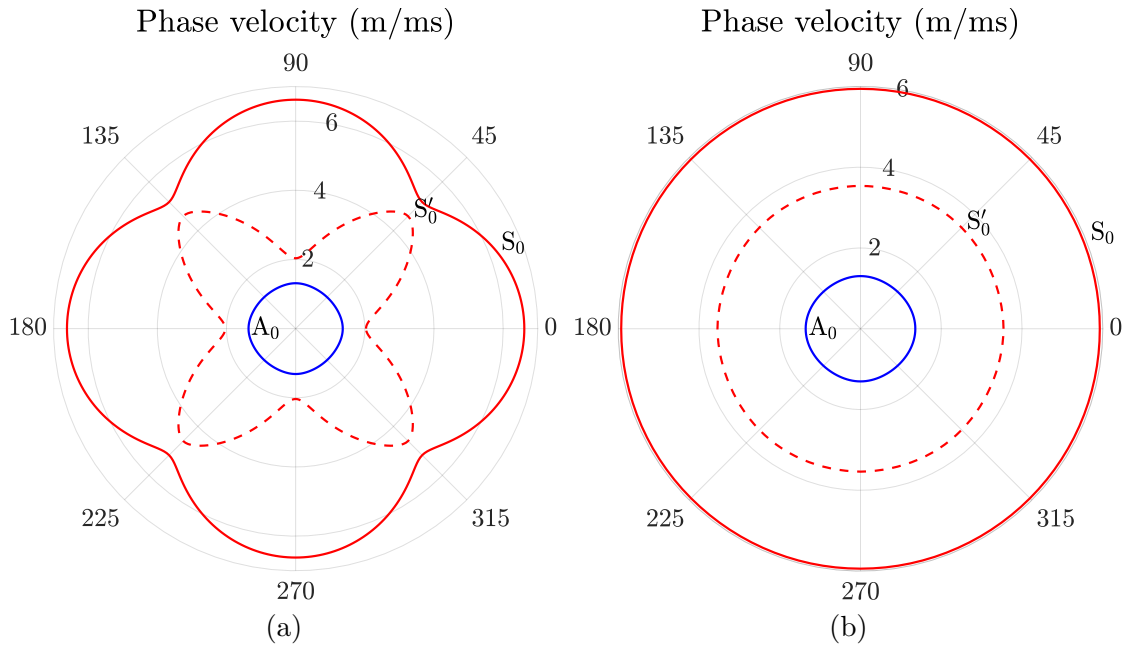


FIG. 2.57. Phase velocity of the fundamental modes in SAERTEX[®]7006919/RIMR135 at 0.4 MHz·mm. (a) $[0/90]_{4s}$ and (b) $[0/90/45/-45]_{2s}$ layup.

2.7.3 Large Numbers of Layers

The key requirement imposed on the DC is the capability to calculate laminates consisting of four hundred layers. These are the largest specimens we have encountered so far in the rocket booster manufacturing at the DLR in Augsburg. In the current section, we prove that the DC meets this key requirement. For this purpose, we assume two thick-walled layups. For convenience, the wave propagation in both layups is supposed to be along the 0° -direction. Firstly, we calculate a 50 mm thick $[0/90/45/-45]_{50s}$ layup, containing four hundred layers. This layup poses the challenging obstacle to the tracing algorithms that Lamb waves and shear horizontal waves are coupled so that we have to face the crossing of dispersion curves. Secondly, we model a 125 mm thick $[0/90]_{250s}$ layup, containing one thousand layers. With the decoupling of the Lamb and shear horizontal waves, the crossing of modes is absent, and therefore the tracing becomes much easier. The corresponding dispersion diagrams are shown in Figs. 2.58(a) and 2.58(b), respectively.

By analyzing the displacement components of various modes in both layups, we make an interesting observation. Comparing the displacement of A_2 in $[0/90/45/-45]_{50s}$ (see Fig. 2.58(c)) with A_1 in $[0/90]_{250s}$ (see Fig. 2.58(d)), both at 5 MHz·mm, shows that both modes have practically the same shape. In particular, the shear

horizontal displacement component u_2 of A_2 in $[0/90/45/-45]_{50s}$ nearly vanishes, making A_2 almost a pure Lamb wave like A_1 in $[0/90]_{250s}$. Also, the dispersion curves of both modes have a comparable shape. It turns out that each mode in Fig. 2.58(a), let us call them *quasipure* modes, has its *true* pure counterpart in Fig. 2.58(b). Let us pick an example for a quasipure shear horizontal mode, namely A_4 in $[0/90/45/-45]_{50s}$. Its sagittal displacement components u_1 and u_3 , depicted in Fig. 2.58(e), are close to zero while its u_2 -component has the typical shape of a shear horizontal mode, as the case in the true pure counterpart, the shear horizontal wave A'_2 in $[0/90]_{250s}$, drawn in Fig. 2.58(f). Again, we see in the dispersion diagrams that both dispersion curves have a comparable shape. Dispersion curves of pure shear horizontal modes never have plateaus and turning points unlike those of Lamb waves. We notice also that the fundamental shear horizontal mode S'_0 in Fig. 2.58(a) is nondispersive, as usually the case only in decoupled cases. To further investigate our observation, we approximate the $[0/90/45/-45]_{50s}$ layup by $[0/90/45/-45]_{5s}$, having only forty layers with ten times the original layer thickness. The corresponding displacement profiles of A_2 and A_4 are shown in Figs. 2.59(a) and 2.59(b), respectively. Accordingly, A_2 now has a substantial shear horizontal displacement component u_2 , shifting it far from a pure Lamb-type behavior. Similarly, A_4 now has notable sagittal displacement contributions u_1 and u_3 , putting it away from the characteristics of a pure shear horizontal mode.

The phenomenon of quasipure coupled modes reported here is related to the homogenization of periodically layered laminates. Rokhlin provides a detailed discussion about this topic in his book [59], chapter 7. Accordingly, if the wavelength of the bulk waves, which the guided wave is composed of (also referred to as *Floquet waves*), is large compared to the layer thickness, the effect of the layering is negligible. Then, the laminate behaves like an effective medium with averaged elastic properties. Physically, the bulk waves do not “feel” the anisotropy anymore, and the coupling between them becomes small. This is the case only in the *homogenization domain* located below a certain critical frequency f_{crit} . Rokhlin approximates this frequency with

$$f_{\text{crit}} = \frac{0.5v_{\min}(\Theta_{\text{in}})}{d_{\text{uc}} \cos \Theta_{\text{in}}}, \quad (2.227)$$

where d_{uc} is the thickness of the unit cell, and $v_{\min}(\Theta_{\text{in}})$ is the minimum phase velocity among all bulk waves in each layer of the unit cell excited at an incidence angle Θ_{in} in the fluid. Clearly, the modeling of a large laminate by one effective layer in the homogenization domain would be very worthwhile considering that the calculation of the dispersion diagram for the $[0/90/45/-45]_{50s}$ laminate in Fig. 2.46(a) took many hours, whereas for one layer it takes only some seconds. However, Rokhlin states in his book that “even at relatively modest frequencies in commercially important composite layup geometries, a full consideration of lami-

nate microstructure is essential for the accurate description of guided elastic wave behavior in these materials.”.

Driven by this statement, we turn our focus to another approximative method for periodic laminates, which is not burdened by a limited frequency range, namely the grouping of layers. The idea is to model a certain number of repetitions of a unit cell by a single unit cell with the layer thicknesses scaled by the number of repetitions so that the resulting unit cell has the same thickness as the total of the repeated original unit cells. The benefit is, of course, the saving of computational expense achieved through the reduction of the number of layers to be computed. In the following, we determine how good the dispersion curves match if we reduce the number of layers by a factor of ten, and how much computation time is saved.

We approximate the $[0/90]_{250s}$ layup by $[0/90]_{25s}$, having only one hundred layers with ten times the original layer thickness. We perform the calculation with the DC v1.4 running on an i7-6700 CPU at 4×3.4 GHz. The calculation of the full laminate took 31 min, compared to 5.6 min for the approximation - a saving of 82%. Figure 2.60 compares the Lamb wave dispersion curves of the full laminate, drawn in red color, with those of the approximative model, drawn in blue color. Apparently, the approximative laminate fits the full laminate relatively well, especially in case of the fundamental modes. Only for some of the higher order modes at high phase velocities, we observe notable deviations. In an earlier study presented by Huber and Sause [63], a $[0/90/45/-45]_{50s}$ layup was approximated by $[0/90/45/-45]_{10s}$, having one fifth of the original number of layers. In this study, the calculation time was reduced by 85% (from 101 min to 15 min). The fundamental modes were fitted quite well, too, while somewhat more deviation on the higher order modes was observed.

Hence, provided a layup allows for the grouping of layers, this can be an appropriate approach to obtain dispersion curves with minimized computational expense, in particular if one is only interested in the fundamental modes, as usually the case in NDI applications. However, as was already mentioned above, the grouping of layers usually cannot be applied in typical thick-walled components used at the DLR since the layups are often too complicated.

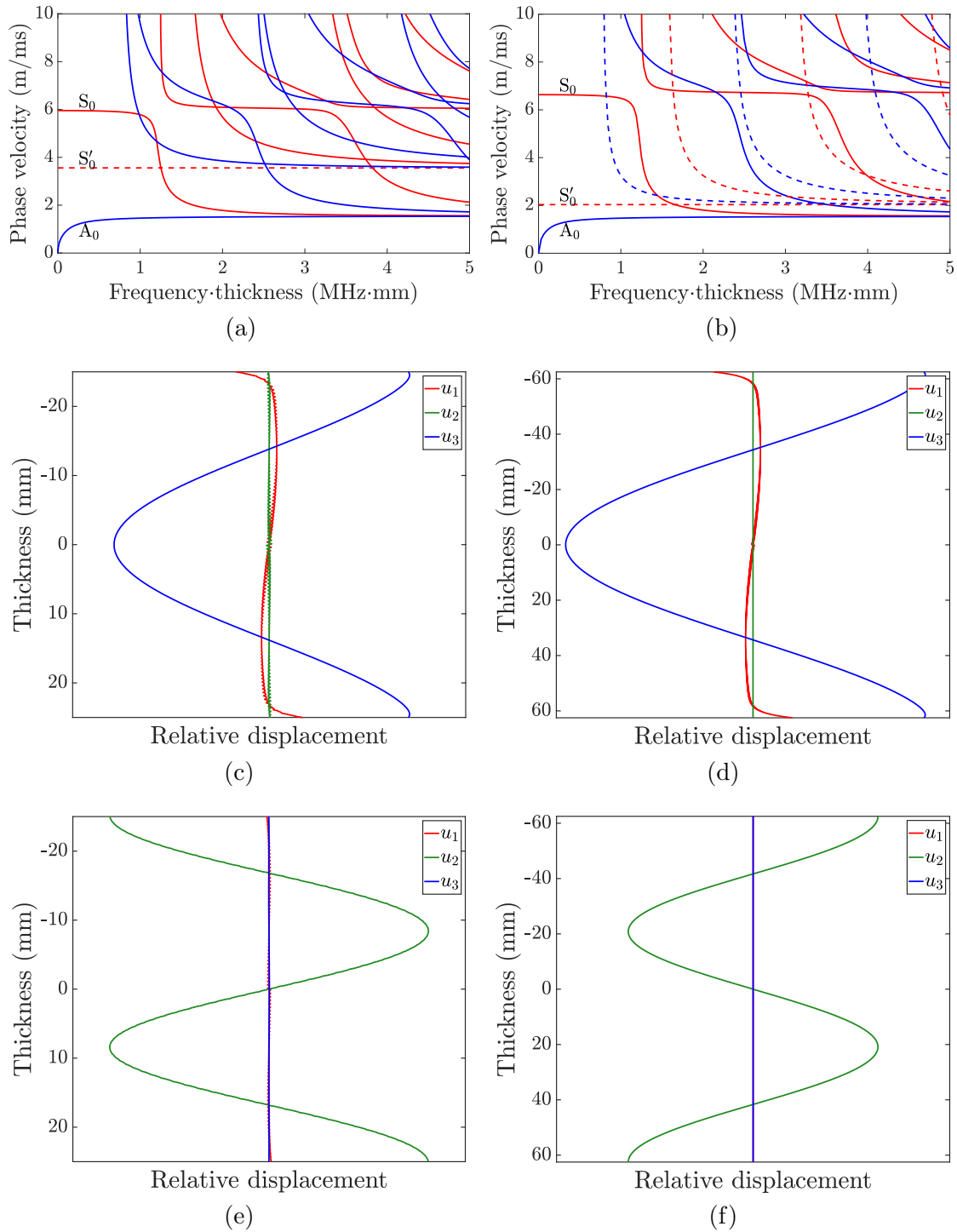


FIG. 2.58. Dispersion diagrams for wave propagation along 0° in (a) 50 mm thick $[0/90/45/-45]_{50s}$ and (b) 125 mm thick $[0/90]_{250s}$ SAERTEX[®] 7006919/RIMR135. Through thickness displacement profiles of (c) A_2 in $[0/90/45/-45]_{50s}$, (d) A_1 in $[0/90]_{250s}$, (e) A_4 in $[0/90/45/-45]_{50s}$, and (f) A'_2 in $[0/90]_{250s}$ at 5 MHz·mm.

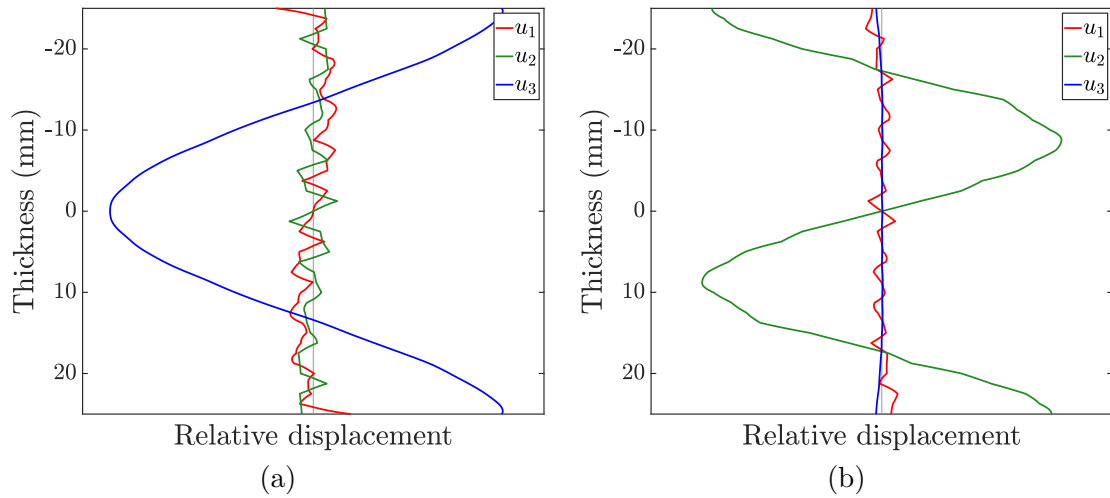


FIG. 2.59. Through thickness displacement profiles of (a) A_2 and (b) A_4 for wave propagation along 0° in 50 mm thick $[0/90/45/-45]_{5s}$ SAERTEX[®]7006919/RIMR135.

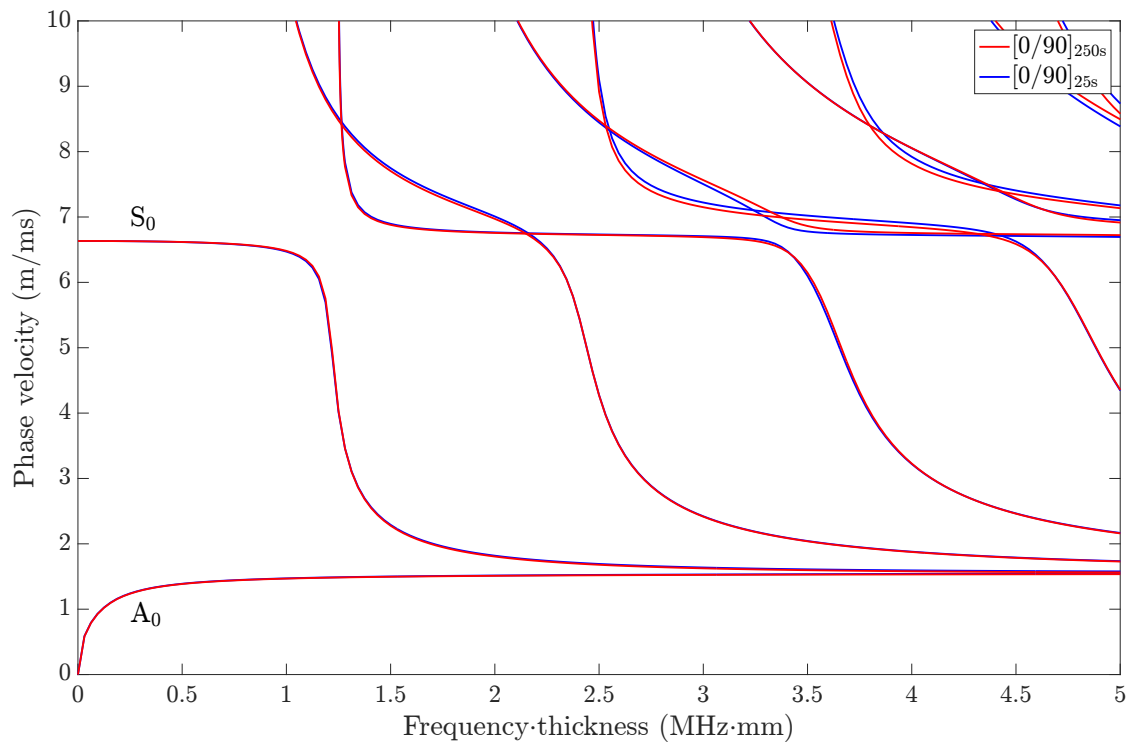


FIG. 2.60. Lamb wave dispersion diagram for wave propagation along 0° in 125 mm thick $[0/90]_{250s}$ (red) and $[0/90]_{25s}$ (blue) SAERTEX[®]7006919/RIMR135. The approximative model (blue) deviates notably from the full model (red) only for some higher order modes at high phase velocities.

3 Air-coupled Ultrasonic Inspection

In this chapter, we present the nondestructive inspection method of air-coupled ultrasonic testing by means of Lamb waves. This is the application for which we need the dispersion diagrams obtained by the methods presented in Chapter 2. Specifically, the excitation of a Lamb wave mode requires the adjustment of the correct excitation angle with respect to the component to be inspected. The excitation angle is yielded from the corresponding dispersion diagram via Snell's law. However, real components like aircraft skin elements have variations both in the layup as well as in the curvature, causing a variation also in the excitation angle. Therefore, the aim of the Procomp project was the development of a robotic end-effector, which adapts the excitation angle on-the-fly during the scanning of a component according to an a priori calculated *excitation angle map* (EAM). To pave the track for this new end-effector, we first discuss and compare the different measurement modes in Sec. 3.1, namely the *normal transmission mode* (NTM) and the *focused slanted reflection mode* (FSRM), where only the latter works through the excitation of Lamb waves. Finally, Sec. 3.2 presents the AEE and the corresponding new inspection mode, the *adaptive slanted reflection mode* (ASRM), which clearly outperforms the conventional nonadaptive FSRM.

3.1 Fundamental Concepts and Application

Aerospace vehicles are constructed from an increasing amount of CFRP because its superior strength-to-weight ratio compared to traditional metal alloys yields weight savings that enable these vehicles to operate more efficiently. However, the manufacturing of composites is still very expensive due to the high amount of handcraft that is involved and due to the usage of high-performance but also high-cost prepreg material. Therefore, it is the aim of the ZLP to establish automated and cost-efficient manufacturing processes for large-scale and light weight aerospace vehicle components made from CFRP (see Fig. 3.1). This is accompanied by the goal to enable infusion processes for large structures at high performance and moderate cost.

In order to guarantee cost-efficiency, an inline quality assurance (QA) system based on NDI methods must be established. Endline inspection is considered an additional step that takes time and cost after a component has been completed, which should be avoided consequently. It has been concluded that ACUT is a suitable NDI method [152]. An NDI method has to meet certain key criteria such as



FIG. 3.1. A particular achievement by the ZLP was the manufacturing of a light weight rocket booster pressure vessel demonstrator for the Ariane 6 launcher in 2017. This vessel had a diameter of 3.4 m and a length of 6 m. It was subjected to a final bursting test where it bore even more pressure than required while the weight limit was met.

fast measurement speed and data evaluation as well as the ability to inspect large components. This can only be achieved through the automation of the inspection processes. However, there are more key criteria like noncontact measurement and imaging options, the flaw detection resolution and probability of detection (*POD*) as well as penetration depth and accessibility of the component. ACUT makes a good compromise of these conditions. Compared to WCUT, ACUT is a relatively new NDI method, and not developed as much, although the advantages of ACUT as an inline QA method are obvious. We can abstain from all infrastructure that is related to the coupling medium water like immersion tanks, tubes, water conditioning, etc. Furthermore, robots and electrical equipment are not affected by moisture, and no water can infiltrate the CFRP components or cause corrosion. Crucial parameters known from WCUT like contact pressure and flow rate of the coupling medium are nonrelevant. Firm contact on uneven and rough surfaces is also not an issue with ACUT. Furthermore, CFRP with a high amount of porosity like thermoplastics can be inspected, where water-coupled ultrasound

gets scattered heavily due to its shorter wavelengths.

An inline QA would not only have the benefit of merely removing the endline inspection. Detecting a flaw when it happens to develop would allow to determine what process deviation has caused the flaw. One would seek for deviations in the process parameters taking place at the same instant of time. This would be possible since process parameters such as the tow tension in a dry fiber winding process or the heat source temperature in an in-situ consolidation process are monitored. The process could then be optimized accordingly, a repair attempt be made, and then the manufacturing be continued, or, if repair is impossible and the flaw is critical, the manufacturing could be canceled, and the component discarded without wasting time on finishing the component and finding out only by an endline inspection that the component is waste. We can go one step further and think of self-optimizing manufacturing processes. A deviation in the component's quality would be detected automatically and correlated with deviations in the process or environment parameters, and appropriate measures would be taken accordingly. The smart production line would be able to learn and optimize itself with only minimal engagement required from humans, an idea described by the term *Industry 4.0*. The ZLP has already implemented data bases where manufacturing process parameters as well as inspection data are stored. It is a matter of ongoing research of how to store a large amount of data (*Big Data*) in a convenient way so as to enable easy access and interpretability to the human. *Machine learning* with respect to the automated evaluation of ultrasonic images or of any inspection data is another field of research to assist the human and to improve the cost-efficiency of the inspection processes.

Before ACUT can be integrated into the production line, it must first be set up independently. At this stage, two main tasks have to be achieved. Firstly, the method must be made operational at all. Therefore, the mechanical and electrical integration into a robotic cell was conducted. The robot featuring high flexibility, accuracy, speed, and range would carry the transducers and enable the scanning of multi-dimensionally curved components while maintaining the orientation of the transducers with respect to the component's surface. On the other hand, the electrical integration allows the simultaneous monitoring of the ultrasonic data (A-scans) and the corresponding positions so that three-dimensional ultrasonic images (C-scans) can be generated in the post processing or in real-time. The second task is to learn actually how the quality of a component can be inspected (and assured later in the production process) with the method. This requires comprehensive testing of many different components with artificial flaws, various geometries, materials, layups, and so on. By varying the many parameters like transducer frequency, output voltage, and gain as well as software and hardware filters, but also settings like scanning speed, measurement grid size, and working distance, we learn how to apply the method to its best and ultimately detect as

many flaws as possible. In case of inspection by means of guided waves, the additional complication of the excitation angle adjustment (and adaptation) as well as the more sophisticated image interpretation has to be managed. We should be able at that point to locate the position and determine the size of any flaw. Well-tried reference systems like the Olympus OmniScan SX/MX device (Olympus K.K., Tokyo, Japan) which is based on water-coupled ultrasonic testing, are used for comparison and validation. The determination of the type of a flaw is also desirable but difficult in prototypic components and inspection setups where we lack the experience of serial production. We cannot rely on well-known flaw image characteristics occurring frequently in a production line, and we also usually cannot apply a simple threshold like the common -6 dB amplitude criterion used in aerospace. Since the appearance of anomalies in composite structures is so manifold¹, a vast and complex field of research has emerged upon the questions of what an indication in an ultrasonic image is caused by and whether it should be classified as a flaw or not. These questions are closely related to the topic termed *effects of defects*, and to tackle them, a physical understanding of the wave propagation in the inspected body as well as of the interaction between the elastic waves and anomalies is essential. In Chapter 2, we have covered the first aspect, while the interaction with flaws is investigated more by means of the FEM. An impressive study was conducted by Zelenyak *et al.* who have obtained the microstructure of a composite from computed tomography (CT) images, and who created a model of a pulse-echo ultrasonic measurement using COMSOL Multiphysics[®] (COMSOL Inc., Burlington, MA, USA). By including realistic models of the transducer as well as of the composite, they were able to simulate ultrasonic signals affected by porosity in good agreement with experimental signals [153]. Owing to all these considerations, the evaluation of ultrasonic data at the ZLP is not conducted by commercial software. The ultrasonic data and measurement coordinates are stored and retrieved as raw data, namely as technical data management streaming files (TDMS)² and comma-separated values (CSV), respectively, and they are evaluated by MATLAB[®]-scripts written by the author. Since the ultimate task is to integrate ACUT in the production process, a raw data interface also helps to maintain the required flexibility and adaptability of the inspection data processing to the digital workflow running behind the physical production line.

In the above-described vision, we are currently at the point where we have gained a profound understanding of the physics of the method, and where we have also achieved a remarkable progress in terms of the automation of the method and its application. In the following, we discuss the different measurement modes, namely

¹Typical flaw types in composites are delaminations, porosity, cracks, inclusions, fiber or ply misalignment or waviness, debonding, etc.

²The TDMS file format was developed by National Instruments (National Instruments, Austin, TX, USA).

the NTM in Sec. 3.1.1 and the FSRM in Sec. 3.1.2. Both measurement modes will be compared in terms of their imaging capabilities in Sec. 3.1.3. The AEE as the most recent and unprecedented automation technology will be presented only in the following Sec. 3.2. The next and final step is the integration of the method into the production line. This work has begun in the summer of 2019 and it is in progress as this thesis is completed. Therefore, it is beyond the scope of the work presented here.

3.1.1 Normal Transmission Mode

The NTM is the simplest configuration. The ultrasonic beam is directed normally to the surface of the inspected component, and the transmitted amplitude is monitored. The inspected component must be accessible from both sides. Figure 3.2(b) shows a robotic cell at the ZLP while performing ACUT of a CFRP plate in NTM. The robot used here is a KUKA KR120 R2700 extra HA (KUKA AG, Augsburg, Germany) run by a KRC4 controller, possessing six axes and a particularly high accuracy. Since the CFRP plate is relatively small, it is sufficient to attach the ultrasonic transducers on a C-frame end-effector, which in turn is mounted on the robot's flange. However, for large structures like aircraft fuselages, one would have to use two cooperating robots. The ACUT device used at the ZLP was constructed by Inoson (Inoson GmbH, St. Ingbert, Germany), providing the interfaces for the communication with the robotic controlling unit as well as for retrieving the ultrasonic data as a TDMS file. The ultrasonic testing device can be triggered by

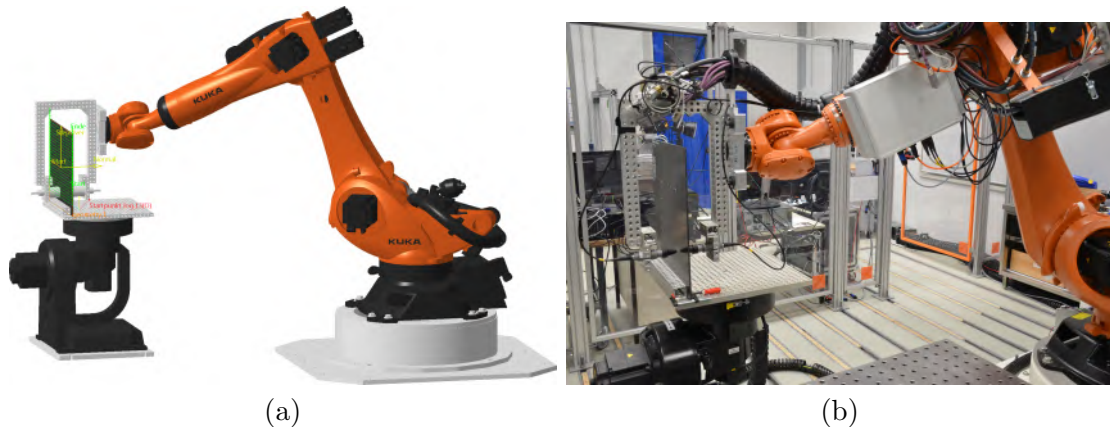


FIG. 3.2. ACUT in normal transmission mode at the ZLP. (a) The robot is programmed offline in a CAD-like environment, containing a digital twin of the real component. (b) Robot-assisted inspection of a CFRP plate with focused 570 kHz transducers. The plate is scanned on a meander-like path, while the transducers are triggered path-equidistantly.

the robot controlling unit path-equidistantly with a maximum pulse repetition frequency (PRF) of 250 Hz. This means that the sender transmits ultrasonic pulses on-the-fly at every equidistant measurement point on the programmed path, no matter how complicated the path is, and unaffected by acceleration ramps and high velocities, as far as the maximum PRF is not exceeded. The offline programming (OLP) was performed by using FASTSURFTM in conjunction with DELMIATM (Dassault Systèmes, Vélizy-Villacoublay, France), as shown in Fig. 3.2(a). Thereby, a meander-like path was programmed on the digital twin of the real component. By simultaneously monitoring the ultrasonic data together with its respective measurement coordinates x_i, y_i, z_i , three-dimensional C-scans resembling the geometry of the inspected body can be generated.

The disadvantages of the NTM compared to the pulse-echo mode (PEM) are that it does not provide information about the depth of a flaw and that access from both sides of the component is required. In the PEM, a single transducer transmits at normal incidence and collects the reflected signal. As pointed out however by Castaings in Ref. [102], the enormous acoustic impedance mismatch between air and the solid to be inspected causes the reflection of almost the complete energy from the surface, with only minimal energy transmitted into the solid. Therefore, the reflected signal from the interior of the solid will be much weaker than the one reflected from the surface. Since the transducer is set up to detect the weak signal from the interior, it will be overloaded by the surface reflection and unable to recover fast enough to detect the interior signal, unless the plate is very thick, as demonstrated by Hayward and Farlow [154]. The author has tested all ACUT transducers available at the ZLP (64 kHz, 110 kHz, 200 kHz, and 570 kHz) in PEM. No reflection from the back wall could be detected. New opportunities would arise if the new broad-band polyCMUTs discussed above enabled the PEM in noncontact ultrasonics.

3.1.2 Focused Slanted Reflection Mode

In this section, we discuss how the FSRM works and how we have automated the method at the ZLP. Then, the inspection of a rocket booster pressure vessel demonstrator using the FSRM is reported.

Working Principle

The FSRM is generally more sophisticated in its application than the NTM. This inspection mode is based on the interaction of Lamb waves with flaws inside a plate. Most importantly, the FSRM requires knowledge of the excitation angle (respectively incidence angle) Θ_{in} (see Eq. (2.171)) for a certain mode. In fact, this is the actual reason why the numerical modeling and dispersion diagram calculation

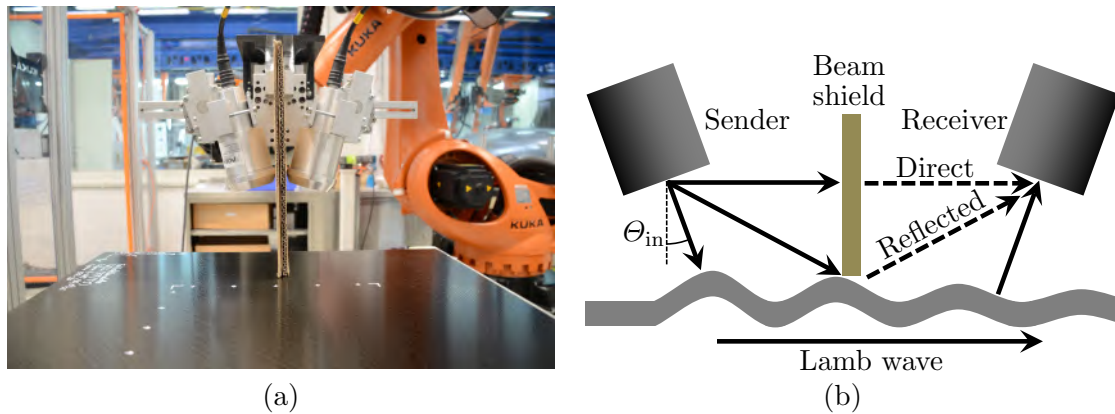


FIG. 3.3. ACUT in focused slanted reflection mode at the ZLP. (a) The conventional FSRM end-effector carries nonfocusing 200 kHz transducers, specifically designed for the excitation of Lamb waves. The excitation angle can be adjusted manually. (b) The working principle of the FSRM. A beam shield is used to block the direct sound so that only the signal emitted by the Lamb waves propagating in the plate reaches the receiver.

for guided waves in the frame of this thesis was done. It is the reason why the DC was created. Without the possibility to calculate θ_{in} , we have to find it manually by rotating the transducers until the desired Lamb wave (usually A_0) is excited at its maximum amplitude.

A Lamb wave propagating along a plate causes displacement throughout its whole thickness. Since ultrasound is reemitted along the propagation path of the Lamb wave, it can be detected with the receiver. As depicted in Fig. 3.3, both the sender and the receiver must be oriented at the same excitation angle with respect to the surface normal. A flaw causes a change in the displacement amplitude, and can be detected thereby. In principle, this can be achieved on the same side where the Lamb waves are excited from as well as on the opposite side, as shown here. In the first case, the method is called *focused slanted transmission mode* (FSTM). However, the obvious advantage of the FSRM is that single-sided access to the specimen, as we have it in the rocket booster manufacturing, is sufficient. Figure 3.3(a) shows the conventional FSRM end-effector mounted on an industrial robot. A beam shield made of cardboard is attached between the two transducers to screen the sound propagating directly from the sender to the receiver. Both transducers can be rotated and moved horizontally and vertically, but only manually. Similarly as in the NTM, the industrial robot scans the specimen while ultrasonic pulses are triggered such that a square grid of measurement points, comprising the base coordinates x_i, y_i, z_i , and the corresponding ultrasonic data, is generated.

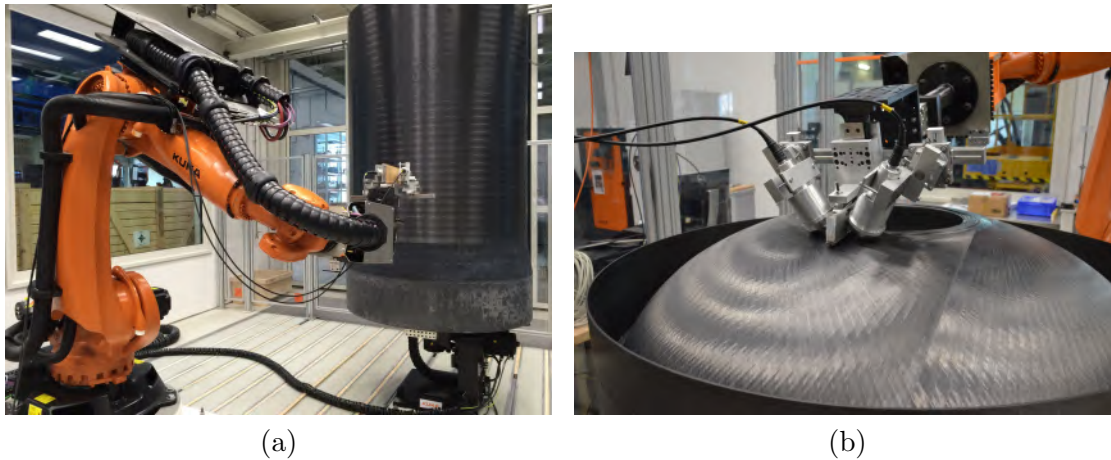


FIG. 3.4. ACUT in focused slanted reflection mode on a down-scaled rocket booster pressure vessel demonstrator at the ZLP. (a) The longer one of the two parts of the pressure vessel is mounted on the tilt-turn table. (b) Inspection of one of the domes of the pressure vessel. The winding structure is clearly visible.

Inspection of a Rocket Booster Pressure Vessel Demonstrator

The largest component inspected with ACUT at the ZLP so far was a down-scaled rocket booster pressure vessel demonstrator in 2014. This work was published in Ref. [118]. The vessel was manufactured at the Chair of Carbon Composites of the Technical University of Munich (TUM), München, Germany, from carbon fiber thermoplastic prepreps by using a winding process with in-situ laser consolidation. It contained a high amount of porosity of 2% to 4%, which made the inspection by using WCUT impossible. Compared to the real size of a pressure vessel, the inspected demonstrator was scaled down to about one third. It consisted of two parts, which together had a length of 3.7 m and a diameter of 1.4 m. In Fig. 3.4(a), the longer part of the pressure vessel (2.3 m) was mounted on a tilt-turn table (TTT), which allowed the rotation of the structure. The task was a complete inspection of both parts of the vessel, the detection of all flaws with a diameter of at least 10 mm, and the visualization of the results in two-dimensional and three-dimensional C-scans.

Before the inspection of the pressure vessel, a test had to be conducted to clarify whether Lamb waves could be excited in a 40 mm thick laminate at all, which was the maximum thickness of the pressure vessel. To get a test component, a ring with a height of 120 mm was cut from the 40 mm thick area (at the lower end of the vessel shown in Fig. 3.4(a)). As shown in Fig. 3.5(a), 10 mm thick layers of different sizes of the thermal protection material (ethylene propylene diene monomer rubber, EPDM) of the booster were glued on the inner side of the ring. If

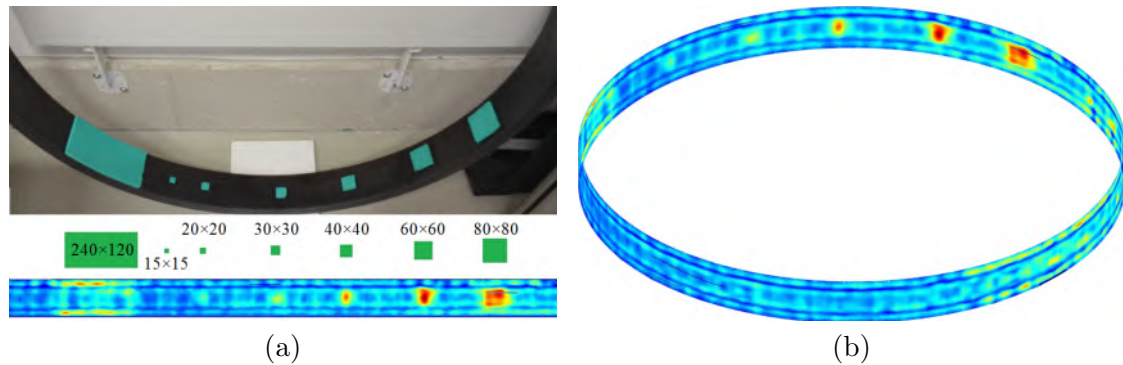


FIG. 3.5. (a) EPDM layers glued on the inner side of the test ring to prove the excitation of Lamb waves in a 40 mm thick laminate, and a C-scan obtained with 64 kHz transducers in 2-D and (c) 3-D. The EPDM layers affect the Lamb wave's amplitude, thereby proving the excitation of Lamb waves rather than Rayleigh surface waves.

Lamb waves could be excited (from the outside of the ring), a change in amplitude was expected upon scanning an EPDM layer. By contrast, if only Rayleigh surface waves would be excited, no change in amplitude should occur, and therefore the laminate could not be inspected throughout its whole thickness. In thin laminates, this test can be done simply by pressing the thumb on the far side of the laminate. Figure 3.5(b) displays the resultant three-dimensional C-scan obtained by using 64 kHz transducers, and at the bottom of Fig. 3.5(a), a 2-D cutout of the 3-D representation is displayed. The positions and sizes of the EPDM layers are drawn true to scale in green color. The EPDM layers become visible by an increase of the Lamb wave's amplitude (indicated by red color), beginning at a size of $20 \times 20 \text{ mm}^2$. Hence, the excitation of Lamb waves in a 40 mm thick laminate using 64 kHz transducers was proven. This was not possible with 110 kHz and 200 kHz transducers.

After this test, the inspection of the pressure vessel was carried out, starting on the cylindrical part and continuing on the domes, which was more sophisticated due to their three-dimensional curvature. Again, the OLP was performed using FASTSURFTM and DELMIATM. For the OLP, a digital twin of the vessel was obtained from a LEICATM T-scan measurement (LEICA AG, Wetzlar, Germany) in order to have its real dimensions. A meander-like scanning was realized by rotating the vessel while keeping the end-effector at one position and triggering the transducers every 2 mm on the path. After a rotation of 360° , the TTT stopped, the robot moved the end-effector up by 2 mm, and then the TTT rotated back in the other direction and so on. Thereby, a $2 \times 2 \text{ mm}$ grid of measurement points on the pressure vessel was generated. Hence, taking the maximum *PRF*

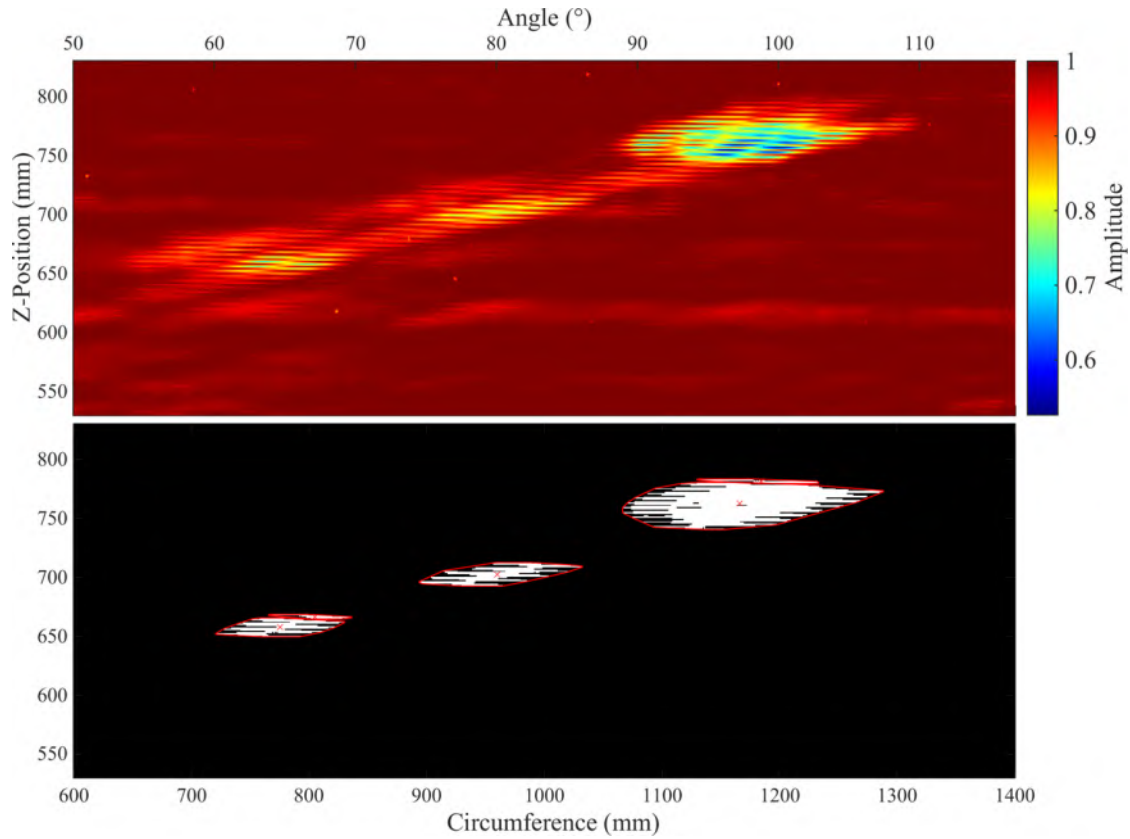


FIG. 3.6. Visualization and evaluation of ultrasonic data. The C-scan in the upper panel shows the Lamb wave's amplitude measured on the cylinder mantle of the pressure vessel using 64 kHz transducers. Red color indicates a high Lamb wave amplitude. The binary image in the lower panel indicates three delaminations.

into account, the highest possible scanning speed for that grid was 500 mm/s, while the actual scanning speed was 230 mm/s. The Lamb wave's excitation angle was adjusted manually on the cylindrical part and on the dome, and it did not have to be changed since the layup and the thickness of the laminate remained practically constant in these areas. Figure 3.4(b) shows the scanning of one of the domes of the vessel. At the top, the nozzle opening can be seen.

Only a cutout from the complete C-scan of the cylinder, covering a circumferential length of 800 mm and a height of 300 mm, may be shown in Fig. 3.6. The image shows distinct delamination indications accounting for deviations during the winding process, possibly caused by an insufficient tension on the tape or by a poor consolidation through the laser. However, these were the only indications found in the cylindrical part of the booster. The top image in Fig. 3.6 shows the Lamb

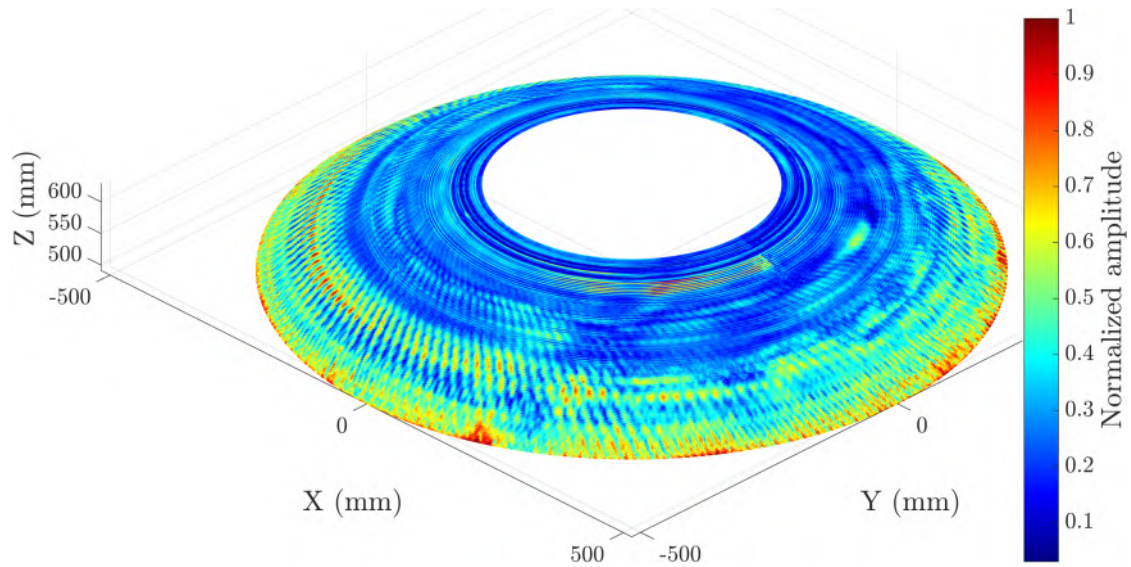
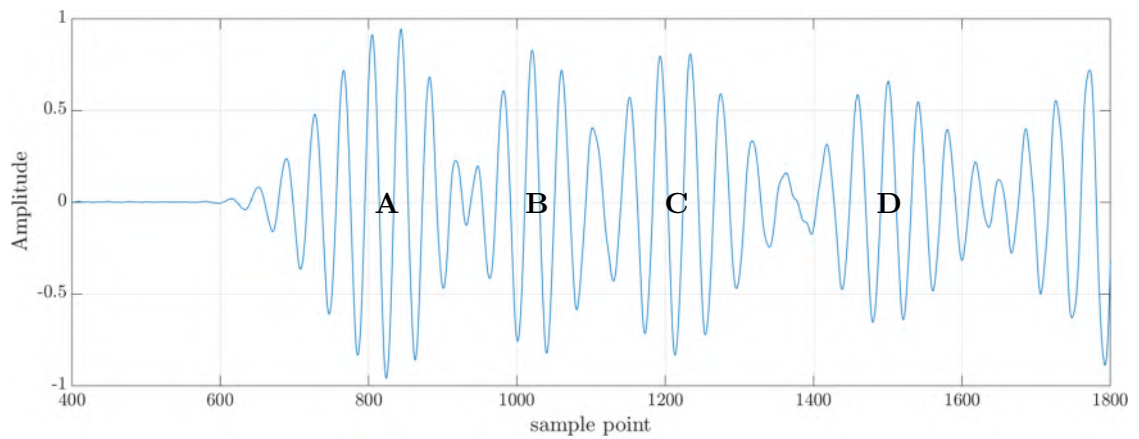


FIG. 3.7. Three-dimensional C-scan of one dome of the pressure vessel. The winding structure has been revealed clearly. In the bluish area, Lamb waves could hardly be excited due to the highly inhomogeneous laminate structure.

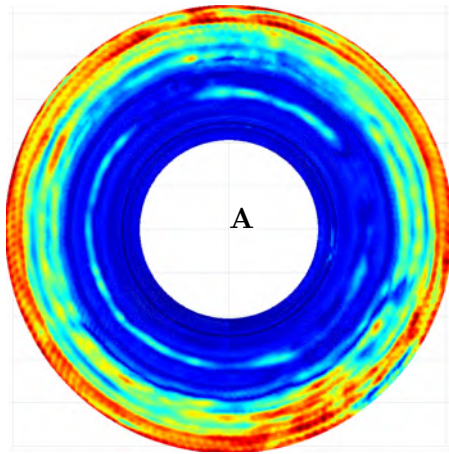
wave's amplitude measured using 64 kHz transducers. Red color indicates a high amplitude. In the lower image of Fig. 3.6, the amplitude is evaluated by applying an amplitude as well as an area criterion. Accordingly, amplitudes less than 0.9 covering an area larger than 100 mm^2 are indicated and declared to be flaws. Certainly, the chosen amplitude and area criteria are debatable since they are more or less arbitrary, much like the well-known -6 dB criterion. Meaningful criteria should correspond to a critical stiffness loss, which can ultimately lead to a failure of the structure.

Finally, the domes were inspected. Figure 3.7 shows the C-scan obtained using 64 kHz transducers, with the winding structure clearly visible. Due to the crossing of the tapes, large cavities were contained in the laminate, making it hard to generate and propagate a Lamb wave, in particular close to the pole opening. However, at some distance from the pole, four Lamb wave modes were excited simultaneously, and these could be evaluated separately. Figure 3.8(a) shows a representative A-scan comprising the four wave packets, which are separated just enough to be evaluable independently from one another. To do this, a so-called *gate* is set around a wave packet, covering a certain sample point range in Fig. 3.8(a), so that only the amplitude within the gate's boundaries is evaluated. The maximum peak-to-peak amplitude within the gate is extracted from every A-scan. Hence, a single amplitude value results from each measurement point. This amplitude value is subsequently scaled to a color map and represents one pixel in a C-scan.

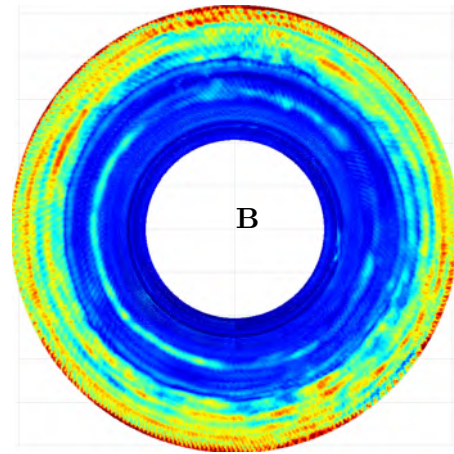
Unfortunately, the layup of the dome as well as the material's stiffness tensor are not available so that we cannot calculate a dispersion diagram and determine which modes were excited. Therefore, we simply denote the modes appearing in Fig. 3.8(a) consecutively with the letters "A", "B", "C", and "D", starting with the highest phase velocity on the left in the A-scan. Figures 3.8(b) to (e) display the C-scans resulting from each Lamb wave mode. As expected, the resolution of the C-scans improves with decreasing phase velocity, which is equivalent to a shorter wavelength since the frequency is constant. It is obvious from this experimental study that each mode interacts individually with the inspected material and the contained anomalies. We have discussed in Sec. 2.7.2 that this is due to the modes' specific shapes, respectively, their distributions and proportions of in-plane and out-of-plane displacements. We have also pointed out that, in general, one should always try, if possible, to excite only single modes since the superposition of multiple modes can result in misleading C-scans. Although it is quite fortunate that the modes excited in the dome could be separated sufficiently, the best choice for a single mode excitation would have been the slowest mode denoted with the letter "D". The three-dimensional C-scan presented in Fig. 3.7 was generated from this mode. It is impossible today to clarify if it was actually possible to excite only the D mode in that dome in 2014.



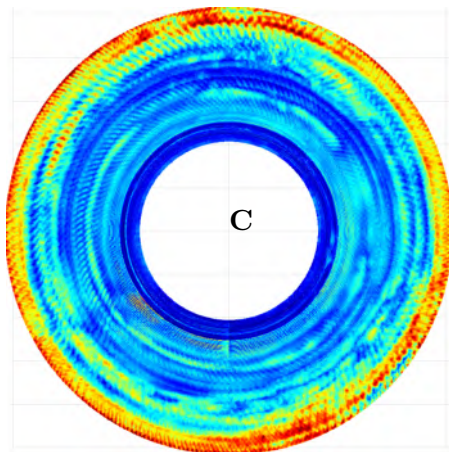
(a)



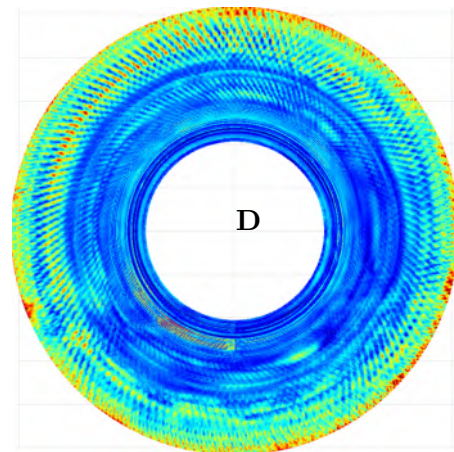
(b)



(c)



(d)



(e)

FIG. 3.8. Inspection results of the dome. (a) Representative A-scan containing four Lamb wave modes excited at the same time. (b)-(e) Top-view C-scans obtained from evaluating each mode separately. Modes with a lower phase velocity yield a higher resolution.

3.1.3 Comparison

We have seen in Secs. 3.1.1 and 3.1.2 that the NTM is easier in its application compared to the FSRM, where we have to adjust the correct excitation angle. On the other hand, the NTM has the drawback of requiring two-sided access to the specimen. In the current section, we want to compare the both inspection modes in terms of their imaging capabilities, in particular their ability to resolve flaws. Therefore, a high quality CFRP plate shown in Fig. 3.9(a) with a size of $550 \times 600 \text{ mm}^2$ and with artificial delaminations was manufactured to perform both inspection modes upon. The noncrimp biaxial fabric PRIFORMTM 24k IMS WNCF 550 gsm with the Cycom[®] 977-20 resin (Cytec Industries, Inc., Woodland Park, NJ, USA) was used, and a vacuum assisted resin infusion process (VARI) applied for the consolidation. The layup is $[45/-45/90/0]_{3s}$ with a thickness of 7 mm and a fiber volume content of 54.5%. As depicted in Fig. 3.9(b), artificial delaminations in the form of twofold polypropylene sheets of different sizes were inserted into various depths. According to the Airbus specifications for the nondestructive inspection of composite parts, the minimum detectable defect size should be $6 \times 6 \text{ mm}^2$ [155]. In order to definitely meet this standard, the smallest defects were sized to $5 \times 5 \text{ mm}^2$.

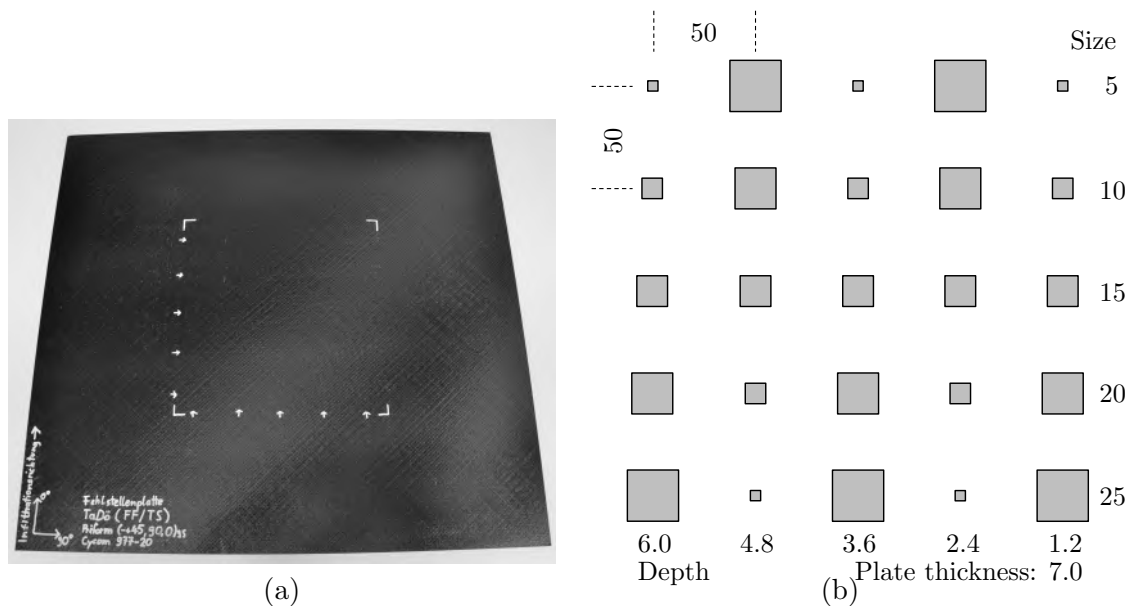


FIG. 3.9. A CFRP plate containing artificial delaminations made from polypropylene sheets was manufactured. (a) The delaminations' positions are marked by arrows. (b) Flaw plan showing the sizes and depths of the delaminations. All measures are in millimeters.

The C-scan displayed in Fig. 3.10(a) was obtained by the NTM measurement shown in Fig. 3.2(b) using focusing 570 kHz transducers. An area of the plate of $260 \times 260 \text{ mm}^2$ containing the delaminations was inspected. In order to achieve a particularly high resolution, a very fine grid of $0.2 \times 0.2 \text{ mm}^2$ was scanned with a speed of 40 mm/s ($PRF = 200 \text{ Hz}$). This resulted in a quite long scanning time of 3:47 h. The C-scan does not directly show the transmitted amplitude. Instead, to reduce the noise, the A-scans were Fast Fourier-transformed (FFT), and the spectral amplitude at the center frequency taken in MATLAB[®]. Obviously, the flaws have been resolved with a high accuracy regarding size and shape. Furthermore, the layup structure is clearly visible on the flaws' indications as well as on the surrounding plate. It appears that, by laying the polypropylene sheets onto the somewhat uneven surface of the dry fabric, small channels between the rovings filled with resin or air had been created. The usual evaluation process for a C-scan is then to apply thresholds for the (spectral) amplitude and for the flaw size. Figure 3.10(c) shows the resulting binary image for spectral amplitudes less than 25 and sizes greater than 10 mm^2 . The white areas represent the flaws, and the convex hulls and flaw centers are marked in red color. The MATLAB[®]-routine then generates the flaw list shown in Appendix F, containing all acquired information about the flaws, most importantly the flaw centers, sizes, and shapes (convex hull points $x_i, y_i, z_i, i = 1, 2, \dots, 20$). The flaw list also reports in the header the number of found flaws as well as the percentage of flaw area of the total inspected area. This facilitates in particular the quality comparison of multiple specimens of the same batch. The flaw list is stored in a data base together with other inspection results and manufacturing data to allow for later investigations with the ultimate goal of optimizing the production processes.

The C-scan displayed in Fig. 3.10(a) demonstrates the excellent imaging capabilities of ACUT in the NTM. However, a scanning time of 3:47 h required for a small area of $260 \times 260 \text{ mm}^2$ is of course not feasible in the use case. Therefore, NTM scans with lower resolutions of $1 \times 1 \text{ mm}^2$ and $2 \times 2 \text{ mm}^2$ were performed, taking only 19 min and 9 min, respectively. The scanning speed in both measurements was 100 mm/s ($PRF = 100 \text{ Hz}, 50 \text{ Hz}$). Considering that the ACUT module could sustain a maximum PRF of 250 Hz, we could have increased the scanning speed to 250 mm/s and 500 mm/s, respectively. However, the robot does not reach that top velocity on a sweep distance of only 260 mm since one acceleration ramp and one deceleration ramp must be carried out. Fortunately, this is not a problem on large components like aircraft fuselages or pressure vessels where the scanning speed can be increased to 250 Hz·grid size. Figures 3.11(a) and 3.11(b) present the C-scans obtained with grid sizes of $1 \times 1 \text{ mm}^2$ and $2 \times 2 \text{ mm}^2$, respectively. The $1 \times 1 \text{ mm}^2$ inspection shows almost the same detailing as the one obtained with the $0.2 \times 0.2 \text{ mm}^2$ grid seen in Fig. 3.10(a), whereas the $2 \times 2 \text{ mm}^2$ inspection is clearly reduced in detail. However, the delaminations are still resolved acceptably.

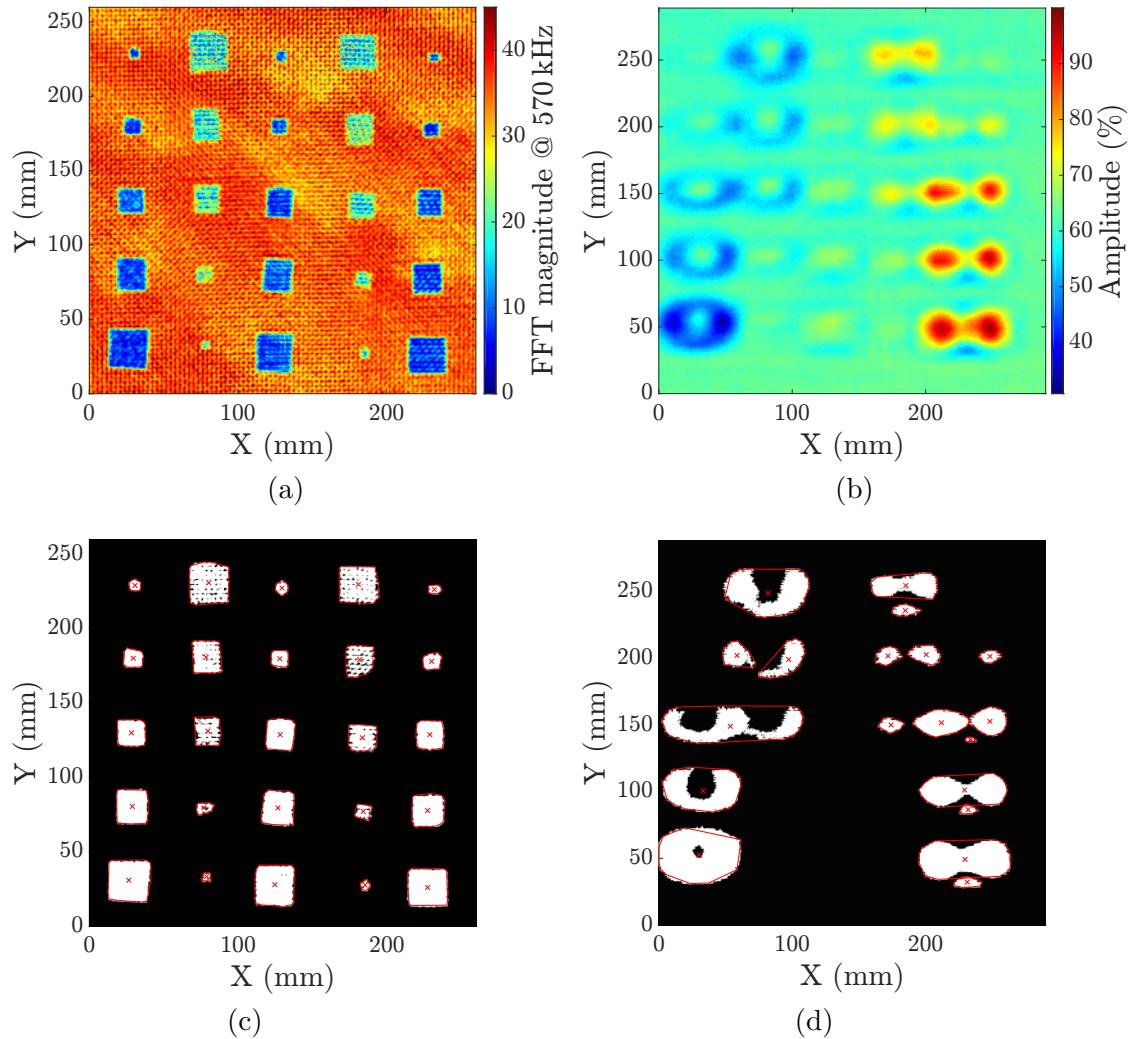


FIG. 3.10. Inspection results of the flaw plate. (a) High resolution C-scan (resolution: $0.2 \times 0.2 \text{ mm}^2$, duration: 3:47 h) obtained by the NTM using focusing 570 kHz transducers. To reduce the noise, the A-scans were Fast Fourier-transformed and the spectral amplitude at the center frequency taken. The structure of the plate as well as of the flaws is resolved in high detail. (b) C-scan (resolution: $1 \times 1 \text{ mm}^2$, duration: 14 min) obtained by the FSRM measurement using 200 kHz transducers. The indications are smeared along the Lamb wave's propagation direction (X -axis) and they consist of two spots. The appearance is also depth dependent. (c) The delaminations from image (a) can be isolated easily by filtering spectral amplitudes less than 25 and sizes larger than 10 mm^2 . (d) The filtering of amplitudes exceeding 70% and less than 55% as well as sizes larger than 10 mm^2 isolates only some of the delaminations from image (b).

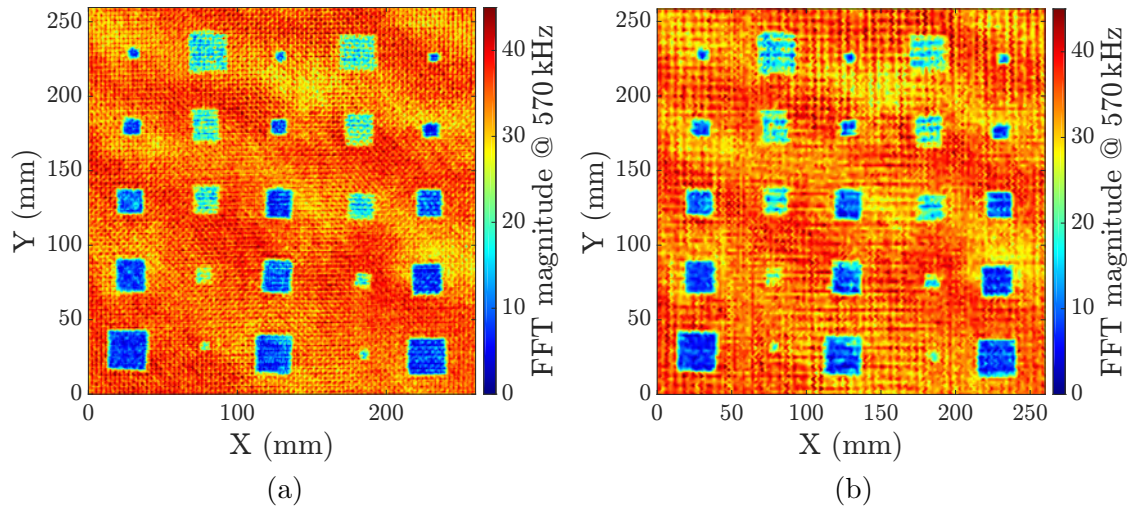


FIG. 3.11. C-scans of the flaw plate obtained by the NTM using focusing 570 kHz transducers. (a) Resolution: $1 \times 1 \text{ mm}^2$, duration: 19 min and (b) resolution: $2 \times 2 \text{ mm}^2$, duration: 9 min. Even at low resolutions, the shape and size of the delaminations is resolved clearly.

Let us now assess the FSRM. The C-scan in Fig. 3.10(b) was obtained by using nonfocusing 200 kHz transducers. Due to the broad and very intense ultrasonic beam, a very high signal-to-noise ratio was achieved so that an FFT of the A-scans, as done for the NTM measurements, was unnecessary here. A grid size of $1 \times 1 \text{ mm}^2$ and a scanning speed of 150 mm/s ($PRF = 150 \text{ Hz}$) were used, resulting in an inspection time of 14 min. The sweeping as well as the Lamb wave propagation were parallel to the X -axis. Sweeping perpendicular to the Lamb wave propagation direction makes no difference in the C-scan. The present C-scan looks strikingly different compared to the ones obtained with the NTM, so more careful interpretation is required. Each flaw has caused two indications aligned parallel to the X -direction. This happens when flaws are smaller than the distance which the Lamb waves propagate between the transducers. Consequently, this distance should be kept as small as possible. Since the transducers have a large housing of 75 mm diameter, this effort is hampered to some extent. However, the distance of Lamb wave propagation could be shortened by elevating the transducers by 80 mm above the plate so that the ultrasonic beam was close to hitting the beam shield (see Fig. 3.3(a)). The increased attenuation suffered from the longer propagation distance in air was over-compensated by the shorter propagation distance in the plate.

Let us examine the indication in the lower right corner in Fig. 3.10(b), caused by a delamination of 25 mm size, residing in a depth of 1.2 mm. Two round spots,

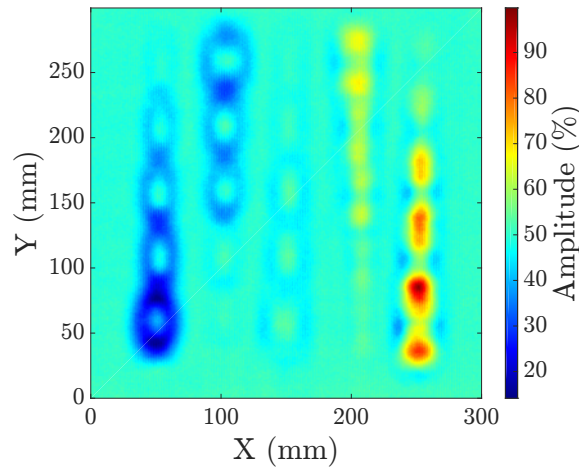


FIG. 3.12. C-scan (resolution: $1 \times 1 \text{ mm}^2$, duration: 14 min) of the flaw plate obtained by the FSRM using 200 kHz transducers. In contrast to Fig. 3.10(b), the Lamb wave propagation direction was parallel to the Y -axis, resulting in a different appearance of the C-scan.

slightly distorted parallel to the X -axis, with approximately 25 mm in diameter have appeared with a center-to-center distance of 35 mm between them, representing the propagation distance of the Lamb waves between the transducers. Upon reducing this distance, the resultant spots would approach each other until theoretically coinciding in the middle between the current spots, which is the actual location of the flaw. We can attempt to explain this picture as follows. When the first transducer reaches the flaw, the amplitude rises. The corresponding indication shows up in the C-scan, shifted by an offset of the half of the propagation distance *before* the actual position of the flaw because the ultrasonic data are assigned to the tool center point (TCP), which is located in the middle between the transducers. When the flaw is between both transducers, the amplitude approaches values similar to those measured in absence of any flaw. Eventually, the second transducer passes the flaw, and another indication shows up, shifted by the same offset *after* the actual flaw location. The size determination of the flaws from its indications is problematic. If one considers all five 25 mm flaws, only the one in 1.2 mm depth has caused two distinct spots of 25 mm size. Moreover, also the shape of the indications is distorted as compared to the real flaws.

Ultrasonic data obtained from the FSRM does not provide depth information. However, in Fig. 3.10(b), it seems that the depth of the flaws has affected the appearance of the indications. In contrast to the 25 mm delamination in 1.2 mm depth discussed above, an opposite effect regarding the amplitude can be observed for the 25 mm delamination in the lower left corner, residing 6 mm deep. There are two spots with reduced amplitudes compared to the surrounding, and they

do not have such a pronounced boundary. Interestingly enough, for the center column of flaws, which are located at nearly the half thickness of the plate, we find an amplitude very close to the surrounding one, and thus the indications can hardly be distinguished. The 25 mm flaws located in depths of 2.4 mm and 4.8 mm show some intermediate picture. However, if we take the smaller flaws into account as well, we find that the amplitude depends on the flaw size as well. Indications caused by smaller flaws reach less striking amplitude leaps. Therefore, we can conclude that the amplitude of flaw indications is a function of flaw depth and size, potentially offering an indirect method of deducing the depth from the amplitude. However, to really understand how the appearance of this C-scan comes about, a FEM simulation similar to the one discussed in the introduction of the present section would help [153]. The appearance of two spots and the distortion along the propagation direction of the Lamb waves are well-known effects, and their overcoming is the topic of ongoing research. For instance, Springmann *et al.* have proposed a deconvolution approach to improve the image sharpness of C-scans obtained by means of Lamb waves [156]. The general problem is that such a solution works only for a given specimen and inspection setup. If any parameter is changed, the calibration process has to be repeated all over. Consider for example Fig. 3.12. The only parameter that had been changed was that the Lamb wave propagation direction was now parallel to the Y -axis, resulting in a different flaw pattern.

The binary image displayed in Fig. 3.10(d) shows an attempt to automatically evaluate the C-scan in Fig. 3.10(b). Owing to the fact that the delaminations cause the amplitude to both rise and fall, we define two thresholds, namely for amplitudes exceeding 70 % and such less than 55 %. Flaw sizes less than 10 mm^2 are filtered out. Clearly, not all flaws have been isolated, namely those of $10 \times 10 \text{ mm}^2$ size and smaller as well as those located at a depth of 3.6 mm. The human inspector, of course, finds more flaw indications in the original C-scan shown in Fig. 3.10(b). The sizes and shapes of the indications do not at all resemble the true dimensions of the found delaminations.

In summary, the advantage of the FSRM to be single-sided comes at the cost of reduced imaging quality as compared to the NTM. However, in our application at the ZLP, namely as a production inline QA method for large components, we do not need to resolve high levels of detail. We reported in Sec. 3.1.2 that it was sufficient to detect flaws with a size of at least $10 \times 10 \text{ mm}^2$ on the rocket booster, and this requirement was met by the FSRM inspection. Indications smaller than $10 \times 10 \text{ mm}^2$ were considered noncritical. For the inline QA process, it will be even beneficial if small indications are not detected at all so as to decrease the amount of indications that have to be processed in real-time, and therefore enabling a shorter reaction time of the system.

3.2 Adaptive End-Effector

In Sec. 3.1, we have presented the inspection of a flat plate and of a pressure vessel by using the FSRM, where the excitation angle was determined manually. Since the layup of the plate was continuous, the inspection could be carried out with one and the same angle. The pressure vessel consisted of three large areas with continuous layups, namely the cylinder mantle, the reinforced area of the cylinder mantle, and the domes. The Lamb waves were propagating along the circumferential direction of the vessel, having of course a constant curvature within each of the aforementioned areas. Therefore, each area could also be inspected with one excitation angle. However, skin elements of aircraft like an A350 for instance have variations both in the layup as well as in the curvature. This means, whenever one or both features change during the scanning, the inspection process had to be interrupted and the orientation of the ultrasonic transducers adapted such that the correct excitation angle is met again. Otherwise, the Lamb wave's amplitude would drop and eventually cease. Since interrupting the inspection process frequently is highly impractical, we have developed the fully automated AEE, which enables the inline adjustment of the ultrasonic transducers such that Lamb waves are excited at optimal efficiency at any location on the component. This measurement mode is called ASRM, and the related work was published in Ref. [119].

The section is organized as follows. In Sec. 3.2.1, we explain the features of our specimen, which we used to validate the AEE. Section 3.2.2 is dedicated to the software tool chain, which we have developed to operate the AEE. The mechanical layout and integration of the AEE into the robotic environment is covered by Sec. 3.2.3, and in Sec. 3.2.4, we compare inspection results obtained with the conventional nonadaptive end-effector and with the AEE.

3.2.1 Aircraft Skin Element Demonstrator

To validate the AEE, a testing specimen (skin element demonstrator) was designed. The following requirements were defined:

- The demonstrator should mimic real components and materials used in aircraft.
- It must possess all possible features that cause a change in the excitation angle, namely variable thicknesses (layups) and curvature.
- Artificial flaws must be inserted into the layup to enable the quantification of the flaw detectability of the AEE.

The skin element demonstrator was manufactured from SAERTEX[®]7006919 dry fabric, infiltrated with RIMR135 resin by VARI. The fiber volume content is 55 %.

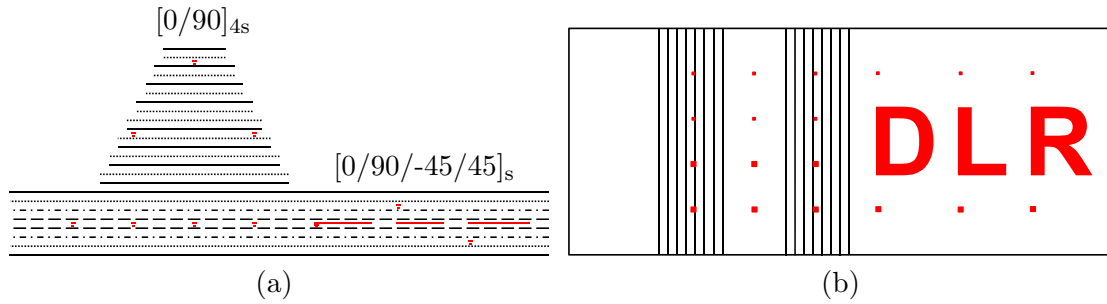


FIG. 3.13. Layup of the skin element demonstrator. (a) Cross sectional sketch and (b) top view. Artificial flaws are drawn in red color.

A schematic of the skin element is drawn in Fig. 3.13. Figure 3.13(a) shows a cross section through the laminate. The base laminate is a 2.2 mm thick quasi-isotropic layup $[0/90/-45/45]_s$. A step-like reinforcement layup $[0/90]_{4s}$ was placed on top of the base laminate with a maximum thickness of 4.4 mm. Therefore, the overall laminate thickness varies between 2.2 mm and 6.6 mm. Artificial flaws made of $5 \times 5 \text{ mm}^2$ and $10 \times 10 \text{ mm}^2$ square pieces of Kapton[®] sheet (DuPont Inc., Wilmington, DE, USA) were laminated into different depths. As shown in Fig. 3.14, the layup was performed in a small area close to the tail of an aircraft fuselage preform where significant curvature gradients occur. The resulting skin element is shown

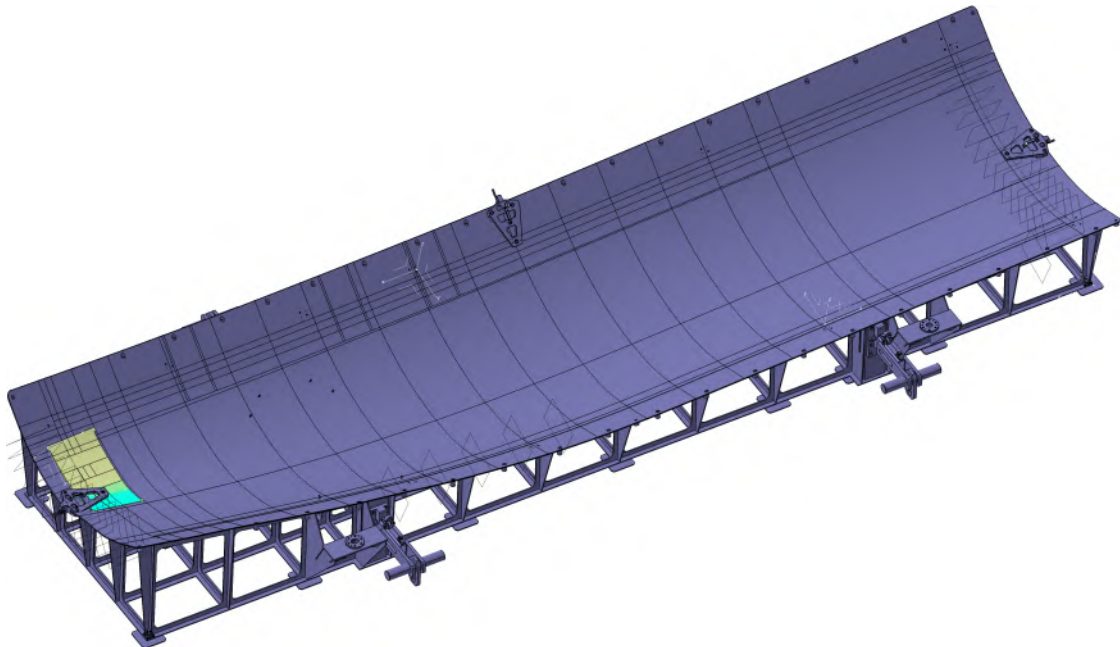


FIG. 3.14. The layup of the skin element was done in an aircraft fuselage preform.

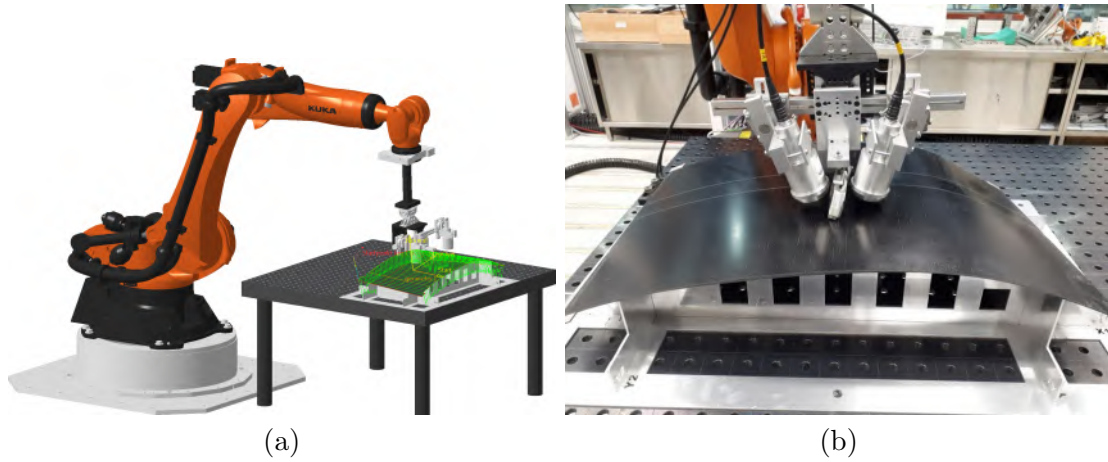


FIG. 3.15. ACUT of the skin element demonstrator with the conventional FSRM end-effector at the ZLP. (a) The OLP was done based on a digital twin of the skin element, using FASTSURFTM and DELMIATM. (b) The inspection was carried out with a fixed excitation angle.

in Fig. 3.15(b). It is 935 mm long, 505 mm wide, and has a maximum height of 110 mm. The reinforcing layup covers a length of 420 mm.

3.2.2 Software Toolchain

Since commercial software could not be used for the OLP of a kinematic system like the AEE, we had to develop our own software tool chain. This section discusses our requirements, the shortcomings of commercial software in this respect, and our solution to the problem.

Problem

Basically, we need to generate a square grid of i measurement points on the skin element with the coordinates x_i, y_i, z_i in the base coordinate system (see Fig. 3.16). This must be done based on a digital twin of the skin element. Once we have the measurement points, we must put them into a suitable order such that the robot scans the skin element on a meander-like path. To fully define the directions of motion and the orientations of the AEE, we must obtain the tripods spanned by the surface normals \vec{n}_i , bi-normals \vec{b}_i , and path tangents \vec{t}_i . Furthermore, we need to calculate the excitation angles $\Theta_{\text{in}(i)}$. To enable this, we must have the layup at each measurement point, which in turn requires the laminate thicknesses d_i . We must also ensure that the distances which the ultrasound propagates in air and in the laminate are always kept constant. From these data, we must calculate

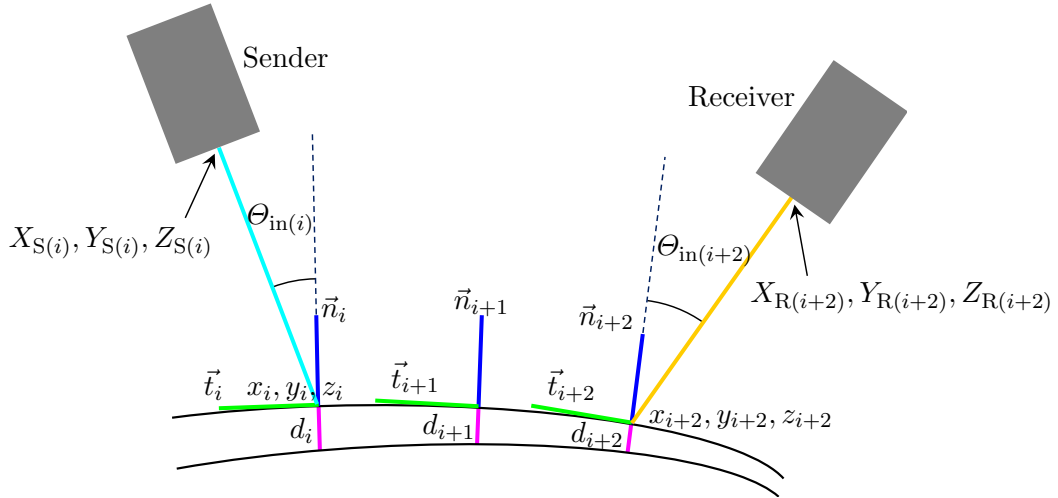


FIG. 3.16. Working principle of the ASRM on a laminate with varying thickness and curvature. For each measurement position, the transducers hit their poses independently from one another according to the excitation angle map (EAM). This enables the excitation and detection of the A_0 Lamb wave at optimal efficiency at every measurement point. The EAM calculation is done by using the same basic routine which the DC uses.

the sender positions $X_{S(i)}, Y_{S(i)}, Z_{S(i)}$ and the orientations $A_{S(i)}, B_{S(i)}, C_{S(i)}$ as well as the receiver positions $X_{R(i)}, Y_{R(i)}, Z_{R(i)}$ and the orientations $A_{R(i)}, B_{R(i)}, C_{R(i)}$ with respect to the measurement points. Since both transducers point at different locations on the skin element at any given time, they must hit different excitation angles/orientations. Therefore, we must implement a pairwise look-up for the required positions and orientations for each measurement instant. Finally, these data must be transformed into axes values for the kinematic system, and a robot program must be generated.

State-of-the-art

Usually, as shown in Fig. 3.15(a), we are using computer-aided design (CAD) and OLP tools like CATIATM, DELMIATM, and FASTSURFTM for the path planning of our robots. Here, we have a digital representation of the robotic environment, and the path as well as the orientation of the end-effector can be generated based on the skin element's surface. However, the required additional kinematics of the AEE as well as events like the adaptation of the excitation angle cannot be simulated with these software. Furthermore, the possibilities to generate a square raster on the skin element and to probe its thicknesses d_i are insufficient in CATIATM.

For the calculation of $\Theta_{in(i)}$, we used a MATLAB[®]-script which is able to calculate

many excitation angles $\Theta_{\text{in}(i)}$ in one loop. For instance, a square grid with 2 mm spacing on the skin element has more than 10^5 points. DISPERSE is unsuitable for this task since one has to enter each layup manually, calculate the complete dispersion diagram, and then extract the excitation angle of the A_0 Lamb wave mode at the transducer's frequency.

Solution

We have mentioned four different software, which were considered essential for the software tool chain initially, but which were found insufficient later. Therefore, our task became to bypass as many of those software as possible, and solve their deficiencies in our own implementation. Our tool chain consists of two software, namely CATIATM and MATLAB[®].

We start with the CATpart of the skin element in CATIATM. We perform separate tessellation of the top and bottom surfaces of the skin element, and export two stereolithography (STL) files. These files can be loaded into MATLAB[®]. The top surface of the skin element is shown in Fig. 3.17(a). We extract the point cloud of the top surface from its vertices, and use the built-in MATLAB[®] Curve Fitting app (it requires the Curve Fitting Toolbox) to obtain a three-dimensional fit. Now, we define the spacing of the measurement grid and whether the transducers should sweep parallel to the X -axis or to the Y -axis. Square grid coordinates x_i, y_i are generated in the X - Y -plane, covering the X - Y -range of the point cloud of the top surface. The grid coordinates are ordered in such a manner that alternating sweeps in the positive and negative sweep direction are performed. By evaluating the fitting function at x_i, y_i , we obtain the yet missing third coordinates z_i . The resulting path is indicated by the black lines in Figs. 3.17(b) and 3.17(c). At each measurement grid point x_i, y_i, z_i , we can now calculate the tripods $\vec{n}_i, \vec{b}_i, \vec{t}_i$, indicated by, respectively, blue, red, and green lines in Fig. 3.17(b).

Next, we probe the thicknesses d_i . The algorithm uses the surface normals \vec{n}_i , seeks the vertex of the lower surface, which is pierced by \vec{n}_i , and calculates the normal distance d_i between this vertex and the corresponding grid point. The thicknesses d_i are indicated by magenta colored lines in Fig. 3.17(b) (their lengths are magnified by a factor of ten for clarity). With the now known d_i , we can determine the local layups as follows. We know that the skin element has twenty-four layers where it is 6.6 mm thick. Hence, we can deduce the number of layers at any given measurement point from d_i . Then, from the sequence of layer orientations in the “maximum” layup, we get the local layup at the i th measurement point.

For the $\Theta_{\text{in}(i)}$ calculation, the basic algorithm used by the DC was adopted. Therein, depending on the sweep direction, the propagation of Lamb waves is supposed to be either along the 0° or 90° -direction of the layup. Since we do not need complete multi-modal dispersion diagrams $\Theta_{\text{in}(i)}(f)$, where f covers a broad

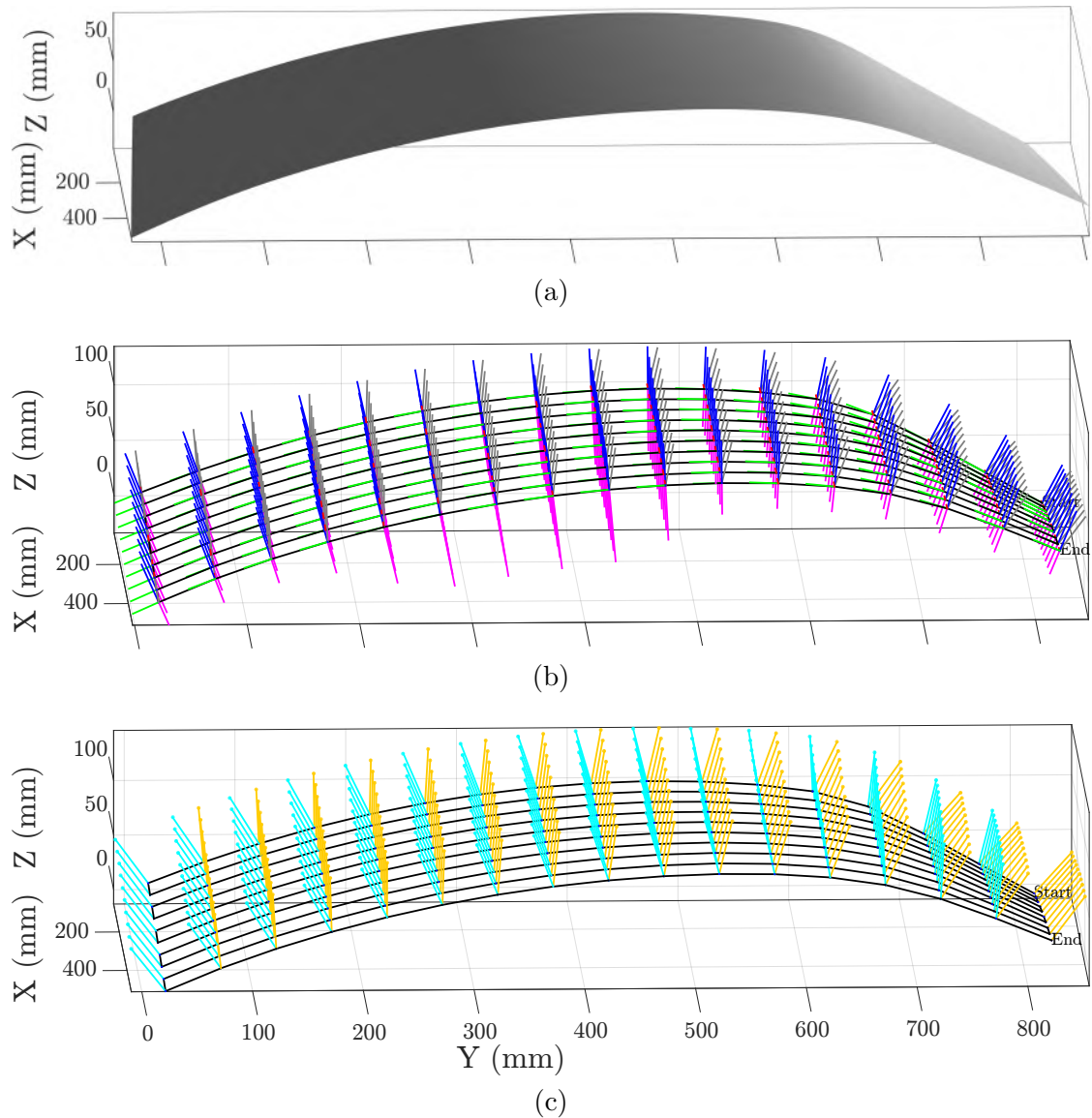


FIG. 3.17. Offline programming (EAM generation) in MATLAB[®]. (a) The STL file representing the digital twin is loaded and fitted. (b) Path (black), surface normals (blue), path tangents (green), excitation angles (gray), and magnified thickness (magenta). (c) The sender positions are located at the ends of the cyan lines and the receiver positions at the orange lines' ends. In this example, a 50 mm grid was generated, whereas a spacing of 2 mm is more realistic in a real measurement.

frequency range, we enter the transducer's frequency ($f = 200$ kHz), and calculate only $\Theta_{in(i)}(200 \text{ kHz})$ for the A_0 Lamb wave, which we intend to excite. As drawn in

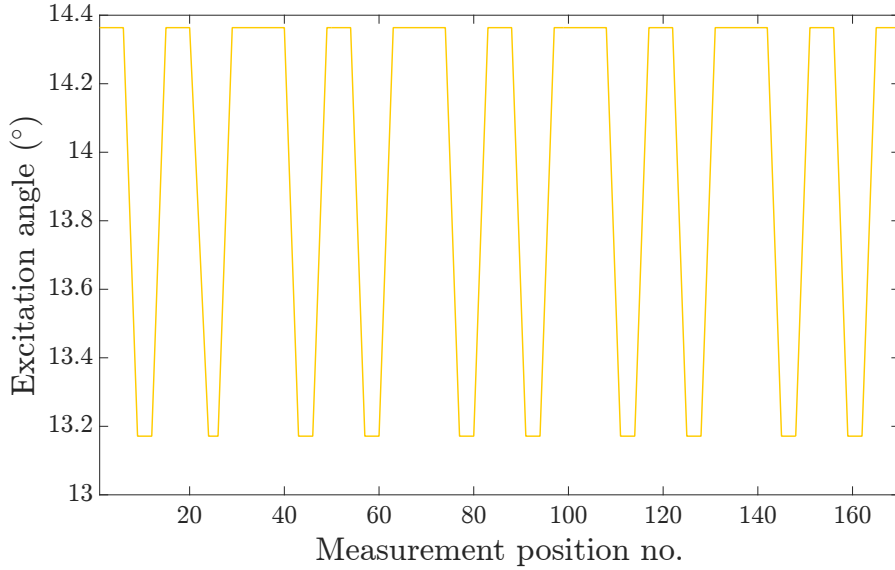


FIG. 3.18. Excitation angles at all 170 measurement points of the EAM shown in Fig. 3.17. The largest angles correspond to measurement points on the 2.2 mm thick area, and the smallest angles correspond to 6.6 mm thick areas.

Fig. 3.18, the excitation angles $\Theta_{\text{in}(i)}(A_0 @ 200 \text{ kHz})$ vary between 14.4° where the skin element is 2.2 mm thick and 13.2° where it is 6.6 mm thick. The excitation angles are indicated by gray lines in Fig. 3.17(b).

Now that we have the coordinate system frames and excitation angles for each measurement point, we can calculate the sender and receiver poses. This is done by applying a local coordinate system displacement that calculates the poses of the ultrasonic transducers according to the excitation angle and fixed distance offsets on and from the surface. Throughout the experiments discussed in this section, we used 50 mm for both offsets. We call the final prepared data set an EAM.

3.2.3 End-Effector Design

The ASRM requires that the positions and the orientations of the sender and the receiver vary with respect to each other independently over time according to the EAM. If we consider Fig. 3.16, it becomes clear that mere rotations of the transducers would not be sufficient because the distances, which the incident and reemitted sound have to propagate in air would vary with the rotation. Similarly, the distance between the points of Lamb wave excitation and detection would change. Hence, the amplitude of the received signal would already vary just from experiencing different amounts of attenuation without the presence of flaws. Therefore, to ensure constant propagation distances, the transducers must be able to move

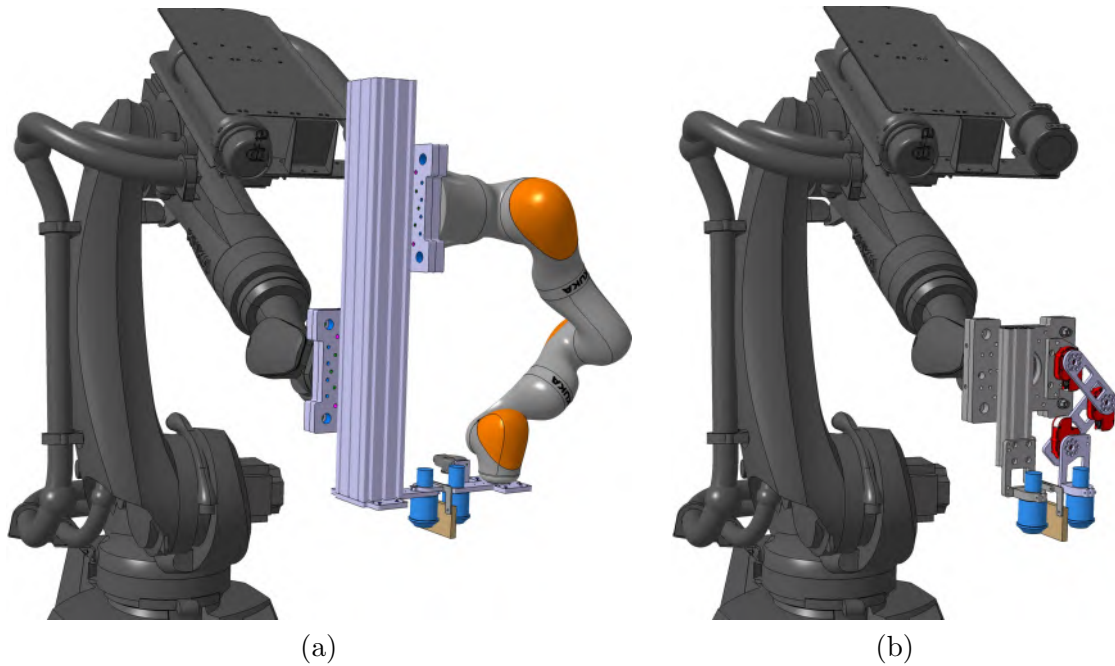


FIG. 3.19. Two prototypes of the AEE. (a) Preliminary design with a KUKA LBR iiwa and (b) more compact final design with HEBITM actuators attached to a KUKA KR120.

freely within the plane of rotation. This requires another two degrees of freedom for each transducer, resulting in a total of six degrees of freedom, namely two rotational and four translational ones. The KUKA robot alone cannot provide that much flexibility, so an additional kinematics, the AEE, has to be attached to the industrial robot. The robot serves as a kinematic for the positioning of the sender, while the second attached arm does the positioning of the receiver. Preliminary tests have been conducted with a KUKA Leichtbauroboter (LBR) iiwa as a second kinematic attached to the KR120, as this robot arm was available at the ZLP (see Fig. 3.19(a)). Since these tests had been promising, a dedicated end-effector was designed. The new design should be as compact and as simple as possible, so it was decided to reduce the functionality to the necessary minimum of six degrees of freedom (see Fig. 3.19(b)). Basically, this can be implemented as a combination of two prismatic joints and one revolute joint or three coplanar revolute joints. We chose the latter because it allowed a more compact and collision-free design while providing the necessary workspace. Three HEBITM X-Series actuators (HEBI Robotics, Pittsburgh, PA, USA) were integrated into the system. As shown in Fig. 3.20, the AEE consists of a quick-release plate, which is a standard at the ZLP, an aluminum profile, and the three X-Series actuators. The actuators are mounted on

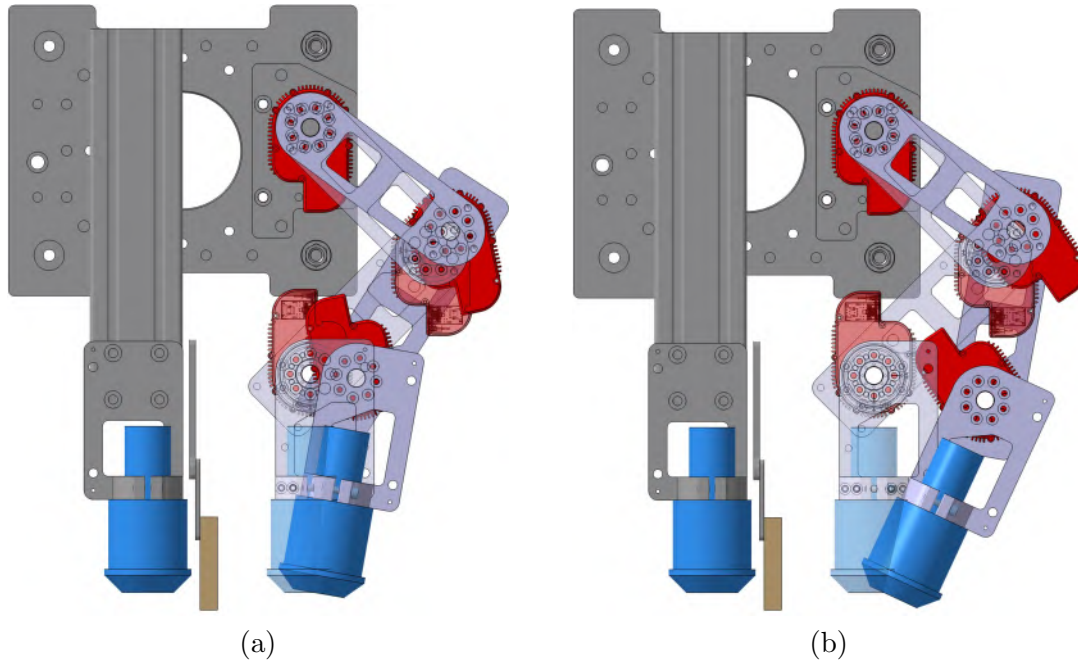


FIG. 3.20. Closeup of the final AEE design in two different situations. Combined with the KUKA robot, each transducer has the required three degrees of freedom.

aluminum links as close as possible to each other without risking collisions. The default positions of the static and moving transducers are parallel to each other with the two links in a 45° - 90° - 45° arrangement. With this default position, a widely adjustable angle between the transducers is possible. Another advantage of this configuration is the reduction of the torques on the axes “One” and “Two” (the axis “Three” holds the receiver) while providing a large workspace. To increase the precision of the AEE, all of the fixed parts as well as the quick-release plate are equipped with counterbores, which can be measured with a LEICATM laser tracker. By this way, the intrinsic dimensions of the AEE could be calibrated with high precision, thereby avoiding the position accuracy of the actuators as a source of imprecision.

For the positioning of the skin element for the inspection process, a framework was manufactured (see Figs. 3.15(b) and 3.21). It was designed in CATIATM from the lower face of the skin element, and produced on a RIDDER WariCut water jet cutter (H.G. RIDDER Automatisierungs-GmbH, Hamm, Germany). This cutter was also used for the trimming of the skin element. With this form fitting framework, it is easy to place the skin element precisely on a welding table in front of the robot repeatedly without recalibration.

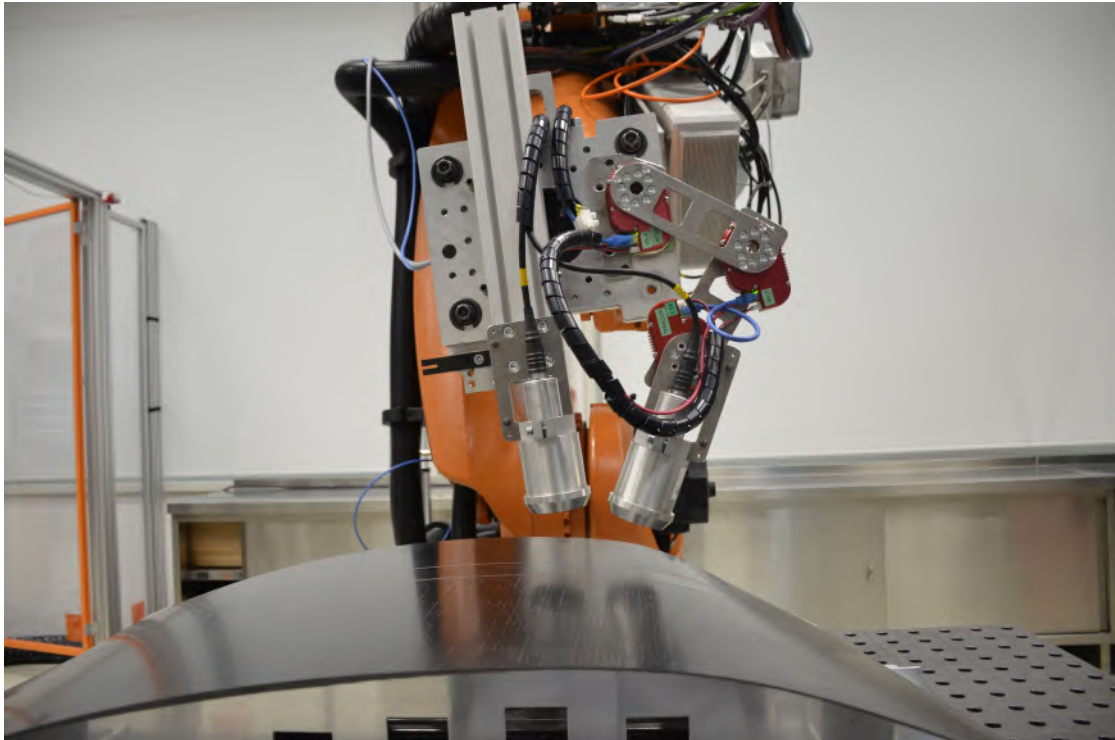


FIG. 3.21. The skin element is mounted on the framework, and the assembled AEE is ready to perform ACUT. The skin element has a strong curvature gradient on the right-hand side and three times the thickness on the left-hand side. These features require an adaptation of the excitation angle during the scanning. We call this new inspection method *adaptive slanted reflection mode*.

3.2.4 Experimental Validation

In this section, we present the inspection results of the skin element obtained with the AEE to prove that it is working correctly, and to demonstrate how the ASRM outperforms the conventional FSRM. The measurements presented here were conducted before a conference at the ZLP, which took place in May 2019. A live demonstration of the AEE was given to the visitors. In fact, there was quite a limited time available for the measurements and demonstration preparations, and the project (and funding) ended directly after the conference. Therefore, the task was to prove the capabilities of the AEE in the most efficient way possible. There was no time to scan the skin element with a square $2 \times 2 \text{ mm}^2$ grid. Instead, sweeps with 25 mm spacing and measurement points at every 2 mm increment on that sweeps were performed, resulting in a total of 8419 measurement points. However, the reader will see that, despite this somewhat perforated coverage of the skin element, the superiority of the ASRM over the FSRM, and therefore the

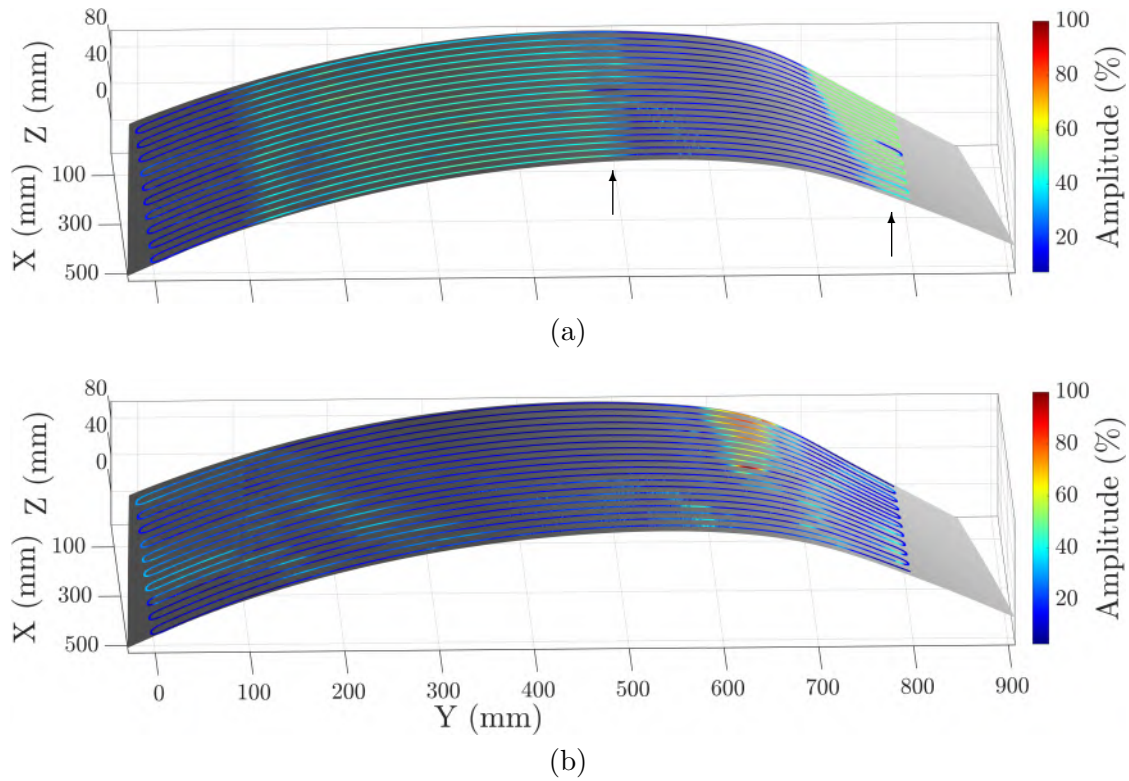


FIG. 3.22. C-scans of the skin element obtained with the FSRM using 200 kHz transducers, superimposed with the digital twin. (a) The excitation angle was adjusted on the thick area and kept constant during the scanning. Lamb waves were excited only in the thick area and in the flat area to the right. Only two flaws, indicated by the arrows, could be detected. (b) If the excitation angle is adjusted to the strongly curved area, Lamb waves are hardly excited anywhere else. No flaws were detected.

function of the AEE is demonstrated clearly. First, we used the AEE to inspect the skin element without excitation angle adaptation, *i.e.*, in the conventional FSRM. This served as a reference measurement to which we compared then the inspection results obtained by using the full functionality of the AEE.

Focused Slanted Reflection Mode

In a first measurement, the excitation angle was adjusted in such a way to excite the A_0 Lamb wave in the 6.6 mm thick area of the skin element (on the left-hand side in Fig. 3.21) using 200 kHz transducers. The gain was set to achieve a Lamb wave amplitude of about 50% to avoid an overload of the receiver upon scanning the 2.2 mm thick area with excitation angle adaptation in a later measurement

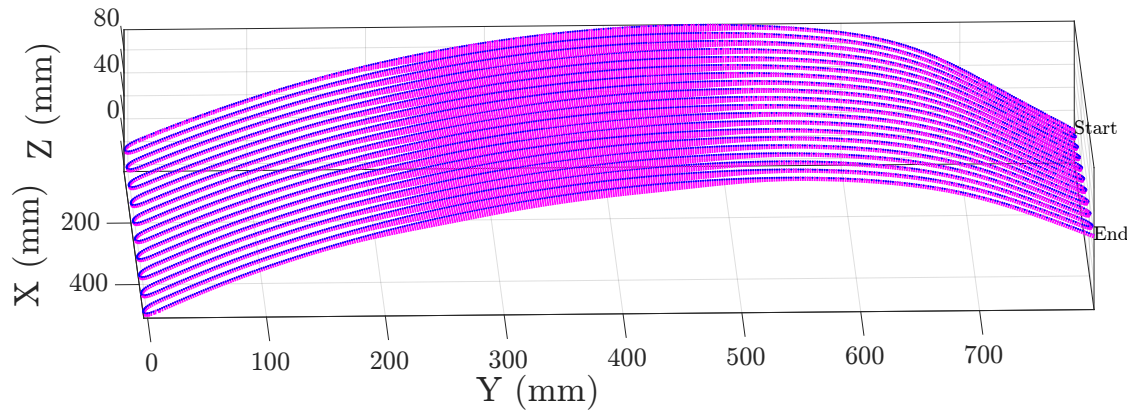


FIG. 3.23. Owing to the limited time available for the measurements, the sweeps had a spacing of 25 mm, while the distance between the measurement points was 2 mm. The blue dots mark the 8419 points, and the magenta lines indicate the corresponding thicknesses.

(we will see later that overloading still happened). Of course though, we could have increased the gain to get a much higher amplitude, but then we could hardly compare this measurement with those conducted using the ASRM later. The scanning speed throughout all measurements was 100 mm/s ($PRF = 50$ Hz). The skin element was scanned without adapting the excitation angle to the variations in the thickness and curvature, *i.e.*, using the FSRM. The resulting C-scan is shown in Fig. 3.22(a). We get a rather stable amplitude in the thick area, but as the thickness and curvature change, the Lamb wave was not excited at all, except in an area close to the right edge. Here, the skin element is 2.2 mm thick and flat, and the excitation angle matched these conditions just by coincidence. In the second measurement, we adjusted the excitation angle in the area possessing the strongest curvature. As can be seen in Fig. 3.22(b), we obtained an amplitude of up to 90% in a small area around $Y = 640$ mm. The gain was the same as the one used in the first measurement, but since the thickness in the strongly curved area is only 2.2 mm, we get a higher amplitude there than in the 6.6 mm thick area in Fig. 3.22(a). However, A_0 was excited only sporadically in the remainder of the skin element. Clearly, the FSRM is unsuitable for the inspection of the skin element, and we shall see in the next section how the ASRM solves the deficiency.

Adaptive Slanted Reflection Mode

Finally, we inspected the skin element in the ASRM, using the full functionality of the AEE. The corresponding C-scan is presented in Fig. 3.25(a). As expected, we find the same amplitude in the thick area as we got it from the FSRM inspection shown in Fig. 3.22(a). However, in the complete remainder of the skin element, we

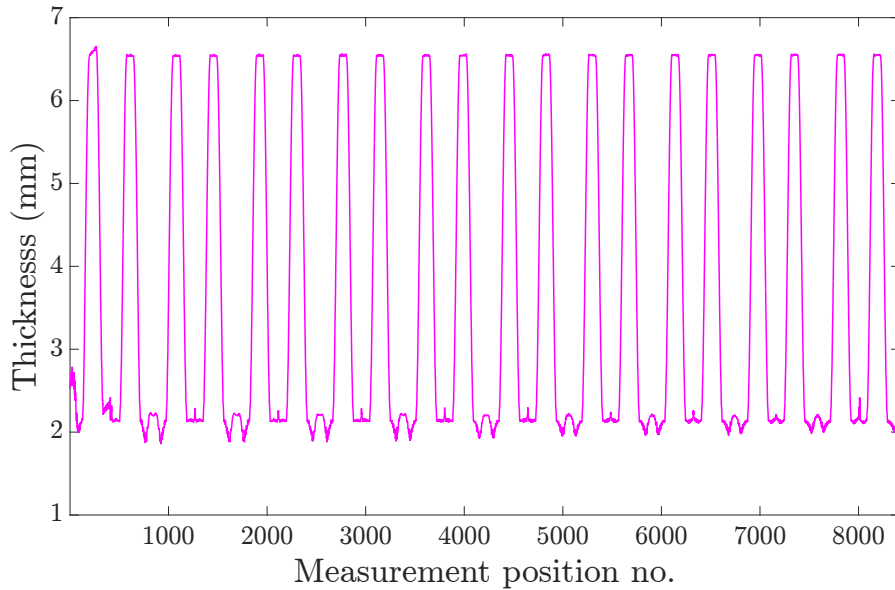


FIG. 3.24. The thickness versus the measurement point number. The C-scan shown in Fig. 3.25(b) is obtained by multiplying the amplitudes with these thickness values.

were now able to excite A_0 despite the different thicknesses and curvatures present there. It turns out that we should have decreased the gain even more because now the amplitude in the 2.2 mm thick areas exceeds 100%. Only in the strongly curved area between $Y = 600$ mm and 700 mm, we had an unstable Lamb wave excitation. This happened due to technical issues with the HEBITM actuators³.

We have seen that the amplitude is affected by the thickness of a specimen not only due to the dispersional effect, but also by the mere fact that a thicker plate takes more energy for the vibration. It is the purpose of the gain to compensate this effect. Therefore, one could think of also adapting the gain according to the thickness at a given measurement point. However, our software tool chain provides us with the thicknesses at every measurement point, and we can use this information upon the amplitude in the post process. The magenta lines in Fig. 3.23 represent the thicknesses of the skin element at every measurement position, whereas Fig. 3.24 plots the actual values. The C-scan in Fig. 3.25(b) plots the multiplication of the raw amplitude values shown in Fig. 3.25(a) with the thicknesses. The thick area shows a higher amplitude-thickness product than the surrounding because the raw amplitude in the thin area was overloaded, *i.e.*, it is actually higher. However, the color difference between both areas is already notably smaller than the one

³They were leased exhibits only, and there was no time and funding left to replace them with new ones.

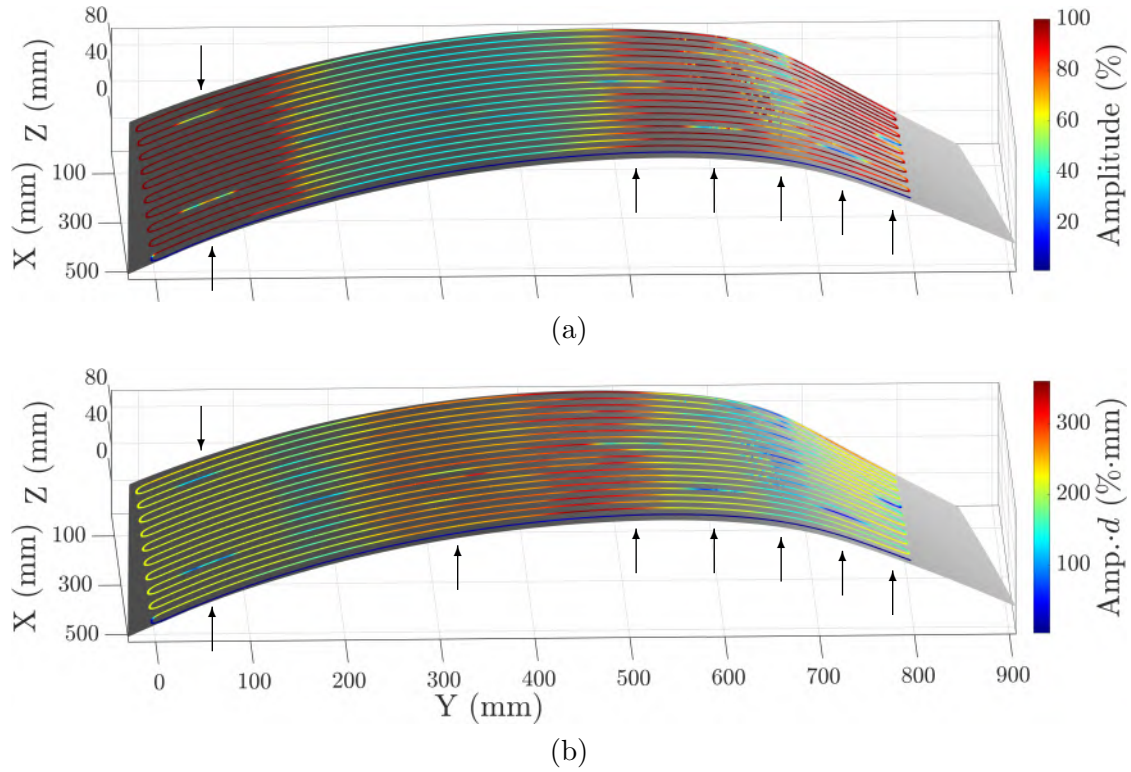


FIG. 3.25. C-scans of the skin element obtained with the ASRM using 200 kHz transducers, superimposed with the digital twin. The C-scans clearly outperform the FSRM results from Fig. 3.22. (a) Raw amplitude. The receiver was overload in the thin areas. At least seven flaws, indicated by the arrows, were detected. (b) Amplitude-thickness product. Since the amplitude in the thin area is actually higher than 100 %, the amplitude-thickness product should be higher as well, and hence closer to the one in the thick area (between $Y = 250$ mm and 520 mm). At least eight flaws could be detected.

seen in Fig. 3.25(a). Unfortunately, there was no time for another inspection with a lower gain to avoid the amplitude overloading in the thin areas. From such a measurement, we may readily expect a (nearly) homogeneous color distribution all over the skin element.

Comparison

Nevertheless, already with this overloaded inspection, the improvements achieved by the ASRM as compared to the FSRM inspection seen in Fig. 3.22 are tremendous. We can excite Lamb waves everywhere on the skin element and achieve a more homogeneous C-scan by the multiplication with the thicknesses. Let us quantify the improvement in terms of the detected flaws, although the large distance of

25 mm between each sweep makes it harder. By using the FSRM, we can detect only two flaws (see Fig. 3.22(a)) compared to (at least) eight flaws identified with our ASRM (compare Fig. 3.25). We count the several indications present in the strongly curved area as one since, owing to the wide gaps between the sweeps, we cannot distinguish them very clearly.

4 Conclusions and Outlook

In this thesis, two developments were presented. Firstly, with the Dispersion Calculator, the first free software for calculating guided wave dispersion diagrams in multilayered composites was released, featuring the unique capability of calculating laminates consisting of several hundreds of layers. And secondly, an Adaptive End-Effector was developed, enabling the automated single-sided air-coupled ultrasonic inspection of components with varying thicknesses and curvatures. Through the on-the-fly adaptation of the Lamb wave excitation angle, the Adaptive End-Effector clearly outperforms the conventional nonadaptive inspection. The development of the Adaptive End-Effector required the creation of a program for the calculation of tens of thousands of excitation angles in one loop. Therefore, the stiffness matrix method was implemented in MATLAB[®], ultimately leading to the creation of the Dispersion Calculator.

4.1 Dispersion Calculator

The MATLAB[®]-based Dispersion Calculator is an interactive and fully validated stand-alone software for the computation of dispersion curves and mode shapes of guided waves in isotropic materials and multilayered composites. The Dispersion Calculator can be downloaded¹ free of charge. For instance, dispersion diagrams are needed for the nondestructive ultrasonic inspection of components by means of Lamb waves, for example in the aerospace manufacturing at the DLR, as well as for acoustical emission investigation or pipe inspection. In fact, there is no other free software available, and in particular there is no software that parallels the capability of the Dispersion Calculator of calculating laminates consisting of several hundreds of layers, as we encounter them in the rocket booster manufacturing at the DLR. To give proof of this capability, we have calculated dispersion diagrams for a 50 mm thick $[0/90/45/-45]_{50s}$ layup, containing four hundred layers as well as for a 125 mm thick $[0/90]_{250s}$ layup, consisting of one thousand layers. User reports and requests prove that the Dispersion Calculator has quite an impact in the scientific community since its initial release in November 2018. In particular, the speed and reliability of the Dispersion Calculator compared to code owned by the NASA (National Aeronautics and Space Administration, Washington, D.C.,

¹https://www.dlr.de/bt/en/desktopdefault.aspx/tabid-2478/11208_read-53373/

USA) was acknowledged by Professor Marvin Hamstad. Similarly, Professor Michel Castaings (Institut National Polytechnique (INP), Bordeaux, France) assessed the performance of the Dispersion Calculator to be very fast. To make this performance possible, the Dispersion Calculator relies basically on three components. Firstly on Rokhlin and Wang's stiffness matrix method, secondly on the implementation of special characteristic functions and boundary conditions for modal solutions, and thirdly on the implementation of highly efficient and robust dispersion curve tracing algorithms. The stiffness matrix method is known for its capability of efficiently calculating many layers, and although it is seventeen years old, to the best of the author's knowledge, it is still unparalleled by any other stable computation method in this respect. However, it was not yet shown how to distinguish the six different mode families (symmetric, antisymmetric, and nonsymmetric Lamb and shear horizontal modes) with it. Depending on the symmetry and coupling properties of a laminate, a maximum of four different mode families can occur simultaneously, and not distinguishing them has a critical effect on the dispersion curve tracing. Crossing dispersion curves pose the well-known risk of jumping to the wrong mode during the tracing. This problem is avoided by assigning the modes to their respective families and by tracing them using family-specific characteristic functions and boundary conditions, thereby providing also the mere information of what family a mode belongs to. Since crossing modes still occur in coupled cases (Lamb and shear horizontal modes cannot be distinguished) and in nonsymmetric layups (symmetric and antisymmetric modes cannot be separated) intrinsically, particularly robust tracing algorithms are implemented to take care of that. Moreover, since the dispersion curve calculation for a multilayered composite would be extremely slow without any curve tracing algorithms, the implementation is optimized for speed without compromising robustness. Parts of this work were published in the Journal of the Acoustical Society of America in 2018 [63].

We have utilized the DC to calculate and discuss mode shapes and bulk wave patterns of Lamb waves propagating in $[0/90]_{2s}$ and $[0/90]_4$ layups. A mode shape plot shows the through thickness displacement pattern of a mode, whereas the bulk wave pattern displays the reflection of the contributing bulk waves in every layer. With the help of the bulk wave pattern, and by considering also the bulk waves' amplitudes, we explained the appearance of the mode shape of the B_{10} Lamb wave in the $[0/90]_4$ layup qualitatively. Whereas DISPERSE can plot modes shapes of guided waves in multilayered specimens, the author is not aware of any other literature or software plotting *quantitative* bulk wave patterns in multilayers. In another study, we have revealed how mode shapes depend on the mode type, mode order, and on the frequency in a given plate. Beside the dispersion diagram, this knowledge is important for an NDI inspector to choose the appropriate mode and frequency for a specific task. The ratio of in-plane and out-of-plane displacement determines a mode's suitability to detect flaws of specific shapes and orientations

within a plate. The through thickness distribution of the displacement field affects the sensitivity of a mode to flaws residing in different depths (for instance, Rayleigh waves are predestined for the detection of near-surface flaws). Modes excited in a region of minimal phase velocity dispersion are well-suited for long-range inspection tasks. Specific points in a dispersion diagram exist where a mode has zero out-of-plane displacement, leading to traction free surfaces in a fluid. Such modes are also suitable for long-range testing. In most scenarios, the fundamental modes A_0/B_0 and S_0/B_1 at rather low frequency-thickness products are optimal for NDI purposes. For transversely isotropic specimens, we have presented polar dispersion diagrams. This kind of diagram displays the anisotropy of guided wave propagation at a given frequency, without the need for calculating multiple dispersion diagrams at different propagation angles. We have reported the existence of quasipure coupled modes in the 50 mm thick $[0/90/45/-45]_{50s}$ layup mentioned above. These kind of modes show nearly-pure characteristics, namely coupled waves where either the shear horizontal displacement almost vanishes (quasipure Lamb waves) or the sagittal displacement is almost zero (quasipure shear horizontal waves). This phenomenon occurs if the wavelength of the bulk waves contributing to the guided wave is large compared to the layer thickness. The bulk waves do not “feel” the anisotropy anymore, and the coupling between them becomes small. Then, the laminate behaves like an effective medium with averaged elastic properties. Theoretically, this offers the possibility of modeling a large laminate by just one layer with averaged elastic properties, thereby reducing the computational expense from hours to minutes or even seconds. However, even at relatively modest frequencies in commercially important composite layups, a full consideration of the layering is essential for the accurate description of guided waves in these materials. We therefore investigated the benefit of another approximation method where a number of unit cells is represented by a single unit cell of larger thickness. Approximating $[0/90]_{250s}$ by $[0/90]_{25s}$ yielded a reduction of the processing time by 82 %, while both dispersion diagrams were in very good agreement, except for some deviations occurring between the higher order modes’ dispersion curves. However, the grouping of layers usually cannot be applied to typical thick-walled components such as rocket booster pressure vessels since the layups are often too complicated. Therefore, we ultimately need the full capacity of the DC to calculate large numbers of layers.

Although the Dispersion Calculator v1.5, available at the time these lines are written, has already reached a high level in terms of functionality, reliability, speed, and user friendliness, the work is far from being terminated after the completion of this thesis. Michel Castaings and Cherif Othmani [157] are awaiting the implementation of viscoelasticity to enable a comparison with their codes. This implementation will provide the attenuation experienced by guided waves, which is of course an important effect when it comes to long range testing applications. The next

important physical phenomenon to be implemented is the energy leakage to a fluid surrounding the laminate, also referred to as *fluid loading*. As the fluid becomes denser and acoustically faster, the amount of energy leaking from the laminate and in turn the attenuation increases, and the dispersion curves change accordingly. Furthermore, since the Dispersion Calculator currently calculates isotropic materials besides the transversely isotropic laminates, it suggests itself to calculate also combinations of them such as fiber metal laminates like glass laminate aluminum reinforced epoxy. Michel Castaings has also asked to have orthotropic materials included with the full set of nine independent stiffness matrix components compared to the five stiffness matrix components of transversely isotropic materials. Another useful future implementation would be the modeling of guided wave propagation along the circumference of a cylinder and along rods. It is also planned to simulate the temporal and frequency responses of guided wave modes propagating in plates. The user will be able to analyze the signal of voltage versus time, which he acquires in his experiment, in terms of what modes are excited. Finally, it will always remain a task to increase the speed of computation.

4.2 Adaptive End-Effector

The second development presented in this thesis is the Adaptive End-Effector, enabling a new inspection mode termed *adaptive slanted reflection mode*. This mode is a significant improvement compared to the conventional *focused slanted reflection mode*. Here, Lamb waves are excited in a component by a sender transmitting ultrasound at the appropriate excitation angle with respect to the component. Likewise, the receiver is oriented under the same angle to detect the ultrasound reemitted by the Lamb waves propagating in the component. Since both transducers are located on the same side of the component, this arrangement enables the single-sided inspection of components, which do not provide access from both sides like rocket booster pressure vessels. However, the Lamb wave excitation angle depends upon the layup and curvature of a laminate. Therefore, if one or both parameters vary from one location to another during the scanning, the excitation angle changes accordingly, and Lamb waves are excited at poor efficiency or not at all. Such geometric variations are common in structures like aircraft fuselages for instance. Therefore, the Adaptive End-Effector allows the on-the-fly adaptation of the excitation angle during the scanning so that Lamb waves are excited at optimal efficiency according to the local layup and curvature. The required excitation angle map of the component is calculated in MATLAB[®], based on the same algorithms used by the Dispersion Calculator. The program loops through all points of the measurement grid covering the component, extracts the local thicknesses and layups and calculates the corresponding excitation angles of the fundamental

Lamb wave mode A_0 at the transducer frequency. The excitation angles in turn are converted into the transducers' poses, and a robot program is generated.

We have inspected an aircraft skin element demonstrator possessing variable layups and curvatures with the Adaptive End-Effector, with and without excitation angle adaptation. Only with this adaptation, it was possible to excite Lamb waves everywhere in the skin element. In addition, we have multiplied the thicknesses obtained at each measurement point with the corresponding ultrasonic amplitudes to balance the effect of a reduced Lamb wave amplitude with increasing laminate thickness. This resulted in a tremendous improvement of the ultrasonic imaging quality and of the probability of flaw detection. Only two of the artificial flaws inserted into the skin element were detected in the focused slanted reflection mode compared to eight using the adaptive slanted reflection mode. The more robotic-focused part of this work was published in the proceedings of the 16th International Conference on Informatics in Control in 2019 [119], while the mainly ultrasonics-concerned part was submitted to the World Conference on Non-Destructive Testing to take place in 2020. Furthermore, a patent process is currently pending at the German Patent and Trademark Office (Deutsches Patent- und Markenamt, Munich, Germany). A patent was granted to an earlier version of the Adaptive End-Effector by the same institution in 2018².

²<https://register.dpma.de/DPMAregister/pat/register?AKZ=1020141051106&CURSOR=0>

A Dispersion Calculator User's Manual

Dispersion Calculator User's Manual



Version 1.7
June 2020
Copyright © 2018-2020 DLR



Deutsches Zentrum
für Luft- und Raumfahrt
German Aerospace Center

Armin Huber

Center for Lightweight Production Technology (ZLP)
Institute of Structures and Design
German Aerospace Center (DLR)
86159 Augsburg
Germany

Email: armin.huber@dlr.de



Contents

1	Introduction	1
2	Quick start	2
3	The graphical user interface	3
3.1	Menu bar	3
3.2	Isotropic	3
3.3	Transversely isotropic	10
3.4	Polar diagrams	14
3.5	Bulk waves	15
3.6	Laminate stiffness	21
3.7	Material editor	22
3.8	Advanced	23
4	Examples	27
4.1	T800M913 single layer @ 45°	27
4.2	T800M913 [0/90] ₄ @ 45°	28
4.3	T800M913 [0/90] _{100s} @ 0°	29
A	List of default materials	31
A.1	Isotropic	31
A.2	Transversely isotropic	32
	References	33

1 Introduction

The nondestructive inspection (NDI) of components by means of guided waves is an emerging technology in fields like aerospace or pipeline construction. The guided waves' capability of propagating many meters in a structure is utilized for swift inspection tasks as well as structural health monitoring by means of acoustical emission. The German Aerospace Center (DLR) uses Lamb waves excited by air-coupled ultrasound for the quality assurance of large-scale aerospace vehicle components made from carbon composites. However, the use of guided waves in NDI requires knowledge of the dispersion curves. DISPERSE¹ (Imperial College London, London, UK) is the most renowned software for the calculation of dispersion curves. It has been developed since the early 1990s by Lowe and Pavlakovic, and it is used for the validation of the Dispersion Calculator (DC).

The task that triggered the development of the DC was the calculation of incidence angles for the excitation of Lamb waves for the air-coupled ultrasonic inspection of rocket booster pressure vessels of the future launcher Ariane 6. These vessels are made of carbon fiber reinforced plastics (CFRP) in order to make them lighter, and therefore enable the launcher to carry more payload. In some areas, such pressure vessels can consist of up to four hundred layers, which is a challenging task to calculate them. To facilitate the calculation, it is a common practice to group layers, but this is not possible here because the layups are very complicated and irregular in terms of the winding angle (fiber orientation) and of the layer thicknesses. Therefore, every single layer has to be calculated, and the *stiffness matrix method* (SMM), which has been developed by Rokhlin and Wang [1, 2], has been implemented with MATLAB[®] (MathWorks, Natick, MA, USA) to perform these calculations [3]. The DC is the compiled version of the MATLAB[®]-scripts and can be downloaded² free of charge since its initial release in November 2018. The DC is an interactive and fully validated stand-alone software for the computation of dispersion curves (phase and group velocity and more) and mode shapes (displacement, stress, strain, and more) of guided waves in isotropic and multilayered composite plates. The DC features the particularly challenging capability of calculating laminates consisting of several hundreds of layers and is able to distinguish the different mode families, like symmetric and antisymmetric Lamb and shear horizontal waves, depending on the symmetry and coupling properties of a given layup. Lastly, the DC features highly efficient and robust dispersion curve tracing algorithms. The specimen geometry is currently limited to plates, but the results can be used for curved specimens with a not too small radius in good approximation. Also, the DC does currently not include attenuation caused by viscoelasticity and energy leakage to the surrounding medium. These features will be implemented in future releases.

The handling of the DC is explained in Sec. 3. Section 4 contains some examples to enable the reader to use the settings systematically depending on what kind of problem

¹<http://www.imperial.ac.uk/non-destructive-evaluation/products-and-services/disperse>

²https://www.dlr.de/zlp/en/desktopdefault.aspx/tabid-14332/24874_read-61142/#/gallery/33485

he encounters in the dispersion curve tracing procedure. The default materials available in the DC are listed in Appendix A.

2 Quick start

1. Go to the **Material editor**.
2. In the **Transversely isotropic materials** panel, enter the engineering constants or stiffness matrix components of your material.
3. Enter a **Material name** and press **Save**.
4. Go to the **Transversely isotropic** tab.
5. Press **Edit**, select your material, and enter your layup.
6. Press **Calculate** to calculate the dispersion diagram.
7. Press **Plot** in the **Dispersion diagrams** panel.
8. Click on a dispersion curve to display values. Press the Shift key to place multiple data tips.
9. Press **Plot** in the **Through thickness profiles** panel to display the displacement components of the A_0 Lamb wave at the highest frequency covered by the dispersion diagram.
10. Activate the **Animate** check box in the **Animation settings** panel and press **Plot** below to animate the displacement pattern of the A_0 Lamb wave at the above frequency.

3 The graphical user interface

The GUI of the DC requires 1200×800 pixels so that it does not fit on smaller screens like the common 1366×768 notebook screen. In this case, maximize the GUI and use the slider in the lower left corner of the **Isotropic** tab to shift the GUI up and down.

3.1 Menu bar

In the **File** menu, an existing project file can be opened or the current project be saved as *.mat by pressing **Open project** or **Save project**, respectively. A project file comprises the complete GUI including your data. If you open a project, wait until the saved GUI opens. You can close the other GUI. Press **Help** to read the DC's manual. Press **Homepage** to open the web page of the DC in your system's browser.

3.2 Isotropic

The **Isotropic** tab consists of several panels. Start by defining the **Specimen** (1) (see Fig. 1). Select an isotropic **Material** from the drop-down menu and set the **Thickness** of the plate in millimeters. You can directly **Calculate** (7) the dispersion diagram or

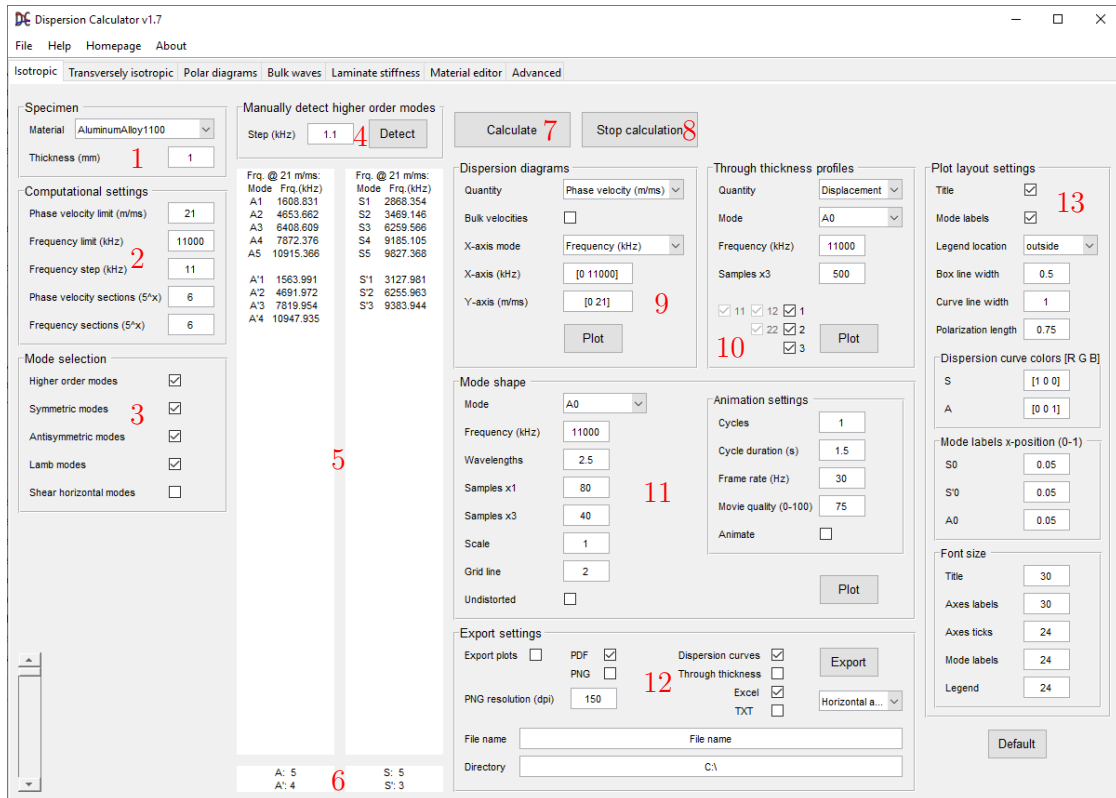


FIG. 1. The tab for the calculation of isotropic specimens.

change the **Computational settings** (2) first. The **Phase velocity limit** determines up to which phase velocity the dispersion curves are calculated. A value is proposed based on the material's plate wave velocity. The **Frequency limit** determines up to which frequency the dispersion curves are calculated. Again, a value is proposed, now depending on the plate wave velocity and the **Thickness** of the plate. The **Frequency step** sets the frequency resolution of the dispersion curves. It is set to 0.0001 of the default **Frequency limit**. The number of **Phase velocity sections** determines the ability to find a modal solution. At each frequency step, starting at low frequency, a first guess is made in which phase velocity search interval the modal solution for a particular mode should lie in-between (find more information in Sec. 3.8). This is necessary to avoid an extremely slow curve tracing. It is then checked, whether there is a modal solution in the search interval (sign change and minimum in the characteristic function). If yes, then a bisection algorithm starts to converge upon the root until the desired phase velocity resolution is obtained. If no root is found, an x -loop starts to divide the search interval into 5^x sections, until a root in a section is found, and then the bisection of the critical section starts unless the desired resolution has already been reached. The number of **Phase velocity sections** x as the power of five sets the maximum number of sections into which the search interval is divided. Since the higher order modes are almost parallel to the phase velocity axis at high phase velocities, the usual phase velocity sweeps at certain frequency steps do not work there very well, and the dispersion curves are often incomplete. Therefore, frequency sweeps are performed at certain phase velocity steps to complete the curves up to the **Phase velocity limit**. The **Frequency sections** work similarly like the **Phase velocity sections**. Higher values in **Phase velocity sections** and **Frequency sections** increase the chance to find modal solutions, and therefore accomplish the tracing successfully at the cost of processing time. However, setting low numbers does not necessarily cause problems in the curve tracing because there is a routine involved that replaces missing samples. This routine fits the already known samples and extrapolates them to the current frequency step. However, if too many samples are missing, the fit goes off and the tracing fails. The modes are traced one after the other and for each mode family separately, starting with the fundamental modes and continuing with increasing mode order.

In the **Mode selection** (3) panel, you can select which mode families shall be calculated and whether the higher order modes shall be calculated in addition to the fundamental ones or not. There exist symmetric and antisymmetric Lamb and shear horizontal waves. Use the check boxes accordingly.

If you want to calculate the higher order modes, a frequency sweep at the **Phase velocity limit** is performed to detect their cut-off frequencies. This can be done in the **Manually detect higher order modes** (4) panel by pressing **Detect**. Otherwise, it will be performed automatically upon pressing **Calculate**. The **Step** determines the increments at which the characteristic functions of all mode families are evaluated. Vary this value if you are not sure whether you have detected all modes. A smaller **Step** yields a higher mode cut-off frequency detection probability. It is essential for the dispersion curve tracing that you must have detected *all* modes.

The upper output windows (5) list the detected modes with their cut-off frequen-

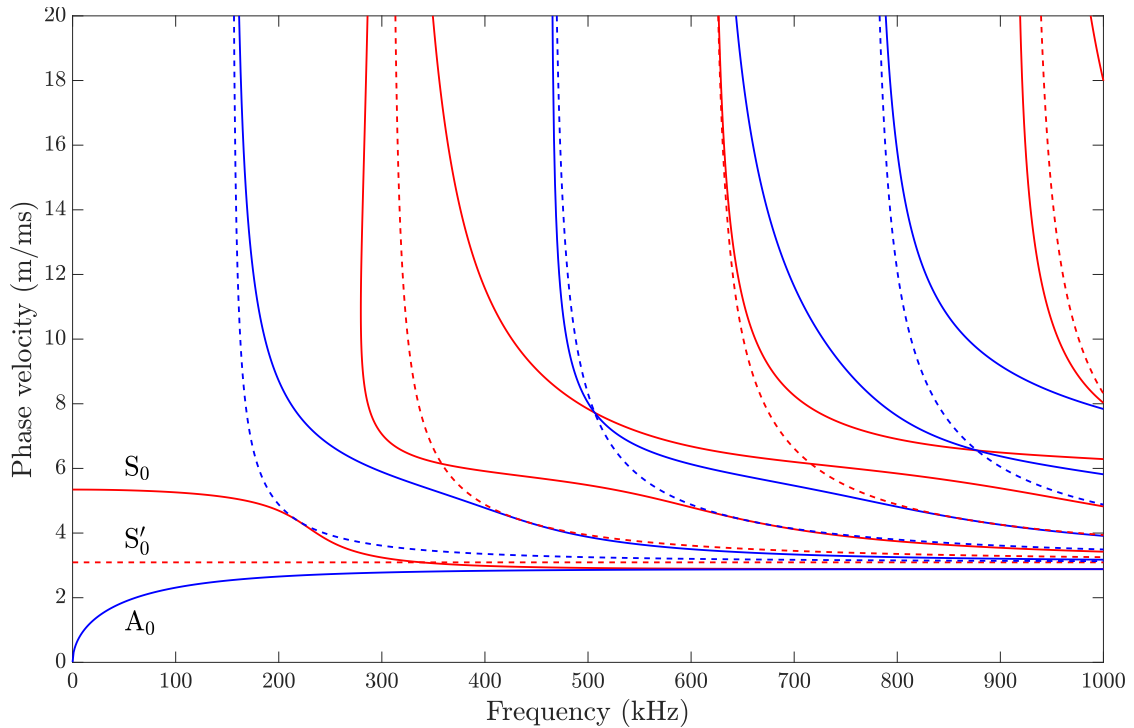


FIG. 2. Dispersion diagram of a 10 mm thick AluminumAlloy1100 plate. Solid lines indicate Lamb modes, dashed lines are shear horizontal modes. Red curves represent symmetric and blue ones antisymmetric modes.

cies. The primed letters denote shear horizontal modes. The lower output windows (6) summarize how many modes of each family have been found.

Upon pressing **Calculate** (7), a window opens showing the dispersion curve tracing in live. Press **Stop calculation** (8) to terminate the calculation. When the calculation is complete, a message informs you about the elapsed time.

Now you can go to the **Dispersion diagrams** (9) panel. Use the **Quantity** drop-down menu to choose between the phase velocity, group velocity, propagation time, excitation angle, wavelength, and wavenumber. The option below **Quantity** switches depending on what kind of **Quantity** you have selected. If you have selected “Phase velocity” or “Group velocity”, you have a check box to choose whether the **Bulk velocities** should be displayed in the dispersion diagram or not. If you have selected “Propagation time”, you can enter the **Distance** for which the propagation time shall be calculated. Finally, if you have chosen “Excitation angle”, you have a drop-down menu that allows to choose the **Couplant**. This coupling medium yet affects only the excitation angle via Snell’s law of refraction (for the calculation of the phase velocity dispersion, a vacuum is assumed to surround the plate so that no energy can leave the plate). The excitation angle is given with respect to the normal to the plate. Use the **X-axis mode** drop-down menu to draw the dispersion curves as function of the frequency in kHz, MHz, or frequency-thickness product in

MHz·mm. Set the **X-axis**, e.g., [0 1000], and the **Y-axis** limits, e.g., [0 20]. Upon pressing **Plot**, the diagram is plotted in a new window. In the menu bar, you can export the plot by going to **File** → **Save**, or **Save As**, or **Export Setup**. The **Show modes** menu allows you to show/hide every particular dispersion curve in an easy way.



Upon hovering the cursor over the plot, the axes toolbar becomes visible. It offers up to seven tools, depending on the plot type (see on the right). The first symbol opens a drop-down menu containing three more symbols. The floppy disk symbol allows to export tightly cropped png and pdf-images, a very useful tool if you want to insert the plots into publications. If you want to remove data or replace them by NaN, toggle the

Brush/Select Data tool and left-click on a data point or drag a rectangle over the data while pressing the left mouse button. Then right-click on the selected data and choose an action from the pop-up menu. Note that data are removed only from the plot, but not from the storage, i.e., your changes will be lost once you close the plot window. Activate the **Data Tips** and click on a curve to display actual values. You can place multiple data tips by pressing the “Shift” key. Move the curves by using **Pan** and **Zoom In** and **Zoom Out**. Use **Restore View** to reset the plot.

Figure 2 shows the phase velocity dispersion of Lamb and shear horizontal waves in 10mm thick AluminumAlloy1100. Red curves indicate modes with a symmetric displacement pattern, blue curves are antisymmetric modes. Solid lines indicate Lamb waves, dashed ones represent shear horizontal waves. The fundamental antisymmetric Lamb mode A_0 starts at zero phase velocity while S_0 starts at the plate wave velocity of that material. Both fundamental modes tend toward the Rayleigh velocity for high frequencies. The fundamental shear horizontal wave S'_0 is nondispersive at the transverse bulk velocity. The higher order modes start at their respective cut-off frequencies at high phase velocity and tend toward the transverse velocity. The higher order modes are labeled $A_n, S_n, A'_n, S'_n, n = 1, 2, \dots$, from left to right in the dispersion diagram. The primed letters denote shear horizontal modes.

Now go to the **Through thickness profiles** (10) panel. Use the **Quantity** drop-down menu to choose between “Displacement”, “Stress”, “Strain”, “Energy density”, “Power flow density”, and “Bulk waves”. Let us introduce a coordinate system $x_i = (x_1, x_2, x_3)$, where the plate lies in the x_1 - x_2 -plane, x_1 is the propagation direction of the guided wave, and x_3 is normal to the plate. The total energy density E_{total} is the energy per unit volume carried by a guided wave. It has two contributions, namely the strain energy density E_{strain} and the kinetic energy density E_{kin} so that $E_{\text{total}} = E_{\text{strain}} + E_{\text{kin}}$, where

$$E_{\text{strain}} = \frac{1}{2} \sigma_{ij} \varepsilon_{ij}, \quad i, j = 1, 2, 3, \quad (1)$$

with the stress tensor σ_{ij} and the strain tensor ε_{ij} , and

$$E_{\text{kin}} = \frac{1}{2} \rho \dot{u}_i^2, \quad (2)$$

where ρ is the material's density and \dot{u}_i is the particle velocity vector, which is obtained from the time derivative of the particle displacement vector u_i . These energy densities

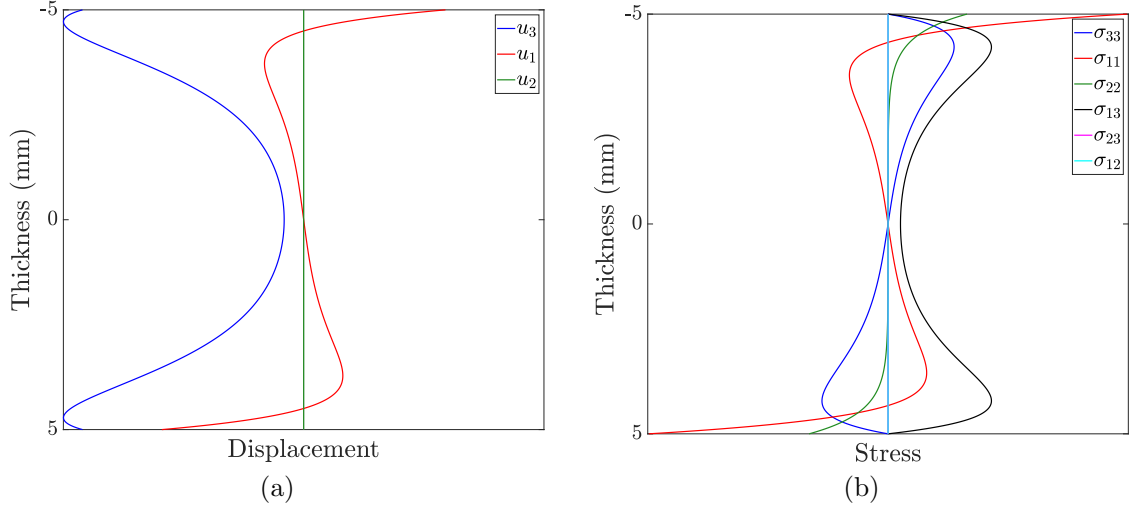


FIG. 3. (a) Displacement and (b) stress field components of the A_0 Lamb wave at 1 MHz in 10 mm thick AluminumAlloy1100.

vary over the thickness (x_3) of a plate, and to obtain the total energy carried by a guided wave, one would integrate the energy density contributions over x_3 (and x_2). The power flow density P_j is the energy flow per unit volume and unit time carried by a guided wave. It is a vector (*Poynting vector*) indicating the magnitude and direction of the power flow

$$P_j = -\frac{1}{2}\sigma_{ij}\dot{u}_i = -\frac{1}{2} \begin{bmatrix} \sigma_{11}\dot{u}_1 + \sigma_{21}\dot{u}_2 + \sigma_{31}\dot{u}_3 \\ \sigma_{12}\dot{u}_1 + \sigma_{22}\dot{u}_2 + \sigma_{32}\dot{u}_3 \\ \sigma_{13}\dot{u}_1 + \sigma_{23}\dot{u}_2 + \sigma_{33}\dot{u}_3 \end{bmatrix}. \quad (3)$$

Much like the energy density, P_j varies over the thickness of the plate. In absence of attenuation caused by energy leakage, there is only power flow along the propagation direction P_1 , (and P_2 in coupled cases in transversely isotropic media) while P_3 (normal to the plate) is zero. An important improvement has been introduced with the DC v1.7, namely the power normalization of the through thickness profiles in accordance with DISPERSE. This means that all quantities like displacement, stress, etc. are calculated for modes having a power flow of unity along the propagation direction. Mathematically, the power flow density component P_1 is integrated over the thickness x_3 . Then, for instance, to get the power normalized displacements, the displacements are divided through the square root of P_1 . The advantage of this is that values of displacement, stress, strain, etc. can now be compared at different points on dispersion curves whereas in earlier releases, only their SHAPES could be compared. The developer of DISPERSE, Mike Lowe, describes the benefit of power normalization as follows: “[...] once we normalise the mode shapes to power flow then we can do some meaningful comparison from one point on a curve to another, provided our understanding of the comparison is in that context only - e.g., if the mode has unit power flow, then it has a displacement at frequency xxx that is yyy times bigger than it would be at frequency zzz.”

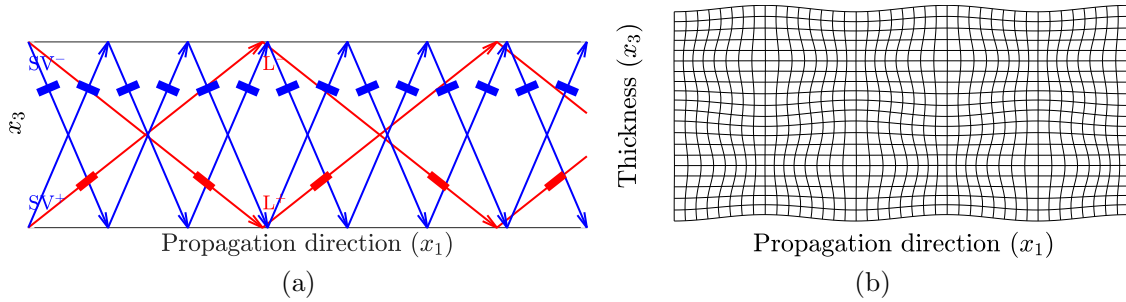


FIG. 4. (a) Bulk wave pattern and (b) mode shape of the A_4 Lamb wave at 1 MHz in a 10 mm thick AluminumAlloy1100 plate.

Select the **Mode** you want to analyze from the drop-down list. Set the **Frequency** at which to analyze the selected mode. The option below **Frequency** switches depending on the selected **Quantity**. In case you have selected any other quantity than “Bulk waves”, **Samples x3** determines the number of sample points over the plate’s thickness (x_3) at which the selected quantity is calculated. Otherwise, if you have chosen “Bulk waves”, you can determine the number of **Reflections** to be displayed. Press **Plot** to plot the through thickness profile of the plate in a new window. The top surface of the plate is represented by the top of the plot. Let us discuss the displacement. u_1 is the in-plane component along the propagation direction (x_1) of the guided wave. u_2 is in-plane but perpendicular (x_2) to the propagation direction, usually referred to as *shear horizontal*, and u_3 is the out-of-plane or normal displacement. In isotropic materials, there exist only pure Lamb and shear horizontal waves. Pure Lamb waves have only u_1 and u_3 components (see Fig. 3(a)), and pure shear horizontal modes have only a u_2 component. A symmetric Lamb wave is defined by having the same displacement component u_1 (sign and absolute value) at the top and bottom of the plate, while an antisymmetric Lamb wave has the same absolute component u_1 at the top and bottom, but with opposite sign, as depicted in Fig. 3(a). The character of a shear horizontal wave is determined by the same rules applied to u_2 . Figure 3(b) displays the four nonzero stress components present in a pure Lamb wave. The components σ_{i3} vanish at the surfaces, i.e., the surfaces are traction-free and no energy can leak to the assumed surrounding vacuum. Now, select the “Bulk waves” from the **Quantity** drop-down menu to display the bulk wave pattern. Since there exist only pure modes in isotropic materials, Lamb waves consist of the superposition of four bulk waves, namely two upward and downward propagating longitudinally polarized bulk waves (L^+ , L^-), and two upward and downward propagating shear vertically polarized bulk waves (SV^+ , SV^-) (see Fig. 4(a)). By contrast, shear horizontal guided waves consist of the superposition of only two bulk waves, namely two upward and downward propagating shear horizontally polarized bulk waves (SH^+ , SH^-). The polarization is indicated by the bold lines. Click on a bulk wave to display its refraction angle, phase velocity, wavelength, amplitude, and phase.

In the **Mode shape** (11) panel, you can visualize the displacement pattern (mode

shape) in a plate as it is deformed by a propagating Lamb or shear horizontal wave (see Fig. 4(b)). This is particularly helpful to get an idea of how a certain mode looks like at a certain frequency. Of course, the displacement is highly exaggerated in this plot. Again, the top of the plot refers to the top of the plate. Select the **Mode** you want to analyze from the drop-down list. Set the **Frequency** at which to analyze the selected mode. **Wavelengths** determines how many wavelengths along the propagation direction are displayed. **Samples x1** determines at how many sample points along the propagation direction the mode shape is calculated, while **Samples x3** determines the number of sample points over the plate's thickness. If you change **Samples x1**, then **Samples x3** will be set to one half of that number, which yields a nearly square grid on most screens. Use **Scale** to scale the displacement for clarity. The value n in **Grid line** specifies that a grid line is drawn at every n th sample point. If you change **Samples x1** by a certain factor, n is adjusted accordingly to maintain the number of grid lines drawn in the mode shape. Check **Undistorted** to toggle the undistorted grid. Go to the **Animation settings** sub-panel to set up an animation of the grid. If you don't want to export a movie, it is enough to calculate only one **Cycles**. That cycle will be repeated as long as the animation is running, and there should not be a notable break between each cycle. If you want to export a movie, however, it is better to compute multiple **Cycles**. The **Cycle duration** determines how long an animated cycle takes. Adjust the **Frame rate** of the movie. The **Movie quality** affects only the quality of the exported movie. Set a value between zero and one hundred. If you check **Animate** and press **Plot**, the animation starts running in an extra window until you close that window. If you leave **Animate** unchecked, only a static grid is plotted.

If you want to export plots and movies in an easy way, you can use the **Export settings** (12). Use the check boxes **PDF** and **PNG** to specify the format of the exported plot. **PDF** is a vectorized graphic that I used for the plots made by the DC for this manual. **PNG** in contrast is a rendered graphic for which you can set the **PNG resolution** in dots per inch (dpi). The better performance of a vectorized graphic becomes obvious upon zooming in. Compare Fig. 4, which is a **PDF**, to one of the DC screenshots, which are **PNG**. The font in all plots made by the DC is the standard L^AT_EX-font "Computer Modern". Type the **File name** and the **Directory** to specify where the plot/movie is exported to. If you check **Export plots** and then press any of the three **Plot** buttons (their labels change to "Export"), the respective plot will be exported. If you check **Animate** in (11) and then press the **Plot** button, the animation is displayed in a new window. Once all frames are captured, the window will close automatically and the movie be exported.

If you want to perform your own processing on the dispersion curves, you can **Export** them. Enable the **Dispersion curves** check box and select to export them to **Excel** sheets and/or **TXT** files. For each mode family, a separate file will be generated in the specified **Directory**, containing all modes belonging to the respective family. For each mode, the frequency-thickness product (MHz·mm), phase velocity (m/ms), group velocity (m/ms), propagation time (μ s), excitation angle ($^\circ$), wavelength (mm), and wavenumber (mm^{-1}) are exported. In the drop-down menu below the **Export** button, you can select to arrange the modes' data horizontally or vertically in the **Excel** or **TXT**

files. You can also export the through thickness profiles (except the bulk waves) selected in the **Through thickness profiles** (10) panel. Enable the **Through thickness** check box and upon pressing **Export**, the selected through thickness **Quantity** of the selected **Mode** at the chosen **Frequency** is exported to **Excel** sheets and/or **TXT** files.

Adjust the **Plot layout settings** (13) according to your preferences. For the plots in this manual, I toggled the **Title** off. You can also toggle the **Mode labels** on the fundamental Lamb modes A_0 and S_0 and on the fundamental shear horizontal mode S'_0 . Use the **Legend location** drop-down menu to place the legend in through thickness plots inside or outside the axes. You can also adjust the **Box line width** and the **Curve line width**. Only for the dispersion curves, you can also adjust the **Dispersion curve colors**, for symmetric modes in the field **S** and for antisymmetric modes in the field **A**. You can compose any color by setting the proportions of red, green, and blue. Set a value between zero and one for each proportion, e.g., [1 0 .5]. Shift the mode labels along the three fundamental modes named above by using **Mode labels x-position**. Set values between zero and one. Change the **Font size** of the **Title**, **Axes labels**, **Axes ticks**, **Mode labels**, and the **Legend**. Press **Default**, to restore the default settings.

3.3 Transversely isotropic

In this section, we conduct guided wave modeling in multilayered composites such as sketched in Fig. 5. These are basically stackings of m layers with layer thicknesses d_m , consisting of a fiber-epoxy combination. For each layer, we assign a local (crystallographic) Cartesian coordinate system $x'_{i(m)} = (x'_1, x'_2, x'_3)_{(m)}$ residing on the top of the m th layer, and we define the layers to lie parallel to the x'_1 - x'_2 -plane. The fibers are

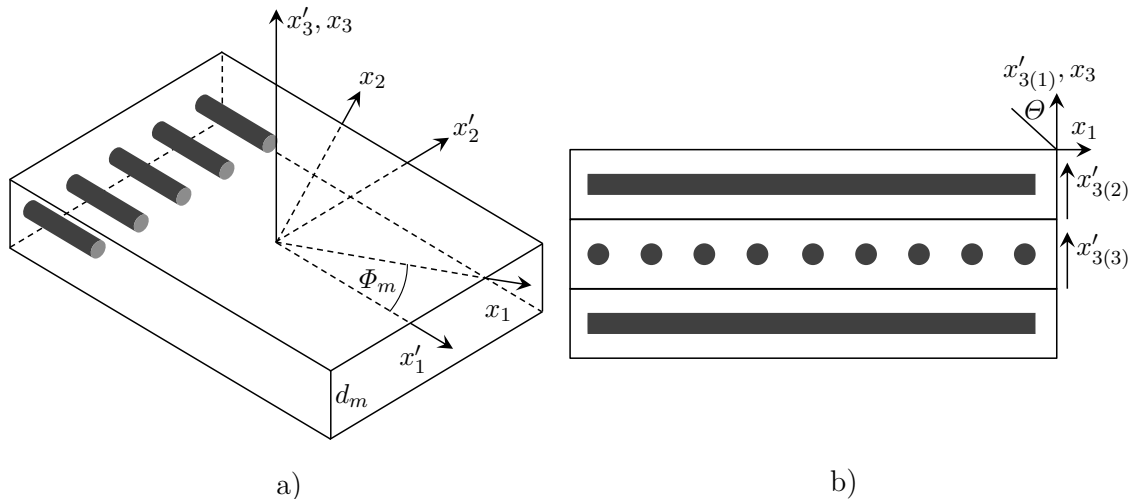


FIG. 5. (a) Single composite layer with local (crystallographic) coordinate system x'_i and global coordinate system x_i , $i = 1, 2, 3$. (b) Layered composite plate with [0/90/0] orientation with respect to the x_1 -axis.

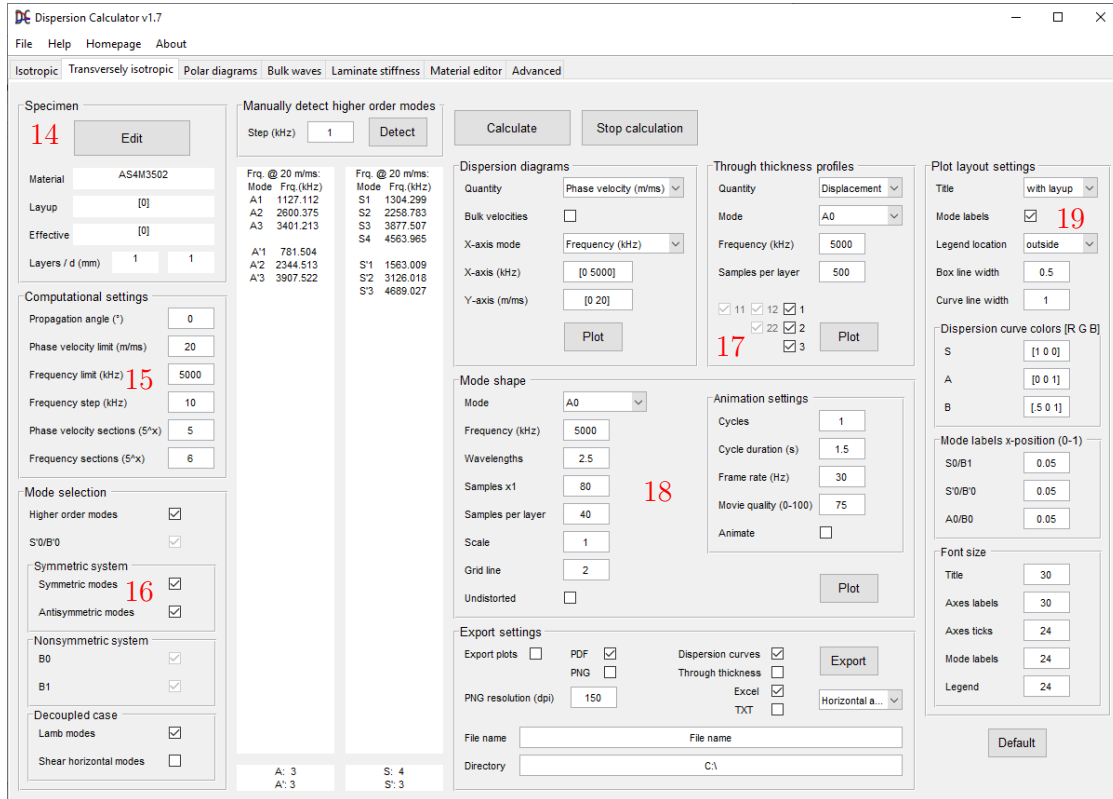


FIG. 6. The tab for the calculation of transversely isotropic specimens.

oriented along $x'_{1(m)}$, while $x'_{3(m)}$ is normal to the layer. To describe this system with arbitrary layer orientations in a convenient way, we introduce the nonprimed global coordinate system $x_i = (x_1, x_2, x_3)$. We choose it such that the x_1 - x_3 -plane coincides with the incidence plane of the incoming plane wave, and guided wave propagation is along the x_1 -direction. With respect to the global coordinate system, the local coordinate systems are yielded by a counterclockwise rotation of an angle Φ_m between x_1 and $x'_{1(m)}$ about the x_3 -axis. Hence, x_3 and $x'_{3(m)}$ coincide.

The **Transversely isotropic** tab looks similar to the **Isotropic** tab. Only panels that are new or different will be explained in this section. First, define the laminate in the **Specimen** (14) panel shown in Fig. 6. Press **Edit** to open the specimen setup depicted in Fig. 7. Select a transversely isotropic **Material** from the drop-down menu. If you check **Uniform layer thickness**, the DC deduces the layer thicknesses from the overall **Plate thickness**. **Unit cell repetitions** specifies how many repetitions of the unit cell are contained in the layup. Use only integer numbers. Check **Symmetric system** if the layup is symmetric with respect to the middle plane of the plate/laminate. In the table on the right, you can define the **Unit cell**. If **Uniform layer thickness** is checked, it is enough to enter the fiber **Orientation** of every layer in the left column. The **Thickness** column is inactive. If you have a layup with nonuniform layer thicknesses, uncheck **Uniform layer thickness** and enter every layer's thickness in the **Thickness**

column, which is now active, in addition to their orientations. The **Unit cell** table offers an immense amount of four hundred entries. This ensures that even the largest rocket booster laminates, which can be a nonrepeated unit cell by their own, can be entered. By contrast, unit cells in more common laminates are much smaller, often having only four or eight layers. Note that the uppermost layer in the table refers to the uppermost layer of the laminate. Now, you can **Save** the specimen definition and **Load** it in future sessions. Press **OK** to accept the specimen definition or **Cancel** to discard it. The setup closes, and the specimen definition is displayed below the **Edit**-button.

Now, go to the **Computational settings** (15). Define the **Propagation angle** Φ for the guided waves with respect to the **Layer orientations**. Consider for example the [0/90/45/-45] layup sketched in Fig. 8. A positive **Propagation angle** Φ results in a counterclockwise rotation of the propagation direction (solid arrow) vs. the fiber orientations, yielding the **Effective** layup, respectively, the angles Φ_m [0/90/45/-45]-10 = [-10/80/35/-55]. Prior to the DC v1.4, the opposite convention was used, namely that a positive Φ resulted in a clockwise rotation (dashed arrow), yielding [0/90/45/-45]+10 = [10/100/55/-35]. This choice was reversed since it contradicted the common convention used for polar angles as well as the notation of the layup, and because the dispersion curves can depend upon this choice. The **Phase velocity limit** is set to 20 m/ms by default and does not change automatically. The **Frequency limit** is set such that a maximal frequency-thickness product of 2 MHz·mm is covered by default. The **Frequency step** is set to 0.005 of the default **Frequency limit**.

The **Mode selection** (16) panel now offers more options than the one in the isotropic case. You will find that some of the check boxes are inactive. This depends on the **Specimen settings** and the **Propagation angle** in the following way:

1. If the laminate consists solely of 0° and 90° layers, and the wave propagation is along either direction, Lamb and shear horizontal waves decouple and can be traced separately.
2. If the laminate is symmetric (including a single layer) or if the laminate is non-symmetric and the propagation direction is centered, like 40° in [0/80] or 45° in [0/45/90], one can distinguish between symmetric and antisymmetric modes.

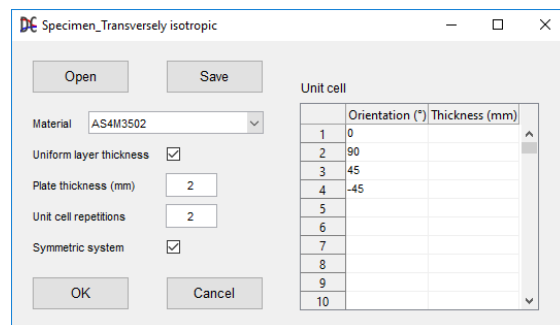


FIG. 7. The specimen setup.

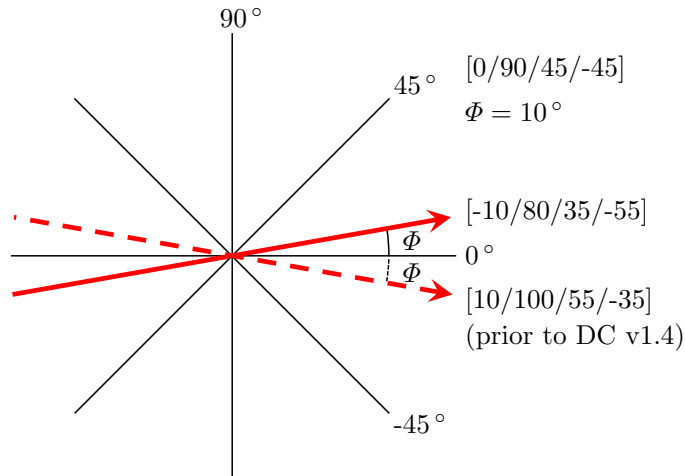


FIG. 8. Wave propagation along a **Propagation angle** of $\Phi = 10^\circ$ in a $[0/90/45/-45]$ layup. A positive Φ results in a counterclockwise rotation of the propagation direction (solid arrow) vs. the fiber orientations, yielding the **Effective** layup $[0/90/45/-45]-10 = [-10/80/35/-55]$. Prior to the DC v1.4, a positive Φ meant a clockwise rotation (dashed arrow), yielding $[0/90/45/-45]+10 = [10/100/55/-35]$.

TABLE 1. Possible configurations in transversely isotropic specimens.

symmetric	decoupled	modes
✓	✓	S, A, S', A'
✓	✗	S, A ^a
✗	✓	B, B'
✗	✗	B

^a S and A exist also in nonsymmetric layups in certain cases.

The four possible configurations are listed in Table 1. If Lamb and shear horizontal waves are coupled, they are called Lamb waves anyway in reminiscence to Sir Horace Lamb who described Lamb waves mathematically for the first time in 1917 [4]. Lamb dealt only with isotropic media wherein the coupling does not occur. In contrast to pure modes, coupled modes have three displacement components. If the laminate is nonsymmetric, the modes do not have a clear symmetric or antisymmetric character. In the DC, these modes are unconventionally denoted with the letter “B”. To the best of my knowledge, there does not exist an official notation for nonsymmetric modes.

If the solutions are coupled, you can toggle the display of the **S'0/B'0** shear horizontal mode. This mode is always located between A_0 and S_0 (or B_0 and B_1 , which are the corresponding modes in nonsymmetric layups). If you have a **Symmetric system** (including a single layer), you can choose to calculate the **Symmetric modes** and/or

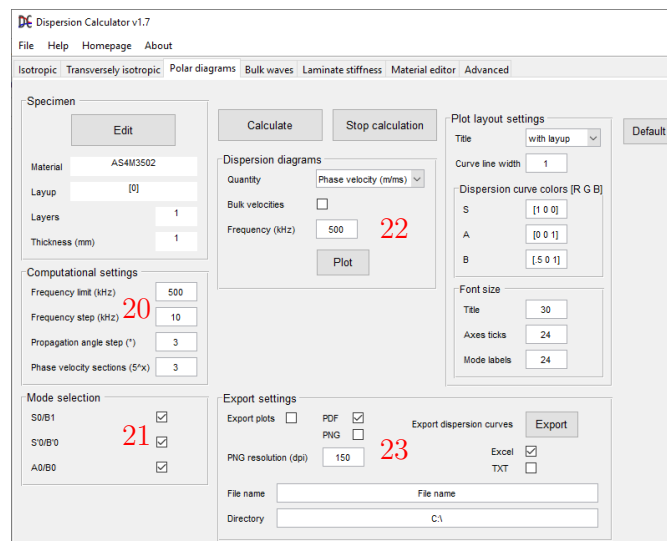


FIG. 9. The tab for the calculation of polar dispersion diagrams of the fundamental modes.

the **Antisymmetric modes**. If it is a **Nonsymmetric system**, you can toggle the two fundamental modes B_0 and B_1 . In the **Decoupled case**, you can calculate **Lamb modes** and **Shear horizontal modes** separately.

In the **Through thickness profiles** (17) panel and in the **Mode shape** (18) panel, the **Samples x3** option is replaced by **Samples per layer**. Of course, now you can also analyze B-type modes. In the **Plot layout settings** (19) panel, you can use the **Title** drop-down menu to display the plot title with or without the layup or no title at all. In the **Dispersion curve colors** sub-panel, you find an additional option for B-type modes.

3.4 Polar diagrams

Often, it is useful to have the guided wave dispersion versus the propagation direction in a laminate at a certain frequency rather than versus the frequency for a certain propagation direction. In the **Polar diagram** tab (see Fig. 9), you can calculate polar diagrams that give a very intuitive picture of the anisotropic propagation characteristics of the fundamental modes in a laminate. Since the wave propagation in isotropic materials is independent from the propagation direction, this tab considers only transversely isotropic materials. These are set up as usual except that only unit cells that contain at least one zero degree layer are accepted. Then use the **Computational settings** (20) panel. The dispersion curves are traced in the frequency space, as usual, up to the **Frequency limit** with a certain **Frequency step**. In case of layups that yield the same propagation characteristics in all four quadrants, the dispersion curves are traced for every propagation angle from zero to ninety degrees with increments defined in the **Propagation angle step** field. Such layups have unit cells which sum up to zero or ninety degrees like [0], [0/90], or [0/90/45/-45]. Otherwise, like for [0/45] or [0/45/90],

the quadrants show different profiles. In these cases, the complete 360° propagation angle range is calculated. In the **Mode selection** (21) panel, you can choose which ones of the fundamental modes A_0/B_0 , S'_0/B'_0 , and S_0/B_1 shall be calculated. In the **Dispersion diagrams** (22) panel, you can choose which **Quantity** to plot, namely the phase velocity, group velocity, propagation time, excitation angle, wavelength, and wavenumber versus the propagation direction. Select a **Frequency**. Note that you can plot the diagram at any **Frequency step** from zero to the **Frequency limit**. Upon pressing **Plot**, a new window will open with a polar diagram like the one displayed in Fig. 10. In the **Export settings** (23) panel, you can export the plots as usual. If you press **Export**, the polar dispersion curves at the selected **Frequency** are exported to **Excel** and/or **TXT** files.

3.5 Bulk waves

Guided waves evolve from the propagation and superposition of bulk waves. In the **Isotropic** and **Transversely Isotropic** tabs (Secs. 3.2 and 3.3), one can display the bulk wave pattern of a mode at a certain frequency (see Fig. 4(a)). In the **Bulk wave** tab (see Fig. 11), you can model the behavior of elastic waves (bulk waves) in bulk material and their scattering on interfaces. In isotropic materials, the phase velocity of bulk waves is independent from the propagation direction, and the polarization is along the wave propagation direction for longitudinal waves (L) and perpendicular for shear vertical

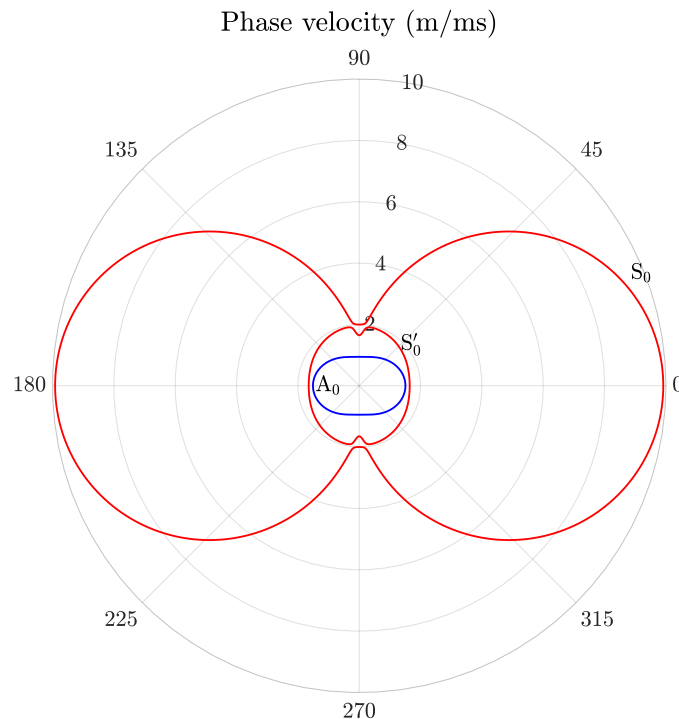


FIG. 10. Polar dispersion diagram at 500 kHz for 1 mm thick unidirectional T800M913.

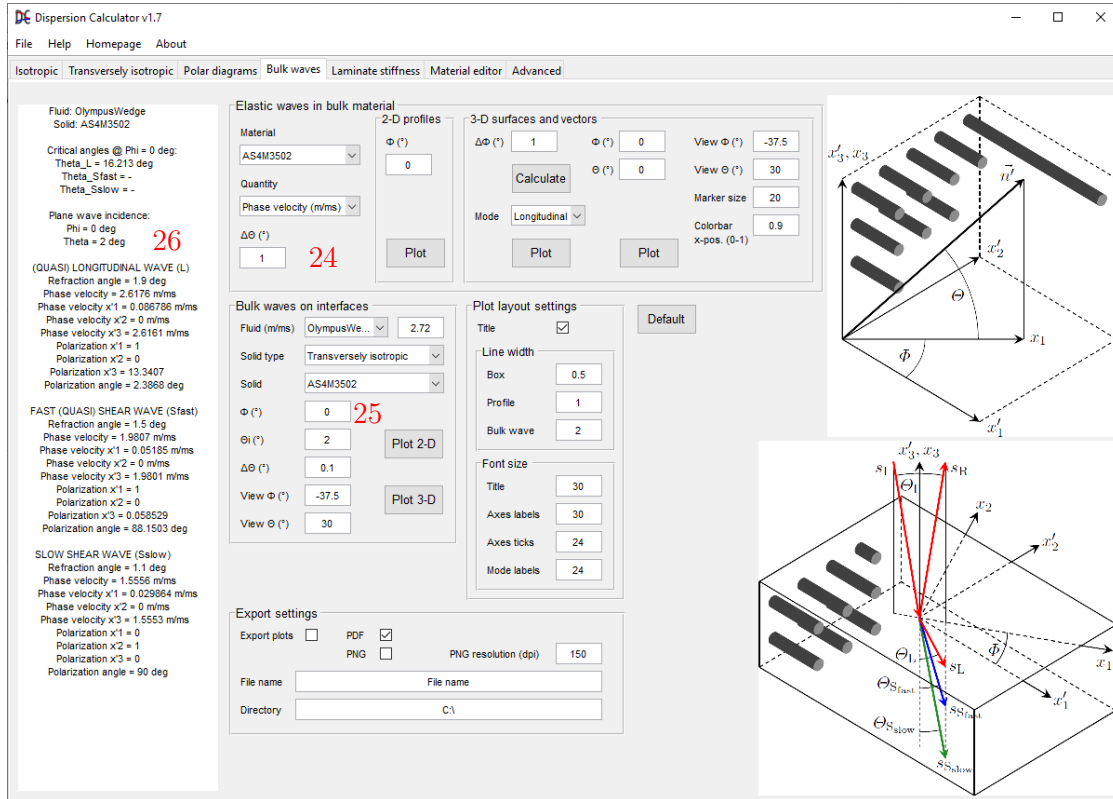


FIG. 11. The Bulk wave tab.

(SV) and shear horizontal waves (SH). Therefore, if we consider bulk waves emanating from a point source in an isotropic bulk material, the phase velocity surfaces for both wave types are spherical with the radii being the longitudinal velocity for L waves and the transverse velocity for SH and SV waves. These velocities are given in the **Material editor** (Sec. 3.7) tab. The group velocity surfaces coincide with the phase velocity surfaces. L waves are polarized along the radial direction, and SH and SV waves normal to it. In transversely isotropic materials, however, each of the three bulk wave types has its own phase velocity, which depends on the propagation direction \vec{n}' in Fig. 12(a), and the group velocity surface does not coincide with the phase velocity surface. In general, the group velocity vector deviates from the phase velocity vector, where the latter is parallel to the propagation direction unit vector \vec{n}' . In absence of attenuation, the group velocity is the same as the energy flow velocity, and its vector represents the actual direction of the acoustic beam. This situation leads also to differences in the magnitude of the phase and group velocities. The bulk waves' polarization is either along or perpendicular to the propagation direction, respectively, only in case of propagation along or perpendicular to the fibers (in these cases, the modes are called 'pure'), except for one shear type bulk wave, which has pure character for any propagation direction. The shear waves do not have the same phase velocity anymore. Because of that, the bulk waves in transversely isotropic materials are called quasilongitudinal waves (L),

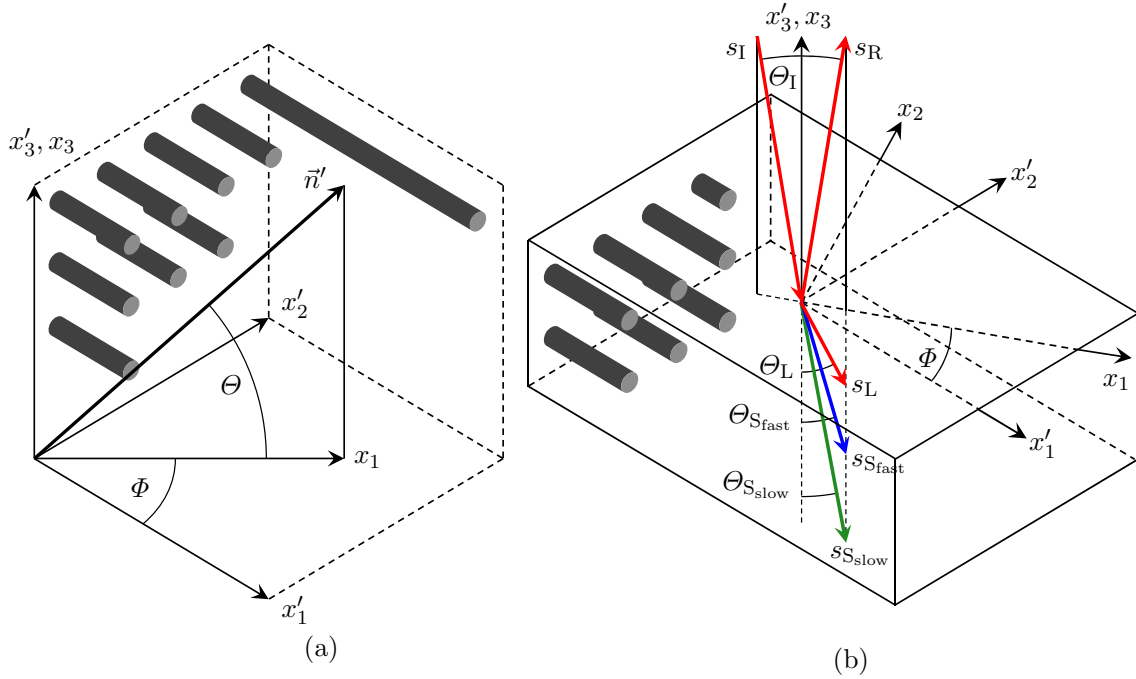


FIG. 12. Crystallographic and global coordinate systems x'_i , x_i and fiber orientation in transversely isotropic material. (a) Elastic wave propagation in the bulk material as treated in the **Elastic waves in bulk material** (24) panel. (b) A plane wave impinging from a fluid generates three bulk waves in transversely isotropic material propagating in the x_1 - x_3 -plane of the global coordinate system. This topic is covered in the **Bulk waves on interfaces** (25) panel.

fast quasishear waves (S_{fast}), and slow shear waves (S_{slow}). Figure 12(a) displays the conventions used for the elastic wave propagation in a transversely isotropic fiber-epoxy system. Here, x'_1 is along the fiber direction, and x'_2 and x'_3 are normal to it. Θ defines the wave propagation angle with respect to the x'_1 - x'_2 -plane (elevation), and Φ is the angle between the propagation direction projected into the x'_1 - x'_2 -plane and x'_1 (azimuth).

In the **Elastic waves in bulk material** (24) panel, you can plot the phase velocity, group velocity, the corresponding slownesses s , the energy deviation angle γ between the bulk waves' phase velocity vectors and the group velocity (or energy) vectors, and the polarization angle deviation δ of bulk waves in transversely isotropic materials in 2-D and 3-D. The slowness is the inverse phase velocity, and the polarization deviation is the deviation angle from perpendicular polarization ($\beta = 90^\circ$) in case of S_{fast} and parallel polarization ($\beta = 0^\circ$) in case of L. δ for S_{slow} is always zero since it is a pure mode for any propagation direction. Select a material from the **Material** drop-down menu. Choose the **Quantity** to be plotted and use $\Delta\Theta$ to determine the Θ resolution. In the **2-D profiles** sub-panel, you can plot the quantity for a given angle Φ , as shown in Figs. 13(a), 13(c), and 13(e) for T800M913 at $\Phi = 45^\circ$. In the **3-D surfaces and vectors** sub-panel, you can plot the complete surface. Now, you have to set $\Delta\Phi$ to determine also the Φ resolution. Upon pressing **Calculate**, the point cloud made up by

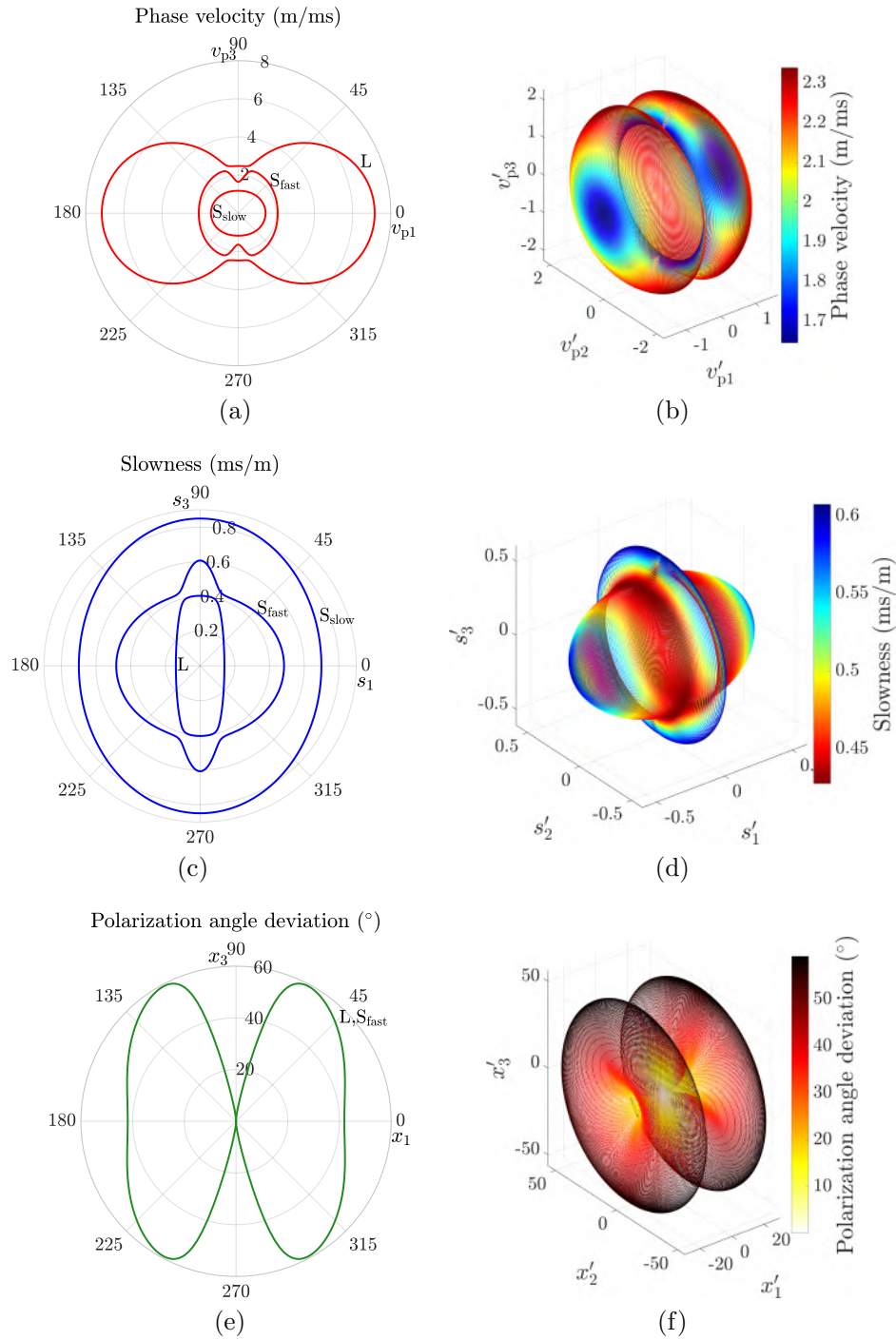


FIG. 13. Bulk waves in T800M913. (a) Phase velocity, (c) slowness, and (e) polarization deviation profiles at $\Phi = 45^\circ$, and (b) S_{fast} phase velocity, (d) S_{fast} slowness, and (f) L and S_{fast} polarization deviation surfaces.

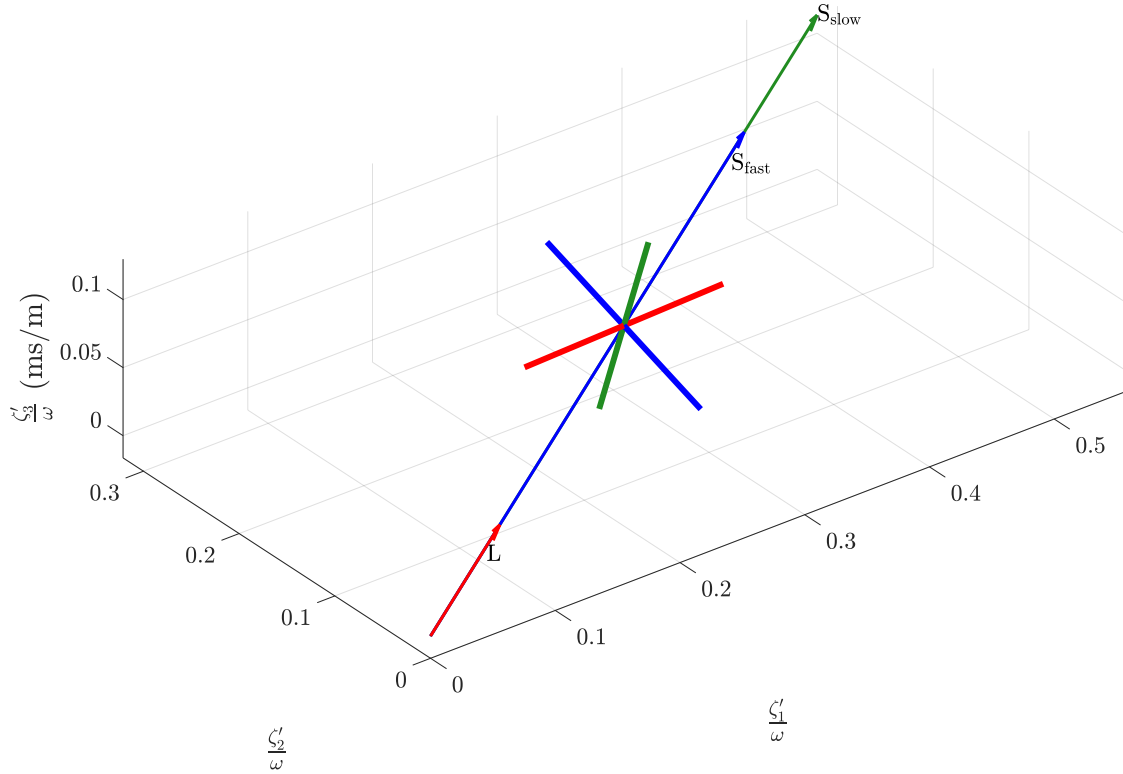


FIG. 14. Bulk wave slownesses and polarizations in T800M913 for propagation along $\Phi = 30^\circ$, $\Theta = 10^\circ$. The polarization vectors are always mutually orthogonal.

$\Delta\Theta$ and $\Delta\Phi$ will be calculated and the key data be displayed in the output window (26). Use the **Mode** drop-down menu to select which one of the three bulk wave mode surfaces you want to plot. Figures 13(b) and 13(d) show the phase velocity and slowness surfaces of S_{fast} in T800M913, respectively, and Fig. 13(f) shows the (coinciding) polarization angle deviation from pure mode polarization of L and S_{fast} . It can readily be seen that the deviation angle becomes zero for wave propagation parallel and normal to the fibers. These are the propagation directions for which pure L and S_{fast} modes occur. In the center column of the **3-D surfaces and vectors** sub-panel, you can plot the slowness and polarization vectors of bulk waves propagating along a specific direction. Define the propagation direction using Φ and Θ , and press **Plot** to get an image like the one shown in Fig. 14. In addition to the **Plot layout settings**, which apply to all plots on the current tab, you find some additional layout settings in the **3-D surfaces and vectors** sub-panel, which apply only to the 3-D plots. You can adjust the view by using **View Φ** and **View Θ** . Of course, you can also use the **Rotate 3-D** tool inside the plot window. You can also change the **Marker size** and the x-position of the colorbar.

In the **Bulk waves on interfaces** (25) panel, you can model the bulk waves that are generated in an isotropic or transversely isotropic material when a plane wave impinges from a fluid. This situation is depicted in Figs. 12(b) and 15(a). Here, the upper half

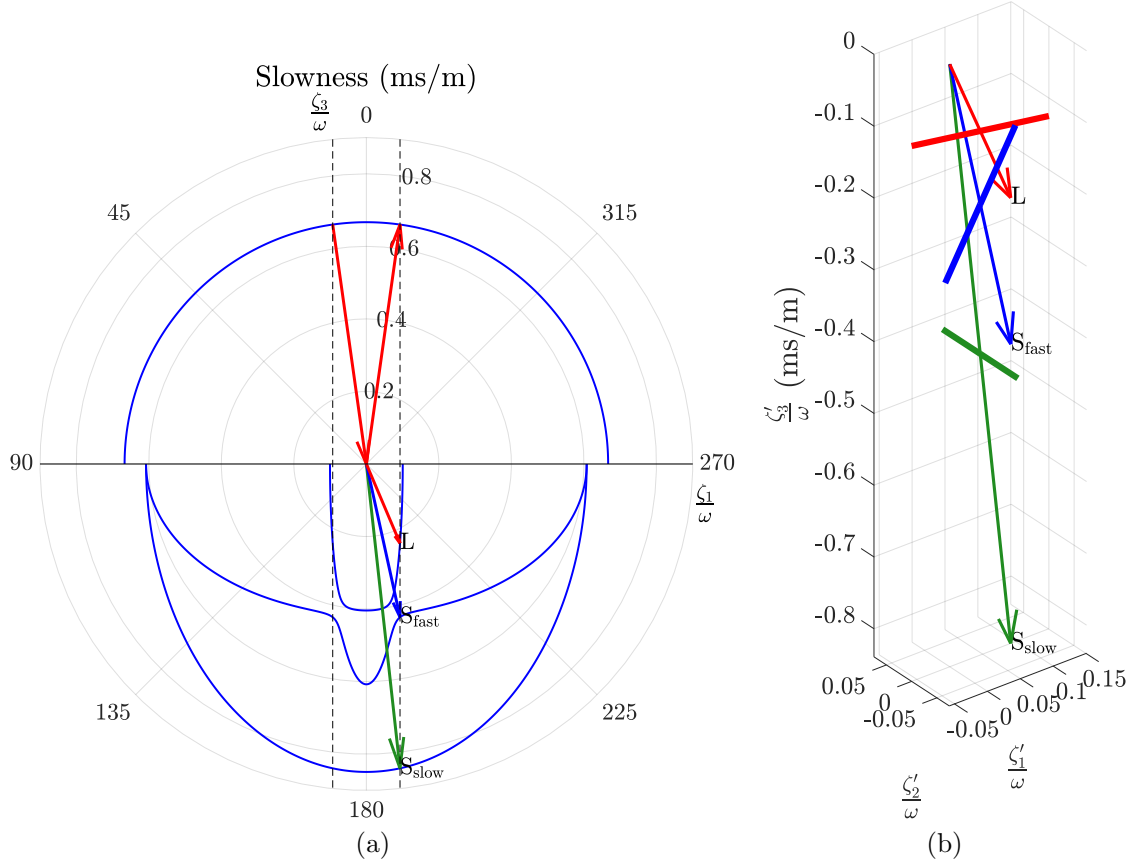


FIG. 15. Bulk waves generated in T800M913 through plane wave incidence from water at $\Phi = 0^\circ$, $\Theta_1 = 8^\circ$. The upper half space is covered by water, the lower half space by T800M913. (a) Construction of the bulk wave slownesses based on Snell's law. (b) Slownesses and polarizations of the generated bulk waves.

space is covered by water and the lower half space by transversely isotropic T800M913. The incident as well as the reflected and transmitted waves propagate in the $\Phi = 0^\circ$ plane, i.e., $x_1 = x'_1$. The blue profiles represent the slownesses in water and T800M913. Water as well as any other nonviscous fluid supports only the longitudinal wave type (because the shear modulus is zero), represented by the red vectors in the upper half space. The plane wave is incident under an angle of $\Theta_1 = 8^\circ$. Its wavenumber ζ_I is given by

$$\zeta_I = \frac{\omega}{v_I} = \omega s_I, \quad (4)$$

where ω is the angular frequency $2\pi f$, with the frequency f , and v_I is the phase velocity in water. At the boundary to the solid, a certain proportion of energy is reflected, and the rest is transmitted into T800M913 where three bulk waves with the wavenumbers $\zeta_L, \zeta_{S_{\text{fast}}}, \zeta_{S_{\text{slow}}}$ are generated. For these waves, Eq. (4) applies with their respective phase

velocities and slownesses $v_L, v_{S_{\text{fast}}}, v_{S_{\text{slow}}}, s_L, s_{S_{\text{fast}}}, s_{S_{\text{slow}}}$. According to Snell's law, all scattered waves (reflected and transmitted ones) must have the same projected wavenumber along the boundary ζ_{Ix_1} as the incident wave, i.e.,

$$\zeta_I \sin \Theta_I = \zeta_{(k)} \sin \Theta_{(k)} = \zeta_{I1}, \quad k = 1, 2, \dots, 4, \quad (5)$$

where $\zeta_{(k)}$ stands for the wavenumber of any scattered wave, and $\Theta_{(k)}$ is the corresponding reflection or refraction angle, respectively. With the use of Eq. (4), we can write Eq. (5) in terms of the slownesses of the scattered waves $s_{(k)}$ as

$$s_I \sin \Theta_I = s_{(k)} \sin \Theta_{(k)} = s_{I1}. \quad (6)$$

This important constraint is indicated by the two vertical guide lines in Fig. 15(a). The utility of this picture is that the wave slowness vectors $\vec{\zeta}_{(k)}/\omega$ can be constructed simply by drawing lines from the origin to the points, where the right guide line intersects the slowness profiles. Then, by assigning a frequency, the actual wavenumber can be obtained. From Fig. 15(a), it becomes also clear that, as the incidence/excitation angle increases, critical angles will be reached beyond which a slowness vector for a given bulk wave cannot be constructed anymore. Physically, these waves are evanescent, i.e., their amplitude decays exponentially with depth, and they are confined to a certain area below the boundary. Basically, these are surface waves (Rayleigh waves). By contrast, below the critical angles, we have propagating bulk waves. Now, let us look at Fig. 15(b) to find out more about the polarization of the bulk waves in T800M913. Here, only the lower half space from Fig. 15(a) is displayed. The bold lines emanating from the middle of the wave vectors indicate their polarization.

To do your modeling, select a **Fluid** from the drop-down menu or enter the phase velocity on the right. Then select the **Solid Type**. Depending on your choice, you can now select an isotropic or transversely isotropic **Solid**. All other parameters in this panel work similarly to those in the **Elastic waves in bulk material** (24) panel. Whenever you make an entry, information about the generated bulk waves in the solid, including critical angles, will be displayed in the output window (26). Press **Plot 2-D** or **Plot 3-D** to generate (and export) the kind of plots shown in Fig. 15.

3.6 Laminate stiffness

The **Laminate stiffness** tab, as depicted in Fig. 16, is an additional tool that allows to calculate the laminate stiffness matrix, which is also referred to as the homogenized stiffness tensor. The laminate stiffness matrix is the stiffness matrix of a layered, anisotropic laminate. It is calculated using the *classical laminate theory* (CLT). First, the layer stiffness matrices are transformed into the global coordinate system to account for their individual fiber orientations, and then the transformed stiffness matrices are multiplied by their respective layer thickness-to-unit cell thickness ratio and summed up to obtain the unit cell stiffness matrix. Since every unit cell has the same stiffness matrix, and because of the multiplication with the thickness ratios, the laminate stiffness matrix does

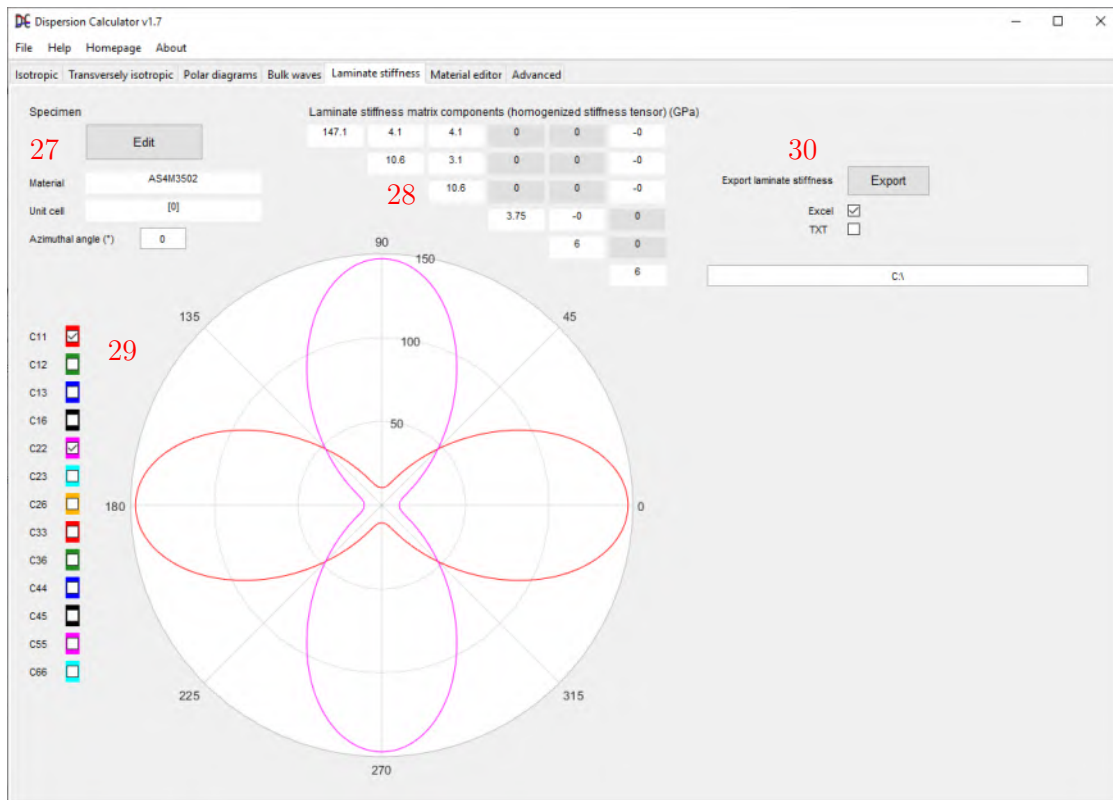


FIG. 16. The Laminite stiffness tab.

not depend on the repetitions of the unit cell, i.e., it is equal to the unit cell stiffness matrix.

The **Specimen** (27) setup is reduced accordingly. The **Laminite stiffness matrix components** (28) are displayed for the chosen **Azimuthal angle**. This matrix has the form of monoclinic material symmetry. In the polar diagram (29), every laminite stiffness matrix component can be plotted with respect to the wave propagation angle in the defined laminate. Use the check boxes on the left accordingly. You can **Export** (30) the laminite stiffness matrix displayed in (28) to an **Excel** and/or **TXT**-file, which is saved to the specified directory.

3.7 Material editor

In the **Material editor** tab, you can view the parameters of the materials available in the three lists and add or remove materials. In the **Isotropic materials** (31) panel in Fig. 17, you can choose an isotropic **Material** from the drop-down menu. From the **Density**, **Poisson's ratio**, and **Young's modulus**, the DC computes **Lamé's 1st param.** and **Lamé's 2nd param.**, and then **Longitudinal velocity**, **Transverse velocity**, **plate velocity**, and **Rayleigh velocity**. There are only two independent **Stiffness matrix components**. Once you change the fields **Density**, **Poisson's ra-**

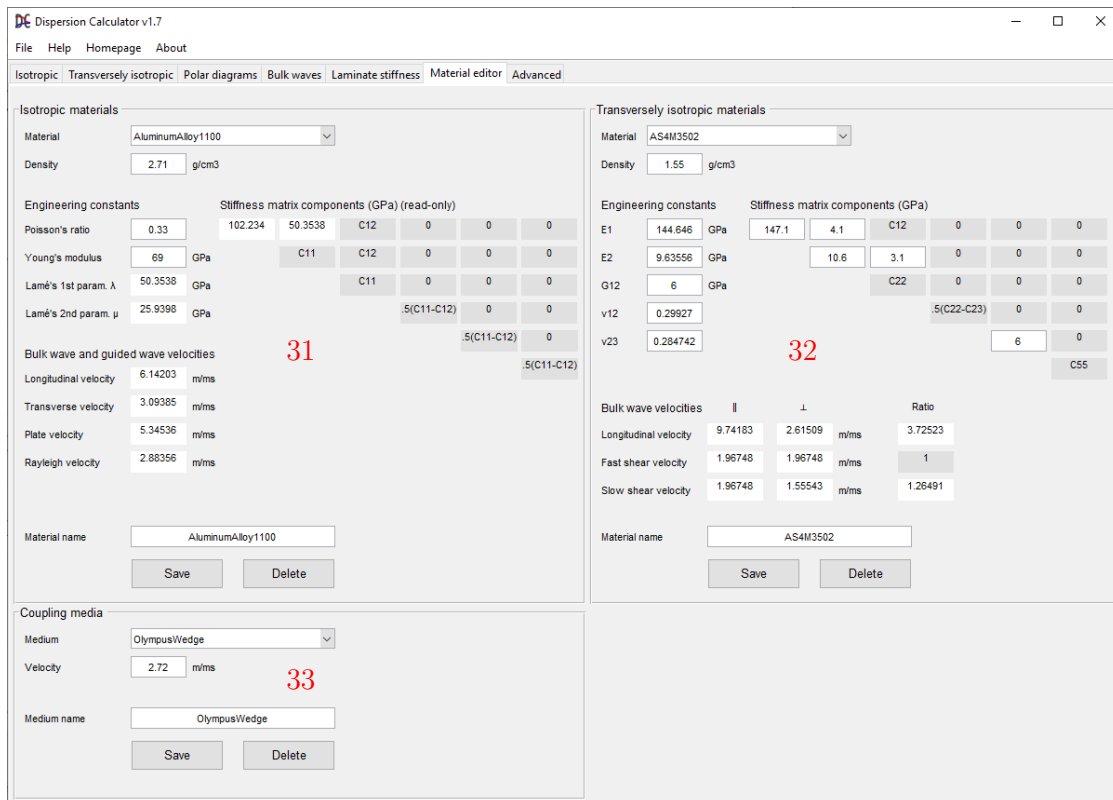


FIG. 17. The Material editor tab.

tio, or **Young's modulus**, the parameters below as well as the **Stiffness matrix components** are recalculated accordingly. After you have edited your material, assign a **Material name** to it and press **Save**. If you want to remove a material from the list, select it from the **Material** drop-down menu and press **Delete**.

The panel **Transversely Isotropic materials** (32) works in the same way except that you can enter the **Stiffness matrix components** also directly without editing the **Engineering constants**. The stiffness matrix contains five independent components. Below, you get the **Longitudinal velocity**, **Fast shear velocity**, and the **Slow shear velocity** of the three bulk wave types for propagation parallel and normal to the fibers, and the **Ratio** between those values. In the **coupling media** (33) panel, you can add coupling media.

3.8 Advanced

The **Advanced** tab offers options, which do not need to be changed on a regular basis, but which might help to overcome specific tracing problems. For each option, you have two fields. The left-hand field is for isotropic materials, the right-hand field is for transversely isotropic materials. First of all, you can also adjust the **Phase velocity resolution**. The bisections are performed until the desired resolution is obtained. Some

FIG. 18. The Advanced tab.

information about the **Phase velocity sweeps** (34) has already been given in Sec. 3.2. In order to understand the **Lamb wave search width for negative curvature**, please have a look at Fig. 19. It shows the tracing of the S_0 Lamb wave in 10 mm thick AluminumAlloy1100. Consider situation **A**. Suppose the sample at 210 kHz has already been obtained, and we are now searching for the 220 kHz sample. It is expected to be at a lower phase velocity. It is therefore taken the difference of the phase velocities between the 200 kHz and the 210 kHz sample Δ_i . The curvature is determined to be negative here. The 220 kHz sample is expected to lie within the search interval $_{i+1}$, which reaches from the 210 kHz sample's phase velocity down by the multiple $n_1 \cdot \Delta_i$, where n_1 is the **Lamb wave search width for negative curvature**. The 220 kHz is indeed found there. As the tracing progresses, we pass the turning point **B** and reach situation **C**. Since the curvature is now positive, the DC uses the **Lamb wave search width for positive curvature** n_2 , which is smaller than the value for negative curvatures n_1 . The **Shear horizontal wave search width** is used for shear horizontal waves in transversely isotropic media only, which have a positive curvature everywhere. In isotropic materials, the shear horizontal modes are calculated by an analytic equation so that the dispersion curve tracing is unnecessary.

If the search interval crosses the next lower mode, the search interval is cut just above the lower mode. In the coupled case in transversely isotropic material, the crossing of modes occurs. This can cause the well-known jumping-mode problem, where a tracing routine follows the wrong mode from the crossing point onward. Therefore, if the current mode crosses a lower mode that has already been traced, the tracing routine will not find a solution above the lower mode. Then, a new search interval will be defined below the lower mode, and the tracing be continued there. This procedure is slow but prevents the jumping to modes that have already been traced effectively. Of course though, before

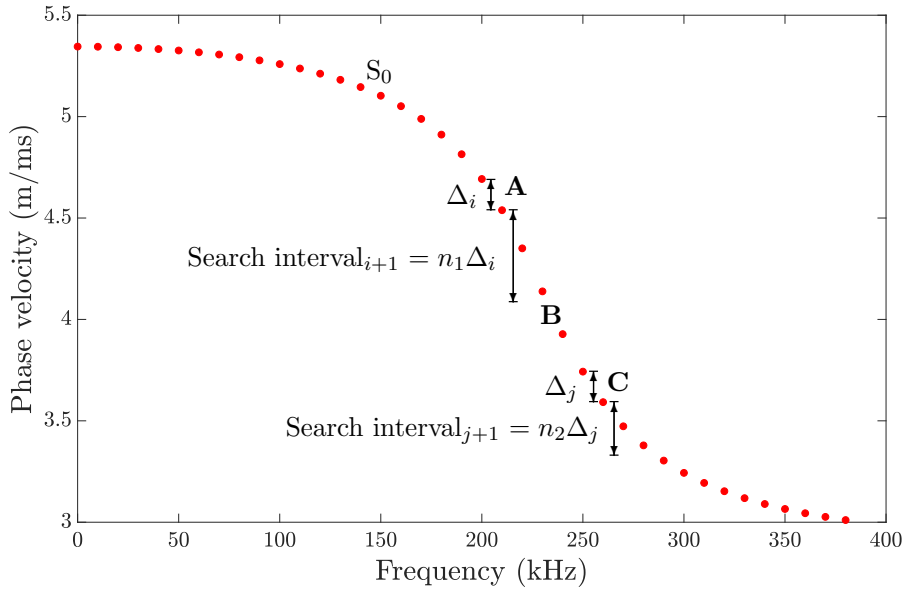


FIG. 19. The search interval as it is applied by the phase velocity sweeps.

such an instance could happen, the lower mode must have crossed the higher mode before the latter mode was traced. The jumping to yet unknown modes basically can not be avoided in any case, but one can try varying the **Frequency step**.

Frequency sweeps to complete dispersion curves at high phase velocity (35) are applied if the phase velocity sweeps fail to do so. Please consider Fig. 20. After the

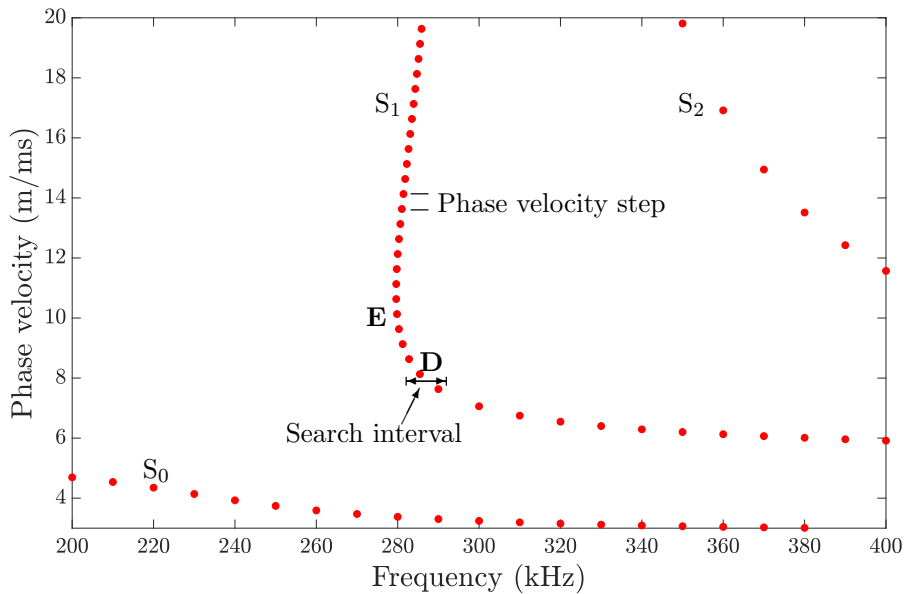


FIG. 20. The search interval and the phase velocity step as used by the frequency sweeps.

tracing of the fundamental modes, the higher order modes are traced. S_1 comes first. The cut-off frequency at 20 m/ms is 286.129 kHz. Since we have a **Frequency step** of 10 kHz, the phase velocity sweeps starts at 290 kHz, leaving the curve incomplete below 290 kHz. The frequency sweeps continue the curve at point **D**, which is above the 290 kHz sample by an amount of **S phase velocity step**. This point is within a search interval spanning from a certain offset above 290 kHz to $290 \text{ kHz} - x/d$, where x is the **S search interval** in kHz·mm and d is the plate's **Thickness** in millimeters. The same search interval is used for the following samples. The aforementioned offset is needed to overcome point **E**, where the curve turns to higher frequencies again. This procedure continues until the cut-off frequency is reached. Different search intervals and phase velocity steps can be defined for S, A, and B type modes.

Lowé describes a different tracing routine in Refs. [5, 6], which he applies in DISPERSE. An extrapolation method is used to make a guess for the next sample point. This works well in the wavenumber space since the curves are more straight there than in the frequency space.

4 Examples

4.1 T800M913 single layer @ 45°

We want to obtain the dispersion diagram for an unidirectional layer of the fiber-matrix system T800M913. The thickness shall be 2 mm and the wave propagation along an angle of 45° with respect to the fiber orientation. Since a single layer is symmetric, we can determine symmetric and antisymmetric modes. Lamb and shear horizontal waves are coupled. Take a look at situation **A** in Fig. 21. The symmetric modes S_{12} and S_{13} are very close without crossing each other (although they should). If you use the default **Frequency step** of 5 kHz, **S phase velocity step** of 100 m/s, and **S search interval** of 20 kHz·mm, the frequency sweeps of S_{13} will hit S_{12} , and follow S_{12} up to its cut-off frequency. That problem can be solved in two ways:

1. Use an **S phase velocity step** of 50 m/s and an **S search interval** of 6 kHz·mm.
2. Or set the **Frequency step** to 1 kHz.

Be aware that the mode designation done by the DC is not always right. Checking the displacement fields of S_{12} and S_{13} above and below **A** reveals that both modes should actually cross each other, although they don't in this tracing. This means that what is now designated as S_{12} below **A** should actually belong to S_{13} and vice versa. There are more instances like that in Fig. 21.

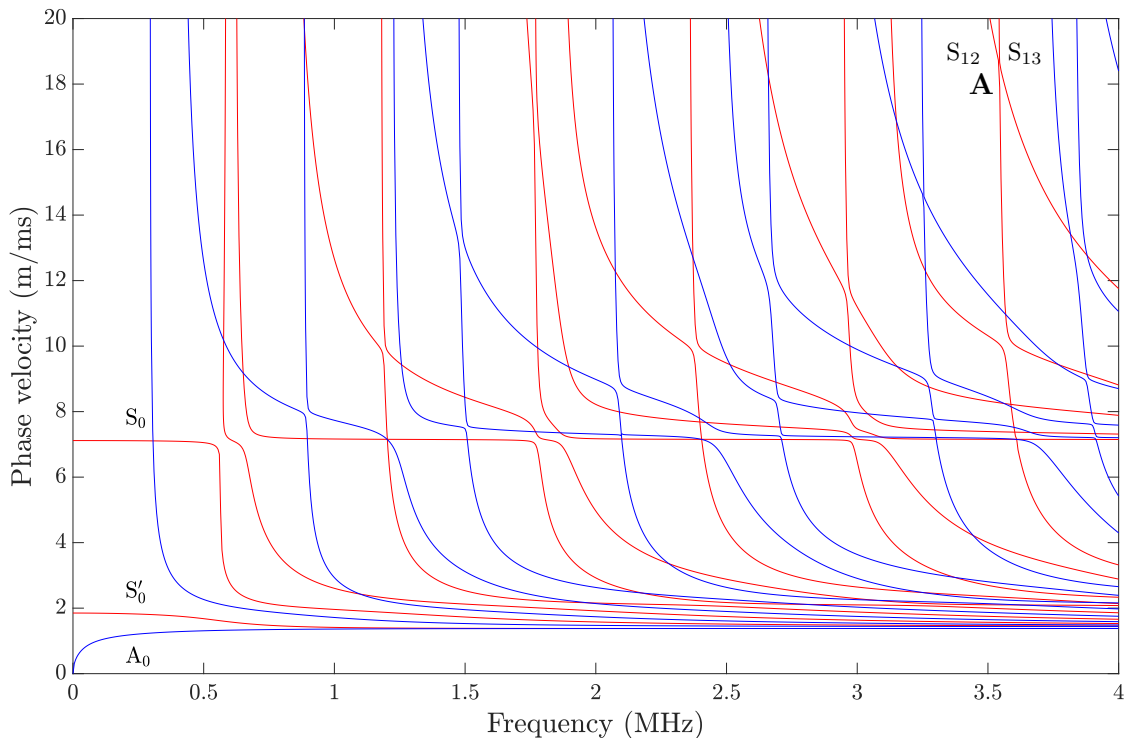


FIG. 21. Dispersion diagram for wave propagation along 45° with respect to the fiber direction in 2 mm thick unidirectional T800M913.

4.2 T800M913 [0/90]₄ @ 45°

Now, let us compute a 2 mm thick layup [0/90]₄ from the same material, and again we let the guided waves propagate along 45°. Although the layup is nonsymmetric in the usual sense, we can distinguish symmetric and antisymmetric modes because the propagation direction is centered to the layup. Lamb and shear horizontal waves are coupled. Look at S_1 and A_1 in Fig. 22. They appear to tend toward the same cut-off frequency and therefore get closer to each other with increasing phase velocity. First of all, you must set the default **Step** of 0.5 kHz to 0.2 kHz in order to detect S_1 at all. Therefore, once you see in the output window that modes have almost the same cut-off frequencies, consider taking finer steps than the default. You can also reduce the **Phase velocity limit** to avoid problems. Then, with the default **Frequency step** of 5 kHz and **Phase velocity sections** of five, S_1 cannot be traced. You can solve the problem by two ways:

1. Increase the search resolution by setting the **Phase velocity sections** to six.
2. Or set the **Frequency step** to 2 kHz.

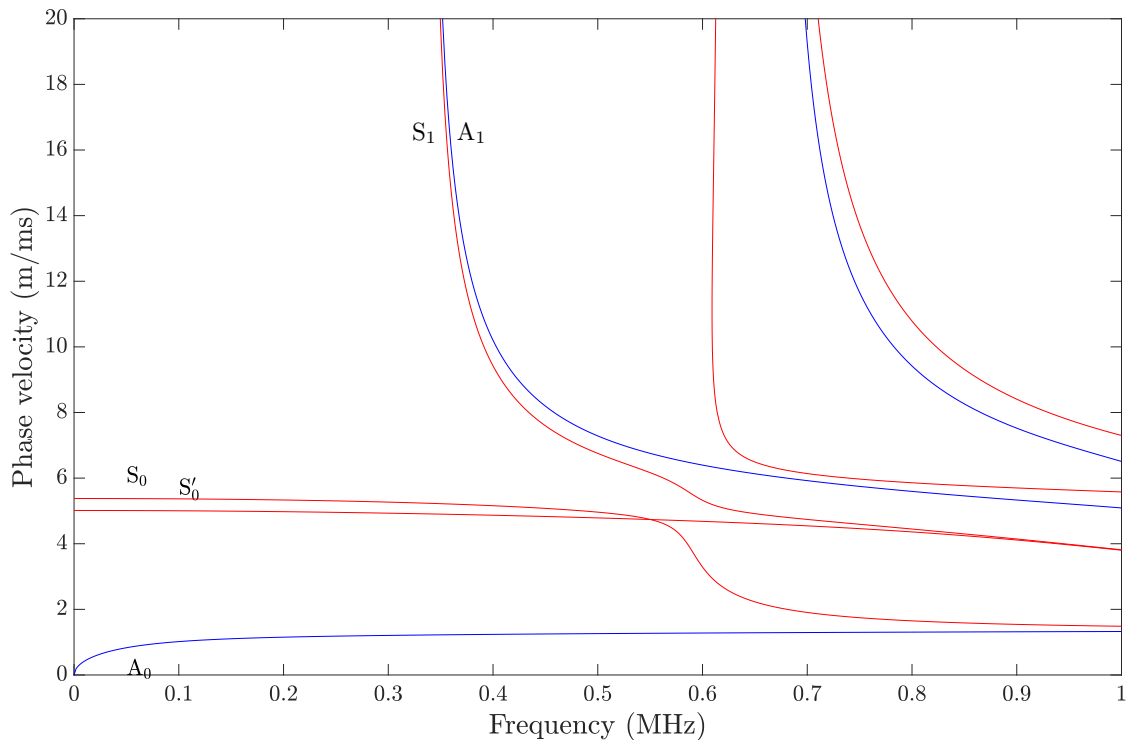


FIG. 22. Dispersion diagram for wave propagation along 45° in a 2 mm thick layup [0/90]₄ T800M913.

4.3 T800M913 [0/90]_{100s} @ 0°

It was mentioned in the introduction that modern rocket booster pressure vessels can consist of up to four hundred layers in certain areas. Now, we want to calculate such kind of laminate. We assume a layup [0/90]_{100s} with layer thicknesses of 0.125 mm yielding a 50 mm thick laminate. In contrast to booster layups, this highly repetitive layup could be simplified to [0/90]_{20s}, for instance, having only 80 layers with layer thicknesses of 0.625 mm, although the dispersion curves would not be exactly the same. However, the point we want to prove here is that the DC can deal with four hundred layers. Set the **Lamb wave search width for negative curvature** to five and the **Lamb wave search width for positive curvature** to two in order to accelerate the calculation. The phase velocity search interval is narrower so that the solution will be found faster. The resulting dispersion diagram is shown in Fig. 23. Lamb and shear horizontal waves decouple and can therefore be calculated separately. Figure 24 shows the displacement and stress field components of the S₀ Lamb wave at 50 kHz. The periodicity of the layup becomes obvious in the displacement u_1 and in the stresses σ_{11} and σ_{22} .

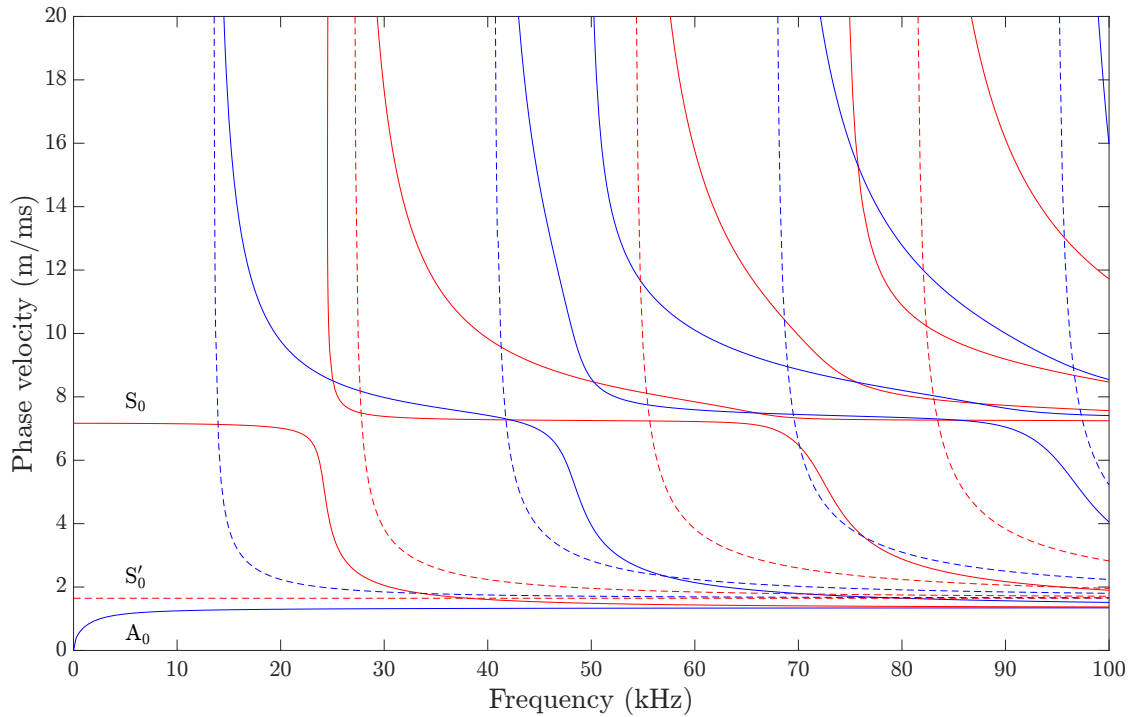


FIG. 23. Dispersion diagram for wave propagation along 0° in a 50 mm thick layup [0/90]_{100s} T800M913.

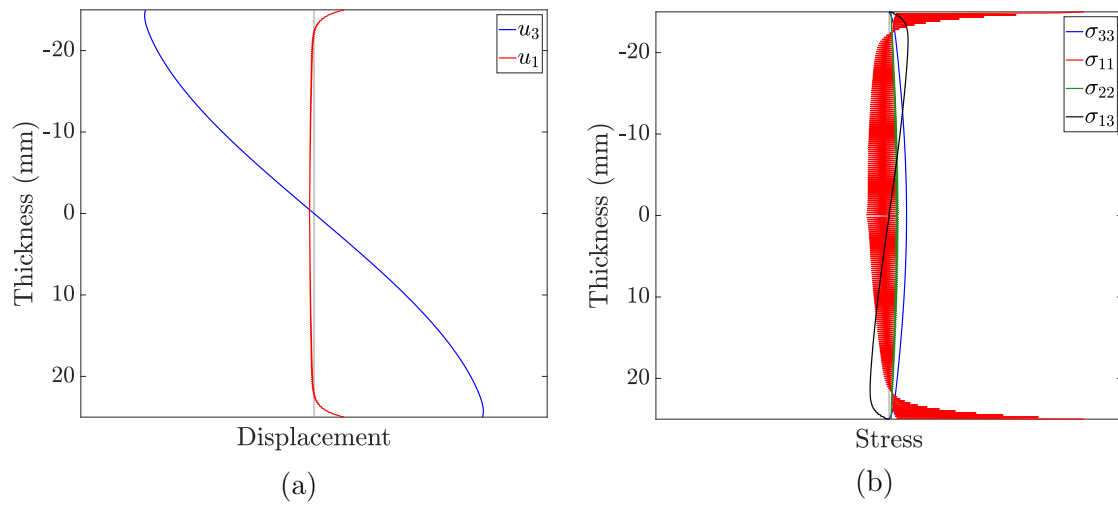


FIG. 24. (a) Displacement and (b) stress field components of the S_0 Lamb wave at 50 kHz in a 50 mm thick layup $[0/90]_{100s}$, T800M913.

A List of default materials

A.1 Isotropic

If not stated otherwise, the materials are taken from Ref. [7].

	Density (g/cm ³)	Young's modulus (GPa)	Poisson's ratio
AluminumAlloy1100	2.71	69	0.33
AluminumAlloy2024	2.77	72.4	0.33
AluminumDisperse [8]	2.7	70.76	0.3375
AluminumOxide	3.98	380	0.22
CastIronG3000	7.3	101.5	0.26
CastIronG4000	7.3	124	0.26
Concrete	2.4	31	0.2
CopperAlloyC17200BerylliumCopper	8.25	128	0.3
CopperAlloyC26000CartridgeBrass	8.53	110	0.35
CopperAlloyC36000FreeCuttingBrass	8.5	97	0.34
CopperAlloyC71500CopperNickel30	8.94	150	0.34
CopperAlloyC93200BearingBronze	8.93	100	0.34
DiamondNatural	3.51	950	0.2
DiamondSynthetic	3.36	863	0.2
Epoxy [8]	1.17	3.94	0.39
GlassBorosilicate	2.23	70	0.2
GlassCeramic	2.6	120	0.25
GlassQuartz	2.2	73	0.17
GlassSodaLime	2.5	69	0.23
Gold	19.32	77	0.42
Ice [8]	0.9	9.55	0.33
Inconel625	8.44	207	0.31
Lead	11.34	13.5	0.44
MagnesiumAlloyAZ31B	1.77	45	0.35
Molybdenum	10.22	320	0.32
Monel400	8.8	180	0.32
Nickel200	8.89	204	0.31
Nylon	1.14	2.69	0.39
Platinum	21.45	171	0.39
Plexiglass	1.19	2.74	0.31
Polycarbonate	1.2	2.38	0.36
Polystyrene	1.05	2.78	0.33
PolyvinylChloride	1.44	3.28	0.38
SiliconNitride	3.3	304	0.3
Silver	10.49	74	0.37

StainlessSteelAlloy304	8	193	0.3
StainlessSteelAlloy405	7.8	200	0.3
SteelAlloy1020	7.85	207	0.3
Tantalum	16.6	185	0.35
Teflon	2.17	0.475	0.46
Tin	7.17	44.3	0.33
Titanium	4.51	103	0.34
TitaniumAlloyTi6Al4V	4.43	114	0.34
Tungsten	19.3	400	0.28
Zinc	7.14	104.5	0.25
Zirconium	6.51	99.3	0.35

A.2 Transversely isotropic

	Density (g/cm ³)	E_1 (GPa)	E_2 (GPa)	G_{12} (GPa)	ν_{12}	ν_{23}
AS4M3502 [9]	1.55	144.646	9.63556	6	0.29927	0.284742
SAERTEX7006919RIMR135	1.454	119.91	7.25	6.02	0.322	0.447
SigrafilCE125023039 [9]	1.5	128.555	6.87324	6.1	0.330357	0.374648
T300M914 [10]	1.56	139.917	10.052	5.7	0.313131	0.478235
T700M21 [11]	1.571	125.5	8.7	4.135	0.37	0.45
T700PPS [9]	1.6	149.956	9.98828	4.5	0.291925	0.368257
T800M913 [9]	1.55	152.137	6.6353	4.2	0.251701	0.543093
T800M924 [12]	1.5	161	9.25	6	0.34	0.41
T800_Michel	1.51	178.96	9.17	5.5	0.355	0.529

References

- [1] S. I. Rokhlin and L. Wang, “Stable recursive algorithm for elastic wave propagation in layered anisotropic media: Stiffness matrix method,” *J. Acoust. Soc. Am.*, vol. 112, pp. 822–834, Sep 2002.
- [2] L. Wang and S. I. Rokhlin, “Stable reformulation of transfer matrix method for wave propagation in layered anisotropic media,” *Ultrasonics*, vol. 39, pp. 413–424, Sep 2001.
- [3] A. M. A. Huber and M. G. R. Sause, “Classification of solutions for guided waves in anisotropic composites with large numbers of layers,” *J. Acoust. Soc. Am.*, vol. 144, p. 3236–3251, Dec 2018.
- [4] H. Lamb, “On waves in an elastic plate,” in *Proceedings of the Royal Society of London*, p. 114–128, 1917.
- [5] M. J. S. Lowe, “Matrix techniques for modeling ultrasonic waves in multilayered media,” *IEEE Trans. Ultrason., Ferroelect., Freq. Control*, vol. 42, pp. 525–542, Jul 1995.
- [6] M. Lowe and B. Pavlakovic, *Disperse User's Manual*. Imperial College London, London, 2013.
- [7] W. D. Callister, *Material Science and Engineering. An Introduction*. John Wiley & Sons, Inc., 2002.
- [8] “Disperse v2.0.20a2, available at.” <http://www.imperial.ac.uk/non-destructive-evaluation/products-and-services/disperse>.
- [9] M. Sause and M. Hamstad, *Acoustic Emission Analysis*. Academic, Oxford, 2018.
- [10] C. Simon, H. Kaczmarek, and D. Royer, “Elastic wave propagation along arbitrary direction in free orthotropic plates. Application of composite materials,” in *4th French Congress of Acoustics, Marseille, France, 1997*.
- [11] J. Moll, J. Kathol, C.-P. Fritzen, M. Moix-Bonet, M. Rennoch, M. Koerdt, A. S. Herrmann, M. G. Sause, and M. Bach, “Open guided waves: online platform for ultrasonic guided wave measurements,” *Structural Health Monitoring*, 2018.
- [12] W. J. Percival and E. A. Birt, “A study of Lamb wave propagation in carbon-fibre composites,” *Insight*, vol. 39, pp. 728–735, 1997.

B Material Parameters

Aluminum Alloy 1100

$$\begin{array}{l} \rho \quad E \quad \nu \\ 2.71 \text{ g/cm}^3 \quad 69 \text{ GPa} \quad 0.33 \text{ [158]} \end{array}$$

$$\begin{array}{l} \lambda \quad \mu \quad v_L \quad v_T \quad c_{\text{Plate}} \quad c_R \\ 50.4 \text{ GPa} \quad 25.9 \text{ GPa} \quad 6.142 \text{ m/ms} \quad 3.094 \text{ m/ms} \quad 5.345 \text{ m/ms} \quad 2.884 \text{ m/ms} \end{array}$$

$$C_{ij} = \begin{bmatrix} 102.2 & 50.4 & 50.4 & 0 & 0 & 0 \\ & 102.2 & 50.4 & 0 & 0 & 0 \\ & & 102.2 & 0 & 0 & 0 \\ & & & 25.9 & 0 & 0 \\ & & \text{sym} & & 25.9 & 0 \\ & & & & & 25.9 \end{bmatrix} \text{ GPa} \quad (\text{B.1})$$

Lead

$$\begin{array}{l} \rho \quad E \quad \nu \\ 11.34 \text{ g/cm}^3 \quad 13.5 \text{ GPa} \quad 0.44 \text{ [158]} \end{array}$$

$$\begin{array}{l} \lambda \quad \mu \quad v_L \quad v_T \quad c_{\text{Plate}} \quad c_R \\ 34.4 \text{ GPa} \quad 4.7 \text{ GPa} \quad 1.964 \text{ m/ms} \quad 0.643 \text{ m/ms} \quad 1.215 \text{ m/ms} \quad 0.608 \text{ m/ms} \end{array}$$

$$C_{ij} = \begin{bmatrix} 43.8 & 34.4 & 34.4 & 0 & 0 & 0 \\ & 43.8 & 34.4 & 0 & 0 & 0 \\ & & 43.8 & 0 & 0 & 0 \\ & & & 4.7 & 0 & 0 \\ & & \text{sym} & & 4.7 & 0 \\ & & & & & 4.7 \end{bmatrix} \text{ GPa} \quad (\text{B.2})$$

SAERTEX[®]7006919/RIMR135

$$\begin{array}{l} \rho \\ 1.45 \text{ g/cm}^3 \end{array} \quad \begin{array}{l} E'_1 \\ 119.9 \text{ GPa} \end{array} \quad \begin{array}{l} E'_2 \\ 7.3 \text{ GPa} \end{array} \quad \begin{array}{l} G'_{12} \\ 6.0 \text{ GPa} \end{array} \quad \begin{array}{l} \nu'_{12} \\ 0.32 \end{array} \quad \begin{array}{l} \nu'_{23} \\ 0.45 \end{array}$$

$$C'_{ij} = \begin{bmatrix} 122.7 & 4.3 & 4.3 & 0 & 0 & 0 \\ & 9.2 & 4.2 & 0 & 0 & 0 \\ & & 9.2 & 0 & 0 & 0 \\ & & & 5.0 & 0 & 0 \\ & \text{sym} & & & 6.0 & 0 \\ & & & & & 6.0 \end{bmatrix} \text{ GPa} \quad (\text{B.3})$$

TABLE B.6. The bulk waves' phase and group velocities parallel and normal to the fibers in m/ms.

		⊥	Ratio
L	9.186	2.517	3.649
S _{fast}	2.035	2.035	1
S _{slow}	2.035	1.313	1.55

C Polynomial Forms of the Christoffel Matrix

Phase velocity form:

$$v_p^6 + A_1 v_p^4 + A_2 v_p^2 + A_3 = 0$$

Wavenumber ratio form:

$$\alpha^6 + A_1 \alpha^4 + A_2 \alpha^2 + A_3 = 0$$

Coefficients of the Phase Velocity Form

$$\begin{aligned}
 A_1 &= (-C'_{11} n_1'^2 - C'_{22} n_2'^2 - C'_{33} n_3'^2 - C'_{44} n_2'^2 - C'_{44} n_3'^2 - C'_{55} n_1'^2 - C'_{55} n_3'^2 \\
 &\quad - C'_{66} n_1'^2 - C'_{66} n_2'^2) / \rho \\
 A_2 &= (C'_{11} C'_{55} n_1'^4 + C'_{22} C'_{44} n_2'^4 + C'_{11} C'_{66} n_1'^4 + C'_{33} C'_{44} n_3'^4 + C'_{22} C'_{66} n_2'^4 \\
 &\quad + C'_{33} C'_{55} n_3'^4 + C'_{44} C'_{55} n_3'^4 + C'_{44} C'_{66} n_2'^4 + C'_{55} C'_{66} n_1'^4 - C'_{12} n_1'^2 n_2'^2 \\
 &\quad - C'_{13} n_1'^2 n_3'^2 - C'_{23} n_2'^2 n_3'^2 + C'_{11} C'_{22} n_1'^2 n_2'^2 + C'_{11} C'_{33} n_1'^2 n_3'^2 \\
 &\quad + C'_{11} C'_{44} n_1'^2 n_2'^2 + C'_{11} C'_{44} n_1'^2 n_3'^2 + C'_{22} C'_{33} n_2'^2 n_3'^2 - 2C'_{13} C'_{55} n_1'^2 n_3'^2 \\
 &\quad - 2C'_{23} C'_{44} n_2'^2 n_3'^2 + C'_{22} C'_{55} n_1'^2 n_2'^2 - 2C'_{12} C'_{66} n_1'^2 n_2'^2 + C'_{22} C'_{55} n_2'^2 n_3'^2 \\
 &\quad + C'_{33} C'_{66} n_1'^2 n_3'^2 + C'_{44} C'_{55} n_1'^2 n_3'^2 + C'_{33} C'_{66} n_2'^2 n_3'^2 + C'_{44} C'_{55} n_2'^2 n_3'^2 \\
 &\quad + C'_{44} C'_{66} n_1'^2 n_2'^2 + C'_{44} C'_{66} n_2'^2 n_3'^2 + C'_{55} C'_{66} n_1'^2 n_2'^2 + C'_{55} C'_{66} n_1'^2 n_3'^2) / \rho^2 \\
 A_3 &= (C'_{12} C'_{44} n_1'^2 n_2'^4 + C'_{13} C'_{44} n_1'^2 n_3'^4 + C'_{12} C'_{55} n_1'^4 n_2'^2 + C'_{13} C'_{66} n_1'^4 n_3'^2 \\
 &\quad + C'_{23} C'_{55} n_2'^2 n_3'^4 + C'_{23} C'_{66} n_2'^4 n_3'^2 - C'_{11} C'_{55} C'_{66} n_1'^6 - C'_{22} C'_{44} C'_{66} n_2'^6 \\
 &\quad - C'_{33} C'_{44} C'_{55} n_3'^6 - C'_{11} C'_{22} C'_{44} n_1'^2 n_2'^4 - C'_{11} C'_{22} C'_{55} n_1'^4 n_2'^2 \\
 &\quad - C'_{11} C'_{33} C'_{44} n_1'^2 n_3'^4 - C'_{11} C'_{33} C'_{66} n_1'^4 n_3'^2 - C'_{11} C'_{44} C'_{55} n_1'^4 n_3'^2 \\
 &\quad - C'_{22} C'_{33} C'_{55} n_2'^2 n_3'^4 + 2C'_{13} C'_{44} C'_{55} n_1'^2 n_3'^4 - C'_{11} C'_{44} C'_{66} n_1'^4 n_2'^2 \\
 &\quad + 2C'_{12} C'_{44} C'_{66} n_1'^2 n_2'^4 - C'_{22} C'_{33} C'_{66} n_2'^4 n_3'^2 - C'_{22} C'_{44} C'_{55} n_2'^4 n_3'^2 \\
 &\quad + 2C'_{23} C'_{44} C'_{55} n_2'^2 n_3'^4 + 2C'_{12} C'_{55} C'_{66} n_1'^4 n_2'^2 + 2C'_{13} C'_{55} C'_{66} n_1'^4 n_3'^2 \\
 &\quad + 2C'_{23} C'_{44} C'_{66} n_2'^4 n_3'^2 - C'_{22} C'_{55} C'_{66} n_1'^2 n_2'^4 - C'_{33} C'_{44} C'_{66} n_2'^2 n_3'^4 \\
 &\quad - C'_{33} C'_{55} C'_{66} n_1'^2 n_3'^4 + C'_{11} C'_{23} n_1'^2 n_2'^2 n_3'^2 + C'_{13} C'_{22} n_1'^2 n_2'^2 n_3'^2 \\
 &\quad + C'_{12} C'_{33} n_1'^2 n_2'^2 n_3'^2 - 2C'_{12} C'_{13} C'_{23} n_1'^2 n_2'^2 n_3'^2 - C'_{11} C'_{22} C'_{33} n_1'^2 n_2'^2 n_3'^2 \\
 &\quad - 2C'_{12} C'_{13} C'_{44} n_1'^2 n_2'^2 n_3'^2 + 2C'_{11} C'_{23} C'_{44} n_1'^2 n_2'^2 n_3'^2 - 2C'_{12} C'_{23} C'_{55} n_1'^2 n_2'^2 n_3'^2 \\
 &\quad + 2C'_{13} C'_{22} C'_{55} n_1'^2 n_2'^2 n_3'^2 - 2C'_{13} C'_{23} C'_{66} n_1'^2 n_2'^2 n_3'^2 + 2C'_{12} C'_{33} C'_{66} n_1'^2 n_2'^2 n_3'^2 \\
 &\quad - 2C'_{12} C'_{44} C'_{55} n_1'^2 n_2'^2 n_3'^2 - 2C'_{13} C'_{44} C'_{66} n_1'^2 n_2'^2 n_3'^2 - 2C'_{23} C'_{55} C'_{66} n_1'^2 n_2'^2 n_3'^2 \\
 &\quad - 4C'_{44} C'_{55} C'_{66} n_1'^2 n_2'^2 n_3'^2) / \rho^3
 \end{aligned} \tag{C.1}$$

Coefficients of the Wavenumber Ratio Form

$$\begin{aligned}
 A_1 &= [2(C_{13}C_{36}C_{45} - C_{16}C_{33}C_{45} - C_{13}C_{44}C_{55} + C_{13}C_{45}^2) \\
 &\quad + C_{11}C_{33}C_{44} + C_{33}C_{55}C_{66} - C_{44}C_{13}^2 - C_{55}C_{36}^2 \\
 &\quad - (C_{33}C_{44} + C_{33}C_{55} + C_{44}C_{55} - C_{45}^2)\rho c_p^2]/\Delta \\
 A_2 &= [2(C_{13}C_{16}C_{36} + C_{13}C_{16}C_{45} + C_{16}C_{36}C_{55} - C_{13}C_{55}C_{66} \\
 &\quad - C_{11}C_{36}C_{45}) + C_{11}C_{33}C_{66} + C_{11}C_{44}C_{55} - C_{11}C_{36}^2 - C_{33}C_{16}^2 \\
 &\quad - C_{11}C_{45}^2 - C_{66}C_{13}^2 + (2(C_{16}C_{45} + C_{13}C_{55} + C_{36}C_{45}) - C_{11}C_{33} \\
 &\quad - C_{11}C_{44} - C_{33}C_{66} - C_{44}C_{55} - C_{55}C_{66} + C_{13}^2 + C_{36}^2 + C_{45}^2)\rho c_p^2 \\
 &\quad + (C_{33} + C_{44} + C_{55})\rho^2 c_p^4]/\Delta \\
 A_3 &= [C_{11}C_{55}C_{66} - C_{55}C_{16}^2 - (C_{11}C_{55} + C_{11}C_{66} + C_{55}C_{66} - C_{16}^2)\rho c_p^2 \\
 &\quad + (C_{11} + C_{55} + C_{66})\rho^2 c_p^4 - \rho^3 c_p^6]/\Delta \\
 \Delta &= C_{33}C_{44}C_{55} - C_{33}C_{45}^2
 \end{aligned} \tag{C.2}$$

Roots

$$\begin{aligned}
 x_{L\pm} &= \pm (((A_1^3/27 - A_2A_1/6 + A_3/2)^2 + (-A_1^2/9 + A_2/3)^3)^{1/2} \\
 &\quad - A_3/2 - A_1^3/27 + A_1A_2/6)^{1/3} - A_1/3 - (-A_1^2/9 \\
 &\quad + A_2/3)/(((A_1^3/27 - A_2A_1/6 + A_3/2)^2 + (A_2/3 - A_1^2/9)^3)^{1/2} \\
 &\quad - A_3/2 - A_1^3/27 + A_1A_2/6)^{1/3})^{1/2} \\
 x_{S_{\text{fast}}^\pm} &= \pm ((-A_1^2/9 + A_2/3)/(2(((A_1^3/27 - A_2A_1/6 + A_3/2)^2 + (A_2/3 \\
 &\quad - A_1^2/9)^3)^{1/2} - A_3/2 - A_1^3/27 + A_1A_2/6)^{1/3}) - (((A_1^3/27 \\
 &\quad - A_2A_1/6 + A_3/2)^2 + (-A_1^2/9 + A_2/3)^3)^{1/2} - A_3/2 - A_1^3/27 \\
 &\quad + A_1A_2/6)^{1/3}/2 - (3^{1/2}(((A_1^3/27 - A_2A_1/6 + A_3/2)^2 \\
 &\quad + (-A_1^2/9 + A_2/3)^3)^{1/2} - A_3/2 - A_1^3/27 + A_1A_2/6)^{1/3} \\
 &\quad + (-A_1^2/9 + A_2/3)/(((A_1^3/27 - A_2A_1/6 + A_3/2)^2 + (A_2/3 \\
 &\quad - A_1^2/9)^3)^{1/2} - A_3/2 - A_1^3/27 + A_1A_2/6)^{1/3})i)/2 - A_1/3)^{1/2} \\
 x_{S_{\text{slow}}^\pm} &= \pm ((-A_1^2/9 + A_2/3)/(2(((A_1^3/27 - A_2A_1/6 + A_3/2)^2 + (A_2/3 \\
 &\quad - A_1^2/9)^3)^{1/2} - A_3/2 - A_1^3/27 + A_1A_2/6)^{1/3}) - (((A_1^3/27 \\
 &\quad - A_2A_1/6 + A_3/2)^2 + (-A_1^2/9 + A_2/3)^3)^{1/2} - A_3/2 - A_1^3/27 \\
 &\quad + A_1A_2/6)^{1/3}/2 + (3^{1/2}(((A_1^3/27 - A_2A_1/6 + A_3/2)^2 \\
 &\quad + (-A_1^2/9 + A_2/3)^3)^{1/2} - A_3/2 - A_1^3/27 + A_1A_2/6)^{1/3} \\
 &\quad + (-A_1^2/9 + A_2/3)/(((A_1^3/27 - A_2A_1/6 + A_3/2)^2 + (A_2/3 \\
 &\quad - A_1^2/9)^3)^{1/2} - A_3/2 - A_1^3/27 + A_1A_2/6)^{1/3})i)/2 - A_1/3)^{1/2}
 \end{aligned} \tag{C.3}$$

Phase velocity form:

$$v_{p(L)} = |\text{real}(x_L)|, \quad v_{p(S_{\text{fast}})} = |\text{real}(x_{S_{\text{fast}}})|, \quad v_{p(S_{\text{slow}})} = |\text{real}(x_{S_{\text{slow}}})| \quad (\text{C.4})$$

Wavenumber ratio form:

$$\alpha_q = \begin{bmatrix} \alpha_{L^-} \\ \alpha_{L^+} \\ \alpha_{S_{\text{fast}}^-} \\ \alpha_{S_{\text{fast}}^+} \\ \alpha_{S_{\text{slow}}^-} \\ \alpha_{S_{\text{slow}}^+} \end{bmatrix} = \begin{bmatrix} x_{L^-} \\ x_{L^+} \\ x_{S_{\text{fast}}^-} \\ x_{S_{\text{fast}}^+} \\ x_{S_{\text{slow}}^-} \\ x_{S_{\text{slow}}^+} \end{bmatrix} \quad (\text{C.5})$$

D Transfer Matrix

Coupled Case

$$\begin{aligned}
 \begin{bmatrix} u_1^{m+1} \\ u_2^{m+1} \\ u_3^{m+1} \\ \sigma_{33}^{*m+1} \\ \sigma_{13}^{*m+1} \\ \sigma_{23}^{*m+1} \end{bmatrix} &= \begin{bmatrix} e^{i\xi\alpha_1 d_m} & e^{i\xi\alpha_3 d_m} & e^{i\xi\alpha_5 d_m} & 1 & 1 & 1 \\ V_1 e^{i\xi\alpha_1 d_m} & V_3 e^{i\xi\alpha_3 d_m} & V_5 e^{i\xi\alpha_5 d_m} & V_1 & V_3 & V_5 \\ W_1 e^{i\xi\alpha_1 d_m} & W_3 e^{i\xi\alpha_3 d_m} & W_5 e^{i\xi\alpha_5 d_m} & -W_1 & -W_3 & -W_5 \\ D_{11} e^{i\xi\alpha_1 d_m} & D_{13} e^{i\xi\alpha_3 d_m} & D_{15} e^{i\xi\alpha_5 d_m} & D_{11} & D_{13} & D_{15} \\ D_{21} e^{i\xi\alpha_1 d_m} & D_{23} e^{i\xi\alpha_3 d_m} & D_{25} e^{i\xi\alpha_5 d_m} & -D_{21} & -D_{23} & -D_{25} \\ D_{31} e^{i\xi\alpha_1 d_m} & D_{33} e^{i\xi\alpha_3 d_m} & D_{35} e^{i\xi\alpha_5 d_m} & -D_{31} & -D_{33} & -D_{35} \end{bmatrix} \\
 &\cdot \begin{bmatrix} 1 & 1 & 1 & e^{i\xi\alpha_1 d_m} & e^{i\xi\alpha_3 d_m} & e^{i\xi\alpha_5 d_m} \\ V_1 & V_3 & V_5 & V_1 e^{i\xi\alpha_1 d_m} & V_3 e^{i\xi\alpha_3 d_m} & V_5 e^{i\xi\alpha_5 d_m} \\ W_1 & W_3 & W_5 & -W_1 e^{i\xi\alpha_1 d_m} & -W_3 e^{i\xi\alpha_3 d_m} & -W_5 e^{i\xi\alpha_5 d_m} \\ D_{11} & D_{13} & D_{15} & D_{11} e^{i\xi\alpha_1 d_m} & D_{13} e^{i\xi\alpha_3 d_m} & D_{15} e^{i\xi\alpha_5 d_m} \\ D_{21} & D_{23} & D_{25} & -D_{21} e^{i\xi\alpha_1 d_m} & -D_{23} e^{i\xi\alpha_3 d_m} & -D_{25} e^{i\xi\alpha_5 d_m} \\ D_{31} & D_{33} & D_{35} & -D_{31} e^{i\xi\alpha_1 d_m} & -D_{33} e^{i\xi\alpha_3 d_m} & -D_{35} e^{i\xi\alpha_5 d_m} \end{bmatrix}^{-1} \begin{bmatrix} u_1^m \\ u_2^m \\ u_3^m \\ \sigma_{33}^{*m} \\ \sigma_{13}^{*m} \\ \sigma_{23}^{*m} \end{bmatrix} \quad (D.1)
 \end{aligned}$$

Decoupled Case

$$\begin{aligned}
 \begin{bmatrix} u_1^{m+1} \\ u_3^{m+1} \\ \sigma_{33}^{*m+1} \\ \sigma_{13}^{*m+1} \end{bmatrix} &= \begin{bmatrix} e^{i\xi\alpha_1 d_m} & e^{i\xi\alpha_3 d_m} & 1 & 1 \\ W_1 e^{i\xi\alpha_1 d_m} & W_3 e^{i\xi\alpha_3 d_m} & -W_1 & -W_3 \\ D_{11} e^{i\xi\alpha_1 d_m} & D_{13} e^{i\xi\alpha_3 d_m} & D_{11} & D_{13} \\ D_{21} e^{i\xi\alpha_1 d_m} & D_{23} e^{i\xi\alpha_3 d_m} & -D_{21} & -D_{23} \end{bmatrix} \\
 &\cdot \begin{bmatrix} 1 & 1 & e^{i\xi\alpha_1 d_m} & e^{i\xi\alpha_3 d_m} \\ W_1 & W_3 & -W_1 e^{i\xi\alpha_1 d_m} & -W_3 e^{i\xi\alpha_3 d_m} \\ D_{11} & D_{13} & D_{11} e^{i\xi\alpha_1 d_m} & D_{13} e^{i\xi\alpha_3 d_m} \\ D_{21} & D_{23} & -D_{21} e^{i\xi\alpha_1 d_m} & -D_{23} e^{i\xi\alpha_3 d_m} \end{bmatrix}^{-1} \begin{bmatrix} u_1^m \\ u_3^m \\ \sigma_{33}^{*m} \\ \sigma_{13}^{*m} \end{bmatrix} \quad (D.2)
 \end{aligned}$$

E Stiffness Matrix

Coupled Case

$$\begin{bmatrix} \sigma_{33}^{*m} \\ \sigma_{13}^{*m} \\ \sigma_{23}^{*m} \\ \sigma_{33}^{*m+1} \\ \sigma_{13}^{*m+1} \\ \sigma_{23}^{*m+1} \end{bmatrix} = \begin{bmatrix} D_{11} & D_{13} & D_{15} & D_{11}e^{i\xi\alpha_1 d_m} & D_{13}e^{i\xi\alpha_3 d_m} & D_{15}e^{i\xi\alpha_5 d_m} \\ D_{21} & D_{23} & D_{25} & -D_{21}e^{i\xi\alpha_1 d_m} & -D_{23}e^{i\xi\alpha_3 d_m} & -D_{25}e^{i\xi\alpha_5 d_m} \\ D_{31} & D_{33} & D_{35} & -D_{31}e^{i\xi\alpha_1 d_m} & -D_{33}e^{i\xi\alpha_3 d_m} & -D_{35}e^{i\xi\alpha_5 d_m} \\ D_{11}e^{i\xi\alpha_1 d_m} & D_{13}e^{i\xi\alpha_3 d_m} & D_{15}e^{i\xi\alpha_5 d_m} & D_{11} & D_{13} & D_{15} \\ D_{21}e^{i\xi\alpha_1 d_m} & D_{23}e^{i\xi\alpha_3 d_m} & D_{25}e^{i\xi\alpha_5 d_m} & -D_{21} & -D_{23} & -D_{25} \\ D_{31}e^{i\xi\alpha_1 d_m} & D_{33}e^{i\xi\alpha_3 d_m} & D_{35}e^{i\xi\alpha_5 d_m} & -D_{31} & -D_{33} & -D_{35} \end{bmatrix} \cdot \begin{bmatrix} 1 & 1 & 1 & e^{i\xi\alpha_1 d_m} & e^{i\xi\alpha_3 d_m} & e^{i\xi\alpha_5 d_m} \\ V_1 & V_3 & V_5 & V_1e^{i\xi\alpha_1 d_m} & V_3e^{i\xi\alpha_3 d_m} & V_5e^{i\xi\alpha_5 d_m} \\ W_1 & W_3 & W_5 & -W_1e^{i\xi\alpha_1 d_m} & -W_3e^{i\xi\alpha_3 d_m} & -W_5e^{i\xi\alpha_5 d_m} \\ e^{i\xi\alpha_1 d_m} & e^{i\xi\alpha_3 d_m} & e^{i\xi\alpha_5 d_m} & 1 & 1 & 1 \\ V_1e^{i\xi\alpha_1 d_m} & V_3e^{i\xi\alpha_3 d_m} & V_5e^{i\xi\alpha_5 d_m} & V_1 & V_3 & V_5 \\ W_1e^{i\xi\alpha_1 d_m} & W_3e^{i\xi\alpha_3 d_m} & W_5e^{i\xi\alpha_5 d_m} & -W_1 & -W_3 & -W_5 \end{bmatrix}^{-1} \cdot \begin{bmatrix} u_1^m \\ u_2^m \\ u_3^m \\ u_1^{m+1} \\ u_2^{m+1} \\ u_3^{m+1} \end{bmatrix} \quad (\text{E.1})$$

Decoupled Case

$$\begin{bmatrix} \sigma_{33}^{*m} \\ \sigma_{13}^{*m} \\ \sigma_{33}^{*m+1} \\ \sigma_{13}^{*m+1} \end{bmatrix} = \begin{bmatrix} D_{11} & D_{13} & D_{11}e^{i\xi\alpha_1 d_m} & D_{13}e^{i\xi\alpha_3 d_m} \\ D_{21} & D_{23} & -D_{21}e^{i\xi\alpha_1 d_m} & -D_{23}e^{i\xi\alpha_3 d_m} \\ D_{11}e^{i\xi\alpha_1 d_m} & D_{13}e^{i\xi\alpha_3 d_m} & D_{11} & D_{13} \\ D_{21}e^{i\xi\alpha_1 d_m} & D_{23}e^{i\xi\alpha_3 d_m} & -D_{21} & -D_{23} \end{bmatrix} \cdot \begin{bmatrix} 1 & 1 & e^{i\xi\alpha_1 d_m} & e^{i\xi\alpha_3 d_m} \\ W_1 & W_3 & -W_1e^{i\xi\alpha_1 d_m} & -W_3e^{i\xi\alpha_3 d_m} \\ e^{i\xi\alpha_1 d_m} & e^{i\xi\alpha_3 d_m} & 1 & 1 \\ W_1e^{i\xi\alpha_1 d_m} & W_3e^{i\xi\alpha_3 d_m} & -W_1 & -W_3 \end{bmatrix}^{-1} \begin{bmatrix} u_1^m \\ u_3^m \\ u_1^{m+1} \\ u_3^{m+1} \end{bmatrix} \quad (\text{E.2})$$

F Flaw List

Component type	Plate	Flaw middle X	Flaw middle Y	Flaw middle Z	Length	Width	Area	Data type	Min	Max	Average	Median	Std deviator
Component ID	Fabiens Fehlstellenplatte												
File	04_2016-02-17_Fabiens Fehlstellenplatte_NTM_570kHz												
Path	X:\Messdaten\Luftultraschall\LUS\01 Grundfinanzierung\2016-02-15_Fabiens Fehlstellenplatte_NTM_570kHz\												
Inspection date	February 17, 2016												
Inspection system	KUKA KR120 R2700 extra HA, INOSON ACUT module												
Inspection mode	Normal transmission												
Transducer	570 kHz												
Summary:													
Flaw count	25												
Total area (mm2)	67652												
Flaw area (mm2/%)	6852.04												
OK area (mm2/%)	60799.96												
Flaw No	Flaw label	Flaw middle X	Flaw middle Y	Flaw middle Z	Length	Width	Area	Data type	Min	Max	Average	Median	Std deviator
1	Flaw_1	26.656	30.649	0.002	28.8	28.2	710.72	Magnitude	0.07759458	32.4893494	9.42181699	8.20564032	5.3707417
2	Flaw_2	28.628	80.049	0.002	21.2	24.2	444.4	Magnitude	0.28152293	33.206562	10.8369432	9.67300701	5.41663471
3	Flaw_3	27.907	129.65	0.002	19.2	18	296.04	Magnitude	0.46780524	31.4856682	12.4919651	11.5764122	5.25774422
4	Flaw_4	29.56	179.849	0.002	13.4	13	132.48	Magnitude	0.09233888	30.9522781	11.3564696	9.73090649	6.13488258
5	Flaw_5	30.546	228.449	0.002	7.8	7.8	44.72	Magnitude	0.34046149	30.8494568	13.0420936	11.9976106	7.28012005
6	Flaw_6	80.206	230.45	0.002	26.6	28.8	537.28	Magnitude	0.50609475	33.3513107	16.7844589	16.9530458	5.36767291
7	Flaw_7	78.799	180.649	0.003	20.2	22	318.12	Magnitude	1.3837707	30.904335	17.3725057	17.4891472	4.77474154
8	Flaw_8	79.559	131.049	0.003	17.8	19.2	214.4	Magnitude	2.5234437	33.4727936	18.5638595	19.1396599	4.9208017
9	Flaw_9	76.686	79.249	0.003	12	8.2	46.08	Magnitude	7.16862154	30.7849312	19.8203154	20.0044603	4.15615526
10	Flaw_10	78.646	32.849	0.003	6.2	5.6	19	Magnitude	9.21609688	30.2895317	20.5891283	20.8320751	3.66039351
11	Flaw_11	124.366	27.649	0.003	27	28	631	Magnitude	0.03822799	31.0918217	10.92942	10.0279512	5.6669515
12	Flaw_12	126.486	79.249	0.003	22.2	24.2	427.32	Magnitude	0.13804057	30.0067387	12.4203231	11.595912	5.75269401
13	Flaw_13	128.439	128.649	0.003	20.2	21.8	352.36	Magnitude	0.1676248	31.3006535	10.5795627	9.3878727	6.05700031
14	Flaw_14	127.879	179.449	0.003	11.4	11.8	109.72	Magnitude	0.31709403	32.1278191	12.689589	12.0272455	6.57459791
15	Flaw_15	129.279	227.05	0.002	8.6	10.2	52.48	Magnitude	0.64115882	30.4001312	14.0247975	13.8769846	6.207672
16	Flaw_16	180.959	229.45	0.002	26.2	25.8	472.56	Magnitude	0.28189254	33.5349274	16.6868716	16.9197025	5.38326721
17	Flaw_17	181.526	179.25	0.003	19.4	21.4	222.04	Magnitude	2.06569076	31.79216	19.2034335	19.6041908	4.35672078
18	Flaw_18	183.319	126.649	0.003	19.4	17.8	242	Magnitude	1.190909394	31.3546162	17.6682995	18.1675215	5.00267305
19	Flaw_19	184.159	77.049	0.003	11.6	10.6	67.04	Magnitude	6.53926802	30.4593277	18.6147241	19.1602297	4.65765271
20	Flaw_20	185.439	27.449	0.003	6.6	7.8	26.8	Magnitude	3.44097018	29.3116798	19.3996133	20.3028851	4.89813971
21	Flaw_21	227.355	25.849	0.002	27.6	25.8	628.24	Magnitude	0.13886882	32.6348877	9.71461417	8.55729675	5.48258295
22	Flaw_22	227.205	77.649	0.002	22	22.2	404.28	Magnitude	0.14548801	30.579414	10.2893499	8.97199917	5.99095523
23	Flaw_23	228.558	128.449	0.002	18.8	20.2	311.68	Magnitude	0.36238697	32.3650742	11.5091853	10.3647318	5.8001168
24	Flaw_24	230.061	177.649	0.002	12.8	11.8	102.68	Magnitude	0.14181043	31.6224251	11.2781863	9.4074316	6.89539851
25	Flaw_25	231.758	226.049	0.002	9.2	6.4	38.6	Magnitude	0.85274792	30.2856407	14.279048	13.4641848	6.45178262

FIG. F.1. Flaw list corresponding to Fig. 3.10(c).

Acronyms and Symbols

Mathematical Notations and Symbols

symbol	description
\cdot	dot product $\mathbf{a} \cdot \mathbf{b} = \sum_i a_i b_i = \mathbf{a} \mathbf{b} \cos \Theta$
\times	cross product $\mathbf{a} \times \mathbf{b} = \mathbf{a} \mathbf{b} \sin \Theta \mathbf{n}$, $\mathbf{n} \perp \mathbf{a}, \mathbf{b}$, $ \mathbf{n} = 1$
\circ	Hadamard product $\mathbf{A} \circ \mathbf{B} = (a_{ij} b_{ij})$
T	transpose \mathbf{a}^{T}
$ $	absolute value $ \mathbf{a} = \sqrt{\sum_i a_i^2}$
$\sum_{i=1}^n$	summation $\sum_{i=1}^n a_i = a_1 + a_2 + \dots + a_n$
∇	Nabla operator $[\partial/\partial x_1 \quad \dots \quad \partial/\partial x_i]$, gradient
δ_{ij}	Kronecker delta property $\delta_{ij} = 1$ if $i = j$, $\delta_{ij} = 0$ if $i \neq j$
Δ	increment $\Delta x = x_{i+1} - x_i $
\parallel	parallel
\perp	perpendicular
\in	element in $x \in [a, b]$
det	determinant
sin	sine function $\sin(\Theta) = \textit{opposite/hypotenuse}$
cos	cosine function $\cos(\Theta) = \textit{adjacent/hypotenuse}$
tan	tangent function $\tan(\Theta) = \textit{opposite/adjacent}$
real	real part a of complex number $a + ib$

Acronyms

General Acronyms

acronym	description
2-D	two-dimensional
3-D	three-dimensional
ACUT	air-coupled ultrasonic testing
AEE	Adaptive End-Effector
ASRM	adaptive slanted reflection mode
CAD	computer-aided design
CFRP	carbon fiber reinforced plastics
CMUT	capacitive micromachined ultrasound transducer
CPU	central processing unit

CSV	comma-separated values (file format)
CT	computed tomography
DC	Dispersion Calculator
DLR	Deutsches Zentrum für Luft- und Raumfahrt
EAM	excitation angle map
EPDM	ethylene propylene diene monomer rubber
FEM	finite element method
FFT	fast Fourier-transform
FML	fiber metal laminate
FSRM	focused slanted reflection mode
FSTM	focused slanted transmission mode
GLARE	glass laminate aluminum reinforced epoxy
GMM	global matrix method
GUI	graphical user interface
HST	homogenized stiffness tensor
INP	Institut National Polytechnique
LBR	Leichtbauroboter
LISA	local interaction simulation approach
NASA	National Aeronautics and Space Administration
NDI	nondestructive inspection
NTM	normal transmission mode
OLP	offline programming
PEM	pulse-echo mode
polyCMUT	polymer-based CMUT
QA	quality assurance
SAFE	semi-analytical finite element method
SCM	spectral collocation method
SHM	structural health monitoring
SMM	stiffness matrix method
STL	stereolithography (file format)
TCP	tool center point
TDMS	technical data management streaming file (file format)
TMM	transfer matrix method
TTT	tilt-turn table
TUM	Technical University of Munich
VARI	vacuum assisted resin infusion
WCUT	water-coupled ultrasonic testing
ZLP	Zentrum für Leichtbauproduktionstechnologie

Bulk Wave and Guided Wave Acronyms

acronym	description
A_p	antisymmetric Lamb wave mode of order $p = 0, 1, 2, \dots$
A'_p	antisymmetric shear horizontal guided wave mode of order $p = 1, 2, 3, \dots$
B_p	nonsymmetric Lamb wave mode of order $p = 0, 1, 2, \dots$
B'_p	nonsymmetric shear horizontal guided wave mode of order $p = 0, 1, 2, \dots$
L	(quasi) longitudinal bulk wave
S_p	symmetric Lamb wave mode of order $p = 0, 1, 2, \dots$
S'_p	symmetric shear horizontal guided wave mode of order $p = 0, 1, 2, \dots$
S_{fast}	fast (quasi) shear bulk wave
SH	shear horizontal bulk wave
S_{slow}	slow shear bulk wave
SV	shear vertical bulk wave

Lower Case Symbols

symbol	unit	description
\vec{b}	-	bi-normal unit vector $\vec{b} \perp \vec{n} \perp \vec{t}$
\mathbf{c}, c_{ijkl}	Pa	stiffness tensor
c_g	ms^{-1}	guided wave group velocity
c_p	ms^{-1}	guided wave phase velocity
c_{Plate}	ms^{-1}	plate wave velocity
c_R	ms^{-1}	Rayleigh wave velocity
d	m	plate/laminate thickness
d_{uc}	m	unit cell thickness
f	Hz	frequency
f_{crit}	Hz	critical frequency (homogenization domain)
h	m	$= d/2$
j^+, j^-	-	search interval factors for positive and negative curvature
\vec{n}	-	surface normal unit vector $\vec{n} \perp \vec{b} \perp \vec{t}$
\mathbf{n}, n_i	-	wave propagation unit vector
\mathbf{p}, p_i	-	polarization vector
p	m^{-1}	L bulk wave wavenumber component $= \alpha_L \xi = \zeta_{3(L)}$
q	m^{-1}	SV bulk wave wavenumber component $= \alpha_{SV} \xi = \zeta_{3(SV)}$
\mathbf{s}, s_{ijkl}	Pa^{-1}	compliance tensor
s	sm^{-1}	slowness
t	s	time
\vec{t}	-	path tangent unit vector $\vec{t} \perp \vec{b} \perp \vec{n}$

\mathbf{u}, u_i	m	particle displacement field
$\mathbf{v}_g, v_{gi}, v_g$	ms^{-1}	bulk wave group velocity
\mathbf{v}_p, v_p	ms^{-1}	bulk wave phase velocity
x_i	-	global coordinate system
x'_i	-	crystallographic coordinate system
x, y, z	m	TCP coordinate in X, Y, Z

Capital Symbols

symbol	unit	description
\mathbf{A}		transfer matrix
A_1, A_2, A_3		Christoffel matrix polynomial coefficients
A_R, B_R, C_R	$^\circ$	receiver orientation (Euler angles)
A_S, B_S, C_S	$^\circ$	sender orientation (Euler angles)
C_{ij}	Pa	Voigt's notation stiffness matrix
D	Pa	$= \alpha C_{44}$
D_1, D_2, D_3	Pa	bulk wave stress amplitudes of $\sigma_{33}, \sigma_{13}, \sigma_{23}$
\mathbf{D}	Pa	bulk wave stress amplitude matrix
\mathbf{E}	-	exponential functions matrix (Nayfeh [22])
E, E_i	Pa	Young's modulus
G, G_{ij}	Pa	shear modulus
\mathbf{H}	-	exponential functions matrix (Rokhlin et al. [59])
\mathbf{I}	-	symmetry identity matrix
\mathbf{K}		stiffness matrix (SMM)
M_{ij}	Pa	Christoffel matrix (wavenumber ratio form)
\mathbf{P}	-	bulk wave displacement amplitude ratio matrix
POD	-	probability of detection
PRF	Hz	pulse repetition frequency
T	-	transmission coefficient
U	Pa	strain energy density
\mathbf{U}, U_i	m	bulk wave displacement amplitude vector
V	-	bulk wave displacement amplitude ratio U_2/U_1
W	-	bulk wave displacement amplitude ratio U_3/U_1
\mathbf{X}		bulk wave displacement and stress amplitude matrix
X, Y, Z	-	robotic coordinate system
X_R, Y_R, Z_R	m	receiver position
X_S, Y_S, Z_S	m	sender position
Z	$\text{kgm}^{-2}\text{s}^{-1}$	acoustic impedance

Greek Symbols

symbol	unit	description
α	-	bulk wave wavenumber component ratio ζ_3/ζ_1
β_{ij}	-	orthogonal transformation tensor
β	°	bulk wave polarization angle
γ_{ij}	-	shear strain
γ	°	angle between bulk waves' phase and energy velocity vectors
Γ_i	ms ⁻¹	phase velocity search interval = $j^\pm \Delta_{i-1}$
δ	°	deviation angle from pure bulk wave polarization
Δ_i	ms ⁻¹	phase velocity difference between neighboring modal solutions
ϵ, ϵ_{ij}	-	strain field
ζ, ζ	m ⁻¹	bulk wave wavenumber
η	-	= $\alpha \xi d$
Θ	°	elevation angle
Θ_{crit}	°	critical incidence angle
Θ_{refr}	°	refraction angle
λ	Pa	Lamé's first parameter
λ_{ijkl}	m ² s ⁻²	= $c_{ijkl} \rho^{-1}$
Λ_{il}	m ² s ⁻²	= $\lambda_{ijkl} n_j n_k$
μ	Pa	Lamé's second parameter
ν, ν_{ij}	-	Poisson's ratio
ξ	m ⁻¹	guided wave wavenumber
ρ	kgm ⁻³	density
σ, σ_{ij}	Pa	stress field
σ^*, σ_{ij}^*	Pam	= $\sigma_{ij}/i\xi$
Υ	m ²	scalar potential (displacement)
Φ	°	azimuthal angle
Ψ	m ²	vector potential (displacement)
ω	Hz	angular frequency

Superscripts and Subscripts

symbol	description
'	quantity defined in the crystallographic coordinate system
0	quantity related to the top of the plate/layer
^c	quantity is complex-valued
-d	quantity related to the bottom of the plate/layer
in	quantity related to an incident bulk wave
L	quantity related to the (quasi) longitudinal bulk wave

max	quantity reaches its maximum
min	quantity reaches its minimum
r	quantity is real-valued
r	quantity related to a reflected bulk wave
S _{fast}	quantity related to the fast (quasi) shear bulk wave
SH	quantity related to the shear horizontal bulk wave
S _{slow}	quantity related to the slow shear bulk wave
SV	quantity related to the shear vertical bulk wave
t	quantity related to a transmitted bulk wave
T	quantity related to the transverse bulk wave
+	quantity related to an upward propagating bulk wave
-	quantity related to a downward propagating bulk wave

Constants and Numbers

symbol	value	unit	description
e	2.71828	-	Euler number
i	$\sqrt{-1}$	-	imaginary number
π	3.14159	-	mathematical constant

Bibliography

- [1] L. Rayleigh, “On Waves Propagated along the Plane Surface of an Elastic Solid,” in *Proc. Lond. Math. Soc.*, pp. 4–11, 1885.
- [2] A. E. H. Love, *Some problems of geodynamics*. Cambridge University Press, London, 1911.
- [3] H. Lamb, “On Waves in an Elastic Plate,” in *Proc. R. Soc. Lond. A*, p. 114–128, 1917.
- [4] R. Stonely, “Elastic waves at the surface of separation of two solids,” in *Proc. R. Soc. Lond. A*, pp. 416–428, Oct 1924.
- [5] J. G. Scholte, “The Range of Existence of Rayleigh and Stoneley Waves,” *Mon. Not. Roy. Astron. Soc. Geophys. Suppl.*, vol. 5, pp. 120–126, May 1947.
- [6] W. T. Thomson, “Transmission of elastic waves through a stratified solid medium,” *J. Appl. Phys.*, vol. 21, pp. 89–93, 1950.
- [7] N. A. Haskell, “The dispersion of surface waves on multilayered media,” *Bull. Seism. Soc. Am.*, vol. 43, pp. 17–34, Jan 1953.
- [8] R. A. Phinney, “Leaking modes in the crustal waveguide: 1. The oceanic PL wave,” *J. Geophys. Res.*, vol. 66, pp. 1445–1469, May 1961.
- [9] F. Press, D. Harkrider, and C. A. Seafeldt, “A fast, convenient program for computation of surface-wave dispersion curves in multilayered media,” *Bull. Soc. Am.*, vol. 51, pp. 495–502, Oct 1961.
- [10] F. Gilbert, “Propagation of transient leaking modes in a stratified elastic waveguide,” *Rev. Geophys.*, vol. 2, pp. 123–153, Feb 1964.
- [11] F. Gilbert and G. E. Backus, “Propagator matrices in elastic wave and vibration problems,” *Geophysics*, vol. 31, pp. 326–332, Apr 1966.
- [12] M. J. Randall, “Fast programs for layered half-space problems,” *Bull. Soc. Am.*, vol. 57, pp. 1299–1315, Dec 1967.
- [13] T. H. Watson, “A note on fast computation of Rayleigh wave dispersion in the multilayered elastic half-space,” *Bull. Soc. Am.*, vol. 60, pp. 161–166, Feb 1970.

- [14] A. H. Fahmy and E. L. Adler, "Propagation of acoustic surface waves in multilayers: A matrix description," *Appl. Phys. Lett.*, vol. 22, pp. 495–497, Oct 1973.
- [15] A. H. Nayfeh and T. W. Taylor, "Surface wave characteristics of fluid-loaded multilayered media," *J. Acoust. Soc. Am.*, vol. 84, pp. 2187–2191, Aug 1988.
- [16] E. L. Adler, "Matrix methods applied to acoustic waves in multilayers," *IEEE Trans. Ultrason. Ferroelec. Freq. Contr.*, vol. 37, pp. 485–490, Nov 1990.
- [17] A. H. Nayfeh and T. W. Taylor, "Dynamic Distribution of Displacement and Stress Considerations in the Ultrasonic Immersion Nondestructive Evaluation of Multilayered Plates," *J. Eng. Mater. Technol.*, vol. 112, pp. 260–265, July 1990.
- [18] A. H. Nayfeh and D. E. Chimenti, "Ultrasonic Wave Reflection From Liquid-Coupled Orthotropic Plates With Application to Fibrous Composites," *J. Appl. Mechs.*, vol. 55, pp. 863–870, Dec 1988.
- [19] A. H. Nayfeh and D. E. Chimenti, *Rev. Prog. QNDE*, ch. Free Wave Propagation in Plates of General Anisotropic Media, pp. 181–188. Plenum Press, New York, 1989.
- [20] A. H. Nayfeh, "The propagation of horizontally polarized shear waves in multilayered anisotropic media," *J. Acoust. Soc. Am.*, vol. 86, pp. 2007–2012, July 1989.
- [21] A. H. Nayfeh, "The general problem of elastic wave propagation in multilayered anisotropic media," *J. Acoust. Soc. Am.*, vol. 89, pp. 1521–1531, Oct 1991.
- [22] A. H. Nayfeh, *Wave Propagation in Layered Anisotropic Media with Applications to Composites*. North-Holland, Amsterdam, 1995.
- [23] J. W. Dunkin, "Computation of modal solutions in layered, elastic media at high frequencies," *Bull. Soc. Am.*, vol. 55, pp. 335–358, Apr 1965.
- [24] E. N. Thrower, "The computation of the dispersion of elastic waves in layered media," *J. Sound Vib.*, vol. 2, pp. 210–226, July 1965.
- [25] R. Kind, "Computation of Reflection Coefficients for Layered Media," *J. Geophys.*, vol. 42, pp. 191–200, Apr 1976.
- [26] R. Kind, "The reflectivity method for a buried source," *J. Geophys.*, vol. 44, pp. 603–12, Dec 1977.

-
- [27] A. Abo-Zena, "Dispersion function computations for unlimited frequency values," *Geophys. J. Int.*, vol. 58, p. 91–105, July 1979.
- [28] W. Menke, "Comment on 'Dispersion function computations for unlimited frequency values' by Anas Abo-Zena," *Geophys. J. Int.*, vol. 59, p. 315–323, Nov 1979.
- [29] R. B. Evans, "The decoupling of seismic waves," *Wave Motion*, vol. 8, pp. 321–328, July 1986.
- [30] D. Lévesque and L. Piché, "A robust transfer matrix formulation for the ultrasonic response of multilayered absorbing media," *J. Acoust. Soc. Am.*, vol. 92, pp. 452–467, Mar 1992.
- [31] M. Castaings and B. Hosten, "Transfer matrix of multilayered absorbing and anisotropic media. Measurements and simulations of ultrasonic wave propagation through composite materials," *J. Acoust. Soc. Am.*, vol. 94, pp. 1488–1495, May 1993.
- [32] M. Castaings and B. Hosten, "Delta operator technique to improve the Thomson-Haskell-method stability for propagation in multilayered anisotropic absorbing plates," *J. Acoust. Soc. Am.*, vol. 95, pp. 1931–1941, July 1994.
- [33] L. Knopoff, "A matrix method for elastic wave problems," *Bull. Seism. Soc. Am.*, vol. 54, pp. 431–438, Feb 1964.
- [34] J. D. Achenbach and S. P. Keshava, "Free Waves in a Plate Supported by a Semi-Infinite Continuum," *J. Appl. Mechs.*, vol. 34, no. 2, pp. 397–404, 1967.
- [35] J. L. Bleustein, "Some Simple Modes of Wave Propagation in an Infinite Piezoelectric Plate," *J. Acoust. Soc. Am.*, vol. 45, no. 3, pp. 614–620, 1969.
- [36] F. A. Schwab, "Surface-wave dispersion computations: Knopoff's method," *Bull. Seism. Soc. Am.*, vol. 60, pp. 1491–1520, Oct 1970.
- [37] A. H. Nayfeh, D. E. Chimenti, L. Adler, and R. L. Crane, "Ultrasonic leaky waves in the presence of a thin layer," *J. Appl. Phys.*, vol. 52, no. 8, pp. 4985–4994, 1981.
- [38] D. E. Chimenti, A. H. Nayfeh, and D. L. Butler, "Leaky Rayleigh waves on a layered halfspace," *J. Appl. Phys.*, vol. 53, no. 1, pp. 170–176, 1982.
- [39] M. J. S. Lowe, *Plate waves for the NDT of diffusion bonded titanium*. PhD thesis, University of London, 1992.

- [40] M. J. S. Lowe, "Matrix Techniques for Modeling Ultrasonic Waves in Multilayered Media," *IEEE Trans. Ultrason. Ferroelec. Freq. Contr.*, vol. 42, pp. 525–542, Jul 1995.
- [41] H. Schmidt and G. Tango, "Efficient global matrix approach to the computation of synthetic seismograms," *Geophys. J. R. Astr. Soc.*, vol. 84, pp. 331–359, July 1986.
- [42] H. Schmidt and F. B. Jensen, "Efficient numerical solution technique for wave propagation in horizontally stratified environments," *Comp. and Maths. with Appls.*, vol. 11, pp. 699–715, July 1985.
- [43] H. Schmidt and F. B. Jensen, "A full wave solution for propagation in multilayered viscoelastic media with application to Gaussian beam reflection at fluid–solid interfaces," *J. Acoust. Soc. Am.*, vol. 77, no. 3, pp. 813–825, 1985.
- [44] A. K. Mal, "Wave propagation in layered composite laminates under periodic surface loads," *Wave Motion*, vol. 10, pp. 257–266, June 1988.
- [45] A. K. Mal, "Guided waves in layered solids with interface zones," *Int. J. Engng. Sci.*, vol. 26, pp. 873–881, June 1988.
- [46] E. Kausel and J. M. Roesset, "Stiffness matrices for layered soils," *Bull. Seis. Soc. Am.*, vol. 71, pp. 1743–1761, Dec 1981.
- [47] Y. Wang and R. K. N. D. Rajapakse, "An Exact Stiffness Method for Elastodynamics of a Layered Orthotropic Half-Plane," *J. Appl. Mech.*, vol. 61, no. 2, pp. 339–347, 1994.
- [48] L. Wang and S. I. Rokhlin, *Rev. Prog. QNDE*, ch. Time Resolved Line Focus Acoustic Microscopy of Composites, pp. 1321–1328. Plenum Press, New York, 1999.
- [49] L. Wang and S. I. Rokhlin, *Rev. Prog. QNDE*, ch. Analysis of ultrasonic wave propagation in multiply composites: Homogenization and effective anisotropic media, pp. 1015–1022. Plenum Press, New York, 2000.
- [50] B. L. N. Kennett, *Seismic Wave Propagation in Stratified Media*. Cambridge University Press, New York, 1983.
- [51] B. L. N. Kennett and N. J. Kerry, "Seismic waves in a stratified half space," *Geophys. J. Int.*, vol. 57, p. 557–583, June 1979.
- [52] G. J. Fryer and L. N. Frazer, "Seismic waves in stratified anisotropic media," *Geophys. J. Int.*, vol. 78, p. 691–710, Sep 1984.

-
- [53] G. J. Fryer and L. N. Frazer, “Seismic waves in stratified anisotropic media — II. Elastodynamic eigensolutions for some anisotropic systems,” *Geophys. J. Int.*, vol. 91, p. 73–101, Oct 1987.
- [54] S. I. Rokhlin and W. Huang, “Ultrasonic wave interaction with a thin anisotropic layer between two anisotropic solids: Exact and asymptotic-boundary-condition methods,” *J. Acoust. Soc. Am.*, vol. 92, pp. 1729–1742, June 1992.
- [55] “DISPERSE v2.0.20a.” <http://www.imperial.ac.uk/non-destructive-evaluation/products-and-services/disperse>.
- [56] S. Pant, J. Laliberte, M. Martinez, and B. Rocha, “Derivation and experimental validation of Lamb wave equations for an n-layered anisotropic composite laminate,” *Compos. Struct.*, vol. 111, pp. 566–579, May 2014.
- [57] S. I. Rokhlin and L. Wang, “Stable recursive algorithm for elastic wave propagation in layered anisotropic media: Stiffness matrix method,” *J. Acoust. Soc. Am.*, vol. 112, pp. 822–834, Sep 2002.
- [58] L. Wang and S. I. Rokhlin, “Stable reformulation of transfer matrix method for wave propagation in layered anisotropic media,” *Ultrasonics*, vol. 39, pp. 413–424, Sep 2001.
- [59] S. I. Rokhlin, D. E. Chimenti, and P. B. Nagy, *Physical Ultrasonics of Composites*. Oxford University Press, Oxford, 2011.
- [60] V. G. A. Kamal and V. Giurgiutiu, “Stiffness Transfer Matrix Method (STMM) for Stable Dispersion Curves Solution in Anisotropic Composites,” in *Proc. SPIE*, 2014.
- [61] M. Barski and P. Pajak, “An application of stiffness matrix method to determining of dispersion curves for arbitrary composite materials,” *Journal of KONES Powertrain and Transport*, vol. 23, no. 1, pp. 47–54, 2016.
- [62] M. Barski and P. Pajak, “Determination of Dispersion Curves for Composite Materials With the Use of Stiffness Matrix Method,” *Acta Mech. et Autom.*, vol. 11, pp. 121–128, May 2017.
- [63] A. M. A. Huber and M. G. R. Sause, “Classification of solutions for guided waves in anisotropic composites with large numbers of layers,” *J. Acoust. Soc. Am.*, vol. 144, p. 3236–3251, Dec 2018.

- [64] “Dispersion Calculator, available at.” https://www.dlr.de/zlp/en/desktopdefault.aspx/tabid-14332/24874_read-61142/#!/gallery/33485.
- [65] L. Gavric, “Computation and propagative waves in free rail using a finite element technique,” *J. Sound Vib.*, vol. 185, pp. 531–543, Aug 1995.
- [66] T. Hayashi, W.-J. Song, and J. L. Rose, “Guided wave dispersion curves for a bar with an arbitrary cross-section, a rod and rail example,” *Ultrasonics*, vol. 41, pp. 175–183, May 2003.
- [67] M. Castaings and M. J. S. Lowe, “Finite element model for waves guided along solid systems of arbitrary section coupled to infinite solid media,” *J. Acoust. Soc. Am.*, vol. 123, pp. 696–708, Nov 2008.
- [68] Z. Fan, M. J. S. Lowe, M. Castaings, and C. Bacon, “Torsional waves propagation along a waveguide of arbitrary cross section immersed in a perfect fluid,” *J. Acoust. Soc. Am.*, vol. 124, pp. 2002–2010, July 2008.
- [69] Z. Fan and M. J. S. Lowe, “Elastic waves guided by a welded joint in a plate,” in *Proc. R. Soc. Lond. A*, pp. 2053–2068, 2009.
- [70] I. Bartoli, A. Marzani, F. L. di Scalea, and E. Viola, “Modeling wave propagation in damped waveguides of arbitrary cross-section,” *J. Sound Vib.*, vol. 295, pp. 685–707, Aug 2006.
- [71] A. Marzani, E. Viola, I. Bartoli, F. L. di Scalea, and P. Rizzo, “A semi-analytical finite element formulation for modeling stress wave propagation in axisymmetric damped waveguides,” *J. Sound Vib.*, vol. 318, pp. 488–505, Aug 2008.
- [72] S. Sorohan, N. Constantin, M. Găvan, and V. Anghel, “Extraction of dispersion curves for waves propagating in free complex waveguides by standard finite element codes,” *Ultrasonics*, vol. 51, pp. 503–515, Aug 2011.
- [73] P. P. Delsanto, R. S. Schechter, and R. B. Mignogna, “Connection machine simulation of ultrasonic wave propagation in materials III: The three-dimensional case,” *Wave Motion*, vol. 26, pp. 329–339, Dec 1997.
- [74] M. Ruzzene, S. M. Jeong, T. E. Michaels, J. E. Michaels, and B. Mi, *Rev. Prog. QNDE*, ch. Simulation and Measurement of Ultrasonic Waves in Elastic Plates Using Laser Vibrometry, pp. 172–179. Green Bay, Wisconsin, 2005.

-
- [75] K. S. Nadella and C. E. S. Cesnik, “Local interaction simulation approach for modeling wave propagation in composite structures,” *CEAS Aeronaut. J.*, vol. 4, p. 35–48, Apr 2013.
- [76] A. T. I. Adamou and R. V. Craster, “Spectral methods for modelling guided waves in elastic media,” *J. Acoust. Soc. Am.*, vol. 116, pp. 1524–1535, June 2004.
- [77] F. Karpfinger, B. Gurevich, and A. Bakulin, “Modeling of wave dispersion along cylindrical structures using the spectral method,” *J. Acoust. Soc. Am.*, vol. 124, pp. 859–865, May 2008.
- [78] F. Karpfinger, B. Gurevich, and A. Bakulin, “Modeling of axisymmetric wave modes in a poroelastic cylinder using spectral method,” *J. Acoust. Soc. Am.*, vol. 124, pp. EL230–EL235, July 2008.
- [79] F. Karpfinger, H.-P. Valero, B. Gurevich, A. Bakulin, and B. Sinha, “Spectral-method algorithm for modeling dispersion of acoustic modes in elastic cylindrical structures,” *Geophysics*, vol. 75, pp. H19–H27, May 2010.
- [80] F. Karpfinger, B. Gurevich, H.-P. Valero, A. Bakulin, and B. Sinha, “Tube wave signatures in cylindrically layered poroelastic media computed with spectral method,” *Geophys. J. Int.*, vol. 183, p. 1005–1013, Nov 2010.
- [81] B. Yu, S. Yang, C. Gan, and H. Lei, “A new procedure for exploring the dispersion characteristics of longitudinal guided waves in a multi-layered tube with a weak interface,” *J. Nondestruct. Eval.*, vol. 32, p. 263–276, Sep 2013.
- [82] T. Zharnikov, D. Syresin, and C.-J. Hsu, “Application of the spectral method for computation of the spectrum of anisotropic waveguides,” in *Proc. Mtgs. Acoust.*, vol. 19, p. 045065, Jan 2013.
- [83] F. H. Quintanilla, M. J. S. Lowe, and R. V. Craster, “Modeling guided elastic waves in generally anisotropic media using a spectral collocation method,” *J. Acoust. Soc. Am.*, vol. 137, pp. 1180–1194, Mar 2015.
- [84] F. H. Quintanilla, Z. Fan, M. J. S. Lowe, and R. V. Craster, “Guided waves’ dispersion curves in anisotropic viscoelastic single- and multi-layered media,” in *Proc. R. Soc. Lond. A*, pp. 1–23, Nov 2015.
- [85] F. H. Quintanilla, M. J. S. Lowe, and R. V. Craster, “Full 3d dispersion curve solutions for guided waves in generally anisotropic media, journal of sound and vibration,” *J. Sound Vib.*, vol. 363, pp. 545–559, Feb 2016.

- [86] F. H. Quintanilla, M. J. S. Lowe, and R. V. Craster, “The symmetry and coupling properties of solutions in general anisotropic multilayer waveguides,” *J. Acoust. Soc. Am.*, vol. 141, pp. 406–418, Jan 2017.
- [87] I. A. Viktorov, *Rayleigh and Lamb Waves: Physical Theory and Applications*. Plenum, New York, 1967.
- [88] M. Luukkala, P. Heikkilä, and J. Surakka, “Plate wave resonance - A contactless test method,” *Ultrasonics*, vol. 9, pp. 201–208, Oct 1971.
- [89] M. Luukkala and P. Meriläinen, “Metal plate testing using airborne ultrasound,” *Ultrasonics*, vol. 11, pp. 218–221, Sept 1973.
- [90] P. D. Wilcox, M. J. S. Lowe, and P. Cawley, “Mode and transducer selection for long range Lamb wave inspection,” *J. Intell. Mater. Syst. Struct.*, vol. 12, pp. 553–565, Aug 2001.
- [91] M. J. S. Lowe, D. N. Alleyne, and P. Cawley, “Defect detection in pipes using guided waves,” *Ultrasonics*, vol. 36, pp. 147–154, 1998.
- [92] M. J. S. Lowe and P. Cawley, “The applicability of plate wave techniques for the inspection of adhesive and diffusion bonded joints,” *J. Nondestr. Eval.*, vol. 13, pp. 185–200, Sep 1994.
- [93] T. Kundu, A. Maji, T. Gosh, and K. Maslov, “Detection of kissing bonds by Lamb waves,” *Ultrasonics*, vol. 35, pp. 573–580, June 1998.
- [94] K. Maslov and T. Kundu, “Selection of Lamb modes for detecting internal defects in composite laminates,” *Ultrasonics*, vol. 35, pp. 141–150, 1997.
- [95] S. S. Kessler, S. M. Spearing, and C. Soutis, “Damage detection in composite materials using Lamb wave methods,” *Smart Mater. Struct.*, vol. 11, pp. 269–278, 2002.
- [96] N. Toyama, J. Noda, and T. Okabe, “Quantitative damage detection in cross-ply laminates using Lamb wave method,” *Compos. Sci. Technol.*, vol. 63, pp. 1473–1479, March 2003.
- [97] Z. Su, L. Ye, and Y. Lu, “Guided Lamb waves for identification of damage in composite structures: A review,” *J. Sound Vib.*, vol. 295, pp. 753–780, March 2006.
- [98] K. Diamanti and C. Soutis, “Structural health monitoring techniques for aircraft composite structures,” *Prog. Aeronaut. Sci.*, vol. 46, p. 342–352, May 2010.

-
- [99] A. S. Purekar and D. J. Pines, “Damage detection in thin composite laminates using piezoelectric phased sensor arrays and guided Lamb wave interrogation,” *J. Intell. Mater. Syst. Struct.*, vol. 21, pp. 995–1010, July 2010.
- [100] C. Ramadas, K. Balasubramaniam, M. Joshi, and C. V. Krishnamurthy, “Sizing of interface delamination in a composite T-joint using time-of-flight of Lamb waves,” *J. Intell. Mater. Syst. Struct.*, vol. 22, pp. 757–768, May 2011.
- [101] H. Cunfu, L. Hongye, L. Zenghua, and W. Bin, “The propagation of coupled Lamb waves in multilayered arbitrary anisotropic composite laminates,” *J. Sound Vib.*, vol. 332, p. 7243–7256, Sep 2013.
- [102] M. Castaings and P. Cawley, “The generation, propagation, and detection of Lamb waves in plates using air-coupled ultrasonic transducers,” *J. Acoust. Soc. Am.*, vol. 100, pp. 3070–3077, Nov 1996.
- [103] M. Castaings, P. Cawley, R. Farlow, and G. Hayward, “Single Sided Inspection of Composite Materials Using Air Coupled Ultrasound,” *J. Nondestr. Eval.*, vol. 17, pp. 37–45, Mar 1998.
- [104] M. Castaings and B. Hosten, “Lamb and SH waves generated and detected by air-coupled ultrasonic transducers in composite material plates,” *NDT&E Int.*, vol. 34, pp. 249–258, June 2001.
- [105] M. Castaings and B. Hosten, “Ultrasonic guided waves for health monitoring of high-pressure composite tanks,” *NDT&E Int.*, vol. 41, pp. 648–655, April 2008.
- [106] I. Solodov, R. Stoessel, and G. Busse, “Material characterization and NDE using focused slanted transmission mode of air-coupled ultrasound,” *Res. Nondestr. Eval.*, vol. 15, pp. 65–85, Aug 2004.
- [107] I. Solodov, K. Pfeiderer, H. Gerhard, and G. Busse, “Nonlinear acoustic approach to material characterisation of polymers and composites in tensile tests,” *Ultrasonics*, vol. 42, p. 1011–1015, 2004.
- [108] I. Solodov, K. Pfeiderer, H. Gerhard, S. Predak, and G. Busse, “New opportunities for NDE with air-coupled ultrasound,” *NDT&E Int.*, vol. 39, pp. 176–183, Apr 2006.
- [109] M. Rheinfurth, F. Schmidt, D. Döring, I. Solodov, G. Busse, and P. Horst, “Air-coupled guided waves combined with thermography for monitoring fatigue in biaxially loaded composite tubes,” *Compos. Sci. Technol.*, vol. 71, pp. 600–608, Mar 2011.

- [110] M. Rheinfurth, N. Kosmann, D. Sauer, G. Busse, and K. Schulte, “Lamb waves for non-contact fatigue state evaluation of composites under various mechanical loading conditions,” *Composites: Part A*, vol. 43, pp. 1203–1211, 2012.
- [111] M. Rheinfurth, *Geführte Ultraschallwellen zur Bewertung der Schadensakkumulation in Faser-Kunststoff-Verbunden*. PhD thesis, Fakultät Luft- und Raumfahrttechnik und Geodäsie der Universität Stuttgart, 2013.
- [112] S. D. Holland and D. E. Chimenti, “High contrast air-coupled acoustic imaging with zero group velocity Lamb modes,” *Ultrasonics*, vol. 42, p. 957–960, Sep 2004.
- [113] R. Raisutis, R. Kazys, E. Zukauskas, and L. Mazeika, “Ultrasonic air-coupled testing of square-shape CFRP composite rods by means of guided waves,” *NDT&E International*, vol. 44, pp. 645–654, July 2011.
- [114] L. Zenghua, Y. Hongtao, H. Cunfu, and W. Bin, “Delamination damage detection of laminated composite beams using air-coupled ultrasonic transducers,” *Science China*, vol. 56, p. 1269–1279, May 2013.
- [115] E. Cuevas and S. Hernandez, “Robot-based solution to obtain an automated, integrated and industrial non-destructive inspection process,” in *6th International Symposium on NDT in Aerospace*, Nov 2014.
- [116] C. Mineo, J. Riise, S. G. Pierce, P. I. Nicholson, and I. Cooper, “Robotic path planning for non-destructive testing through RoboNDT,” in *54th Annual Conference of the British Institute of Non-Destructive Testing*, Sept 2015.
- [117] W. Hillger, R. Oster, J. Schuller, R. Stössel, S. Lang, J. Bosse, B. Thaler, D. Ilse, and L. Bühling, “Automated Air-Coupled Ultrasonic Technique for the Inspection of the EC 145 Tail Boom,” in *4th International Symposium on NDT in Aerospace*, pp. 1–7, Nov 2012.
- [118] A. Huber, “Non-destructive Testing of Future Rocket Boosters Using Air-Coupled Ultrasound,” in *19th World Conference on Non-Destructive Testing*, pp. 1–9, June 2016.
- [119] M. Schönheits, A. Huber, and P. Gänswürger, “Air-coupled Ultrasonic Inspection with Adaptive Lamb Wave Control,” in *ICINCO*, 2019.
- [120] W. Gebhardt, W. Hillger, and P. Kreier, “Airborne Ultrasonic Probes: Design, Fabrication, Application,” in *7th European Conference on Nondestructive Testing*, pp. 3098–3105, May 1998.

-
- [121] W. A. Smith and B. A. Auld, "Modeling 1-3 composite piezoelectrics: thickness-mode oscillations," *IEEE Trans. Ultrason. Ferroelec. Freq. Contr.*, vol. 38, pp. 40–47, Jan 1991.
- [122] D. Schindel, D. A. Hutchins, L. Zou, and M. Sayer, "The design and characterisation of micro machined air-coupled capacitance transducers," *IEEE Trans. Ultrason. Ferroelec. Freq. Contr.*, vol. 42, no. 1, pp. 42–50, 1995.
- [123] D. Schindel and D. A. Hutchins, "Applications of micro machined capacitance transducers in air-coupled ultrasonics and non destructive evaluation," *IEEE Trans. Ultrason. Ferroelec. Freq. Contr.*, vol. 42, no. 1, pp. 51–58, 1995.
- [124] M. I. Haller and B. T. Khuri-Yakub, "A surface micro machined electrostatic ultrasonic air transducer," in *Proc. IEEE Ultrason. Symp.*, vol. 2, pp. 1241–1244, 1994.
- [125] M. J. Anderson, J. A. Hill, C. M. Fortunko, N. S. Dogan, and R. D. Moore, "Broadband electrostatic transducers: modelling and experiments," *J. Acoust. Soc. Am.*, vol. 97, pp. 262–272, 1995.
- [126] C. D. Gerardo, E. Cretu, and R. Rohling, "Fabrication of Circuits on Flexible Substrates Using Conductive SU-8 for Sensing Applications," *Sensors*, vol. 17, pp. 1–15, June 2017.
- [127] C. D. Gerardo, E. Cretu, and R. Rohling, "Fabrication and testing of polymer-based capacitive micromachined ultrasound transducers for medical imaging," *Microsystems & Nanoengineering*, vol. 4, pp. 1–12, Aug 2018.
- [128] A. Harrer, M. Daschewski, J. Prager, M. Kreutzbruck, M. Guderian, and A. Meyer-Plath, "Thermoacoustic generation of airborne ultrasound using carbon materials at the micro- and nanoscale," *Int. J. Appl. Electromag. Mech.*, vol. 39, pp. 35–41, Sept 2012.
- [129] M. Daschewski, R. Boehm, J. Prager, M. Kreutzbruck, and A. Harrer, "Physics of thermo-acoustic sound generation," *J. Appl. Phys.*, vol. 114, pp. 1–12, Sept 2013.
- [130] W. Voigt, *Lehrbuch der kristallphysik*. Teubner, Leipzig, 1910.
- [131] B. A. Auld, *Acoustic Fields and Waves in Solids*, vol. 1. Krieger Malabar, FL, 1990.
- [132] M. Lowe and B. Pavlakovic, *Disperse User's Manual*. Imperial College London, London, 2013.

- [133] J. C. Maxwell, “A Dynamical Theory of the Electromagnetic Field,” *J. Philosophical Transactions of the Royal Society of London (1776-1886)*, vol. 155, p. 459–512, 1865.
- [134] R. Hook, *De Potentia Restitutiva, or of Spring Explaining the Power of Springing Bodies*. London, 1678.
- [135] A. Einstein, “Die Grundlage der allgemeinen Relativitätstheorie,” *Ann. Phys.*, vol. 354, no. 7, pp. 769–822, 1916.
- [136] T. Young, *A Course of Lectures on Natural Philosophy and the Mechanical Arts*, vol. 1. Taylor and Walton, 1845.
- [137] S. Poisson, *Traité De Mécanique*. Bachelier, Paris, 1833.
- [138] F. I. Fedorov, *Theory of Elastic Waves in Crystals*. Plenum, New York, 1968.
- [139] M. J. P. Musgrave, *Chrystal Acoustics*. Holden Day, San Francisco, 1970.
- [140] E. B. Christoffel, “Untersuchungen über die mit dem Fortbestehen linearer partieller Differentialgleichungen verträglichen Unstetigkeiten,” *Ann. Mat.*, vol. 8, p. 81–112, Jan 1877.
- [141] E. B. Christoffel, “Ueber die Fortpflanzung von Stößen durch elastische feste Körper,” *Ann. Mat.*, vol. 8, p. 193–243, Jan 1877.
- [142] R. Descartes, *La Dioptrique*. 1637.
- [143] G. Neau, *Lamb waves in anisotropic viscoelastic plates. Study of wave fronts and attenuation*. PhD thesis, University of Bordeaux, 2003.
- [144] L. Wang and F. G. Yuan, “Group velocity and characteristic wave curves of Lamb waves in composites: Modeling and experiments,” *Compos. Sci. Technol.*, vol. 67, pp. 1370–1384, Sep 2007.
- [145] E. Glushkov, N. Glushkova, and A. Eremin, “Group velocity of cylindrical guided waves in anisotropic laminate composites,” *J. Acoust. Soc. Am.*, vol. 135, no. 1, pp. 148–154, 2014.
- [146] M. Sause, *Identification of Failure Mechanisms in Hybrid Materials Utilizing Pattern Recognition Techniques Applied to Acoustic Emission Signals*. PhD thesis, Mathematisch-Naturwissenschaftliche Fakultät der Universität Augsburg, 2010.
- [147] M. Sause and M. Hamstad, *Acoustic Emission Analysis*. Academic, Oxford, 2018.

-
- [148] J. L. Rose, *Ultrasonic Waves in Solid Media*. Cambridge University Press, Cambridge, 1999.
- [149] B. A. Auld, *Acoustic Fields and Waves in Solids*, vol. 2. Krieger Malabar, FL, 1990.
- [150] J. D. Achenbach, *Wave Propagation in Elastic Solids*. North-Holland, New York, 1984.
- [151] J. L. Rose, “A Baseline and Vision of Ultrasonic Guided Wave Inspection Potential,” *J. Pressure Vessel Technol.*, vol. 124, pp. 273–282, July 2002.
- [152] T. Ullmann, Y. Shi, N. Rahner, M. Schmücker, P. Fey, G. Busse, and S. Becker, “Quality Assurance for the Manufacturing of Oxide Fiber Reinforced Ceramic Composites for Aerospace Applications,” in *4th International Symposium on NDT in Aerospace*, pp. 1–11, Nov 2012.
- [153] A.-M. Zelenyak, R. Oster, M. Mosch, P. Jahnke, and M. G. R. Sause, “Numerical Modeling of Ultrasonic Inspection in Fiber Reinforced Materials with Explicit Microstructure,” in *19th World Conference on Non-Destructive Testing*, pp. 1–8, June 2016.
- [154] R. Farlow and G. Hayward, “Real-time ultrasonic techniques suitable for implementing noncontact NDT systems employing piezoceramic composite transducers,” *Insight*, vol. 36, pp. 926–935, 1994.
- [155] “Airbus Test Method For Inspection Processes, Non Destructive Inspection of Composite Parts,” *AITM6-0011*, pp. 1–28, Mar 2009.
- [156] M. Springmann, P. Fey, G. Busse, and M. Kreuzbruck, “Reduktion von Abbildungsfehlern bei luftgekoppeltem Ultraschall mit einseitigem Zugang,” in *DACH Jahrestagung*, pp. 1–8, May 2015.
- [157] C. Othmani, S. Dahmen, A. Njeh, and M. H. B. Ghazlen, “Investigation of guided waves propagation in orthotropic viscoelastic carbon–epoxy plate by Legendre polynomial method,” *Mech. Res. Commun.*, vol. 74, pp. 27–33, June 2016.
- [158] W. D. Callister, *Material Science and Engineering. An Introduction*. John Wiley & Sons, Inc., 2002.

Curriculum Vitae

Personal Data

Name Armin Huber
Date of birth August 20, 1982
Place of birth Augsburg
Nationality German



Education and Professional Experience

2021 Dr. rer. nat. (PhD), Faculty of Mathematics, Natural Sciences, and Materials Engineering of the University of Augsburg, Augsburg, Germany
Since 08/2013 Scientist at the Center for Lightweight Production Technology (ZLP) of the German Aerospace Center (DLR), Augsburg, Germany

- Production process-integrated robot-assisted air-coupled ultrasonic inspection of CFRP components for aerospace vehicles
- Single-sided inspection by using Lamb waves and transmissive inspection
- Water-coupled ultrasonic inspection (Olympus Omni-Scan SX)
- Physical ultrasonics
- Software development in MATLAB[®]

10/2009 - 07/2013 Scientist at the Chair for Experimental Physics II of the University of Augsburg, Augsburg, Germany

- Infrared spectroscopy on high-temperature superconductors under high pressure and low temperatures
- Teaching in solid state physics

10/2003 - 04/2009 M. Sc. Material Sciences, University of Augsburg, Augsburg, Germany

Publications

1. **Air-coupled Ultrasonic Inspection with Adaptive Lamb Wave Control**

Manfred Schönheits, Armin Huber, and Philipp Gänswürger

Conference Proceedings: 16th International Conference on Informatics in Control, Automation and Robotics, Prague, Czech Republic (2019)

2. **Classification of solutions for guided waves in anisotropic composites with large numbers of layers**

Armin M. A. Huber and Markus G. R. Sause

The Journal of the Acoustical Society of America, 144(6), pp. 3236-3251 (2018)

doi: 10.1121/1.5082299

3. **Dispersion Calculator**

Armin Huber

DLR-homepage (2018)

https://www.dlr.de/zlp/en/desktopdefault.aspx/tabid-14332/24874_read-61142/#/gallery/33485

4. **Tailor-made Thermoplastics: Production Technology and Quality Assurance of a Thermoplastic Aircraft Fuselage Skin Segment**

Matthias Beyrle, Roland Glück, Georg Braun, Manuel Endrass, Frederic C. Fischer, Armin Huber, Michael Kühnel, Alfons Schuster, Stefan Jarka, Lars Brandt, Stefan Schneyer, Christian Rähitz, Philipp Gänswürger, Tobias Gerngross, and Michael Kupke

Conference Proceedings: 21st International Conference on Composite Materials, Xi'an, China (2017)

5. **Non-destructive Testing of Future Rocket Boosters Using Air-Coupled Ultrasound**

Armin Huber

Conference Proceedings: 19th World Conference on Non-Destructive Testing, Munich, Germany (2016)

Patents

1. **DE: 10 2014 105 110.6**

Verfahren zum Prüfen von Bauteilen und Prüfeinrichtung

Thomas Schmidt, Armin Huber, and Stefan Nuschele

Deutsches Patent- und Markenamt, Munich, Germany (2018)

<https://register.dpma.de/DPMAregister/pat/register?AKZ=1020141051106&CURSOR=0>